n

MacKenzie, Lewis Edward (2016) *In vivo mirovacular oximetry using multispectral imaging*. PhD thesis.

http://theses.gla.ac.uk/7732/

Available under License Creative Commons Attribution Non-commercial Share Alike.

When referring to this work, full bibliographic details including the author, title, awarding institution and date of the thesis must be given

Glasgow Theses Service
http://theses.gla.ac.uk/
theses@gla.ac.uk

In vivo microvascular oximetry using multispectral imaging

Lewis Edward MacKenzie

B.Sc. (Hons.), M.Sc.

Submitted in fulfilment of the requirements

for the degree of Doctor of Philosophy.

31st October 2016

School of Physics and Astronomy

College of Science and Engineering

University of Glasgow

Abstract

This thesis describes the application of multispectral imaging to several novel oximetry applications. Chapter 1 motivates optical microvascular oximetry, outlines oxygen transport in the body, describes the theory of oximetry, and describes the challenges associated with *in vivo* oximetry, in particular imaging through tissue. Chapter 2 reviews various imaging techniques for quantitative *in vivo* oximetry of the microvasculature, including multispectral and hyperspectral imaging, photoacoustic imaging, optical coherence tomography, and laser speckle techniques.

Chapter 3 describes a two-wavelength oximetry study of two microvascular beds in the anterior segment of the eye: the bulbar conjunctival and episcleral microvasculature. This study reveals previously unseen oxygen diffusion from ambient air into the bulbar conjunctival microvasculature, altering the oxygen saturation of the bulbar conjunctiva. The response of the bulbar conjunctival and episcleral microvascular beds to acute mild hypoxia is quantified and the rate at which oxygen diffuses into bulbar conjunctival vessels is quantified.

Chapter 4 describes the development and application of a highly novel non-invasive retinal angiography technique: Oximetric Ratio Contrast Angiography (ORCA). ORCA requires only multispectral imaging and a small perturbation of blood oxygen saturation to produce angiographic sequences. A pilot study of ORCA in human subjects was conducted. This study demonstrates that ORCA can produce angiographic sequences with features such as sequential vessel filling and laminar flow. The application and challenges of ORCA are discussed, with emphasis on comparison with other angiography techniques, such as fluorescein angiography.

Chapter 5 describes the development of a multispectral microscope for oximetry in the spinal cord dorsal vein of rats. Measurements of blood oxygen saturation are made in the dorsal vein of both healthy rats, and in rats with the Experimental autoimmune encephalomyelitis (EAE) disease model of multiple sclerosis. The venous blood oxygen saturation of EAE disease model rats was found to be significantly lower than that of healthy controls, indicating increased oxygen uptake from blood in the EAE disease model of multiple sclerosis.

Chapter 6 describes the development of video-rate red eye oximetry; a technique which could enable stand-off oximetry of the blood-supply of the eye with high temporal resolution. The various challenges associated with video-rate red eye oximetry are investigated and their influence quantified. The eventual aim of this research is to track circulating deoxygenation perturbations as they arrive in both eyes, which could provide a screening method for carotid artery stenosis, which is major risk-factor for stroke. However, due to time constraints, it was not possible to thoroughly investigate if video-rate red eye can detect such perturbations. Directions and recommendations for future research are outlined.

Table of Contents

List of Tables

List of Figures

Acknowledgements

I would like to acknowledge the help, support, and advice from the plethora of people who have helped make this research possible.

First of all, I would like to thank my supervisor, Professor Andrew Harvey, for his enthusiasm, expertise, knowledge, ideas, and support throughout the duration of this research. Thanks also to my second supervisor, Dr Ik Siong Heng, for his insights into image and signal processing, and general support.

It has been a pleasure to work with all my colleagues in the Imaging Concepts Group, who have been very friendly, supportive, and knowledgeable. I'd particularly like to thank Dr Tushar Choudhary for encouraging new ideas and providing key insights into the bulbar conjunctival oximetry project. Thanks to Javier Fernadez-Ramos for his help with configuring IRIS and for developing the multispectral oximetry algorithm employed in Chapter 5. Thanks also to Marieke van der Putten for helping develop the multispectral oximetry algorithm and her work on the associated analysis of the rat spinal cord oximetry data.

The team at the UCL Institute of Neurology have been brilliant collaborators through many hard days in the lab. Thanks to Dr Andrew Davies for his friendliness and expertise, and also for teaching me how to play the great sport of darts. Thanks to Dr Roshni Desai and Dr Maria Sajic for their help with animal work, and thanks to Professor Ken Smith for supporting the project and providing valuable insight.

Acknowledgements (cont.)

Multiple medical and clinical collaborators have provided invaluable insight to these projects. Thanks to Professor Andy McNaught for his enthusiasm, expertise, and support for the bulbar conjunctival and episcleral oximetry and insight to retinal angiography.

Thanks to Professor Nigel Benjamin for providing the idea of inducing and tracking a transient deoxygenation wave as it flows around the body.

Thanks to Professor Christian Delles for his support of the dye-free angiography work, including ethical proposals, cardiovascular expertise, and provision of equipment and resources; it is greatly appreciated.

Thanks also to Professor Matthew Walters and Dr Jesse Dawson for their support of the dye-free angiography study.

Thanks also to my viva committee for arranging a thorough and intellectually stimulating examination. Thanks to Prof. John Girkin for agreeing to be the external examiner, and thanks to Prof. Lyndsay Fletcher for agreeing to be the internal examiner. Thanks to Dr Jonathan Taylor for organising.

Thanks to Cecilie Osnes for brightening up my days and listening to me ramble on about blood vessels far too often. Finally I would like to thank my family (June, Jack, Allan, and Isla) for supporting and encouraging me to pursue science research.

Abbreviations

AOTF: Acousto Optical Tuneable Filter.

CTIS: Computed Tomography Imaging Spectrometer.

DOF: Depth of Field.

DWPT-OCT: Dual Wavelength Photothermal Optical Coherence Tomography.

EAE: Experimental Autoimmune Encephalomyelitis.

FA: Fluorescein Angiography.

FiO_2: Fraction of Inspired Oxygen.

FOV: Field of View.

GUI: Graphical User Interface.

Hb: Haemoglobin.

HSI: Hyperspectral Imaging.

IMS: Image Mapping Spectrometer.

IR: Intensity Ratio.

IRIS: Image Replicating Imaging Spectrometer.

LSCI: Laser Speckle Contrast Imaging.

mmHg: millimetre of Mercury.

MS: Multiple Sclerosis.

MSI: Multispectral Imaging.

MS-PAT: Multispectral Photoacoustic Tomography.

NIR: Near Infrared.

O_2Hb: Oxygenated Haemoglobin.

Abbreviations (continued)

OCT: Optical Coherence Tomography.

OD: Optical Density.

ODR: Optical Density Ratio.

ORCA: Oximetric Ratio Contrast Angiography.

OSLO: Objective Speckle Laser Oximetry.

PAM: Photoacoustic Microscopy.

PAT: Photoacoustic Tomography.

pO_2: Partial Pressure of Oxygen.

RBC: Red Blood Cell.

SD: Standard Deviation.

SE: Standard Error.

SLO: Scanning Laser Ophthalmoscopy.

SMSI: Snapshot Multispectral Imaging.

SO_2: Blood Oxygen Saturation.

S-OCT: Spectroscopic Optical Coherence Tomography.

TDOW: Transient Deoxygenation Wave.

TIFF: Tagged Image File Format.

VIS: Visible.

Author Declaration

I declare that, except where explicit reference is made to the contribution of others, that this thesis is the result of my own work and has not been submitted for any other degree at the University of Glasgow or any other institution.

Lewis MacKenzie

31st October 2016

Attributions

Some of the research in this thesis was conducted collaboration with other researchers. The following people are directly attributed with the following contributions. These contributions are additionally acknowledged within the text and footnotes of this thesis where appropriate.

Chapter 2

- Figure 2-2 provided of Javier Fernandez Ramos.

Chapter 4

- Data for Figure 4-5 provided by Javier Fernandez Ramos.

Chapter 5.

- The multispectral oximetry algorithm was developed by Javier Fernandez Ramos and Marieke van der Putten.
- Analysis of *in vivo* data shown in Section 5.5.2 conducted by Marieke van der Putten. Figure 5-31, and Figure 5-32 provided by Marieke van der Putten. Data in Table 5-4, Table 5-5, and Table 5-6 provided by Marieke van der Putten.
- All animal procedures were undertaken at UCL by Andrew Davies and Roshni Desai in accordance with the Home Office Animals (Scientific Procedures) Act 1986.

Chapter 6:

- Figure 6-2 provided by Tushar Choudhary.

Figures reproduced.

- Figure 1-2, Figure 2-3, Figure 4-7, and Figure 5-1 are reproduced from the public domain. The source for each figure is denoted in an accompanying footnote for each figure, and is directly stated as being reproduced from the public domain in a footnote for each figure.

- Figure 1-1, Figure 1-3, Figure 1-16, Figure 4-1, and Figure 4-2 are reproduced under various Creative Commons licences. Each source and license is directly acknowledged in a footnote for each figure.

1 Introduction to optical microvascular oximetry

Summary: *this chapter introduces the motivation for microvascular oximetry. Key concepts in blood flow and oxygen transport are described. The key challenges associated with in vivo optical oximetry are outlined, and the influence of optical absorption and scattering by tissue on oximetry measurements are described and discussed. The theory of multispectral oximetry techniques are reviewed and discussed.*

1.1 Motivation

Measuring localised microvascular blood oxygen saturation (SO_2) is important for both the monitoring and understanding of disease development and progression. A lack of oxygen reaching bodily tissues (i.e. hypoxia) can have severe consequences, including tissue necrosis and angiogenesis,[1] whilst an over-supply of oxygen (i.e. hyperoxia) can impair cell function and induce disruptive blood vessel development.[2] However, common oximetry techniques, such as pulse oximetry and *ex vivo* blood gas analysis, cannot provide the highly localised measurements of microvascular SO_2 required to provide useful insight into disease development. However, optical multispectral imaging (MSI) techniques be utilised for localised oximetry of the microvasculature with high spatial and temporal resolution. MSI oximetry has provided useful insight into the development of a variety of diseases and conditions associated with cardiovascular impairment, such as diabetes,[3,4] glaucoma,[5–7] retinal vessel occlusion,[8] tumour development,[9] and multiple sclerosis.[10]

Optical MSI oximetry is possible because the spectral absorption of haemoglobin within blood is dependent on SO_2. When oxygen binds or unbinds to haemoglobin, the structure of the haemoglobin molecule is altered. This results in a change in the optical absorption spectra of haemoglobin (see Section 1.4), which can be inferred

by imaging blood vessels at multiple wavelengths and analysing the optical transmission of blood at each wavelength.

Pre-existing broadband optical imaging systems can be adapted for MSI oximetry, including research microscopes,[11] retinal fundus cameras,[12] and slit lamps.[13] This enables oximetry a wide range of imaging applications. Recent advances in snapshot multispectral imaging (SMSI) techniques have also enabled oximetry with sub-second temporal resolution, limited only by detector frame-rate. This has enabled the observation of rapid biological processes such as oxygen release from red blood cells (RBCs).[11]

However *in vivo* oximetry of the microvasculature remains highly challenging due to the complex optical nature of biological tissues, which impair imaging and mar spectral measurements.

The overall aim of this research was to develop new applications of multispectral imaging, particularly in the microvasculature (the smallest blood vessels). Three novel applications of *in vivo* MSI oximetry are described in detail.

Chapter 3 describes the use of SMSI to observe the oxygen dynamics of the bulbar conjunctival and episcleral microvasculature. The bulbar conjunctival microvessels are uniquely situated on the outer surface of the sclera and so are exposed directly to the ambient air. This enables oxygen diffusion into these vessels to occur; the high temporal resolution of snapshot MSI enabled the observation of the rapid (~ 1 second) novel oxygen dynamics of these vessels. Episcleral blood vessels in contrast are embedded within the sclera and so were found to not undergo oxygen diffusion, instead behaving in a more conventional manner, with their SO_2 resembling the systemic blood supply. This study paves the way for future oximetry studies in these microvascular beds.

Chapter 4 describes the development of a new angiography technique which utilises the SO_2-dependent absorption spectra of haemoglobin, and computational image processing, to track blood flow. This non-invasive technique can visualise blood flow features (i.e. sequential vessel filling, and laminar flow) which could only previously be visualised by fluorescein angiography.

Chapter 5 describes the development of a multispectral microscope for oximetry in the spinal cord dorsal vein of rats. The key finding is that the venous SO_2 of rats with a multiple sclerosis disease model is lower in comparison with healthy controls.

Chapter 6 describes the development of video-rate red eye oximetry. The aim of this research is to develop the sensitivity of the technique where it can track small perturbations of SO_2 as they circulate to each eye. Such measurements could potentially be used to screen for carotid artery occlusion, a major risk-factor for stroke.

1.2 Blood flow and oxygen transport

1.2.1 Overview of the circulatory system

The circulatory system is responsible for transport of oxygen and nutrients around the body. Broadly speaking, the circulatory system consists of the lungs, the heart, and all blood vessels. The heart pumps blood around the body; the lungs supply blood with oxygen; the major arteries and veins transport blood long distances around the body, and the microvasculature supplies oxygen and nutrients to local tissue.[14]

Blood consists of the following components: red blood cells (RBCs) (44% volume), plasma (55% volume), and white blood cells and platelets (< 1 % volume).[15] The function of red blood cells is to transport and deliver oxygen. RBCs contain large quantities of the protein haemoglobin, to which oxygen can bind for transport. Haemoglobin is a strong absorber of light, and it is the dominant optical absorber in blood. The absorption spectrum of haemoglobin is dependent on how much oxygen is bound to it, and thus changes in SO_2 alter the absorption of light by blood. This is the basis for optical oximetry (see Section 1.4).[16]

1.2.2 Size and function of blood vessels

Blood vessels range greatly in structure and diameter depending on function. Broadly speaking there are five classifications of blood vessels: arteries, arterioles, capillaries, venules, and veins. The size of blood vessels can vary between species, individuals, and tissue type. The general size and relative number of the various types of blood vessels is summarised in Figure 1-1.

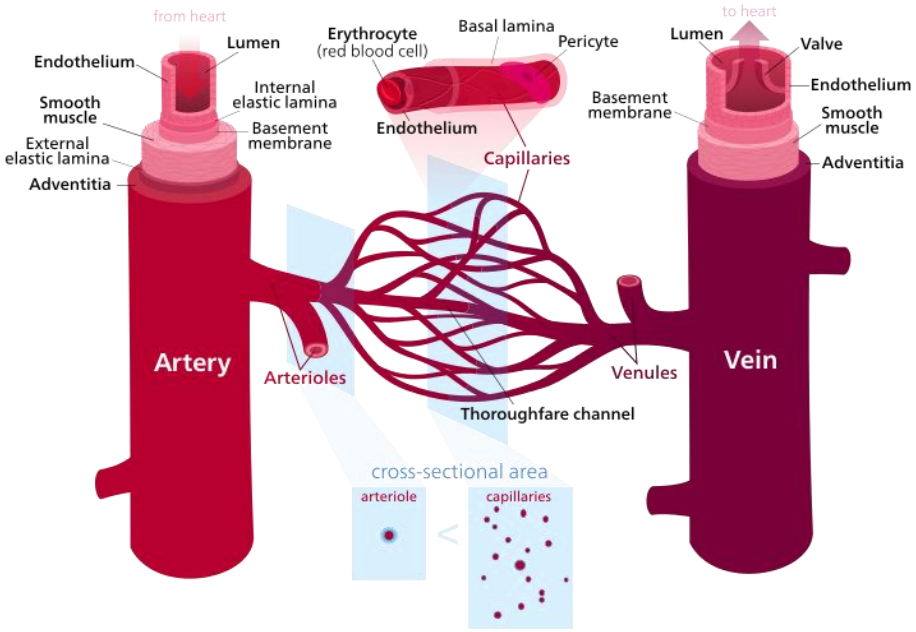

Figure 1-1. A simplified depiction of the blood vessel system.[a]

Arteries transport highly oxygenated blood around the body. Arteries are highly elastic, facilitating the pulsatile blood flow caused by the pumping motion of the heart. This elasticity also allows arteries to dilate, enabling an increase in blood flow if required. The major systemic arteries in humans typically have an inner diameter of ~ 4 mm, with the artery walls being approximately 1 mm thick.

Arterioles branch out from arteries, are much smaller than arteries, and are typically < 200 µm in diameter. Arterioles are muscled, allowing them to expand or contract to moderate blood flow. There are many arterioles for each artery.

Capillaries branch from arterioles, and are where the majority of oxygen diffusion from blood to tissue occurs. Capillaries are the smallest blood vessels in the body, are typically ~ 8 µm in diameter, with thin (0.5 µm) walls. This enables individual RBCs to pass through capillaries and release oxygen via diffusion. Capillaries may

[a] Image reproduced under the Creative Commons Attribution-Share Alike 3.0 Unported license from Wikimedia Commons.[287]

expand or constrict due to blood flow demands. Capillaries are highly numerous, with many capillaries required to supply a region of tissue.

Venules are generally somewhat larger than arterioles in diameter, but comparable in size (i.e. < 200 μm) and number. Capillaries drain into venules. Venules have less capacity for expansion than arterioles.

Veins are the largest blood vessels, with a typical inner diameter of ~ 5 mm in humans. The vessel wall of veins is thinner (0.5 mm) than arteries, with less muscle tissue, and less capacity for expansion.[17] Venules drain into veins.

Arterioles, capillaries, and venules are collectively known as the *microvasculature*. It should be noted that throughout this thesis, the terms arteries and veins are used interchangeably with the terms arterioles and venules because no major systemic arteries or veins are analysed.

1.2.3 Oxygen transport and oxygen diffusion

1.2.3.1 Red blood cells

RBCs are the most numerous constituent cell of blood, with over five million RBCs per cubic millimetre of blood. RBCs are ~ 7 μm in diameter and ~ 2 μm thick. RBCs are a biconcave disk shape (see Figure 1-2). Further, RBCs are highly elastic, enabling them to pass through narrow capillaries (~ 8 μm in diameter) and to preferentially align with blood flow. This shape also provides a large surface area for oxygen diffusion to occur into and from RBCs. Uniquely, RBCs contain no nucleus or organelles, with all room inside the cell dedicated to haemoglobin and oxygen transport. Each RBC contains over 250 million haemoglobin molecules, compromising 95% of the mass of a RBC.[15]

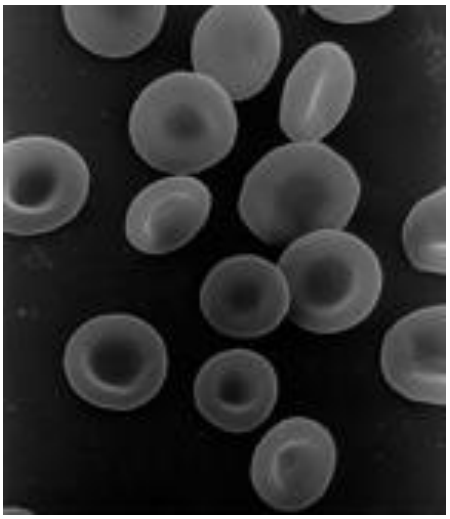

Figure 1-2. A micrograph of red blood cells showing their biconvex shape.[b]

1.2.3.2 Binding of oxygen to haemoglobin

Haemoglobin functions to bind oxygen from the lungs, transport oxygen, and release oxygen where it is required. The haemoglobin molecule consists of four subunits (heme groups) to which an oxygen molecule can bind. When oxygen binds or unbinds to haemoglobin, the structure of the molecule changes, consequently altering the wavelengths of light absorbed by haemoglobin.[18] The structure of the haemoglobin molecule is shown in Figure 1-3.

[b] Figure in the public domain, reproduced from Wikimedia Commons.[288]

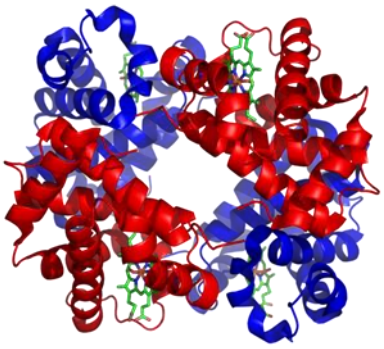

Figure 1-3. The molecular structure of haemoglobin. The four small heme groups are highlighted as green.[c]

Haemoglobin molecules can exist in five oxygenation states: 0, 1, 2, 3, and 4 bound oxygen molecules, corresponding to 0, 25, 50, 75, and 100% SO_2 respectively. When averaged over a population of many haemoglobin molecules, the statistical average SO_2 may range anywhere between 0 and 100% SO_2.[16,19] Haemoglobin molecules with four bound oxygen molecules are referred to as *oxyhaemoglobin* (HbO_2), whereas haemoglobin with no bound oxygen is referred to as *deoxy-haemoglobin* (Hb). Blood SO_2 is defined by:

$$SO_2 = \frac{C_{\mathrm{HbO_2}}}{C_{\mathrm{HbO_2}} + C_{\mathrm{Hb}}}, \qquad 1\text{-}1$$

where $C_{\mathrm{HbO_2}}$ and C_{Hb} are respectively the molar concentrations of oxygenated and deoxygenated haemoglobin.

The oxygen binding affinity of haemoglobin is determined by the local partial pressure of oxygen (pO_2), measured in units of millimeter of mercury (mmHg). The relationship between SO_2 and pO_2 is described by the *oxygen dissociation curve* (see Figure 1-4). The oxygen dissociation curve varies between species,[20,21] and haemoglobin's oxygen affinity can be further altered by factors such as pH and temperature.[22] The sigmoid shape of the oxygen dissociation curve shows that a

[c] Image reproduced from Wikimedia Commons under the Creative Commons Attribution-Share Alike 3.0 Unported license.[289]

large pO_2 is required to reach 100% SO_2 due to decreased oxygen affinity of haemoglobin at high SO_2. Similarly, extracting all oxygen from haemoglobin requires a very low pO_2 because at lower SO_2 values the oxygen affinity of haemoglobin increases. Arterial blood typically has a pO_2 of ~ 100 mmHg, generally corresponding to a SO_2 of ~ 97%. Venous blood typically has a pO_2 of ~ 40 mmHg, generally corresponding a SO_2 of ~ 70%.[16]

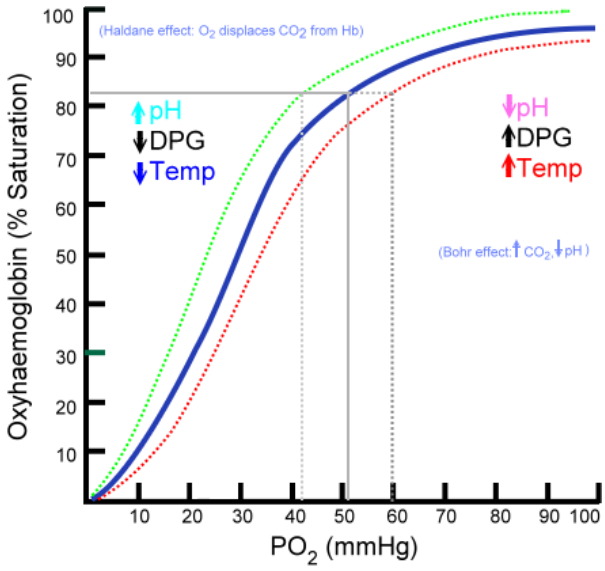

Figure 1-4. The sigmoid-shaped haemoglobin oxygen dissociation curve. The typical oxygen dissociation curve (i.e. at pH = 7.4, T = 37 °C) is shown as solid blue. Various factors can alter the oxygen dissociation curve, such as pH of blood (e.g. due to changes in dissolved carbon dioxide in the blood; i.e. the Bohr effect), temperature, and concentration of diphosphoglycerate (DPG) in blood.[1][d]

1.2.3.3 Oxygen diffusion and partial pressure of oxygen

Diffusion is the primary mechanism for movement of oxygen to and from blood (e.g from air into blood, or from blood into tissue). Oxygen diffusion is driven by pO_2 gradients: oxygen will diffuse from regions of high pO_2 to regions of low pO_2 until a stable equilibrium is reached. The partial pressure of a gas in a given gas mixture is dependent on two factors: the fractional concentration of the gas, and the total pressure of the overall gas mixture. For example, the typical air pressure at sea

[d] Modified version of a figure in the public domain from Wikimedia Commons.[290]

level is ~ 761 mmHg, therefore, pO_2 at sea level will be: pO_2 = 0.21 x 761 = 161 mmHg.[16]

1.2.3.4 Fick's law of diffusion

The rate at which oxygen diffuses through tissue is described by Fick's law of diffusion. In one dimension, the diffusion rate can be described by:

$$J = -D\frac{\mathrm{d}\phi}{\mathrm{d}x}, \qquad 1\text{-}2$$

where J is the diffusion flux (mol/m^{2}s), which is the amount of gas that will flow through a unit area in a unit time; D is the diffusivity (m^2/s); ϕ is concentration of gas (mol/m^3); and x is position (m).

From Equation 1-2 it can be seen that diffusion rate across tissue is inversely proportional to the thickness of that tissue. For example, oxygen will diffuse through a capillary wall (~ 0.5m µm thickness) ~ 2000 times faster than through an artery wall (~ 1 mm thickness).[17] From Equation 1-2 it is also clear that diffusion rate is proportional to the pO_2 gradient. This means that oxygen will readily diffuse from highly oxygenated arterial blood (pO_2 ~ 100 mmHg) into tissue (~ 40 mmHg), however, (as an approximation) little to no diffusion will take place between tissue and venous blood (~ 40 mmHg).[16]

1.2.3.5 Oxygen diffusion in a cylindrical geometry

In 1919, Krogh derived an expression for the pO_2 versus distance from a supplying blood vessel.[23] For the geometry shown in Figure 1-5, the following expression was derived:

$$\Delta pO_2 = \frac{p}{d}\left(\frac{1}{2}R^2\ln\frac{x}{r} - \frac{x^2-r^2}{4}\right), \qquad 1\text{-}3$$

where: ΔpO_2 is partial pressure gradient between the centre of the capillary and point x, p is the gas exchange (i.e. the rate at which tissue consumes oxygen), d is the diffusion rate required to supply the region, r is the radius of the capillary, R is the region of the tissue surrounding the capillary to which oxygen is supplied by the capillary, and x is distance to an arbitrary point in the tissue.[23] By defining $\Delta pO_2 = pO_2(0) - pO_2(x)$, Equation 1-3 can be rearranged to give:

$$pO_2(x) = pO_2(0) - \frac{p}{d}\left(\frac{1}{2}R^2 \ln\frac{x}{r} - \frac{x^2 - r^2}{4}\right). \quad 1\text{-}4$$

By substituting $pO_2(0) = 1,\ p = 1,\ d = 1, R = 1, \text{and } x = 0.1,$ it can be seen that $pO_2(x)$ decays with distance from the edge of the capillary as shown in Figure 1-6. If the initial pO_2 gradient is lowered, then a smaller region of surrounding tissue will be supplied with oxygen via diffusion.

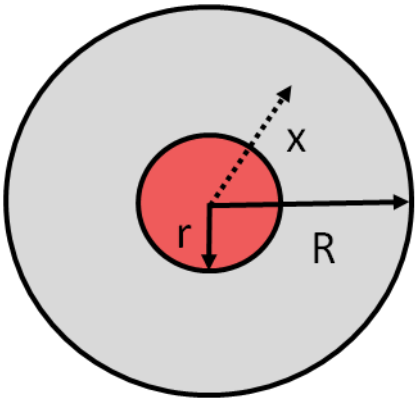

Figure 1-5. The cylindrical geometry for oxygen diffusion from a blood vessel considered by Krogh. The blood vessel (of radius *r*) is shaded red, and the region of tissue to which the blood vessel supplies oxygen (R) is shaded grey. *x* is a point within the tissue at an arbitrary distance from the blood vessel.

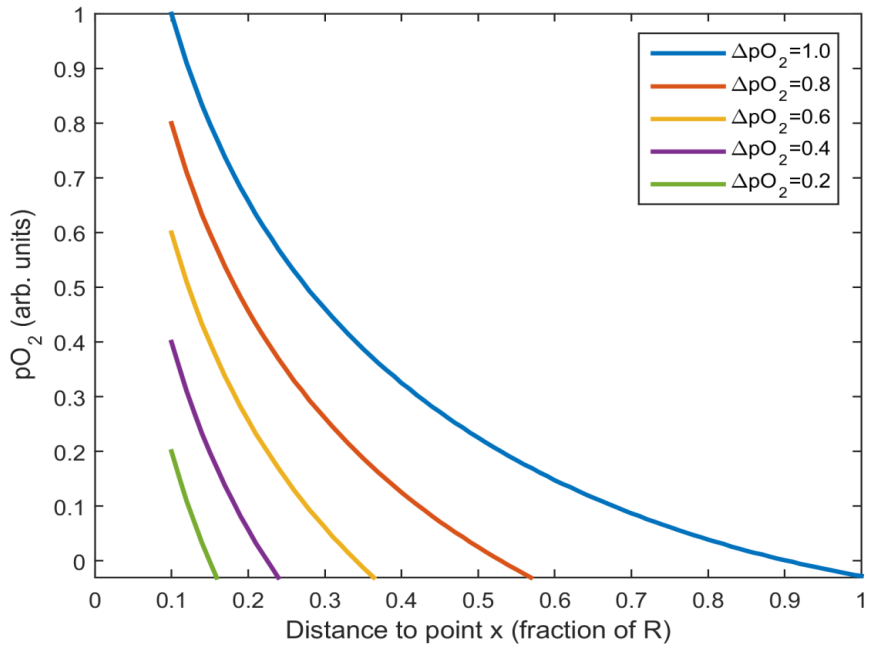

Figure 1-6. pO_2 vs. distance from centre of a blood vessel. Calculations as per Equation 1-4 and assuming the radius of blood vessel (r) to be 0.1 R.

1.2.3.6 Blood vessel diameter and oxygen diffusion.

If oxygen diffuses into blood, then blood SO_2 will be increased; however, the rate at which SO_2 is altered will be proportional to both blood vessel diameter and blood vessel wall thickness. By using some simple calculations and simplifying assumptions, we can estimate how rapidly oxygen diffusion will act to alter SO_2 in both a large vessel (~ 500 μm) and a capillary (~ 10 μm). Figure 1-7 shows a diameter comparison between such vessels.

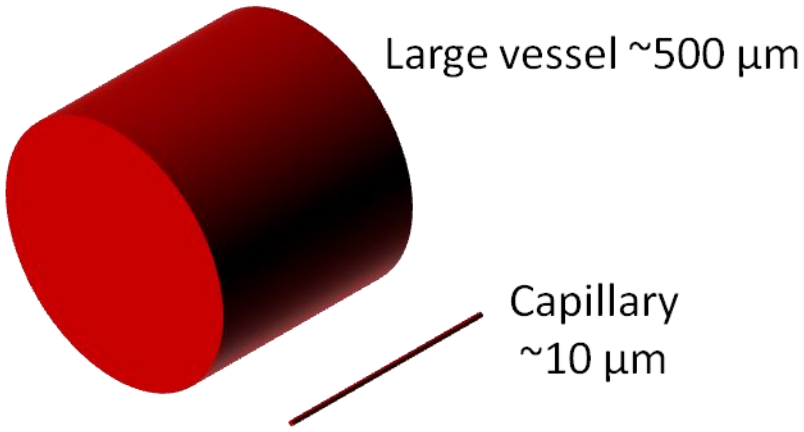

Figure 1-7. Vessel diameter comparison between a capillary and a large vessel (e.g. a systemic vein).

Oxygen diffusion will occur across the entire surface area of a vessel and will alter SO_2 in a manner proportional to the volume of blood contained in the vessel. Thus, a key variable is the surface area to volume ratio. For a cylinder of unit length (i.e. assuming height, *h* =1), this is given by:

$$\frac{Surface\ area}{Volume} = \frac{2\pi rh + 2\pi r^2}{\pi r^2 h} = \frac{2}{r}, \qquad 1\text{-}5$$

where *r* is the radius of the cylinder. By plotting the surface area to volume ratio for vessels of various diameters (see Figure 1-8), we can see that surface area to volume ratio decreases asymptotically with vessel diameter. Assuming that a large vessel is ~ 500 µm in diameter and a capillary is ~ 10 µm, it is possible to estimate that the large vessel will have a surface area to volume ratio ~ 0.08 times that of the capillary. This implies that from geometry alone, the capillary will undergo diffusion 12.5 times faster than the large vessel. Further assuming that the thickness of the capillary wall (0.5 µm) is 200 times less than the thickness of the large vessel (100 µm),[17] and that the oxygen diffuses through the vessel wall tissue at an equal rate, then we can see that diffusion through the capillary wall will occur 200 times faster for the capillary wall than through the large vessel wall. Combining these factors, we arrive at an estimation that the SO_2 of blood in the capillary is altered by oxygen diffusion 2,500 times more rapidly than SO_2 of blood in the large vessel.

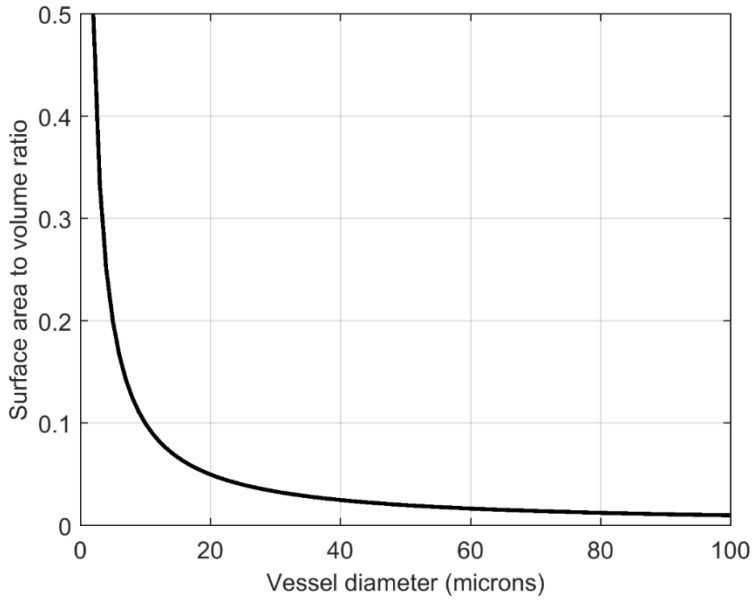

Figure 1-8. Surface area to volume ratio vs. blood vessel diameter, assuming cylindrical geometry and negligible vessel wall thickness.

This simple estimation does not include effects such as the diffusion of oxygen through the blood itself, the oxygen affinity of haemoglobin, blood flow velocity, or density of vessel wall tissue. All these factors will alter how rapidly oxygen diffusion can change SO_2.

Oxygen diffusion is an important consideration in Chapter 3, where oxygen diffusion from ambient air was seen to completely reoxygenate hypoxic bulbar conjunctival vessels with a half-time-to-reoxygenation of approximately three seconds. Oxygen diffusion is also of concern in Chapter 5, where blood vessels are exposed for imaging via surgery.

1.2.4 The blood supply of the eye

1.2.4.1 Anatomy and function of the eye

Oximetry of blood vessels in the eye is a major component of this thesis; chapters 3, 4, and 6 focus on oximetry of various vascular beds in the eye. Thus, it is essential to understand the anatomy of the eye to understand the challenges of oximetry in these blood vessels.

The purpose of the eye is to sense light in a manner such that sensory information can be interpreted as images by the brain [24] ; as such, the anatomy of the eye serves this function (see Figure 1-9).

The human eye is an oblate spheroid approximately 25 mm in diameter, which sits within the orbits of the skull.[24,25] The outer protective layer of the eye is the sclera, which is made of parallel bundles of collagen fibres, and which is opaque and white in apperance.[26] The sclera ranges between ~ 420 - 850 µm in diameter.[27] The eyelids serve to protect the eye, and can be moved open and closed in a voluntary and involuntary manner (e.g. blinking).[24]

Towards the anterior (front) of the eye, is the lens which is avascular and has no nerves; the lens is used to focus light onto a light-sensitive region at the posterior (back) of the eye: the retina.[26] The variable focus of the lens is controlled by the anterior ciliary muscles.[26] The lens also functions as a filter for ultraviolet light (see Section 1.3.5: '*Challenges of imaging and oximetry in the eye*'). The pupil acts as a limiting aperture, typically ~ 3 – 7 mm in diameter,[28] which in turn constrains the overall intensity of light that reaches the retina. Pupil size is controlled by the muscles of the iris. The cornea is a transparent tissue made of collagen fibres which overlies the lens, and which serves to protect the eye from contaminants and ultraviolet light, as well as to help guide light to the lens. Between the cornea and lens is the anterior chamber of the eye, which is filled with the watery aqueous humour. The aqueous humour helps supply the lens and cornea with nutrients and remove waste products. The cornea is also supplied with oxygen via diffusion from ambient air. [26,29] Within the eye, the transparent, acellular, gel-like, vitreous body serves to separate the retina from the lens.[30]

Spanning two-thirds of the posterior of the eye, the retina contains many light sensitive photoreceptor cells: i.e. rods (monochromatic) and cones (red, green, blue colour vision). The retina also contains the nerve network associated with these photoreceptors (see Figure 1-10). The region of the retina with most light-sensitive cells is the fovea, which is in the centre of the macula: a somewhat avascular region bounded by the temporal retinal blood vessels. At the posterior of the retina, between the retina and choroid, is the retinal pigment endothelium which acts to absorb stray light and protect against UV light exposure.[31] Retinal nerve fibres from

photoreceptors converge at the optic disk to form the optic nerve, which perforates the sclera and sends nerve signals to the brain. The optic nerve is disk is located ~ 20° from the centre of the retina, towards the nasal side of the eye (see Figure 1-9).[32]

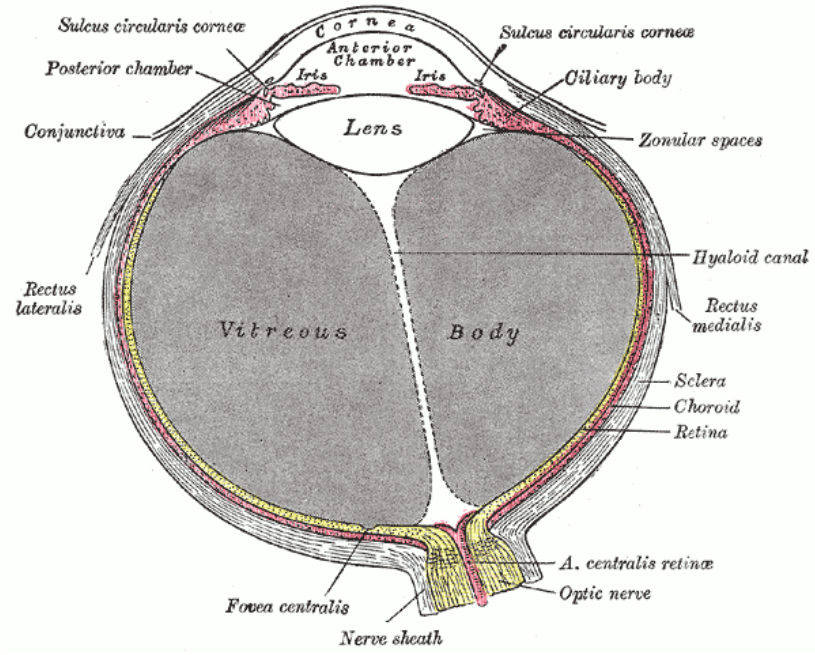

Figure 1-9. The anatomy of the eye. [e]

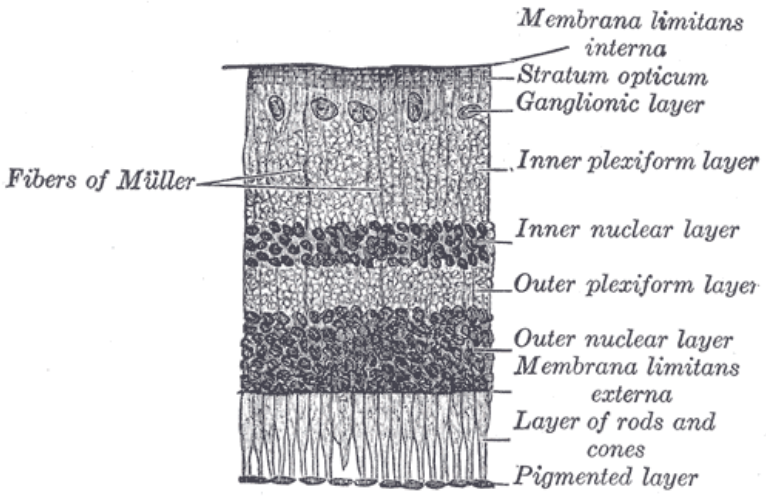

Figure 1-10. The retinal layers. [f]

[e] Figure in the public domain, reproduced from Wikimedia Commons. Originally from 'Gray's Anatomy'.[291]

[f] Figure in the public domain, reproduced from Wikimedia Commons. Originally from 'Gray's Anatomy'.[292]

1.2.4.2 The blood supply to the retina and choroid

The eye is supplied with blood via various branches of the ophthalmic artery, which itself is a branch of the internal carotid artery (see Figure 1-11).[33] The only exception is the bulbar conjunctiva, which has a contribution of its blood supply from the external carotid artery via the palpebral artery in the eyelid.[34] The retinal blood vessels are the focus of Chapter 4 of this thesis, whilst the choroidal circulation is features predominately in the red eye reflection oximetry described in Chapter 6.

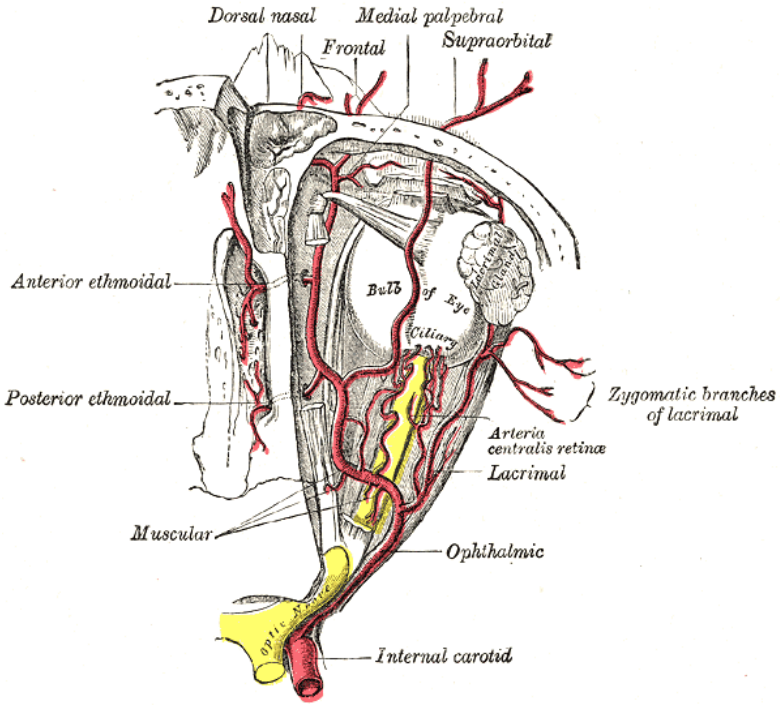

Figure 1-11. The branches of the ophthalmic artery. [g]

The retina is a region of high metabolic demand, requiring high volumes of blood flow to supply oxygen and nutrients to the retinal tissue. Consequently, two blood vessel beds supply the retina; the retinal blood vessels and the choroid. The inner retina is supplied by the retinal blood vessels, and the outer layers of the retina (which includes the photoreceptor cells) are supplied by the choroid.[26,35] The position of these blood vessels with respect to the retina is depicted in Figure 1-12.

The retinal blood vessels originate from the central retinal artery, which enters the eye via the optic disk. These blood vessels overlay the retinal tissue and vary in

[g] Figure in the public domain, reproduced from Wikimedia Commons. Originally from 'Gray's Anatomy'.

length and tortuosity. The retinal vessels include arterioles, venules, and numerous capillaries. The retinal region that has fewest vessels (i.e. which is avascular) is the fovea, and to a lesser extent, the macula. The overlying blood vessels do not typically interfere with vision because the eye is constantly moving, which enables the brain to compensate for the effects of these overlying vessels. Retinal blood vessels also help to supply oxygen to the lens via oxygen diffusion in through the vitreous humour.[30] The typical artery-vein difference in the retina is ~35%.[36] It has been shown that the metabolic demand of the retina is changed under certain stimuli, e.g. flicker illumination; this consequently alters the SO_2 of retinal blood vessels.[37]

The choroid is a densely vascularised region between the retina and the sclera, approximately ~ 180 ± 51 to 250 ± 80 μm in thickness.[38,39] The blood supply of the choroid is derived from the perforating posterior ciliary arteries, which branch off from the ophthalmic artery and perforate the posterior sclera; the choroid is drained by vortex veins. The choroidal circulation presents a small SO_2 difference of ~3% between arteries and veins,[40] considerably less than the artery-vein difference of ~35% in the retina.[36]

At visible wavelengths, the choroidal blood vessels are often obscured by the retinal pigment endothelium; however, the choroidal blood vessels can be directly observed in some subjects with minimal pigmentation.[41] Alternatively, angiography with a dye which emits fluorescence at near infra-red wavelengths (e.g. Indocyanine Green) can be used to observe and study choroidal blood flow.[42]

The volume of the choroid has been recorded to increase by ~ 5% as a result of human subjects consuming one litre of water; this volume increased is due to increased blood volume due to the liquid intake.[38] Thus in studies of the choroid it is particularly important to limit liquid intake in subjects.

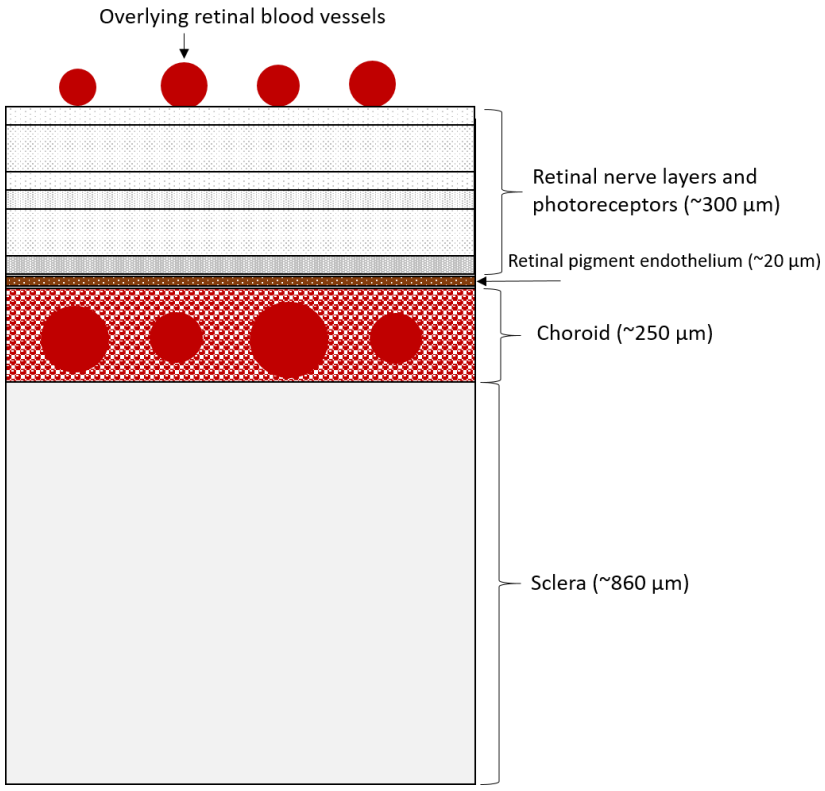

Figure 1-12. Retinal layers and the retinal blood supply. Exact thickness of each layer varies depending on the location in the eye.

1.2.4.3 Episcleral blood supply

Chapter 3 of this thesis describes oximetry of the episcleral blood vessels.

The episcleral blood vessels lie within the sclera and supply scleral tissue. Posterior (rear) episcleral vessels are derived from the short ciliary arteries, which branch from the ophthalmic artery (see Figure 1-13). Episcleral vessels towards the anterior (front) of the eye derive from the long ciliary arteries and supply the iris (see Figure 1-14). Some episcleral vessels (prominently anterior ciliary arteries) can be observed if they come close to the scleral surface, however, fluorescein angiography is typically required for most episcleral vessels to be observed clearly.[43,44]

The aqueous humour can be observed to sporadically drain into anterior episcleral vessels; these vessels are known as aqueous veins.[45] In these vessels, aqueous humour displaces blood, causing vessels to appear temporarily transparent; this is pulsatile in manner.

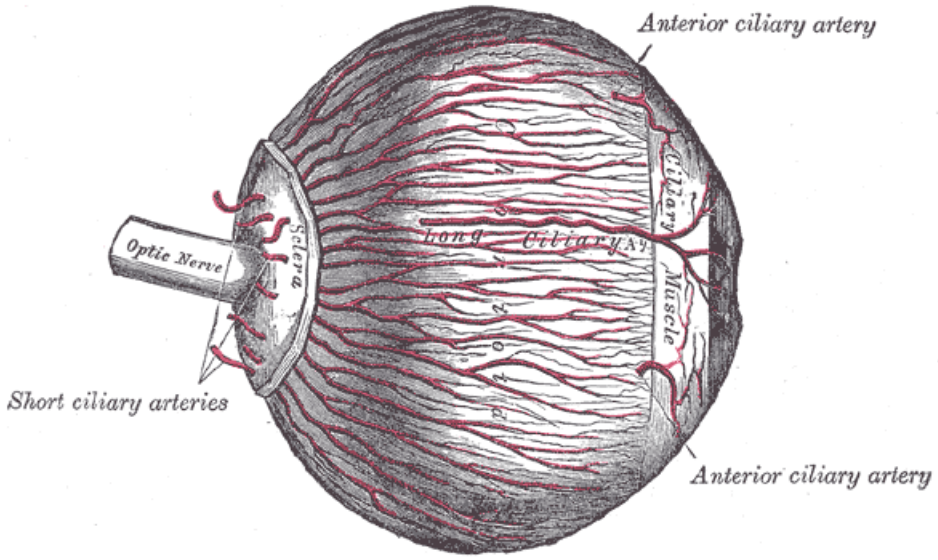

Figure 1-13. The long and short ciliary arteries. [h]

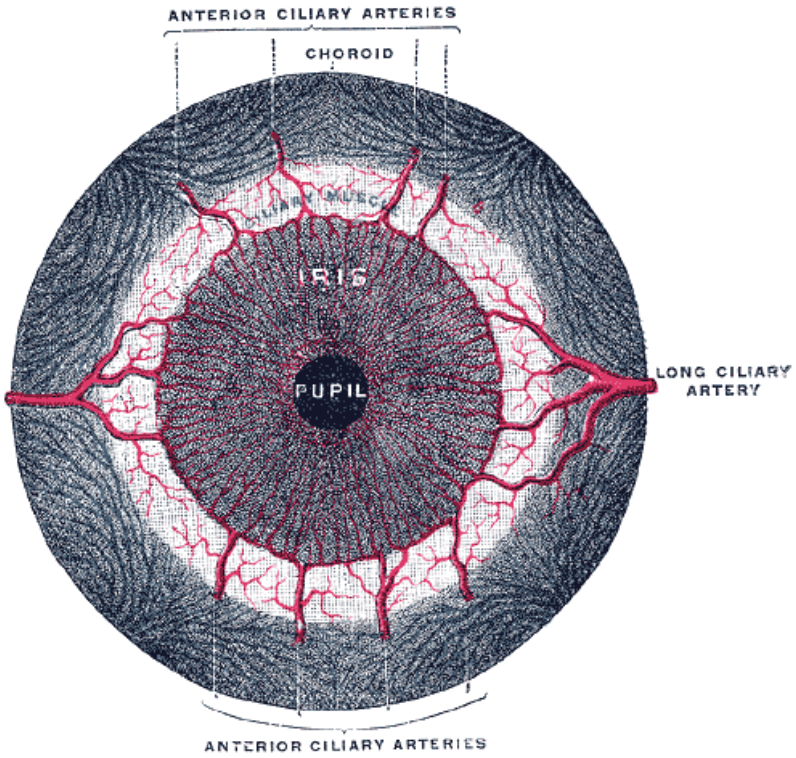

Figure 1-14. The anterior ciliary arteries. [i]

[h] Figure in the public domain, reproduced from Wikimedia Commons. Originally from 'Gray's Anatomy'.[293]

[i] Figure in the public domain, reproduced from Wikimedia Commons. Originally from 'Gray's Anatomy'.[294]

1.2.4.4 Bulbar conjunctival blood supply

Chapter 3 describes a study of the blood vessels of the bulbar conjunctiva.

The bulbar conjunctiva is a semi-mobile, transparent, thin (~ 33 μm), mucous membrane which lies above the sclera.[26] The bulbar conjunctiva extends from the eyelid margin to the cornea limbus, and thus serves to stop debris from entering the socket of the eye.[46]

The bulbar conjunctival blood supply derives mainly from the ophthalmic artery but also has a lesser contribution from the external carotid artery via palperbral artery in the eyelid; the palperbral artery also supplies the palpebral conjunctiva.[26,34] The bulbar conjunctiva contains many arterioles, venules, and capillaries.[47] The bulbar conjunctival vessels are highly reactive to stimuli, including diurnal variations,[48] emotion,[49] allergens,[50] and disease.[51–53] An example of dilated bulbar conjunctival blood vessels is shown in Figure 1-15.

Figure 1-15. The blood vessels of the bulbar conjunctiva. NB: blood vessels are dilated in this image.[j]

[j] Image reproduced from Wikimedia Commons under a Creative Commons Attribution-ShareAlike 3.0 Unported licence.[295]

1.3 Challenges of *in vivo* optical microvascular oximetry

In vivo oximetry of blood vessels is challenging due to absorption and scattering of light by tissue, pigmentation, and red blood cells. These factors must be considered when conducting oximetry experiments.

1.3.1 Absorption of light in tissue

The absorption of light by substances other than blood vessels of interest may decrease visibility of blood vessels and reduce the light intensity reaching a detector. At visible and near infra-red (NIR) wavelengths, there are four dominant absorbers of light in tissue: haemoglobin; melanin pigmentation; water, and adipose fat tissue. The degree of absorption is dependent on the concentration of each absorber, which can vary between tissue type, species, and subject.

Haemoglobin is the dominant absorber of visible light, strongly absorbing wavelengths less than 590 nm, with low absorption at red and near infra-red wavelengths. The absorption spectrum of haemoglobin is discussed in detail in Section 1.4.1. Melanin pigmentation also strongly absorbs blue and green light, with low absorption at red and near infra-red wavelengths. Melanin is typically found in the skin and retina, but concentration of melanin varies between subject and species.

Water in tissue barely absorbs visible light, but at near infra-red wavelengths (>1000 nm) absorption by water dominates over absorption by blood. Adipose fat and tissue and yellow pigment also add to absorption, but these are a minor concern. The absorption of all these substances is summarised in detail by Jacques (2013).[54]

The overall absorption of light by tissue is generally low in the so-called "near infra-red biological window" at ~ 650 - 1000 nm. Due to the reduced scattering and absorption at these wavelengths it is possible to transmit light several centimetres in tissue at these wavelengths, enabling non-imaging deep-tissue oximetry techniques such as near infra-red spectroscopy and pulse oximetry.

1.3.2 Optical scattering

1.3.2.1 Rayleigh and Mie Scattering

Scattering of light can be broadly classified as any phenomenon which causes a photon to be redirected from its initial trajectory; e.g. refractive index mismatches between cells in tissue and suspended particles in a solution. Scattering alters the optical path of light, changing the apparent absorption of a blood vessel, and thus marring spectral measurements for oximetry. Light can be singly scattered in optically thin media, or can undergo multiple scattering in optically thick media (e.g. tissue). Two scattering regimes are discussed in this section: Rayleigh scattering and Mie scattering.

Rayleigh scattering theory describes scattering by non-absorbing spherical particles that are much smaller than the wavelength of incident light. Rayleigh scattering is strongly wavelength-dependent (proportional to c/λ^4, where c is a constant). The classic example of Rayleigh scattering is the scattering of blue sunlight by atmospheric gas particles.[55]

Mie scattering theory[56] is a more generalised theoretical approach to electromagnetic scattering with no constraints on the size of the scattering particle and is thus applicable to scattering by cells and organelles in tissue.[54] The degree of Mie scattering is not as strongly wavelength dependent as Rayleigh scattering, but nevertheless decreases as a function of wavelength (proportional to k/λ, where k is a constant). [57] Mie scattering is highly anisotropic, with a strong forward-dependence. Scattering geometries for Rayleigh and Mie scattering are shown in Figure 1-16.

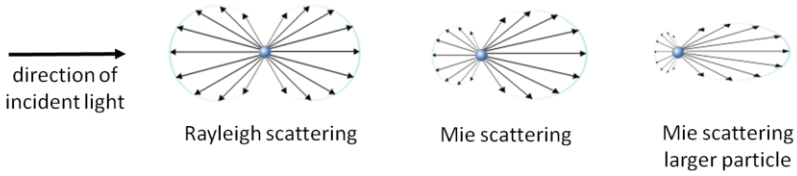

Figure 1-16. Diagram of polar scattering anisotropies for Rayleigh and Mie scattering.[k]

The key parameter for determining whether Raleigh or Mie scattering is applicable is the size parameter of a particle (α), given by:

$$\alpha = \frac{2\pi a}{\lambda}, \qquad 1\text{-}6$$

if α <<1 then Rayleigh scattering is applicable. For α >>1 then Mie scattering is applicable. For α ~ 1 then an intermediate scattering state exists. For red blood cells (~ 8 μm diameter) α >> 1, thus Mie scattering dominates.[57] Table 1-1 shows an example of particle size vs. α for 532 nm light.

Table 1-1. Particle size parameter (α) vs. scattering regime, assuming the wavelength of light to be 532 nm.

Particle Size (nm)	α	Scattering regime
17	0.1	Rayleigh
170	1	Intermediate
1700	10	Mie

1.3.2.2 Scattering by tissue

Mie scattering is applicable to scattering of light by tissue due to inhomogeneities in the refractive index, such as cells and organelles. The scattering properties of tissue such as the skin,[58–60] the retina,[61] the sclera,[62] and blood[63] have been well characterised. Generally, blue and green wavelengths are strongly scattered by biological tissues with red and near infra-red wavelengths undergoing less scattering. The decreased absorption and scattering at red and near infra-red

[k] Figure reproduced and modified from Wikimedia Commons under the Creative Commons Attribution-Share Alike 3.0 Unported license.[296]

wavelengths gives rise to the so called “biological window” between ~ 650 - 1000 nm, where light can penetrate several centimetres into tissue.

1.3.2.3 Scattering of light by blood

Scattering by blood must be considered when interpreting oximetry measurements; in particular, changes in scattering properties due to altered absorption, changes in blood volume, or changes in blood flow rate.

In blood, light is predominately Mie scattered by individual RBCs which make up approximately 44% of blood volume.[64] Proteins in blood plasma also contribute Rayleigh scattering, but the magnitude of this scattering is 100-1000 times less than scattering from RBCs.[64] Factors such as hematocrit,[65] blood vessel diameter, and blood flow velocity also alter the scattering properties of blood.[36,66]

The primary parameters of interest for scattering of light by blood are the absorption coefficient (μ_a) [$cm^{-1}M^{-1}$], the scattering coefficient (μ_s) [cm^{-1}], the anisotropy factor (g), and the effective scattering coefficient: $\mu'_s = \mu_s(1- g)$ [cm^{-1}].[64] g is computed as: $g = cos(\theta)$, where θ is the typical angle of deflection for light which has experience a scattering event (i.e. $g = 1$ indicates complete forward-scattering, and $g = 0$ indicates complete back scattering). For whole blood, g has been estimated to be ~ 0.985 - 0.997 (i.e. highly forward scattering).[67] Experiments have found that the anisotropy factor of blood is higher than Mie theory predictions, because Mie theory considers RBCs as spherical particles rather than their true biconcave shape.[68]

1.3.2.4 Oxygen saturation and scattering

Changes in SO_2 have been shown to alter the scattering properties of blood. Friebel et al., (2009)[63] ran Monte Carlo simulations of optical scattering in blood. They found that when absorption of light increased (due to decreased SO_2), then more light was scattered at larger angles and less light was forward-scattered (i.e. the anisotropy factor, g, decreased). This decreases the transmission of a blood vessel by more than just the expected change in absorption. LeBlanc et al., (2011)[69] found that scattering by RBCs introduced a significant systematic change in transmission measurements in the 520-546 nm wave range which could mar estimation of SO_2.

These studies suggest that changes in optical scattering properties due to changes in SO_2 should be considered as a potential source of error in transmission measurement for oximetry. However, exact quantification of this effect is highly challenging and is not usually incorporated in simple two-wavelength oximetry analysis. Multispectral oximetry models however, do tend to incorporate scattering, typically by incorporating values of blood scattering parameters from the literature (see Section 1.4.7)

1.3.2.5 Blood flow velocity and reflection

Scattering by RBCs is dependent on the orientation of RBCs, which in turn is dependent on blood flow velocity. If blood is static then RBCs will be randomly orientated randomly and take biconcave shaped, however if blood is flowing then RBCs will preferentially align with the flow and elongate (see Figure 1-17).[70]

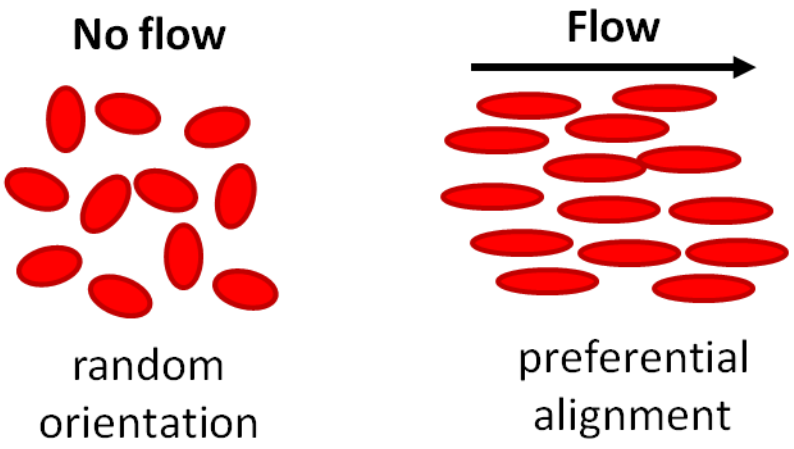

Figure 1-17. Alignment of RBCs under laminar flow.

Klose et al., (1972)[66] demonstrated that this preferential alignment of RBCs will decrease transmission of light through blood due to increased reflectivity.[66] This was further confirmed by Schweitzer et al., (1999)[36] who demonstrated that preferential alignment of RBCs with flow would act to increase the reflectivity of a blood vessel across all wavelengths. However, they found that reflectivity would reach a constant value once all RBCs had reached a preferential alignment state. For a blood vessel of 50 µm diameter, this flow speed was 6.4 mm/s.[36]

This indicates that changes in blood flow velocity (e.g. due to auto regulation) should be considered as a possible source of uncertainty in oximetry

measurements; however, the extent of this uncertainty is entirely dependent on the context of an individual experiment.

1.3.3 Optical paths in blood vessels

1.3.3.1 Light transmission scenarios

When imaging blood vessels, light does not simply follow a single path; photons may take many paths through blood vessels and tissue, with absorption, scattering, and reflection all playing a role. Hammer et al., (2001)[71] investigated scenarios for light transmission through blood vessels in the retina using a Monte Carlo simulation of ray propagation. This study considered single pass, double pass, backscattered, and specularly reflected light paths through a blood vessel (see Figure 1-18). The main finding of this study was that transmission in retinal vessels is dominated by single-pass and backscattered light, and that the probability of light undergoing double pass transmission is very small. However, this study only considered light at 560 nm, which is strongly absorbed by both haemoglobin and pigmentation, and so will be relatively constrained in the retina in comparison to longer wavelengths (i.e. red and infrared). However, these findings are valid for the wave-range 520 nm – 586 nm,[71] and should be applicable to oximetry scenarios in which a similar reflecting background is present.

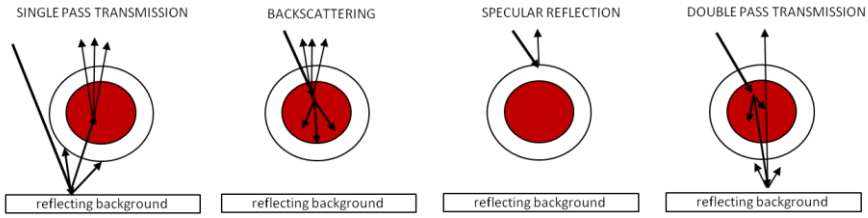

Figure 1-18. Potential light paths through a blood vessel as described in Hammer et al.,(2001).[71] The reflecting background represents tissue such as the sclera or spinal cord white matter.

Smith et al., (2000)[72] investigated the effects of different light path contributions on *in vivo* retinal oximetry measurements in swine using a multispectral oximetry algorithm with a single/double pass contribution. However, obtaining a consistent *in vivo* calibration for vessel path length contributions was found to be difficult.

A Monte Carlo model of path length distributions in the retina was conducted by Rodmell et al., (2014)[73] This study showed that if a vessel is not directly illuminated,

but adjacent tissue is, then the illumination light will be diffusely scattered through tissue, effectively back-illuminating the vessel, and resulting in single-pass transmission through the vessel (see Figure 1-19). This is important because light-path factors inform the development of multi- and hyper-spectral oximetry algorithms (Section 1.4.7).

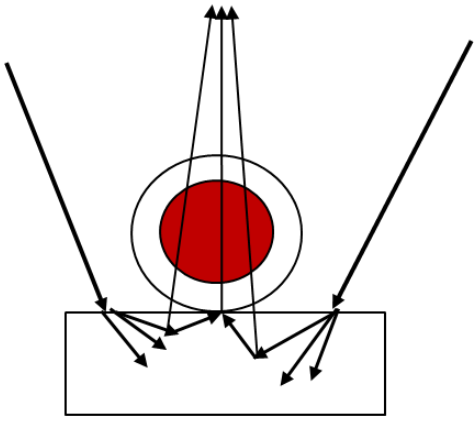

Figure 1-19. Single-pass back-illumination of a blood vessel by indirect illumination and diffuse multiple scattering.

1.3.3.2 Specular reflection from a blood vessel

The specular reflection from a blood vessel (see Figure 1-18) can mar transmission measurements by creating a bright central-reflex in the vessel, altering the shape of the vessel profile (see Figure 1-20). There are several approaches to dealing with this: orthogonal polarisation imaging, modified vessel fitting analysis, and illuminating blood vessels from alternative angles (in the retina this is intra-vitreal illumination, i.e. illumination through the sclera).

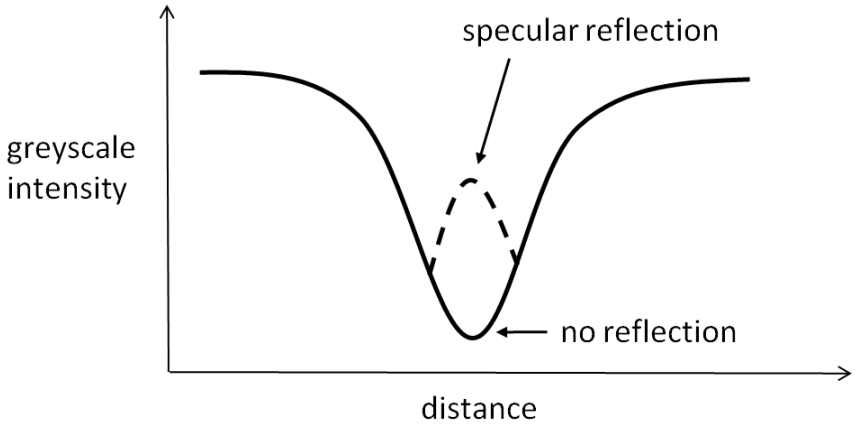

Figure 1-20. Specular reflection alters vessel line profile shape.

Modified fitting algorithms have been widely employed to estimate transmission in the absence of reflections. However these may introduce systematic errors. Illuminating from other angles introduces vessel shadowing; in retinal imaging, intravitreal retinal illumination is highly invasive and may also alter partial pressure of oxygen in the eye, and thus altering SO_2 measurements.[74]

Perhaps the simplest approach to null specular reflections is to use orthogonal polarisation imaging (OPI). In OPI, illumination light is linearly polarised; when this linearly polarised light is incident upon tissue, the light undergoes multiple scattering events (~ 10 times or greater) and becomes depolarised. However, light which is either specularly reflected or only scattered once is likely to retain its polarisation.[75] By placing a second linear polariser in the imaging path, and orientating this polariser orthogonally to the first, then only multiply scattered light will be imaged; this eliminates specular reflections. The disadvantage of OPI is that a minimum of 75% of initial light intensity is lost due to the low (~ 50%) transmission of unpolarised light by most polarisers; however, this is not a significant issue for many applications. OPI has been employed in each study reported in this thesis.

1.3.4 Imaging through tissue and the biological window

To image through tissue, photons must enter tissue, interact with tissue, and be returned to a detector. Absorption and scattering fundamentally limit the maximum imaging depth for visible light in tissue to approximately 1 – 2 mm.[76,77] Imaging depth can be increased by imaging longer wavelengths where absorption and scattering are reduced: the so-called "near infrared window" (~ 650 – 1000 nm). At these wavelengths, light can penetrate several centimetres in tissue, enabling deep tissue spectroscopy and diffuse imaging measurements.[54,59] However, NIR wavelengths are of limited use for microvascular oximetry due to the relatively weak spectral contrast and absorption of blood at these wavelengths, limiting oximetry to either large systemic vessels or regions of dense vasculature, such as the choroid in the eye.

Optical imaging depth can potentially be increased by use of optical clearing agents, which match the refractive index of tissue, decreasing refractive index inhomogeneities, and thus reducing scattering This can greatly improve image

quality in tissue, however, such optical clearing agents may alter various tissue properties, and may require invasive injections.[78,79]

Deep tissue microvascular imaging and oximetry can be achieved by photoacoustic tomography (PAT), which uses ultrasound detection rather than optical detection, enabling imaging up to several centimetres in tissue (see Section 2.2). However, PAT has numerous drawbacks, such as high cost and complexity, the requirement for complex image reconstruction algorithms, and also a low image acquisition rate (~ 3 Hz), fundamentally limited by repetition rate of laser sources.[80]

1.3.5 Challenges of imaging and oximetry in the eye

The function, anatomy, and complex optical environment of the eye presents multiple challenges for spectral imaging in the eye.

Firstly, the eye is constantly moving so that areas of interest are scanned over the fovea. These rapid, small, involuntary movements are known as micro-saccades and are one of the factors that limits resolution of conventional imaging techniques in the eye.[81] Adaptive-optic scanning laser ophthalmoscopes have been developed to compensate for this motion, enabling oximetry in retinal vessels < 50 μm in diameter; however, such equipment adds complexity and has a limited field-of-view.[82] In experiments in this thesis (Chapters 3, 4, and 7), subjects fixate upon a fixation target, but this does not stop micro-saccades.

The cornea is birefringent, and thus contributes polarisation effects. This birefringence arises from the orientation of collagen fibres in the cornea. This is of concern when imaging the eye in cross-polarised light,[83] or when conducting polarisation-sensitive measurements (e.g. of the retinal nerve fibre layer).[84] Birefringence effects are also complicated by the curved geometry of the cornea. Birefringence is also induced in the retinal nerve fibre layer due to orientation of parallel retinal nerve fibres.[84]

The lens of the eye adapts to focus light from scenes of varying distance: this is known as accommodation. Accommodation can be semi-controlled in retinal imaging experiments by requiring subjects to gaze upon a gaze fixation target. However, if accommodation is not controlled, a change in apparent magnification of retinal features may be observed. Further, the power of the lens degrades with age,

so compensating optics may have to be deployed for good-quality retinal imaging; retinal fundus cameras have such optics as standard.[85]

The lens acts to filter ultraviolet light ($\lambda < 400$ nm); the transparency of the lens to all visible wavelengths is reduced with age, but most significantly so for blue wavelengths.[86,87] Cataracts may also form in the lens, clouding the lens, decreasing subject eyesight, decreasing the transmission of the lens, and altering the spectral transmission of the lens.[88] Around 75% of people over 65 years old develop cataracts, rising to 95% of people aged 85 or over.[24]

The degree of pigmentation in the retinal pigment endothelium will have significant effect on viability and calibration of oximetry measurements. Firstly, in subjects with minimal pigmentation, the choroidal blood vessels can be clearly observed. This enables oximetry of choroidal vessels, but also contributes considerable background variability for oximetry in overlying retinal vessels.[41] Secondly, degree of pigmentation will change the intensity of light reflected from the sclera, which is of concern in fundus reflectometry or red-eye oximetry measurements (i.e. in Chapter 6). However, this is not usually a limiting factor in viability of oximetry. Thirdly, pigmentation is non-uniformly distributed in the retina; this results in variability in vessel background, which may mar the estimation of optical absorption of blood vessels that is required for oximetry.

Optical scattering from retinal tissue and blood can result in choroidal blood vessels having negative optical densities (i.e. appearing darker than surrounding tissue). This means that standard commercial oximeter calibrations cannot be applied to choroidal vessels, and instead results must be reported in terms of Optical Density Ratio (ODR) (see Section 1.4.4).[41] Multi-spectral or hyper-spectral oximetry algorithms (see Section 1.4.7) are required to estimate scattering of light by blood and tissue, and thus compensate for the effects of scattering.

The concave curvature of the retina will also result in defocus of blood vessels; this effect will be stronger for vessels further away from the posterior of the eye. This could change the apparent diameter and the apparent transmission of blood vessels. To counter this, best practice is to limit oximetry measurements to a well-defined, well-constrained region; many studies report results for vessels in terms of distance from the centre of the optic disk.[89] Likewise, the concave curvature of the

outer sclera presents a challenge for imaging bulbar conjunctival and episcleral vessels: this is discussed in context within Chapter 3 (see Section 3.1.4).

1.4 Theory and application of optical oximetry

1.4.1 The absorption spectra of haemoglobin

Optical oximetry techniques are based upon the SO_2-dependent absorption spectrum of haemoglobin (see Figure 1-21). When SO_2 changes, the optical absorption of light by blood will change proportionally. It is possible to estimate changes in SO_2 by measuring change in optical absorption by a blood vessel at two or more wavelengths and then applying two-wavelength oximetry, three-wavelength oximetry, or a multi-wavelength oximetry algorithm.

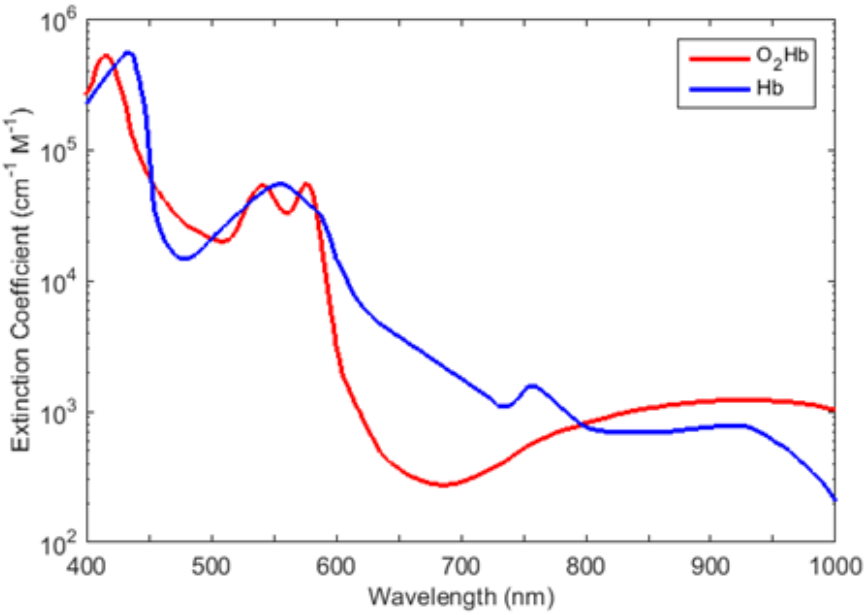

Figure 1-21. The optical absorption spectra of oxygenated (O_2Hb) and deoxygenated haemoglobin (Hb).[I]

1.4.2 Transmission of light through blood

1.4.2.1 Simple Beer-Lambert law

The transmission of light via a homogenous non-scattering absorbing substance is described by the Beer-Lambert law:

[I] Data from Prahl (1999).[19]

$$I_\lambda = I_{\lambda o} \exp(- c\ \varepsilon_\lambda\ d), \quad 1\text{-}7$$

where I_λ is the intensity of the transmitted light (arbitrary units), $I_{\lambda o}$ is the intensity of the incident light (arbitrary units), c is the concentration of absorbers [M], ε_λ is the extinction coefficient of absorbers at that wavelength [$cm^{-1}M^{-1}$], and d is the optical path length [m]. Defining transmission of a blood vessel as $T = \left(\frac{I_\lambda}{I_{\lambda o}}\right)$, the optical density ($OD_\lambda$) of a blood vessel is calculated by:

$$OD_\lambda = -\log(T) = -\log_{10}\left(\frac{I_\lambda}{I_{\lambda o}}\right) = c\,d\,\varepsilon_\lambda. \quad 1\text{-}8$$

Assuming that path length and concentration of absorbers is the same for both wavelengths, then the optical density ratio (ODR) is calculated by:

$$ODR = \frac{OD_{\lambda 1}}{OD_{\lambda 2}} = \frac{c\ d\ \varepsilon_{\lambda 1}}{c\ d\ \varepsilon_{\lambda 2}} = \frac{\varepsilon_{\lambda 1}}{\varepsilon_{\lambda 2}}. \quad 1\text{-}9$$

In blood, the dominant absorber is haemoglobin. The SO_2-dependent effective extinction coefficient (ε_λ) of haemoglobin is expressed by:

$$\varepsilon_\lambda = \left(SO_2 * \varepsilon_{\lambda \mathrm{HbO_2}}\right) + \left((1\text{-}SO_2)\ \varepsilon_{\lambda \mathrm{Hb}}\right), \quad 1\text{-}10$$

where $\mathbf{SO}_2$ is the fractional blood oxygen saturation, $\boldsymbol{\varepsilon_{\lambda \mathbf{HbO_2}}}$ is the wavelength-dependent extinction coefficient of oxygenated haemoglobin, and $\boldsymbol{\varepsilon_{\lambda \mathbf{Hb}}}$ is the extinction coefficient of deoxygenated haemoglobin. If one wavelength is chosen to be isobestic (i.e. insensitive to changes in SO_2), and one sensitive to changes in SO_2, then ODR will be linearly proportional to SO_2.[90,91] If reference SO_2 values are known (e.g. by invasive measurement), then *ODR* can be empirically calibrated to SO_2 by:

$$SO_2 = a * ODR + b, \quad 1\text{-}11$$

where a and b are calibration coefficients which are empirically derived from plotting SO_2 versus *ODR*. This is the basis for two-wavelength oximetry.

1.4.2.2 The modified Beer-Lambert law

The Beer-Lambert law does not account for the effects of optical scattering. Twersky (1970)[92] derived an expression for transmission of light through blood which incorporated multiple scattering. This is given by:

$$OD = -\log_{10}\left(\frac{I}{I_o}\right) \qquad 1\text{-}12$$
$$= c\ d\ \varepsilon - \log\ \left[10^{fH(1-H)d}\ + q\left(1 - 10^{-fH(1-H)d}\right)\right],$$

where H is the haematocrit of whole blood; q is a light detection efficiency factor, and f is a scattering factor which is dependent on wavelength, size, and orientation of the scattering particle. This expression was simplified by Pittman and Duling (1975)[93] by rewriting the scattering dependence as an additive term, B_λ:

$$OD_\lambda = -\log(T)\ = -\log_{10}\left(\frac{I_\lambda}{I_{\lambda o}}\right) = c\ d\ \varepsilon_\lambda + B_\lambda. \qquad 1\text{-}13$$

Delpy et al., (1988) [94] introduced a term to account for modified path length due to scattering, (d'):

$$OD_\lambda = -\log(T)\ = -\log_{10}\left(\frac{I_\lambda}{I_{\lambda o}}\right) = c\ d'\varepsilon_\lambda + B_\lambda. \qquad 1\text{-}14$$

The total extinction coefficient, $\mu_{\mathrm{ext}}(\lambda)$, is defined as:

$$\mu_{\mathrm{ext}}(\lambda) = \mu_{\mathrm{a}}(\lambda) + \mu_{\mathrm{s}}(\lambda), \qquad 1\text{-}15$$

where $\mu_a(\lambda)$ is the total absorption coefficient, and $\mu_{\mathrm{s}}(\lambda)$ is the total scattering coefficient. By substituting ε_λ for $\mu_{\mathrm{ext}}(\lambda)$, we arrive at the modified Beer-Lambert law:

$$OD_\lambda = -\log(T)\ = -\log_{10}\left(\frac{I_\lambda}{I_{\lambda o}}\right) \qquad 1\text{-}16$$
$$= c\ d'\left(\mu_{\mathrm{a}}(\lambda) + \mu_{\mathrm{s}}(\lambda)\right)\ +\ B_\lambda.$$

This is the basis for three-wavelength oximetry (see Section 1.4.6).

1.4.3 Two-wavelength pulse oximetry

Early oximetry devices measured changes in absorption of red and infra-red wavelengths transmitted through the earlobe. However, these oximeters were limited in that the earlobe had to be squeezed to evacuate blood from the earlobe and thus give a calibration reading to account for optical absorption by tissue. Further, SO_2 measurements were an average of arterial and venous blood.[91,95,96] This basic oximetry method was used until the innovation of pulse oximetry in 1972.

In pulse oximetry, light transmission through tissue is recorded, but only the component altering due to pulsating arterial blood is analysed. In theory, this

approach allows absorption and scattering by tissue and venous blood to be excluded from analysis.[97] Pulse oximeters calculate SO_2 using two-wavelength oximetry and empirically derived coefficients (see Equation 1-11). Calibration is derived by relating pulse oximeter ODR to *ex vivo* blood gas samples from many subjects at various SO_2 levels. Calibration accuracy is typically quoted as ± 2% in the range 80 - 100% SO_2.[98] Pulse oximeters are not well calibrated at SO_2 < 80% due to the ethical constraints of lowering subject SO_2.[99,100] Pulse oximetry has been widely adopted for patient monitoring in hospital settings. However, pulse oximetry cannot provide the spatially-resolved SO_2 measurement required for microvascular oximetry; for this, photographic measurements are required.

1.4.4 Two-wavelength imaging oximetry

Photographic measurement of blood vessel transmission enables spatially-resolved measurement of SO_2 in microvasculature. The first photographic retinal oximetry study was conducted by Hickam et al., (1959).[90] Images of both the human retina and blood-filled quartz capillaries in a model eye were acquired at 640 nm (SO_2 contrast) and 800 nm (isobestic) wavebands using a modified retinal fundus camera. Measurements in the model eye established that ODR was linearly proportional to SO_2. *In vivo* SO_2 measurements were calibrated from SO_2 measurements of ex vivo blood samples obtained by the brachial artery of 10 subjects at a variety of fraction of inspired oxygen (FiO_2) levels. To minimise the influence of pigmentation only veins overlying the optic disk were analysed. Retinal venous SO_2 of 34 healthy subjects was estimated to be 57 ± 11% (mean ± standard deviation); arterial SO_2 was not reported. The large standard deviation of venous SO_2 is likely in part due to normal physiological variation and also part due to the sub-optimal absorption of the imaging wavelengths for oximetry (see Section 1.4.5.1).

A later study by Hickam and Frayser (1963)[101] compared two-wavelength combinations; 510 and 640 nm (green/red), and 640 and 800 nm (red/infrared). Average venous SO_2 across all subjects was very similar for both filter combinations: 60 ± 16% (green/red) and 58 ± 10% (red/infrared) (mean ± standard deviation). It is now known that neither of these wavelength combinations is optimal for oximetry.[102]s Vasodilation was noted in response to hypoxia; this was seen to alter ODR slightly, but not alter estimated SO_2 after calibration. This vessel diameter-

dependent ODR alteration had also been observed in *ex vivo* blood samples of varying thickness,[101] and is still an important consideration for two-wavelength oximetry studies to this day.[103]

A further study by Hickam and Frayser (1966)[104] used two-wavelength oximetry to measure retinal artery-vein difference, along with fluorescein angiography to estimate blood flow rate; this enabled estimation of metabolic rate of retinal tissue. Measurements were made at hyperoxia and hypoxia. This study also investigated response of healthy, hypertensive, and diabetic subjects to hyperoxia intervention (i.e. inhalation of 100% oxygen). It was found that diabetic and hypertensive subjects underwent a smaller change in SO_2 in response to hyperoxia in comparison to healthy controls due to impaired vascular reactivity.[104]

The first digital two-wavelength oximetry system to use a CCD detector was developed by Beach et al., (1999).[105] Digital processing enabled the use of computerised vessel tracking and vessel fitting algorithms (such as that depicted in Figure 1-22) to estimate the intensity of light absorbed by a vessel in comparison to local surroundings of the retina away from the optic disk. Imaging was conducted at two near-optimal wavebands (569 and 600 nm) simultaneously, eliminating oximetry artefacts produced in time-sequential multispectral imaging systems.[106] ODR calibration was achieved non-invasively by recording arterial SO_2 with an earlobe pulse oximeter and varying FiO_2 levels. Venous SO_2 was determined to be 55 ± 3.3% (mean ± standard error, 10 healthy subjects).[105] As with earlier studies,[101] it was noted that ODR calibration was dependent on vessel diameter; i.e. vessels of different diameters had different ODR vs. SO_2 regression slopes.

Hammer et al., (2008)[103] studied the retina using the *Imedos* commercial two-wavelength retinal oximetry system. They noted that when using two-wavelength oximetry, the SO_2 of retinal veins decreased linearly with vessel diameter. This is an artefact of ODR calibration because ODR is known to be dependent on vessel diameter.[101,105] Estimated arterial SO_2 was not dependent on vessel diameter because this was implicitly calibrated for by pulse oximetry measurements. This study compensated for this vessel-diameter ODR effect by introducing an empirically derived calibration of SO_2 and vessel diameter. Similarly, they introduced a correction factor for the influence of pigmentation.[103]

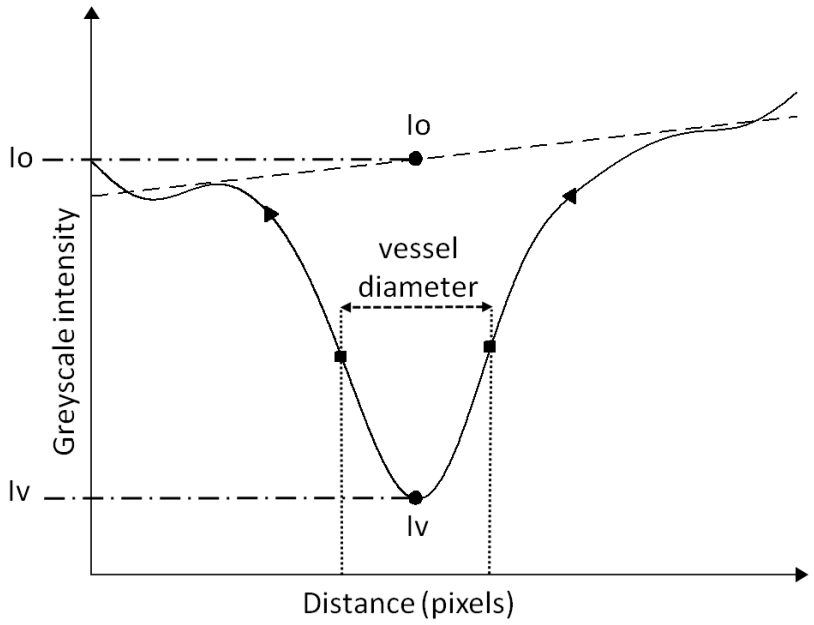

Figure 1-22. Vessel profile fitting algorithm to estimate the optical absorption and diameter of a blood vessel. The points denoted by squares are the point of maxium rate of change of greyscale intensity. These points are used to measure vessel diameter.

A commercial two-wavelength oximetry system, *Oxymap,* was developed by Hardarson et al., (2006).[107] *Oxymap* combines simultaneous acquisition at four wavelengths with automated two-wavelength oximetry analysis. For *Oxymap*, a generic calibration of ODR to SO_2 was derived from a meta-analysis of SO_2 values reported in five previous oximetry studies, arriving at a normal arterial SO_2 = 96%, and a venous SO_2 = 54%.[107] The *Oxymap* system has found use in ophthalmological research, enabling high-powered oximetry studies.[108]

A similar calibration approach to the *Oxymap* system was used by Choudhary et al. (2013).[12] This study used snapshot multispectral imaging with the Image Replicating Imaging Spectrometer (IRIS) at 570 nm and 600 nm (see Section 2.1.3.2) to observe a decrease in retinal SO_2 and increase of retinal vessel diameter in response to acute mild hypoxia. A very low variation across all subjects was reported: 98.5 ± 1.6% and 70.7 ± 2.7% for arteries and veins at normoxia (mean ± standard deviation).[12]

Kristjansdottir et al., (2014)[109] reported the use of a dual-wavelength (532 nm and 633 nm) scanning laser ophthalmoscopy system for retinal oximetry. Calibration of two-wavelength oximetry was achieved by using SO_2 values reported by Schweitzer et al. (1999) [36], which were estimated via hyperspectral oximetry (see Section 1.4.7). This study reported arterial SO_2 of 92 ± 13% for arterioles and 57 ± 12% for venules (mean ± standard deviation). The large standard deviation of results may be due to sub-optimal wavelength choice (see Section 2.1.2.3).

Two-wavelength oximetry has also been employed for oximetry studies where no reference SO_2 values are known. Kristjansdottir et al., (2013) [41] used the *Oxymap* system for oximetry of choroidal blood vessels that were visible in retinal images of subjects with minimal retinal pigmentation. The standard *Oxymap* calibration could not be applied to choroidal vasculature because the SO_2 of choroidal vessels had not been previously reported and choroidal vessels are embedded in highly scattering retinal tissue. Thus results were reported simply in terms of ODR. This study found minimal difference in ODR of choroidal arteries and veins, suggesting low oxygen extraction in choroidal vessels due to high blood flow rate through the choroid.

Two-wavelength oximetry is widely using in photoacoustic tomography (PAT) oximetry studies. In the deep-tissue applications SO_2 is not usually known, so SO_2 is assumed (e.g. 95% in arteries and 65% in veins).[110] Needles et al., (2013)[111] employed this calibration for deep-tissue imaging of a mouse model breast cancer tumour vasculature and estimated SO_2 was found to correlate with invasive measurements of pO_2. A study by Figley et al., (2013) utilised a commercial photoacoustic tomography system (*Vivo Lazr)* to estimate SO_2 in the spinal cord dorsal vein of rats. They reported a baseline venous SO_2 of ~ 45% in a single rat, but two-wavelength oximetry calibration procedure was not reported.

Whilst two-wavelength oximetry is relatively simple to implement, the need for calibration reduces the applicability of the method for applications where SO_2 is unknown. In such scenarios, multi waveband or hyperspectral oximetry algorithms are better suited because they can provide calibration-free estimation of SO_2 (see Section 1.4.7).

1.4.5 Optimising two-wavelength oximetry

1.4.5.1 Optimal vessel transmission

For accurate oximetry, blood vessels must absorb enough light to permit measurement relative to a background (i.e. are not completely transparent or opaque), but still transmit enough light so that useful measurement of transmission can be made. Based upon work by Assendelft (1970),[112] Smith (1999)[102] derived the following expression to arrive at the optimal transmission of light to minimise potential errors in oximetry arising from a small error in estimation of transmission (e.g. due to systematic or other effects). Starting with optical density (*OD*) and transmission (T):

$$OD = -\log\,(T) = -\frac{\ln(T)}{\ln(10)}. \qquad 1\text{-}17$$

The absolute error in OD can be found by differentiating to give:

$$\Delta OD = \frac{dOD}{dT}\Delta T = -\frac{\Delta T}{\ln(10)}\frac{1}{T}. \qquad 1\text{-}18$$

The relative error is then:

$$\frac{\Delta OD}{OD} = \frac{\Delta T}{T\ln(T)}. \qquad 1\text{-}19$$

To minimise the relative error, the first derivative of Equation 1-19 with respect to T is found, and then set to zero.

$$\frac{d(\Delta OD/OD)}{dT} = -\frac{\ln(T)+1}{[\mathrm{T}\ln(\mathrm{T})]^2}\,\Delta T = 0\,. \qquad 1\text{-}20$$

This results in one physical solution for minimal error in transmission:

$$\begin{gathered}\ln(T)+1=0,\\ \Rightarrow T = 1/\mathrm{e} = 36.8\%,\\ \Rightarrow OD = 0.434.\end{gathered} \qquad 1\text{-}21$$

This shows that the optimal transmission for a blood vessel is 36.8%, corresponding to *OD* = 0.434. The transmission region deemed appropriate for accurate oximetry is between 10% and 70% transmission because outside this range the error function grows rapidly.[102,112]

1.4.5.2 Optimal wavelength combinations

A study by Smith (1999)[102] extensively investigated the theoretical optimal choice of two-wavelengths for oximetry of blood vessels of varying diameters and oxygenations by analytical functions, concluding that the combinations of 635 nm & 965 nm, and 488 nm & 635 nm would be optimal for retinal oximetry.[102] These theoretical waveband combinations are, however, not practical because they do not take the practical constraints of imaging sources, available imaging filters, tissue irradiance limits, or optical path length contributions into account; optical path length will be very different for visible (i.e. blue/green) and near infra-red light; blue/green absorption will be dominated by retinal vessels and pigmentation, and near infra-red light will be dominated by absorption by choroidal vessels; this would result in dubious oximetry measurements.

In reality, optimal-wavelength choice for a given application is dictated by the size of blood vessels being investigated, potential absorption by pigmentation, and also the constraints of the illumination and imaging systems. The optimal wavelength combinations for each oximetry application presented within this thesis are discussed in the relevant chapters.

1.4.6 Three-wavelength oximetry

1.4.6.1 Principle of three-wavelength oximetry

Two-wavelength oximetry is based upon the assumption that transmission of light through blood follows the Beer-Lambert law. However, Kramer et al., (1951)[113] demonstrated that light transmission through blood was not well-described by the Beer Lambert law; this is due to the effects of optical scattering and the non-uniform concentration of absorbers.

To account for the influence of optical scattering and non-uniform concentration of absorbers in oximetry, Pittman and Duling (1975) [93] developed three-wavelength oximetry. Their technique requires three-wavelengths, all of which are similar wavelengths: two isobestic wavelengths are used to estimate scattering contributions, and a third wavelength is chosen to be sensitive to changes in SO_2.

Three-wavelength oximetry follows from the basis of two-wavelength oximetry; SO_2 can be empirically related to the absorption of light at two-wavelengths by:

$$SO_2 = a\left(\frac{OD_{\lambda 1}}{OD_{\lambda 2}}\right) + b, \quad 1\text{-}22$$

where OD_λ is measured optical density at a given wavelength, and a and b are empirically derived constants. OD_λ is described by the modified Beer-Lambert law as:

$$OD_\lambda = \varepsilon_\lambda\, c\, d + B_\lambda, \quad 1\text{-}23$$

where ε_λ is the extinction coefficient of blood of a given oxygenation, c is concentration of haemoglobin, d is the optical path length of light through blood, and B_λ is a composite term describing the effect of scattering on measured optical density. Assuming proximity in wavelength, B_λ will be equal for isobestic wavelengths, $\lambda 1$ and $\lambda 2$:

$$B_{\lambda 1} = B_{\lambda 2} = B. \quad 1\text{-}24$$

The optical density of these wavelengths can then be written as:

$$OD_{\lambda 1} = \varepsilon_\lambda\, c\, d + B, \quad 1\text{-}25$$

$$OD_{\lambda 2} = \varepsilon_\lambda\, c\, d + B. \quad 1\text{-}26$$

Solving 1-25 and 1-26 simultaneously yields an expression for B:

$$B = \frac{(\varepsilon_{\lambda 1}/\varepsilon_{\lambda 2})\, OD_{\lambda 1} - OD_{\lambda 2}}{(\varepsilon_{\lambda 1}/\varepsilon_{\lambda 2}) - 1}, \quad 1\text{-}27$$

where $\varepsilon_{\lambda 1}$ and $\varepsilon_{\lambda 2}$ are the extinction coefficients of haemoglobin at $\lambda 1$ and $\lambda 2$. Once B is known, then it can then be incorporated into Equation 1-22 to give:

$$SO_2 = a\left(\frac{OD_{\lambda 3}+B}{OD_{\mathrm{ref}}+B}\right) + b, \quad 1\text{-}28$$

where $OD_{\lambda 3}$ is the optical density at a third oxygen sensitive wavelength, and OD_{ref} is the optical density at an isobestic wavelength. Equation 1-28 is then applied in a similar manner to two-wavelength oximetry. It should be noted that if $(\varepsilon_{\lambda 1}/\varepsilon_{\lambda 2})$ is close to 1, then large errors can result in the estimation of B from Equation 1-27.

1.4.6.2 Wavelength combinations for three-wavelength oximetry

Three-wavelength oximetry is applicable only to a limited range of wavelengths where optical scattering by blood is similar. Pittman and Duling (1975)[93] found that recovered scattering properties for blue wavelengths (420 nm, 436 nm, and 450 nm) showed significant variation due to a change in refractive index in this region due to the significant change in absorption of haemoglobin at these wavelengths. Instead they employed the triad of 520 nm, 546 nm, and 555 nm which was found to have suitable similar scattering properties. With this wavelength choice, they reported an uncertainty in SO_2 measurement of ± 1% in *ex vivo* blood samples.

Delori et al., (1988)[114] employed three-wavelength oximetry at 558 nm, 569 nm, and 586 nm. Reported SO_2 in healthy human subjects was 98 ± 8% for retinal arteries and 45 ± 7% for retinal veins. However, when compared to blood-gas analyser measurements, this system consistently over-estimated SO_2 below 50%.

Smith (1999)[102] thoroughly investigated optimal wavelength choices for three-wavelength oximetry in retinal arteries and veins via analytical calculations. Smith concluded that there are three optimal waveband triads for three-wavelength retinal oximetry: 488 nm, 635 nm, & 905 nm; 600 nm, 635 nm, & 905 nm; and 635 nm, 720 nm, & 905 nm. However it should be noted that imaging the retina over such a broad spectrum of wavelengths is technically very challenging, and that the optical path length of blue light will be very different from the optical path length of near infra-red light. Thus, the 488 nm, 635 nm, 905 nm combination will likely be sub-optimal for oximetry in reality.

Whilst three-wavelength oximetry may offer improved accuracy over two-wavelength oximetry, it still requires an ODR calibration, and the potential choice of imaging wavebands is limited. Further, the effects of scattering and non-uniform concentration of absorbers are incorporated into multispectral and hyperspectral oximetry algorithms. For these reasons, three-wavelength oximetry has not been widely employed, with most oximetry studies either using two-wavelength oximetry or MSI/HSI oximetry algorithms.

1.4.7 Multispectral and hyperspectral oximetry algorithms

1.4.7.1 Principle

MSI and HSI oximetry algorithms estimate SO_2 values without the need for calibration of SO_2 to ODR. Instead, MSI/HSI algorithms fit experimentally recovered transmission values at many wavelengths to a model of expected theoretical transmission. The exact theoretical model used varies between studies, but at a minimum will include the absorption spectra of oxygenated and deoxygenated haemoglobin. Further terms may be added to account for vessel diameter; scattering parameters; concentration of absorbers; single/double pass parameters, and a contrast reduction parameter. The maximum number of parameters that can be fitted to the model is equal to the degrees of freedom (i.e. total number of wavelengths) incorporated into the transmission model. Studies which have applied MSI/HSI algorithms in the retina are summarised in Table 1-2. Likewise, MSI/HSI studies in other oximetry applications are summarised in Table 1-3.

The disadvantage of MSI/HSI imaging techniques is that they require either time-sequential spectral imaging or more sophisticated snapshot imaging techniques (see Section 2.1). Further, validation of oximetry algorithms may be challenging due to the variation of optical parameters between *in vivo* and *ex vivo* applications.

Table 1-2. Retinal oximetry studies utilising MSI/HSI oximetry algorithms.

Study	Wave-range	Known parameters	Estimated parameters	Recovered normoxia SO_2
Schweitzer et al., (1999)[36]	510 – 586 nm 76 wavebands	ε, εmel	SO_2 , c, d, η	A: 92.2 ± 4.1% V: 57.9 ± 9.9%
Drewes et al., (1999)[115]	629, 678, 821, & 899 nm.	ε	SO_2, S, c, d	A: 101% V: 65%
Smith et al., (2000)[116]	488, 635, 670, 752, & 830 nm	ε	SO_2, S, c, d, η	V: 42-56%
Alabboud et al., (2007)[117]	500 – 700 nm 27+ wavebands	ε, S	SO_2, d, c, η	A: 96%. V: 55%
Mordant et al., (2011)[118]	500 - 650 nm 300 wavebands	ε, S	SO_2, d, c, η	A: 104% V: 35%
Khoobei et al., (2007)[119]	522 – 586 nm 7 wavebands	ε	SO_2	A: 92% V: 76%
Arimoto et al., (2010)[120]	510 – 600 nm 45 wavebands	ε	SO_2	2D map of relative SO_2
Furukawa et al., (2012)[120]	510 – 600 nm 7 wavebands	ε	SO_2	2D map of relative SO_2
Gao et al., (2012)[121]	510 - 586 nm 8 wavebands	ε	SO_2	2D map of SO_2
Salyer et al., (2006)[74]	420 – 700 nm 29 wavebands	ε	SO_2, S	Correlated well with *ex vivo* measurements

Key**:** A = arteries, V = veins. SO_2 = oxygen saturation, ε = extinction coefficient of Hb and HbO_2, εmel = extinction coefficient of melanin, S = scattering contribution; c = concentration of haemoglobin, η = single/double pass contribution factor; d = diameter of vessels; K = contrast reduction factor.

Table 1-3. Oximetry studies utilising MSI/HSI oximetry algorithms.

Study	Application	Wave-range	Known parameters	Estimated parameters	Estimated SO_2 & notes
Shonat et al., (1997)[122]	Mouse brain	504-600 nm 12 bands	ε	SO_2, S, η	A: 80% V: 30%
Sorg et al., (2005)[9]	Mouse skin-fold window chamber (tumour)	505-575 nm	ε	SO_2, S, η	A: 77±2% V: 68±2%
Sorg et al., (2008)[123]	Mouse skin-fold window chamber (tumour)	505-575 nm	ε	SO_2, S, η	A: 66±3% V: 37±2%
Chapter 5 of this thesis	Rat spinal cord dorsal vein	546, 560, 570, 584, 590, 600 nm	ε, S, d	SO_2, c, K, η	V:68%
Hendargo et al., (2015)[106]	Mouse skin-fold window chamber	540, 560, 580, and 610 nm	ε	SO_2, c	A: ~ 40% V: ~ 29%
Fernandez-Ramos et al., (2014)[11]	*Ex vivo* red blood cells	560 - 600 nm 8 bands	Spectral end-members	SO_2	SO_2 map
Wang et al., (2015)[124]	retinal vessel phantom	650 - 1000 nm 35 bands	ε	SO_2	SO_2 map
Clancy et al., (2014)[125]	Porcine bowel	440 – 700 nm. 28 bands	ε	SO_2	50-74%
Yudovsky et al., (2011)[126]	Diabetic foot ulcers	550-660 nm 15 wavebands	ε, εmel	c, cMel, S	Relative concentration of Hb and HbO_2
Chin et al., (2012)[127]	Diabetic foot ulcers	500 – 600 nm	ε	SO_2	SO_2 map

Key: A = arteries, V = veins. SO_2 = oxygen saturation, ε = extinction coefficient of Hb and HbO_2, εmel = extinction coefficient of melanin, S = scattering contribution; c = concentration of haemoglobin, η = single/double pass contribution factor; d = diameter of vessels; K = contrast reduction factor.

1.4.7.2 MSI/HSI oximetry algorithm calibration

Calibration *of in vivo* MSI/HSI oximetry models is challenging, especially when no reference SO_2 values are known and when the imaging environment is optically complex. For example, in the retina, estimated SO_2 can be compared to well-established reference values used to calibrate two-wavelength oximetry (e.g. 96% for arteries and 54% for veins).[107] However, in applications like tumour development, normal SO_2 values are not known, and may be very different from physiological norms because tumours may promote angiogenesis of blood vessels and have highly atypical metabolic demand compared to healthy tissue. A study of tumour development by Sorg et al., (2005)[9] reported an arterial SO_2 of 77% and a venous SO_2 of 68%; this is an abnormally low artery-vein difference (9% compared to ~ 30%), and the baseline arterial SO_2 is very low (normally ~ 97% normally). However, it is not known if this may be due to calibration of the oximetry algorithm or actually due to biological variation caused by the tumour. Inaccurate or spurious SO_2 estimation may be simpler to infer in healthy controls. For example, Hendargo et al., (2015)[106] reported a very low arterial SO_2 of ~ 40%; This is highly unlikely because deviates greatly from physiological norms for arteries (normally 97-100% SO_2). Thus, this likely indicates a calibration issue in the oximetry algorithm employed.

One validation strategy is to change SO_2 *in vivo* by altering FiO_2. The response to this intervention can then be analysed to test for physiological plausibility; i.e. do the measured changes in SO_2 correlate with changes in FiO_2? However, this is still somewhat limited and subjective. Precise, quantitative validation would be preferable. Correlating SO_2 with pulse oximetry may also be of limited use, depending on the application because arterial SO_2 can only increase by a few percent at hyperoxia, but venous SO_2 can increase significantly.

Shonat et al., (1997)[122] employed a highly novel non-invasive validation technique by non-invasively measuring pO_2 of blood concurrently with SO_2. pO_2 measurement was enabled by injection of a molecule with pO_2-dependent phosphorescence properties; measuring this phosphorescence required a second, separate, MSI system. Whilst elegant, this validation strategy has not been pursued in other oximetry studies, perhaps due to the requirement for invasive injection of a phosphorescent molecular probe. Further, the non-linear relationship between pO_2 and SO_2 will complicate measurements. This approach could provide some degree

of quantitative validation of SO_2 estimation *in vivo*, however, without independent non-invasive measurement of SO_2 *in vivo*, true validation cannot be achieved.

1.5 Summary

This chapter motivated the need for *in vivo* oximetry and has introduced the key concepts and challenges associated with *in vivo* oximetry. The circulatory system and physiology associated with the oxygen delivery via the blood was described in Section 1.2, with particular emphasis on the physiology of the eye because Chapters 3, 4, and 6 all focus on oximetry of blood vessels in the eye.

Artefacts in transmission caused by spurious optical absorption and scattering *in* vivo require significant consideration throughout this thesis. These challenges are described in detail in Section 1.3.

The various oximetry algorithms, their advantages and disadvantages, and optimal employment are described in Section 1.4. Two-wavelength oximetry is utilised in Chapter 3, whilst simple intensity-ratio measurement is utilised in Chapters 4 and 6. A multi-spectral calibration-free oximetry model is applied to the spinal cord dorsal veins of rats in Chapter 5.

2 A review of microvascular imaging techniques for oximetry

Summary: *This chapter reviews the multiple optical imaging modalities that are capable of microvascular oximetry, and discusses the unique advantages and disadvantages associated with each modality. Of all the modalities reviewed, only multispectral imaging (MSI) was found to be capable of providing the high spatial and temporal resolution (<1 second) required for monitoring rapid changes in SO_2 in the human microvasculature in a non-contact manner. This informs the choice to use MSI for the applications presented in this thesis, where the high temporal resolution of snapshot MSI enables observation of rapid changes in SO_2.*

2.1 Multispectral and hyperspectral imaging (MSI/HSI)

2.1.1 Overview

In multispectral imaging (MSI) and hyperspectral imaging (HSI), images are acquired at multiple wavelengths to create a spectral data cube (x,y,λ); enabling imaging spectroscopy of blood vessels for oximetry. HSI and MSI can be adapted to conventional broadband imaging systems, such as retinal fundus cameras or research microscopes with relative ease, and the spatial resolution of HSI/MSI systems can theoretically be as good as the parent modality (e.g. diffraction limited optical microscopy).[11]

In HSI, a large number of spectral images are captured across dozens or hundreds of wavebands, building up a high spectral resolution data cube. However, this produces extremely large datasets and requires either significant acquisition time or complex scanning spectroscopy systems, such as push-broom spectrometers. In MSI, a more limited number of wavelengths (typically between two and ten) are acquired, reducing time for acquisition and/or the need for scanning or complexity acquisition systems. Recently, snapshot MSI systems have been developed, allowing concurrent acquisition of images at several wavelengths, enabling video-rate MSI. Video rate acquisition is not possible with HSI systems, so

MSI is better suited to biomedical applications where a high temporal resolution is beneficial. This subsection reviews the capabilities of relevant MSI and HSI techniques and their application to oximetry.

2.1.2 Time sequential spectral imaging systems

Time sequential imaging is the simplest MSI/HSI imaging approach, where images at various wavebands are acquired sequentially. Time-sequential filtering technologies include simple bandpass interference filters, liquid crystal tuneable filters (LCTFs), and acousto-optical tuneable filters (AOTFs). Light sources such as wavelength tuneable lasers and switchable LEDs can provide a variety of high-power illumination wavelengths for time-sequential applications. However, the time required for imaging makes time-sequential systems poorly suited to the study of rapid biological processes which occur in the timescale of < 1 second.

2.1.2.1 MSI and HSI oximetry with Liquid Crystal Tuneable Filters (LCTFs)

Liquid Crystal Tuneable Filters (LCTFs) are spectral filtering devices commonly employed for HSI oximetry due a wide range of accessible wavelengths, lack of moving components, electronic switching, and ease of incorporation into existing imaging systems. LCTFs are constructed layers of liquid crystal filters, each which pass various frequencies of linearly polarised light. These layers can be switched electrically to pass a user-defined pass band. Electrical switching can be as fast as ~ 50 ms. Unpolarised light is passed at a maximum of 50% efficiency as one polarisation state is rejected.[128] The pass band efficiency of LCTFs are maximum at red wavelengths but can be as low as 15% at blue wavelengths.[129] LCTF bandwidth varies with wavelength, but is typically around 10 nm. The wide range of accessible wavelengths makes LCTFs suitable for oximetry of blood vessels in a variety of applications, including retinal oximetry, tissue oximetry, and tumour oximetry. Oximetry studies using LCTFs are summarised in Table 2-1.

2.1.2.2 MSI and HSI oximetry with acousto-optic tuneable filters (AOTFs)

AOTFs use the electrical switching of applied RF acoustic pressure waves to tune the spectral output of a crystal, enabling wavelength filtering across a broad spectral range. Wavelength switching can be as fast as 25 µm (approximately 2000x faster than LCTFs). AOTFs have a narrow bandwidth typically ~ 2 nm, with a peak transmission efficiency of ~ 30%, and are more efficient at shorter blue wavelengths

than LCTFs.[128] However, unlike LCTFs, AOTFs require a small-format well-collimated input light beam which limits their practical usage to spectrally filtering light incident on the target, and not spectrally filtering the resulting image. Oximetry studies using AOTFs are summarised in Table 2-2.

Table 2-1. Summary of MSI/HSI oximetry studies utilising LCTFs.

Study	Application	Wavelengths	Oximetry technique
Khoobei et al., (2007)[119]	Retina of monkeys	522-586 nm 7 wavebands	MSI oximetry algorithm
Hirhohara et al., (2007)[130]	Human retina and model eye phantom	500-720 nm, 23 wavebands	HSI oximetry algorithm
Alabboud et al., (2007)[117]	Human retina	500 - 700 nm	HSI oximetry algorithm
Mordant et al., (2011a)[131]	Model eye phantom	500 - 650 nm, 2 nm increments	HSI oximetry algorithm
Mordant et al., (2011b)[118]	Human retina	500 - 650 nm, 2 nm increments	HSI oximetry algorithm
Sorg et al., (2005) [10]	Tumour development in mice	500 - 575 nm, 5nm increments	HSI oximetry algorithm
Sorg et al., (2008)[11]	Tumour development in mice	500 – 575 nm, 5 nm increments	HSI oximetry algorithm
Yodovsky et al., (2011)[126]	Diabetic foot ulcer development	500 - 600 nm, 15 wavebands	HSI oximetry algorithm
Chin et al., (2012) [127]	Human skin	500 – 600 nm, 15 wavebands	HSI oximetry algorithm
Clancy et al., (2014)[125]	Bowel laparoscopy	440-700 nm, 10 nm increments	HSI oximetry algorithm
Mordant et al., (2014)[6]	Glaucomatous human retina	556 – 650 nm, 2 nm increments	HSI oximetry algorithm

Table 2-2. Summary of MSI/HSI oximetry studies using AOTFs.

Study	Application	Wavelengths	Oximetry technique
Shonat et al., (1997)[122]	Murine brain oximetry	500 – 600 nm, 13 wavebands	HSI oximetry algorithm
Gupta et al., (2008)[133]	Skin tissue oximetry	400 – 800 nm, 10 nm increments	HSI oximetry algorithm
Arimoto et al., (2010)[120]	Retinal oximetry	510 - 600nm, 2 nm increments or 5 wavebands	HSI/MSI oximetry algorithm
Furukawa et al., (2012)[134]	Retinal oximetry	510 – 600 nm, 5 wavebands	MSI oximetry algorithm
Patel et al., (2013)[135]	Retinal oximetry	500 – 600 nm, 5nm increments	HSI oximetry algorithm
van der Putten et al., (2015)[136]	Murine capillary oximetry	410 - 450 nm, 6 wavebands	MSI oximetry algorithm

2.1.2.3 MSI with scanning laser ophthalmoscopes (SLOs)

Scanning laser ophthalmoscopes (SLOs) can offer improved contrast, spatial resolution, and some models (i.e. the Optos 200TX) offer improved field of view (up to 200°)[137] when compared to standard retinal fundus cameras (typically 15 - 35 ° field of view).[85,138] In SLOs, images are formed by scanning a tightly focused beam of laser illumination across the retina. The intensity of the resultant backscattered light is then recorded by a photodiode at each point to form an image. Laser illumination has advantages in that adaptive optics can be employed to stabilize the images,[82] and also that mydriasis (dilation of the pupil) is not necessary; this is particularly helpful in imaging infants because avoiding mydriasis is desirable in infant retinal imaging.[139]

A number of retinal oximetry studies have employed SLOs for oximetry; these are summarised in Table 2-3. Oximetry is achieved by sequentially imaging using multiple lasers, each with a different wavelength. However, choice of laser wavelengths is limited by commercially-available laser wavelengths, which may be sub-optimal for oximetry,[102] resulting in reduced accuracy in comparison with MSI retinal fundus cameras. For example. the typical repeatability of measurements reported in SLO oximetry is in the range of 5 – 17%[140]; in comparison, a retinal fundus camera with snapshot capability reported a repeatability of ± 1% for retinal arterioles.[12]

Table 2-3. Summary of multispectral SLO oximetry studies.

Study	Application	Wavebands
Denninghoff et al., (1997)[141]	Retinal oximetry of swine	629, 678, 821, 899 nm
Denninghoff et al., (1998)[142]	Retinal oximetry of swine	629, 678, 821, 899 nm
Drewes et al., (1999)[115]	Model eye phantom and human retinal oximetry	629, 678, 821, 899 nm
Smith et al., (2000)[72]	Model eye phantom	629, 678, 821, 899nm vs. 488, 635, 670, 830 nm
Ashman et al., (2001)[143]	Human retinal oximetry	633 and 815 nm
Denninghoff et al., (2003),[144]	Retinal oximetry of swine	629, 678, 821, 899 nm
Denninghoff et al., (2011)[140]	Retinal oximetry of humans and swine	456, 477,488, 497, 515 nm
Li et al., (2011)[82]	Human retinal oximetry	680 and 796 nm
Kristjansdottir et al., (2014)[109]	Human retinal oximetry	532 and 633 nm
Vehmeijer et al., (2016)[139]	Retinal oximetry in human infants	532 and 633 nm

2.1.2.4 Scanning spectrograph systems

Scanning spectrograph hyperspectral imaging systems consist of a line-scan imaging spectrograph system which is spatially scanned to form a hyperspectral data cube. These systems are advantageous in that they do not spectrally filter light, and are thus more optically efficient than filter-based systems. Further, because they scan across a target, the overall illumination light intensity on an imaging target can be relatively low, which is advantageous for applications as art conservation of biomedical imaging.[145] Scanning spectrograph systems are typically deployed for remote sensing applications where the relative movement between a target and

imaging system can be used to scan the target and create a hyperspectral image (e.g. on a satellite, or inspecting goods on a conveyer belt).[146] However, this need for scanning is highly disadvantageous in biomedical applications where intrinsic motion of the target can produce significant artefacts within a scan. Schweitzer et al. (1999),[36] Beach (2002),[147] and Khoobei et al., (2004)[148] have employed scanning spectrographs for retinal oximetry, albeit in limited retinal regions.

2.1.3 Snapshot multispectral imaging (SMSI) for oximetry

2.1.3.1 Motivation

Snapshot multispectral imaging (SMSI) techniques enable simultaneous acquisition of image at multiple spectral wavebands without the need for time-sequential scanning. Snapshot techniques are particularly advantageous for biomedical imaging, where rapid biological processes can occur on the timescale of a few seconds or less and where time-sequential scanning has been shown to produce artefacts in oximetry when compared to SMSI.[106]

2.1.3.2 Image Replicating Imaging Spectrometer (IRIS)

The Image Replicating Imaging Spectrometer (IRIS) is a SMSI device developed by the Imaging Concepts Group at the University of Glasgow. IRIS enables 8-band SMSI onto a single detector array. Because IRIS is passive, acquisition rate of MSI is limited only by detector frame-rate enabling very high frame rate multispectral imaging (> 30 Hz); ideal for observation of fast biological processes.[11]

IRIS operates by spectrally de-multiplexing an input broadband image into 2^n separate spectral waveband images. The principle of IRIS is shown in Figure 2-1. Initially, an unpolarised broadband white light image passes through a linear polariser that is orientated vertically. This light then passes through a quarter wave plate with its fast-axis orientated at 45° to the vertical axis of the polariser. Subsequently, the light is resolved into co-propagating horizontal and vertical polarisations of equal amplitude due to the birefringence of the quarter wave plate. This effect is wavelength-dependent. The light then reaches a Wollaston prism where interference between vertical and horizontal polarisations occurs. The Wollaston prism then resolves these into two orthogonally-polarised divergent rays, effectively creating two images, each with a different spectral filter-function. This

process is repeated 2^n times where n is the number of filter plate and Wollaston prism assemblies. The filter function can be tuned by changing the birefringence or thickness of the quarter wave-plates.[149–151] The spectral filter functions of IRIS are described by:

$$T_{||}(k,t) = cos^2 btk/2, \quad 2\text{-}1$$

$$T_{\perp}(k,t) = sin^2 btk/2. \quad 2\text{-}2$$

IRIS has 100% spectral throughput because it does not reject light. However, the spectral purity of waveband images can be enhanced by a subsequent clean-up filter plate assembly, which will absorb some light.[11]

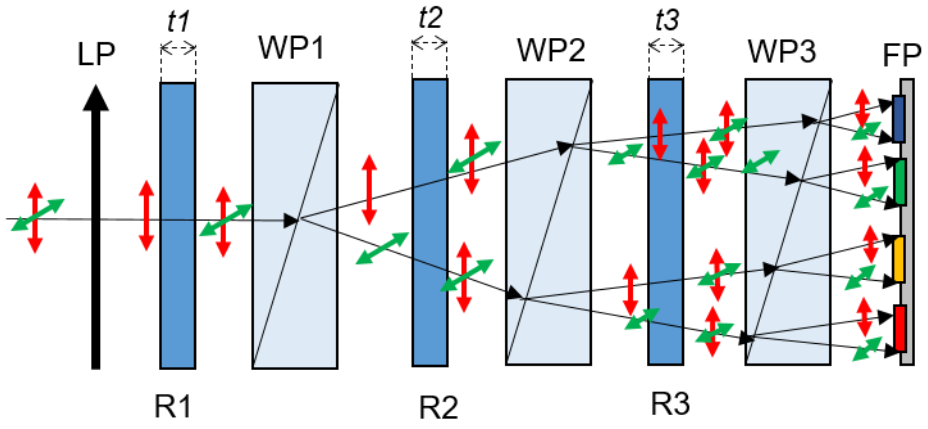

Figure 2-1. The components and principle of IRIS. LP = linear polariser; R1, R2, R3 = quarter wave plates; WP1, WP2, WP3 = Wollaston Prisms; FP = filter plate; t1, t2, t3 = thickness of each quarter wave plate. Red arrows represent the vertical polarisation component of light, and green arrows represent the horizontal polarised component of light.

Several IRIS configurations have been demonstrated, including an 8 band visible to near-infra red IRIS (540 - 780 nm),[151] a 16 band visible and near infra-red IRIS (440 – 840 nm),[11] a 8 band short wave infra-red IRIS (700-1700 nm),[152] and a narrowband 8-band visible IRIS (560 - 600 nm) for oximetry. The central wavelengths of the wavebands are: 560, 567, 571,577,579, 584, 591, and 600 nm, corresponding to isobestic or high contrast wavelengths in the haemoglobin absorption spectra. These wavebands are shown in Figure 2-2.

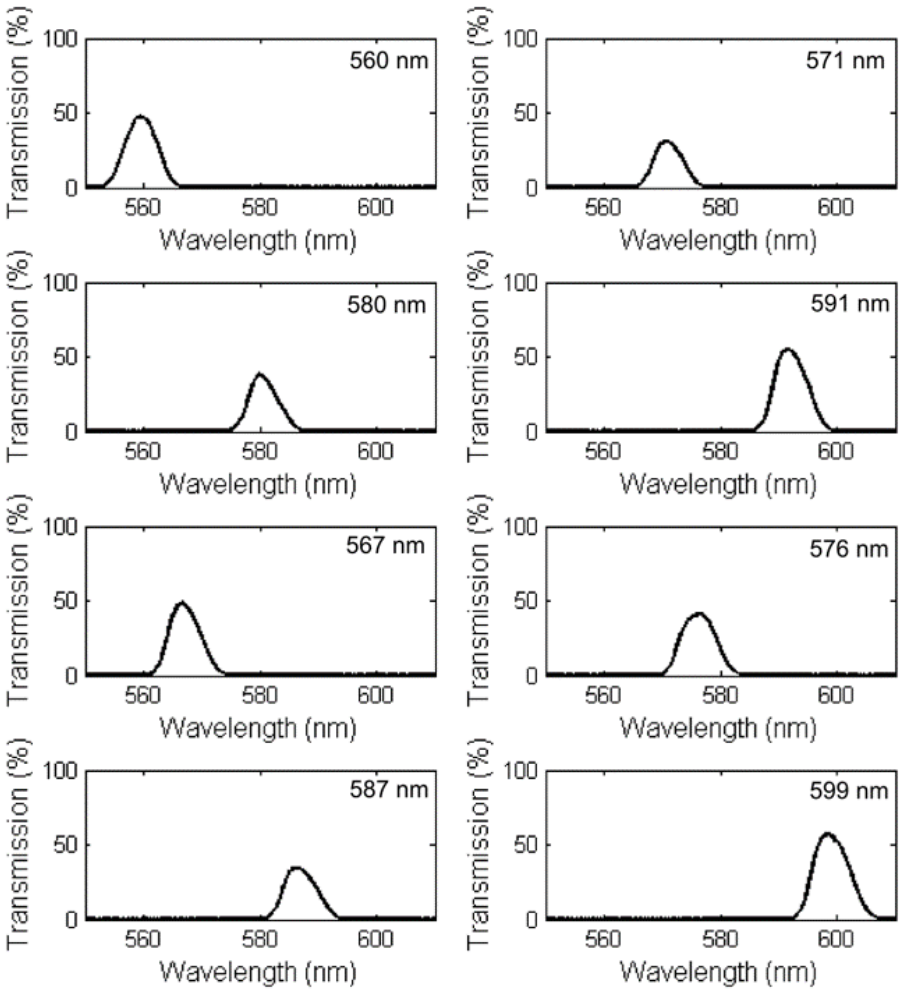

Figure 2-2. Transmission spectra of IRIS wavebands with the clean-up filter plate.

This narrowband IRIS system (hereby referred to as IRIS for simplicity) has been utilised for several oximetry studies. The first proof-of-concept study of IRIS for SMSI oximetry was reported by Alabboud et al., (2007),[117] which showed that arteries and veins could be classified by their spectral transmissions. Mordant et al., (2011) demonstrated principle component analysis of IRIS images for identifying arteries and veins, by using an 8-band narrowband IRIS system between 574 and 613 nm. Choudhary et al., (2013)[12] used IRIS for 2 wavelength snapshot retinal oximetry. This study quantified changes in SO_2 levels, and changes in diameter of retinal blood vessels at normoxia and acute mild hypoxia conditions; this study found very high repeatability of oximetry measurements in arterioles (± 1% standard

deviation). The same IRIS configuration has been operated at near infra-red wavelengths by Chouhdary et al., (unpublished)[153] for non-invasive choroidal imaging using red-eye reflection. This study showed that changes in spectra of red eye reflection could be used to quantify hypoxia in the choroid. Fernandez-Ramos et al., (2014) [11] demonstrated the use of IRIS with a spectral clean-up filter plate (see Figure 2-1 and Figure 2-2) and a spectral unmixing algorithm for video-rate oximetry in individual *ex vivo* red blood cells. The 30 Hz frame rate achieved enabled rapid quantification of this oxygen release process, which had not previously been quantified in a population of red blood cells at video rates.[136]

2.1.3.3 Snapshot MSI with beam splitters

The simplest form of SMSI utilises one or more beam splitters to create two images, each of which can be filtered separately and imaged onto one or more digital detectors. A two-wavelength beam splitter imaging system was first demonstrated for retinal oximetry by Tideman et al., (1998)[3] and Beach et al., (1999).[105] This basic concept is also used by the *Oxymap* retinal oximetry system.[107] Notably, the *Oxymap* system uses a beam splitter assembly to capture images at four wavelengths simultaneously, but only uses two for analysis. Hendargo et al., (2015)[106] developed a four-wavelength beam splitter system for oximetry in dorsal skin fold microvasculature in mice. Their system comprises a sequence of beam-splitters of varying transmission (30/70, 40/60, 50/50) to maximise light throughput at each waveband. However, multiplexing this approach to more several wavelengths quickly becomes highly inefficient as each beam splitter used diminishes the intensity of light.

2.1.3.4 Lenslet array SMSI

Ramella-Roman et al., (2007)[154] demonstrated basic retinal oximetry with an lenslet array based approach for SMSI. Their system re-imaged a broadband image from a fundus camera onto a single detector via a lenslet array, with an array of bandpass filters used to spectrally individually filter each lenslet image. Two configurations were demonstrated: 6-band (540 – 680 nm) and 18-band (460 - 660 nm). However, no further oximetry studies have been published, possibly due to the relatively poor image quality and limited field of view of the lenslet approach.

2.1.3.5 Imaging mapping spectrometer (IMS)

Gao et al., (2010)[155] demonstrated the imaging mapping spectrometer (IMS) for SMSI. The IMS utilises a lenslet array, dispersive prisms, and computational image reconstruction to create a 60-waveband spectral image (at 450 – 600 nm) on a single detector. The feasibility of the IMS for monitoring sub second haemodynamics changes in retinal vessels was demonstrated by Gao et al., (2012).[156] However, despite this capability for high spectral and temporal resolution, no further oximetry studies with the IMS have been published.

2.1.3.6 Computed Tomography Imaging Spectrometer (CTIS)

Johnstone et al., (2007)[157] demonstrated the use of the Computed Tomography Imaging Spectrometer (CTIS) for retinal oximetry. The CTIS uses dispersive diffraction optics, a CCD detector, and computational image recovery to produce a hyperspectral data cube of 30 wavebands between 450 and 750 nm. The CTIS was used for oximetry of two healthy subjects, but despite the suitability of the system for oximetry, no further oximetry studies have been reported.

2.2 Photoacoustic Imaging

2.2.1 Basic principle

Photoacoustic imaging (also known as optoacoustic imaging) is a hybrid imaging modality that combines optical contrast with the deep-tissue detection capability of ultrasound. There are two variants of photoacoustic imaging: photoacoustic tomography (PAT) and photoacoustic microscopy (PAM). PAT enables deep-tissue imaging whereas in PAM offers optical resolution with low depth penetration. In both modalities, the basic principle is the same: a high-intensity low-duration pulse of laser light (<10ns) is absorbed by blood, causing the blood to rapidly heat up by <0.1 degrees.[158] The blood expands and contracts, generating ultrasound waves which propagate through tissue relatively unimpeded. This ultrasound signal can then be detected by one or more ultrasound transceivers coupled to the tissue (e.g. via gel or water) and an image of the absorber reconstructed. As a first approximation, the amplitude of detected ultrasound waves is directly proportional to the degree of optical absorption by blood at that wavelength of illumination light,[159] so photoacoustic imaging can be used for oximetry by simply imaging at multiple wavelengths.

2.2.2 Photoacoustic Tomography (PAT)

PAT enables deep tissue imaging and oximetry up to a depth of several centimetres in tissue. In PAT, a volume of tissue is diffusely illuminated ("floodlit") by a nanosecond high-energy laser pulse, resulting in ultrasound signals from all blood vessels in the illuminated volume. These multiple signals are then detected and reconstructed into a volumetric image by using back-projection algorithms.[160]

The spatial resolution and depth-penetration of PAT is limited by the frequency of ultrasound transceivers used: higher frequency transceivers have higher spatial resolution, but decreased depth penetration due to increased attenuation of ultrasound by tissue at higher frequencies. The exact spatial resolution achieved varies with application and set-up, but is typically on the order of 10 – 100 µm; typically ~ 1/200th of imaging depth.[161] Further, application of PAT is limited by the high laser energy required, making it unsuitable for imaging the eye safely.

To date, applications of PAT oximetry include monitoring the development and treatment of cancer tumours,[80,111,162,163] monitoring osteoarthritis in finger joints,[164] hand-held deep tissue oximetry measurements,[111] oximetry of the rat spinal cord dorsal vein,[165] and oximetry of blood vessels in the brains of rats.[166] Many of these applications are not possible with non-invasive MSI/HSI due to the presence of thick surrounding tissue. However, PAT requires expensive laser sources, transducer arrays, complex back-projection algorithms, and high-intensity laser illumination.[80]

2.2.3 Photoacoustic Microscopy (PAM)

PAM is a high resolution vascular imaging and oximetry modality where images are created by raster scanning a dual focused optical beam and a high-frequency focused ultrasound transducer across a target. The resolution of PAM is determined by the convolution of the point spread function (PSF) of the laser spot and the PSF of the focused ultrasound transducer.[167] This gives arise to two PAM variants: acoustic-resolution PAM (AR-PAM) and optical-resolution PAM (OR-PAM).

In AR-PAM, the resolution is solely determined by the PSF of the focused ultrasound transceiver; this can be as high as ~ 10 μm for depths of <1 cm. However due to ballistic optical scattering, the penetration depth of AR PAM is limited to < 1 mm.[167] In OR-PAM, very high lateral resolution (up to ~ 1 μm)[168,169] can be achieved by using a very high frequency ultrasound transceiver (~ 100 MHz) which has a very small PSF. However, at these frequencies the depth penetration of the ultrasound is extremely limited, limiting the depth penetration of AR-PAM to ~ 100 μm,[167] which is less than the depth penetration of pure optical imaging in tissue (~ 2 mm). The highest resolution OR-PAM oximetry study has been able to quantify SO_2 and oxygen release in individual red blood cells flowing within a mouse ear.[168]

The advantages of PAM oximetry in comparison to conventional optical imaging is that PAM is less affected by scattering of light by tissue; however this scattering may be minimal anyway due to low penetration depths of PAM. The disadvantages of PAM are that PAM systems are complex, PAM require both optical scanning and ultrasonic coupling to tissue, and that PAM has very low axial resolution. Further, PAM systems are highly sensitive to motion of the target. These combinations make PAM suitable only to select applications.

2.3 Optical Coherence Tomography (OCT)

2.3.1 Basic principle

Optical coherence tomography (OCT) is a non-contact imaging technology which is capable of high-resolution (1 - 10 μm)[170] 3D volumetric imaging of tissue. OCT is uses low coherence-length broadband interferometry to measure light backscattered from tissue; in OCT images, blood vessels appear as dark regions with a “shadow” where light is absorbed. OCT systems typically image at near infra-red wavelengths (700 – 1400 nm) to take advantage of reduced scattering and absorption by tissue at these wavelengths, thereby maximising imaging depth. Typical maximum depth penetration of an OCT system is ~ 2 mm,[171] with a lateral resolution between 1 and 10 μm.[170] OCT is widely used for retinal imaging because it can provide high resolution 2D and 3D visualisation of the structure of retinal layers. There are two OCT-based oximetry methods: spectroscopic OCT (S-OCT) and dual-wavelength photothermal OCT (DWPT-OCT).

2.3.2 Spectroscopic OCT (S-OCT) oximetry

OCT measures light which is back-scattered or reflected from a sample; this makes measurement of optical absorption by OCT fundamentally challenging. However, it is possible to infer optical absorption by blood by measuring the attenuation of an OCT signal in a blood vessel, and fitting this data to a SO_2-dependent theoretical model of absorption and scattering by blood.[172] This principle was initially demonstrated in 2007 by demonstrating the difference in absorption of light by arteries and veins in the human retina.[173] S-OCT measurements of *ex vivo* blood were subsequently found to correlate well with vivo blood gas analyser measurements.[174]

Visible wavelength S-OCT (VIS S-OCT) systems were developed to take advantage of increased oximetric contrast at visible wavelengths to improve accuracy of S-OCT oximetry. Several VIS S-OCT studies have been conducted, looking at oximetry in *ex vivo* blood where it was found to have improved accuracy in comparison to NIR S-OCT oximetry.[175,176] VIS S-OCT oximetry has been further applied *in vivo* oximetry in rats, including applications in a dorsal skin fold imaging chamber,[177,178] the retina,[179,180] and the brain.[181,182] These studies report long

acquisition times (tens of minutes) for volumetric data sets, limiting their use to oximetry in anesthetised small animals.

Whilst S-OCT is capable of depth-resolved oximetry measurements, the long image acquisition times required for S-OCT and complex optical instrumentation are clear disadvantages when compared with the simple implementation or snapshot capabilities of MSI oximetry.

2.3.3 Dual-wavelength photothermal OCT (DWPT-OCT) oximetry

In DWPT-OCT, light incident on a blood vessel produces small (nanometre sized) photothermal perturbations in blood. The size of resulting perturbations is directly proportional to absorption of light by blood, giving a relation between perturbation magnitude at two-wavelengths and SO_2. The size of these perturbations can be measured by highly-sensitive phase-sensitive OCT systems. DWPT-OCT oximetry has been applied to *ex vivo* phantoms[183,184,185] and to oximetry of blood vessels in a mouse brain *in vivo*.[186] These studies found good correlation with blood gas analyser measurement, with a reported spatial resolution of ~ 16 μm and an SO_2 precision of ± 6.3%; somewhat lower than MSI or HSI techniques.[183] DWPT-OCT is highly-sensitive to motion (e.g. due to blood flow), which may cause spurious measurements and DWPT-OCT oximetry has not been demonstrated in humans.

2.4 Laser speckle

2.4.1 Generation of laser speckle

Laser speckle can be exploited to provide measurements of blood flow and oximetry. Laser speckle occurs when coherent laser light interacts with an optically rough surface or turbid medium and is subsequently scattered. This scattering causes the coherent light to randomly self-interfere, producing a granular pattern of high contrast light and dark regions due to constructive and destructive interference: i.e. a speckle pattern (see Figure 2-3). Laser speckle techniques are divided into two categories depending on how the speckle pattern is recorded: objective and subjective laser speckle.

Objective laser speckle is where a speckle pattern is recorded directly by a detector without being imaged by a lens (see Figure 2-4) and can be exploited for oximetry (see Section 2.4.2).

Subjective laser speckle is where the speckle pattern is imaged via a lens, forming an image of the object and speckle pattern (see Figure 2-5). Measurement of the contrast of subjective laser speckle can be used to map regions of blood flow in tissue; as blood flows, the speckle pattern changes, effectively blurring the speckle pattern in that region. This can be computationally analysed to provide maps of relative blood flow velocity.

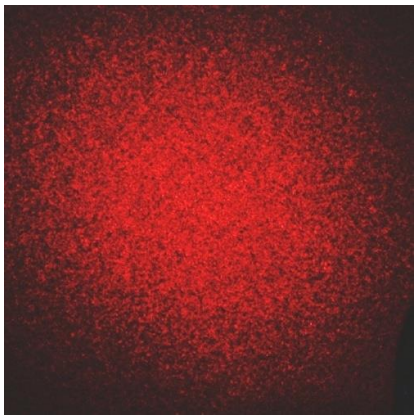

Figure 2-3. A laser speckle pattern.[m]

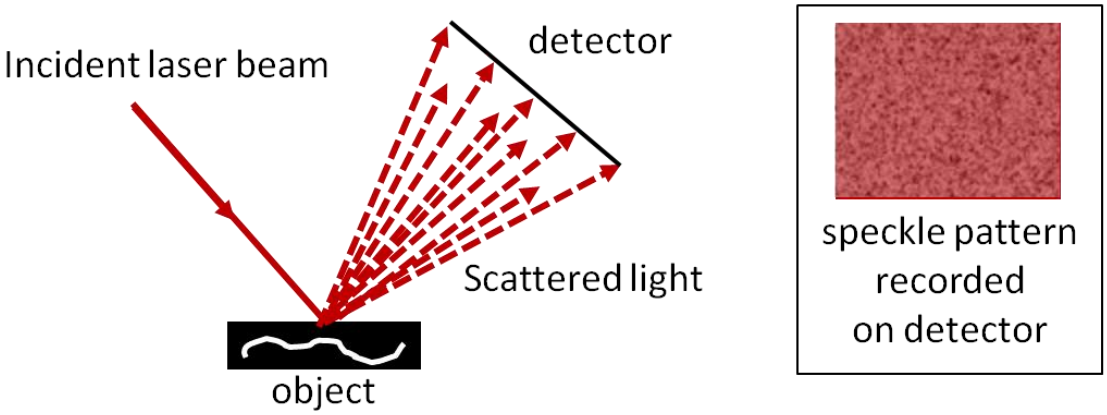

Figure 2-4. Formation of objective laser speckle.

[m] Public domain image reproduced from Wikimedia Commons.[297]

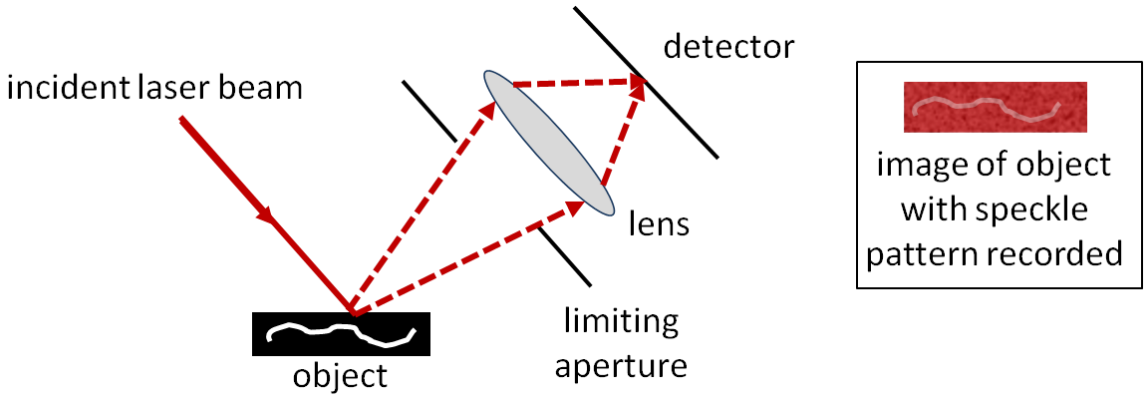

Figure 2-5. Formation of subjective laser speckle.

2.4.2 Objective laser speckle oximetry (OLSO)

An objective laser speckle pattern is formed where laser speckle from a medium is directly recorded by a sensor without a lens. The characteristic size of an individual speckle produced in an objective laser speckle pattern is inversely proportional to the distance between scattering events in a medium, and the distance between scattering events is constrained by the absorption of light in the medium.[187] Thus the average size of speckles (in the frequency domain) can be used to provide information about the optical absorption of illuminated media without directly measuring optical absorption.

For example, in blood, green wavelengths are strongly absorbed; this constrains the light from a laser-point to a small spatial region, and limits the numbering of scattering events the light can undergo before complete absorption occurs. This results in the formation of an objective laser speckle pattern with a low average spatial frequency (i.e. large speckles). In contrast, red light is weakly absorbed by blood, so light from a laser spot can undergo multiple scattering events before being absorbed completely. This creates an objective laser speckle pattern with a high average spatial frequency (i.e. small speckles). The spatial frequency of this speckle pattern will change as a function of blood oxygenation. By measuring speckle spatial frequency at two or more wavelengths, the principle of two-wavelength oximetry can be applied. This is the basis of objective laser speckle oximetry (OLSO).

OLSO has been demonstrated experimentally *in ex vivo* blood and shows good correlation with blood gas analyser measurements.[188] However, this technique is

still in development and like SLO oximetry (see Section 2.1.2.3), it is constrained by the choice of laser wavelengths available, potentially reducing the maximum theoretical accuracy of SO_2 measurement.[188]

However, unlike conventional two-wavelength oximetry, it is proposed that OLSO may be insensitive to artefacts due to the spectral transmission of tissue that can mar ODR calibration. For example, OLSO may be highly advantageous for oximetry in subjects with cataracts.

2.5 Conclusions

Each imaging modality reviewed in this chapter has unique capabilities, and associated advantages and disadvantages. As such, the choice of which imaging modality is informed by the tissue being imaged and the availability of expertise and specialist equipment. A brief summary of the capabilities of the microvascular oximetry modalities reviewed is provided in Table 2-4.

Table 2-4. Summary of microvascular imaging oximetry modalities.

Modality	Oximetry	Flow sensitivity	3D imaging	Maximum lateral resolution
MSI/HSI	✓	X	X	~ 0.5 μm
PAM	✓	X	X	~ 3.4 μm[168]
PAT	✓	X	up to 7 cm	~ 1/200th of imaging depth[161]
S-OCT	✓	X	up to 2 mm	~ 1-10 μm[170]
DWPT-OCT	✓	✓	up to 2 mm	16 μm [186]
OLSO	✓	X	X	laser spot size in tissue
LSCI	X	✓	X	~ 1.25 μm[187] (5x diffraction limit)

Abbreviations:

MSI/HSI = multispectral/hyperspectral imaging

PAM = photoacoustic microscopy

PAT = photoacoustic tomography

S-OCT = spectroscopic optical coherence tomography

DWPT-OCT = dual wavelength photo-thermal optical coherence tomography

OSLO = objective speckle laser oximetry

LSCI = laser speckle contrast imaging

MSI and HSI have been the most extensively utilised microvascular oximetry modalities. MSI is simple to implement and can be adapted to existing broadband optical imaging systems such as fundus cameras, slit-lamps, and microscopes. Broadband-light sources with MSI and HSI enable optimal choice of wavelengths for oximetry, which is a significant advantage over laser-based modalities such as SLO, OLSO, PAT, and PAM. Further, the recent development of snapshot MSI technologies allow video-rate MSI which can be used to observe rapid biological processes, with frame-rates limited only by digital detectors and intensity of imaged light.

HSI is used less-frequently for oximetry than MSI because capturing many wavelengths greatly increases acquisition time or reduces spatial resolution. In contrast, MSI systems using only a few carefully-chosen wavelengths have been shown to provide very good spectral information, whilst retaining high spatial and temporal resolution. HSI studies have been highly useful in informing wavelength choice for MSI studies. Both snapshot and time-sequential MSI are employed in the experiments described in this thesis.

S-OCT is capable of *in vivo* retinal oximetry in anaesthetised animals, but these studies have been limited by the long scan times required (>20 minutes) to create a volumetric image and as such are not suitable for retinal oximetry in human subjects. Whilst promising for 3D volumetric oximetry, S-OCT requires a great deal of development before it will be practical for monitoring rapid changes in SO_2.

DWPT-OCT can provide *in vivo* oximetry measurements, but is highly complex, with limited laser wavelengths, and can be influenced significantly by small perturbations in blood flow. This limits the accuracy of the technique. Further, DWPT-OCT has not been applied in humans.

PAT is the only microvascular oximetry technique capable of deep-tissue imaging (> 2 mm). As such, it is highly advantageous for applications such as tumour monitoring, which are limited to murine dorsal skin-fold windows in MSI/HSI.[9] However, achieving PAT requires a great deal of technical complexity and highly-specialised expertise, making it challenging to apply without prior-expertise. Further,

the requirement for high-powered laser pulses and direct ultrasonic contact makes it unsuitable for non-invasive imaging in the eye.

PAM can provide near high resolution (< 1 µm) images of blood cells flowing *in vivo*, but this resolution requires high-frequency (~ 100 MHz) ultrasound transducers, which limits imaging depth to < 100 µm.[189] This limits the practical applications of PAM to applications such as imaging the microvasculature in the ears of mice. As with PAT, the requirement for contact is also highly disadvantageous, ruling out PAM for retinal oximetry.

OLSO is a unique modality for laser-based oximetry, which may be useful for retinal and tissue oximetry. However, OLSO was developed too-recently (results first presented in 2016) to apply this modality to research within this thesis. Further, OLSO has not-yet been demonstrated *in vivo*.

For the reasons outlined, MSI is the clear choice for *in vivo* oximetry of the microvasculature. The adaptability to existing imaging systems, wavelength choice, and potential for snapshot imaging are particularly advantageous for monitoring rapid changes in SO_2 in the microvasculature. The research presented in chapters 3 and 4 would not be possible with any technique other than MSI because no-other technique can provide the spatial and temporal resolution required to measure the rapid changes in microvascular SO_2 seen in each chapter.

3 Bulbar conjunctival and episcleral microvascular oximetry

Summary: *this chapter details the first application of snapshot multispectral imaging for oximetry two microvascular beds of the anterior segment of the eye: the bulbar conjunctival and episcleral microvasculature. The oxygen dynamics of these vessels were studied at normoxia and acute mild hypoxia with snapshot multispectral imaging (SMSI). The high temporal resolution of SMSI enabled observation and quantification of rapid oxygen-diffusion from ambient air into hypoxic bulbar conjunctival microvasculature. This indicates that bulbar conjunctival microvessels will be highly oxygenated when exposed to ambient air (i.e. when the eyelid is open). In contrast, hypoxic episcleral vessels – which are embedded inside scleral tissue - were observed to remain hypoxic, indicating no oxygen diffusion into these vessels due to the overlying tissue barrier.*

Additional note: *the work presented in this chapter has been published in Experimental Eye Research.*[190] *MacKenzie et al., "In vivo oximetry of human bulbar conjunctival and episcleral microvasculature using snapshot multispectral imaging." Experimental Eye Research 149 (2016): 48-58.*

3.1 Introduction

3.1.1 Motivation

Oximetry of the microvasculature is of interest for studying the development and progression in diseases where microvascular function is altered, such as diabetes. However, achieving microvascular oximetry is highly challenging because the micro vessels are generally embedded in highly scattering tissue that makes imaging extremely problematic. However, on the outer surface of the sclera, two microvascular beds are easily accessible for non-invasive imaging and are yet

unexploited for oximetry: the bulbar conjunctival and the episcleral microvasculature. The bulbar conjunctiva lies above the sclera and presents a plethora of micro vessels, ranging in size from capillaries (< 10 μm) to arterioles and venules (< 100 μm). These vessels can be easily imaged with imaging systems such as fundus cameras and slit-lamps. In contrast, the episcleral vessels are embedded into the sclera, with only few vessels visible near the scleral surface. The episcleral vessels that are visible are generally larger arterioles and venules. Figure 3-1 shows a simplified depiction of the position and number of bulbar conjunctival and episcleral vessels.

Oximetry of these microvascular beds could potentially enable new insight into the oxygen dynamics of the ocular microvasculature. However, there have been no oximetry studies of the episcleral vessels, and prior studies of the bulbar conjunctiva oxygen saturation have been severely limited by the exclusive use of Clark-type electrodes, which are limited to measurement of partial pressure of oxygen at only a single contact point. In contrast, SMSI oximetry can provide spatially-resolved concurrent measurement of oxygen saturation in both the bulbar conjunctival and episcleral microvasculature with high spatial and temporal resolution.

The aim of the research in this chapter is to establish the feasibility of SMSI for oximetry of the bulbar conjunctival and episcleral microvasculature, and to test the response of these microvascular beds to acute mild hypoxia. Further, this research aims to characterise any unique oxygen dynamics associated with these vessels, in particular, any oxygen diffusion from ambient air into the bulbar conjunctival vessels that lie on the scleral surface.

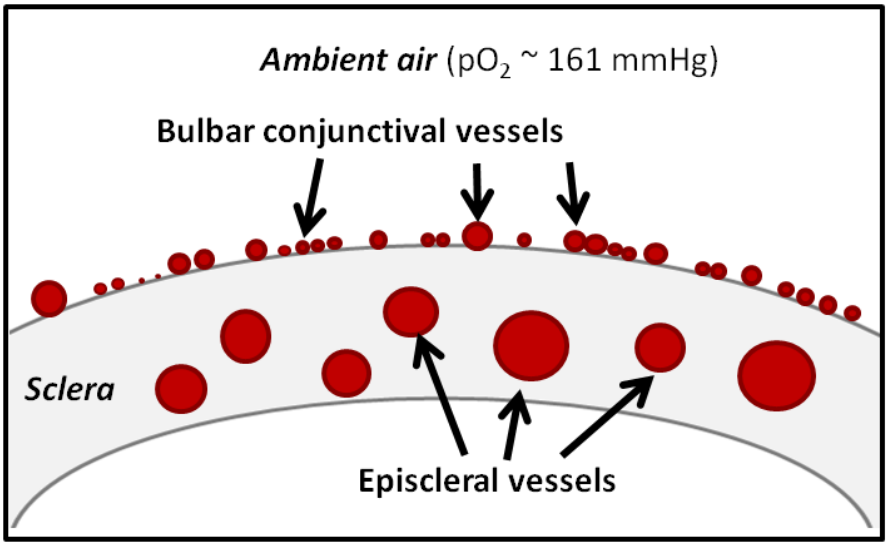

Figure 3-1. Generalised position, size, and number of bulbar conjunctival and episcleral vessels with respect to the sclera and ambient air.

3.1.2 The bulbar conjunctival microvasculature

3.1.2.1 Anatomy

The bulbar conjunctiva is a thin (~ 33 μm),[46] transparent, semi-mobile layer situated above the outer surface of the sclera, containing a great variety of microvasculature, including many arterioles, venules, and capillaries. Vessel number, morphology, and size varies on both an inter-subject and intra-subject basis. Bulbar conjunctival vessels range in diameter from capillaries (< 10 μm) to arterioles and venules (~ 100 μm), with an average vessel size of 15.1 μm (weighted to the small and numerous capillaries).[191] The blood supply of the bulbar conjunctiva is primarily derived from the ophthalmic artery, but has a lesser contribution from the external carotid artery via the eyelid (the palpebral conjunctiva).[53] Muscular meta-arterioles regulate blood flow in arterioles and capillaries.[47,192] In some subjects, arteriole-venule pairs can be observed, however this is not true for all subjects. Crucially, there is minimal tissue between the bulbar conjunctival blood vessels and ambient air; meaning that oxygen can diffuse rapidly from the air into bulbar conjunctival vessels.[193] The bulbar conjunctival vasculature of a human subject is shown in Figure 3-2.

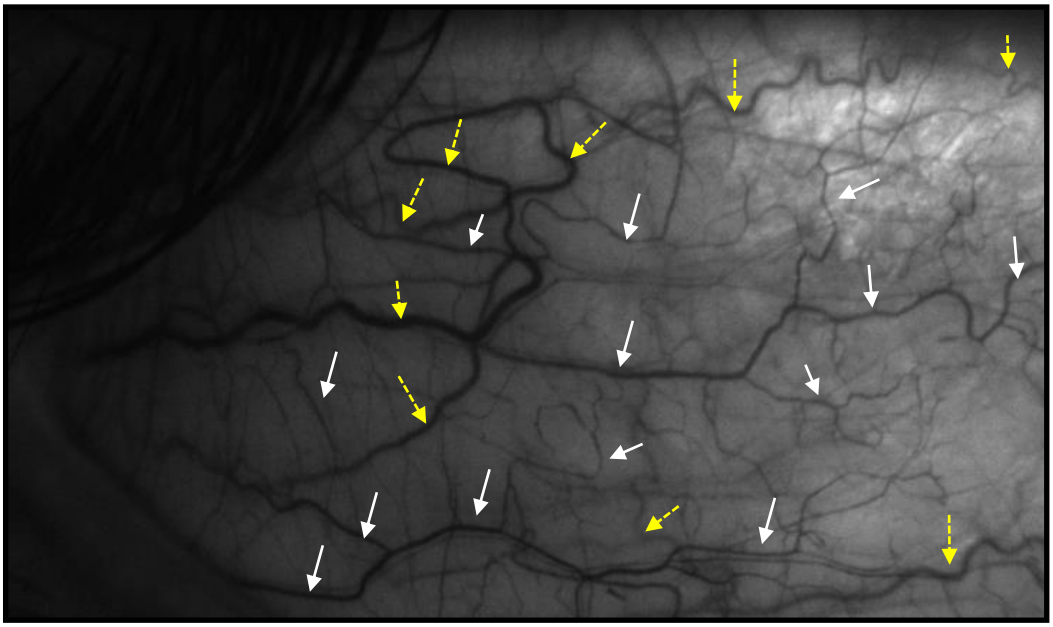

Figure 3-2. Image of a scleral region. Episcleral vessels are marked with yellow dashed arrows whilst bulbar conjunctival vessels are marked with white arrows. Not all bulbar conjunctival vessels are marked because of the large number of small bulbar conjunctival vessels. Microvascular beds were distinguished by the semi-mobile nature of the bulbar conjunctiva over the sclera (see Section 3.4.2). Approximate field of view is ~ 10 mm by 3 mm.

3.1.2.2 Diseases and conditions affecting the bulbar conjunctiva

The bulbar conjunctival microvasculature is highly responsive to conditions both internal and external to the body. External conditions such as allergic reactions,[50,192] temperature, time of day,[48] and emotional state[49] have been observed to influence vessel diameter. Contact lens wear is observed to induce vessel dilation, thought to be due to localised hypoxia induced by the oxygen impermeable (or semi-permeable) nature of contact lenses.[194,195]

Type II diabetes is associated with bulbar conjunctival capillary loss, increased vessel diameter, increased blood viscosity, and decreased partial pressure of oxygen.[196–199] Sickle-cell anaemia is associated with capillary micro-aneurisms, sludging in vessels,[200] and lower partial-pressure of oxygen (oxygen tension).[201] Variations in diameter and blood flow velocity have also been associated with Sickle-Cell anemia.[52] Carotid artery occlusion is associated with decreased blood flow, decreased visibility of capillaries, and vasodilation.[53] Hypertension is

associated with increased tortuosity of vessels and a reduction in the total number of capillaries and arterioles.[192,202–204]

3.1.2.3 Conjunctival oximetry studies using Clark-type electrodes

Despite the widespread usage of multispectral imaging for oximetry, previous studies of bulbar conjunctival oximetry have used only Clark-type contact electrodes. These are extremely limited in their oximetry capabilities (see Table 3-1 for a comparison with SMSI).

Table 3-1. Snapshot MSI oximetry vs. Clark type electrodes.

Snapshot multispectral imaging	Clark-type electrode
Non-contact	Contact required
Spatially resolved, imaging	Single point measurement
Allows natural oxygen diffusion	Blocks oxygen diffusion
Measures SO_2	Measures pO_2
No temperature-dependence	Temperature-dependent calibration

Hill and Fatt (1963)[193] used a Clark-type electrode to demonstrate oxygen diffusion from a limited pO_2 reservoir by the bulbar conjunctiva. They concluded that oxygen diffusion from ambient air to the bulbar conjunctiva will be occurring constantly, but did not state how this would alter SO_2 or what timescales are required for bulbar conjunctival vessels to reach pO_2 equilibrium with ambient air.[193]

All other Clarke-type electrode studies have measured pO_2 in the palpebral conjunctiva (the underside of the eyelid), which shares blood circulation to the bulbar conjunctiva. It is a reasonable assumption to assume pO_2 dynamics of the palpebral conjunctiva are similar to that of the bulbar conjunctiva in the absence of external oxygen diffusion. Studies have shown that pO_2 of palpebral conjunctiva correlates with arterial SO_2 when FiO_2 is varied.[205–208] Other studies have shown that pO_2 decreases when Phenylephrine Hydrochloride eye drops were administered.[209]

3.1.3 Episcleral microvasculature

3.1.3.1 Anatomy

The episcleral microvasculature is embedded within the opaque scleral tissue,[62,210] and although there are many episcleral vessels, only a few vessels visible at the scleral surface.[62,210] Average visible episcleral vessel diameter is typically ~ 70 μm, but can vary significantly on an inter-subject and intra-subject basis. The episcleral blood supply is derived entirely from the ophthalmic artery via the long anterior ciliary arteries.[33,211–213] Some episcleral vessels serve to drain the aqueous humour from inside the eye; these are known as aqueous veins. Aqueous veins are most commonly found in the superior (lower) and nasal regions of the sclera and can range in size from 20 - 100 μm, with an average size of 50 μm.[45]

3.1.3.2 Conditions affecting the episcleral microvasculature

As a generalisation, the hemodynamics of episcleral microvasculature is not well studied, with no episcleral oximetry studies reported. Instead, studies have focused on blood flow in epsiceleral vessels using fluorescein angiography.[43,44,214] Average episcleral vessel diameter has been used to non-invasively measure changes in intra-ocular pressure (IOP). However, it is not known how IOP may affect episcleral blood flow velocity or SO_2, but one can speculate that both parameters are likely to be reduced if vessel diameter is also reduced.

3.1.4 Challenges of bulbar conjunctival and episcleral imaging

The unique physiology of the bulbar conjunctiva and episcleral vessels present several challenges for quantitative imaging.

1) The curvature of the sclera introduces significant variation in the z-axis position of vessels with respect to the imaging plane, thus any imaging system must have a large depth of field (DOF).

2) The bulbar conjunctival vasculature is semi-mobile above the sclera, so subject gaze must be well controlled to minimise any movement. Motion can further be mitigated by maximising the field-of-view imaged.

3) The large variation in vessel morphology necessitates a large FOV to maximise the number of vessels meeting inclusion criteria (see Section 3.5.2).

4) The small average diameter of bulbar conjunctival vessels (15.1 μm) requires a high resolution to be imaged[191] Resolution is a trade-off between FOV and DOF.

5) For oximetry of small vessels, wavebands with appropriately high absorption (e.g. green wavelengths) must be chosen. The small bulbar conjunctival vessels are almost completely transparent at wavelengths > 590 nm.

3.2 General experimental procedures

3.2.1 Overview

This chapter details two sets of experiments. (1) *Ex vivo* phantom experiments to validate the oximetry capability of a SMSI adapted fundus camera. (2) *In vivo* experiments in human subjects to test the feasibility of oximetry in the bulbar conjunctival and episcleral vessels using the SMSI system.

3.2.1.1 SMSI fundus camera

The SMSI system used for all experiments described in this chapter is shown in Figure 3-3. This system consisted of a retinal fundus camera (TR50-DX; *Topcon*) modified with an Image Replicating Imaging Spectrometer (IRIS) and a cooled sCMOS detector (Zyla 5.5; *Andor*). IRIS is described in detail in Section 2.1.3.2. IRIS enables snapshot multispectral imaging at eight wavebands between 560 nm and 600 nm onto a single detector. The light-sources for the fundus camera are a flash-lamp (Xenon Lamp, up to 300 W/s, 1 second recycling time) and an inspection lamp (100 W Halogen Lamp).[138] For optimal performance of IRIS, illumination wavelengths were constrained by placing a 545 nm – 625 nm bandpass filter (hq585/80x; *Chroma*) in the illumination path. The system was configured for orthogonal polarisation imaging to minimise specular reflections and ensure that predominantly light diffused through tissue was imaged.[215,216] To maximise DOF of the fundus camera, the 'small aperture' setting was selected. This increased the experimentally estimated DOF from 4 mm to 10 mm. Of the three possible FOV settings (20°, 35°, and 50°), the 35° FOV was selected to provide a compromise between the need for high magnification and the need to maximise the size of the region of sclera imaged for maximum vessel coverage. This resulted in a FOV of approximately ~ 10 mm by 3 mm at the focal plane. A raw 8-band image of bulbar conjunctival and episcleral vasculature obtained with these settings is shown in

Figure 3-4; most vessels appear almost completely transparent at the 591 nm and 600 nm wavebands.

Figure 3-3. Topcon TR50-DX retinal fundus camera modified with IRIS and a sCMOS detector.

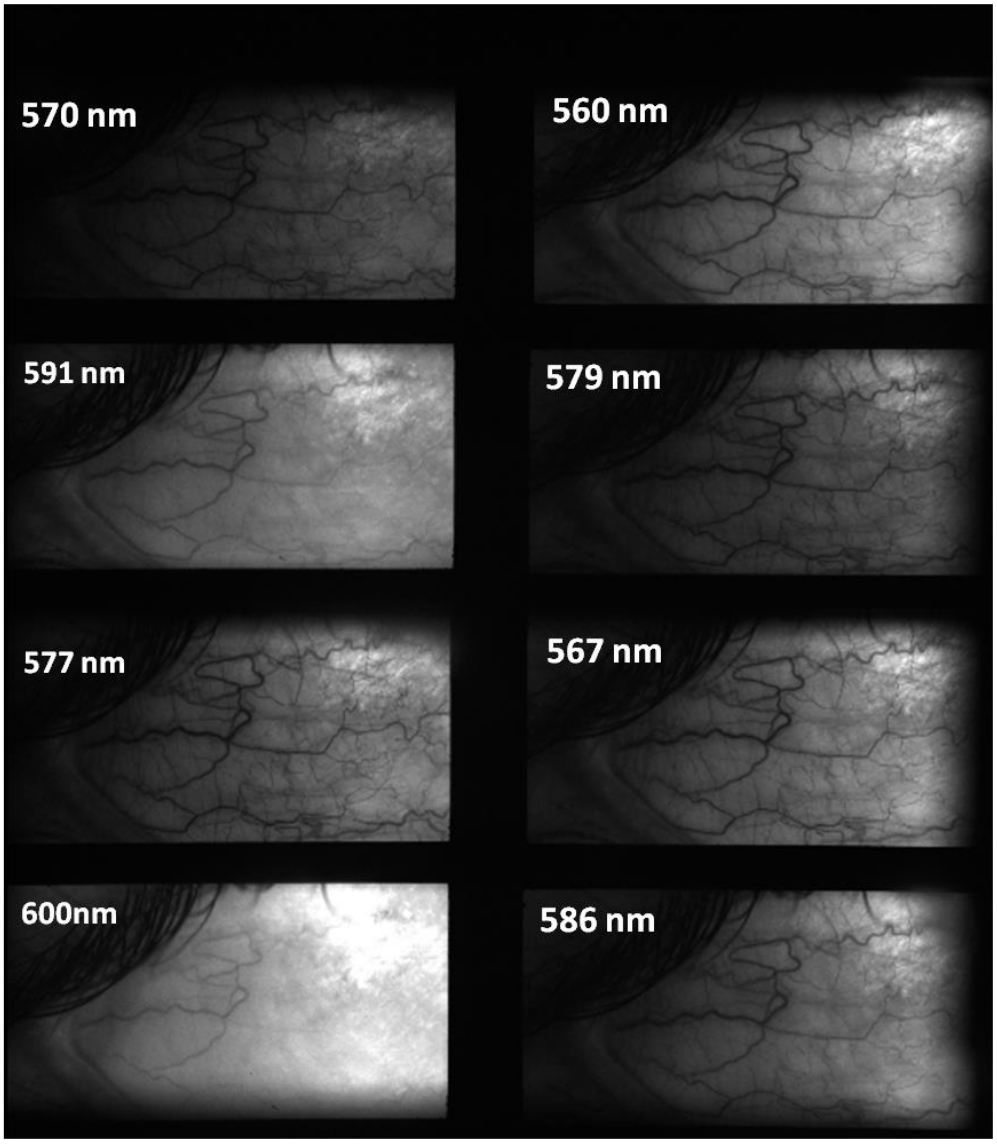

Figure 3-4. An eight waveband IRIS image of the temporal quadrant of the sclera of the right eye of a single subject. The bright region in the top-right of images is glare from the sclera. If orthogonal-polarisation imaging were not used, then this would be the region where a strong specular reflection would manifest. Approximate field of view for each image is ~ 10 mm by 3 mm.

3.2.1.2 Optimal waveband selection for oximetry

To minimise the influence of photometric errors in oximetry, vessel transmission should be between 10% and 70% ($0.15 < OD < 1$)[102] (see Section 1.4.5.1). To test that IRIS wavebands had suitable transmission characteristics for oximetry, the theoretical transmission vs. vessel diameter was calculated for 100% SO_2 and 70% SO_2 blood, assuming single pass transmission, 33% hematocrit, and extinction

coefficients corresponding to central IRIS wavebands from the literature.[19] The results are shown in Figure 3-5; it can be seen that the 589 nm, 591 nm, and 599 nm wavebands are sub-optimal for oximetry in vessels < 100 μm in diameter. Instead the wavelength combination of 570 nm (isobestic) and 560 nm (contrast) was deemed to provide appropriate absorption for a wide range of vessel diameters between 20 μm and 100 μm.

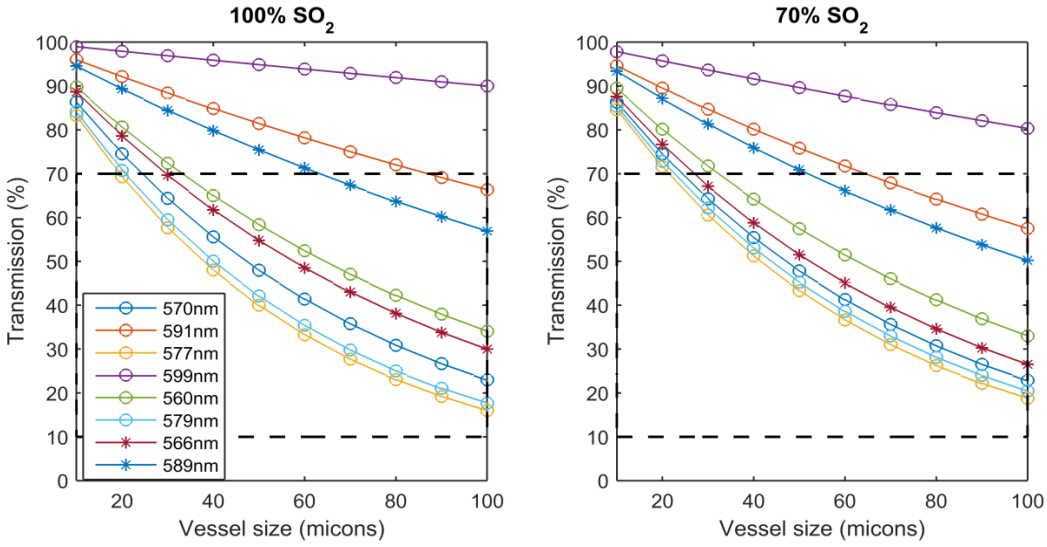

Figure 3-5. Simple model of vessel transmission vs. diameter for 100% SO_2 (left) and 70% SO_2 (right). The region bounded by black-dashed box indicates the region of 10-70% vessel transmission for optimal oximetry.

3.2.2 Vessel tracking and oximetry analysis

3.2.2.1 Image registration and vessel tracking

Raw 8-band IRIS images were cropped and each narrowband IRIS image was co-registered to produce a spectral data cube for each image. The narrowband IRIS image co-registration algorithm used was developed previously and detailed in the thesis of Ied Abbaloud.[129] In brief, this narrowband image registration algorithm maximises the autocorrelation of each narrowband IRIS image with respect to a single high-contrast narrowband IRIS image. This corrects for any distortions introduced by IRIS and creates a cropped spectral data cube, suitable for further analysis. A logic flow-chart of this algorithm is shown in Figure 3-6.

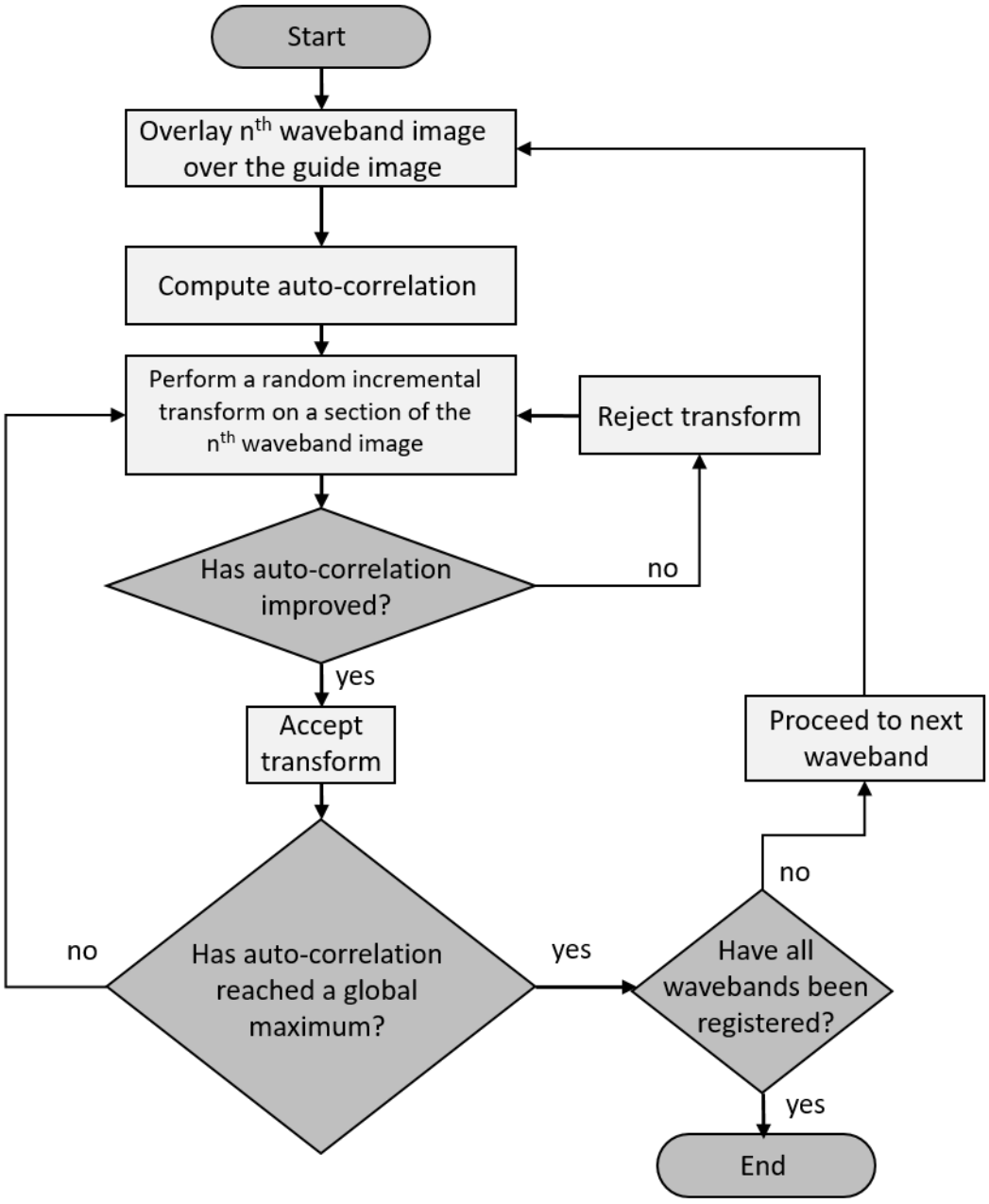

Figure 3-6. Logic flow-chart for the IRIS multi-waveband co-registration algorithm.

Vessels that met inclusion criteria (see Section 3.4.3) were selected for analysis and tracked using a semi-automatic vessel tracking algorithm which utilised user-defined control points to define vessel sections. Variability in semi-automatic tracking introduced minimal variation in ODR when repeated (a standard deviation of < 0.5% in 10 repeated measurements of vessels *in vivo*). Fully automatic tracking was not implemented because bulbar conjunctival vasculature can move with

respect to scleral and episcleral features, making automatic vessel feature tracking difficult and a complex research problem in its own right.[217]

3.2.2.2 Vessel profile fitting

Line profiles of 26 pixels, centred on the tracked vessel and in a direction perpendicular to the tracking vector were extracted from the image. A vessel fitting algorithm (see Figure 3-7) was then applied to the line profile estimated vessel diameter and optical transmission of tracked vessels. This algorithm estimated greyscale intensity in the centre of each vessel (*Iv*), and the background greyscale intensity at the centre of the vessel (*Io*), by fitting a second order polynomial function and a linear function respectively. Vessel diameter (in pixels) was estimated as per the method described by Fischer et al. (2010)[218]: i.e. the point of maximum rate-of-change of intensity either side of the centre of the vessel is taken to be the position of the vessel wall. This algorithm should, theoretically, be insensitive to minor waveband registration errors (e.g. a misalignment << 26 pixels) because transmission was estimated separately for each IRIS waveband image; however, this needs to be verified in future. The spatial size of each pixel was calibrated to true scale by prior imaging of a ruler with a millimetre scale, which was placed in front of the subject's sclera in the focal plane of the fundus camera.

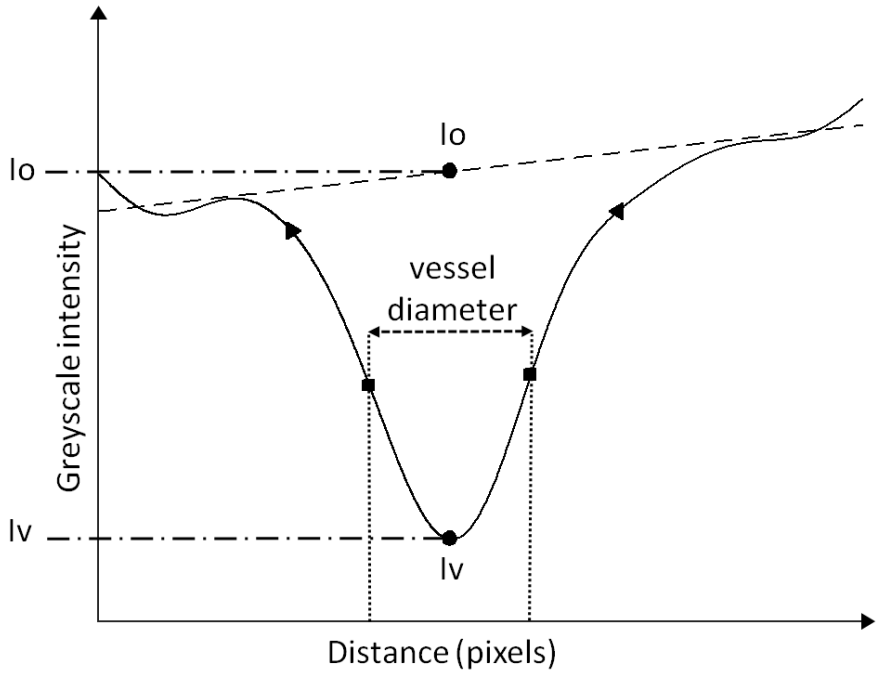

Figure 3-7. Scheme applied to a vessel profile to estimate vessel diameter and greyscale intensity at the centre of vessel (Iv) and the greyscale intensity if the vessel were not present (Io).

3.2.3 Two-wavelength oximetry

From the information provided by the vessel fitting algorithm, the optical density (OD_λ) of vessels at each wavelength is calculated by:

$$OD_\lambda = -\log_{10}\left(\frac{I_v}{I_o}\right), \quad 3\text{-}1$$

Optical Density Ratio (ODR) is then:

$$ODR = \frac{OD_{560}}{OD_{570}}. \quad 3\text{-}2$$

ODR is an inversely proportional proxy for SO_2; i.e. as SO_2 decreases, ODR increases. ODR can be empirically calibrated to SO_2 if two or more reference SO_2 values are known. However, no SO_2 values are reported in the literature for either bulbar conjunctival or episcleral vessels, so oximetry results in this chapter are reported here in solely in terms of ODR.

3.3 Phantom validation experiment

3.3.1 Phantom design

A simple sclera-mimicking phantom was constructed to validate the oximetry capability of the SMSI system and data analysis technique. The phantom consisted of a Fluorinated Ethylene Propylene (FEP) capillary of 100 µm inner-diameter (Custom order, *Zuess Inc*.), filled with *ex vivo* horse blood (40% packed cell volume) (*E&O labs*) under feed from a syringe pump (KDS260, *Linton Instrumentation*). To simulate the sclera, the capillary was placed on a white Spectralon backing. Spectralon is a diffusely scattering reflectance material with uniform spectral reflectance in the visible wave-range and thus appears white.[219] This is similar to the reflectance spectra of scleral tissue.[62] Both the scleral tissue and Spectralon are diffuse scatterers.[210] For imaging, the phantom was placed approximately 5 cm from the fundus camera objective lens; at this position, the illumination of the fundus camera produces a circulation spot of illumination approximately 4 cm in diameter. Figure 3-8 depicts this phantom set up and shows a representative image of a blood filled capillary.

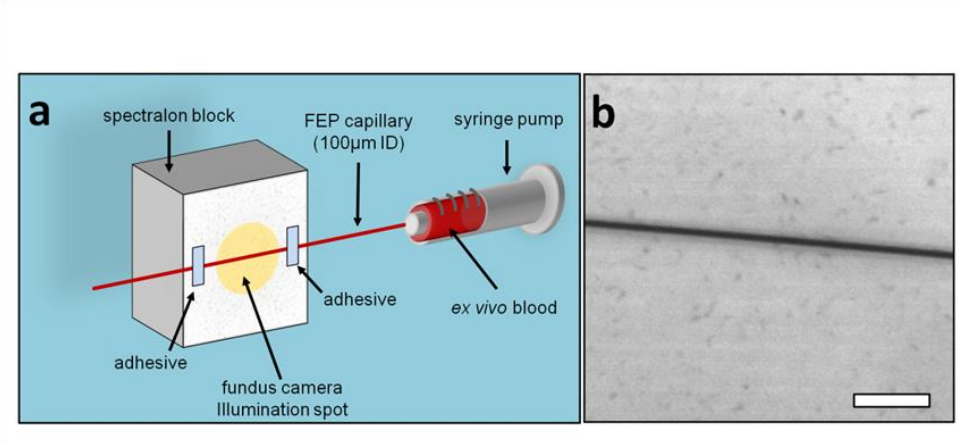

Figure 3-8. The *ex vivo* phantom. **(a)** Diagram of the phantom set up. **(b)** Representative image of a 100 µm inner diameter capillary. Scale bar represents one millimetre.

To vary SO_2, measured quantities of sodium dithionite crystals ($Na_2S_2O_4$) (EMD Millipore) were added to 5 ml blood samples in varying quantities as per Table 3-2.[220] The crystals dissolved into the blood. The blood was then stirred and put

into a plastic syringe. After 30 minutes the blood was shaken in the syringe and the resulting SO_2 of blood samples was then verified by analysis with an optical blood gas analyser (GEM OPL; Instrumentation Laboratory). The blood gas analyser was calibrated before use and is certified by the manufacturer to determine SO_2 between 0% and 100% with an uncertainty of ± 1.8% SO_2.[221] The blood was then inserted and flowed through the capillary and imaged. A total of eight ex vivo samples of SO_2 ranging between 5% and 100% SO_2 were imaged. To assess repeatability, 10 consecutive images of 100% oxygenated blood were acquired.

Table 3-2. Concentration of sodium dithionite required to reduce SO_2 of blood. Data from Briley-Saeobo and Bjornerud (2000). [220]

Desired SO_2 (%)	**Concentration of sodium dithionite** (mg per mL of blood)
100	0.00
90	0.17
80	0.33
70	0.53
60	0.61
50	1.00
40	1.30
30	1.60
20	1.90
10	2.25

3.3.2 Results

ODR was found to decrease with SO_2 and the relationship between ODR and SO_2 was well fitted by a linear trend (see Figure 3-9). This validated the oximetry capabilities of the system.

However, there was some variation in ODR along the length of the capillary, indicating non-homogeneity in optical properties of the blood (see Figure 3-10). This indicates inhomogeneity of ODR of the blood samples being analysed (see Section 3.6.3 for discussion).

The repeatability of ODR phantom measurements was calculated to be under 0.5% (standard deviation of 10 consecutive images of a single sample).

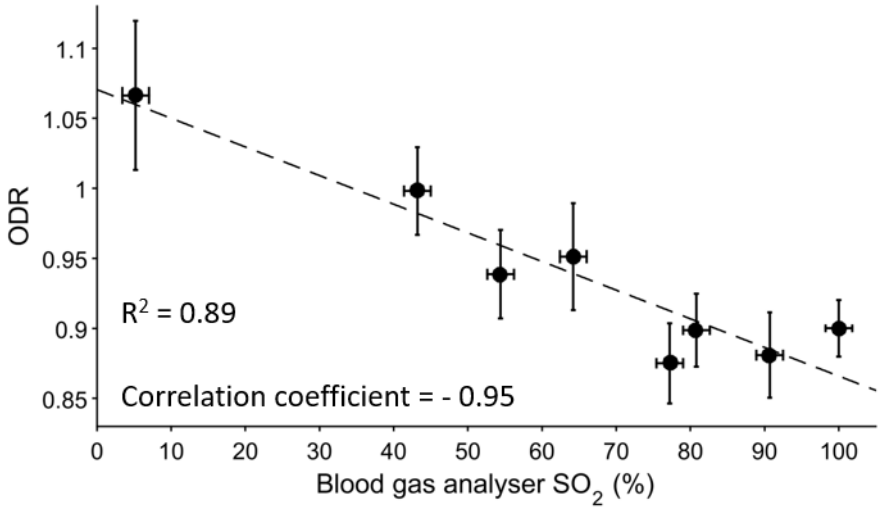

Figure 3-9. Phantom ODR vs. blood gas analyser SO_2. Vertical error bars are ± the standard deviation of ODR, measured along the length of the capillary. Horizontal error bars are the ± 1.8% systematic uncertainty given by the blood gas analyser manufacturer.

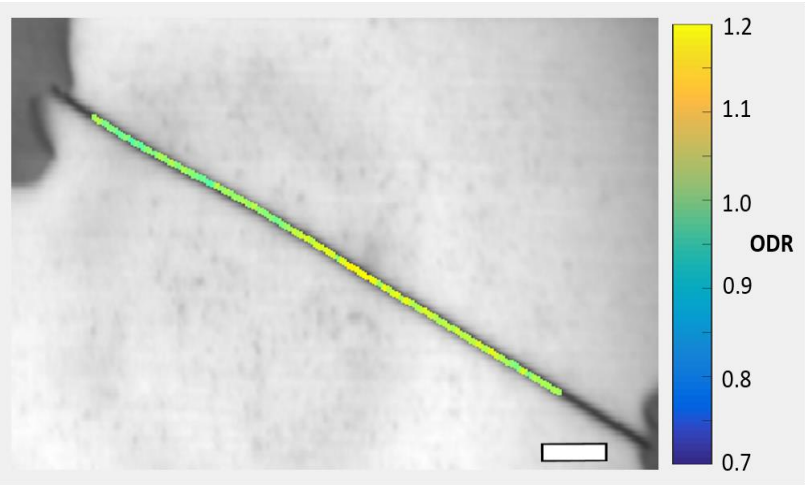

Figure 3-10. ODR variation observed in a 100 µm inner-diameter FEP capillary. Scale bar represents ~1 mm.

3.4 In vivo experiments

3.4.1 Subject recruitment

This study was approved by the Ethics Committee of University of Glasgow, College of Medical, Veterinary and Life Sciences. All volunteers provided written informed consent before participation and all procedures were performed in

accordance with the tenets of the Declaration of Helsinki. Ten healthy human volunteers (age 25 ± 2 years [mean ± standard deviation], six male and four female) were recruited.

Subjects reported no history of ocular, respiratory, or vascular disease. Volunteers who regularly wore contact lenses or who were suffering from allergic conjunctivitis were excluded because these factors are known to induce bulbar conjunctival vasodilatation.[13,192,194] 7 subjects were non-smokers and 3 were smokers.

Subjects were asked to refrain from drinking alcohol 24 hours prior to the study, and not consume caffeinated beverages or smoke for 1 hour before the start of the study.

3.4.2 General imaging procedure

Subjects were imaged in a darkened room with temperature-controlled air-conditioning set between 19 and 22°C. Subjects positioned their head on the standard fundus-camera headrest and the fundus camera objective lens was positioned approximately five centimetres from the subject's sclera, creating a uniform circle of illumination approximately four centimetres in diameter. Subject gaze was controlled by fixating on the fundus camera external fixation target (a movable red LED). Approximate image scale was provided by imaging a millimetre scale placed in front of the subject's sclera. All images were recorded with optimal, sharp focus.

Regions of the sclera were selected for imaging as to maximise the number of bulbar conjunctival vessels meeting the inclusion criteria (see Section 3.4.3). Bulbar conjunctival and episcleral vasculature was distinguished through the semi-mobile nature of the bulbar conjunctiva above the sclera: by moving a subject’s gaze the relative position of episcleral and bulbar conjunctival vasculature changed, enabling classification of individual vessels as either bulbar conjunctival or episcleral. Arteries and veins were not readily identifiable by morphology alone in either the bulbar conjunctiva or episclera.

3.4.3 Vessel analysis inclusion criteria

For each subject the inferior and nasal regions of both their left and right eyes were imaged. Regions which presented the maximum number of suitable bulbar conjunctival and episcleral vessels suitable for analysis were then imaged throughout the experiment. There was operator-bias to image the temporal section of the right eye of subjects because this was the easiest to image due to equipment geometry.

To ensure optimal vessel profile fitting, the following set of inclusion criteria were applied to determine vessel sections suitable for analysis.

(1) Vessel sections were greater than 5 pixels (~ 65 μm) in diameter.

(2) Vessel sections were greater than 30 pixels long (~ 390 μm).

(3) Vessel profiles had to have no vessels within 12 pixels of either side of the vessel. The presence of small vessels (i.e. capillaries) was accepted because this was unavoidable due to the high number of bulbar conjunctival capillaries.

(4) Vessel intersections were avoided.

(5) Vessels in regions of glare (from illumination) were avoided.[n]

(6) Vessels in regions of poor focus were avoided.

(7) Bulbar conjunctival vessels which moved near episcleral vessels were avoided.

(8) Episcleral vessels were only included if they had a high apparent optical contrast compared to the scleral tissue (i.e. appear to not be deeply embedded in the scleral tissue).

(9) Regions of episcleral vessels where transient aqueous flow was observed was avoided (see Figure 3-12).

[n] Strength of manifestation of scleral glare is dependent on degree of orthogonal misalignment of horizontal input polariser and vertical IRIS analyser. Glare may also be depend upon the orientation of polarisers with respect to the orientation of collagen fibres in the sclera, but verification of this hypothesis is required.

All vessel sections analysed were required to meet these inclusion criteria throughout the relevant section of the study (e.g. for an entire normoxia/hypoxia sequence). Examples of such vessel sections are shown in Figure 3-11.

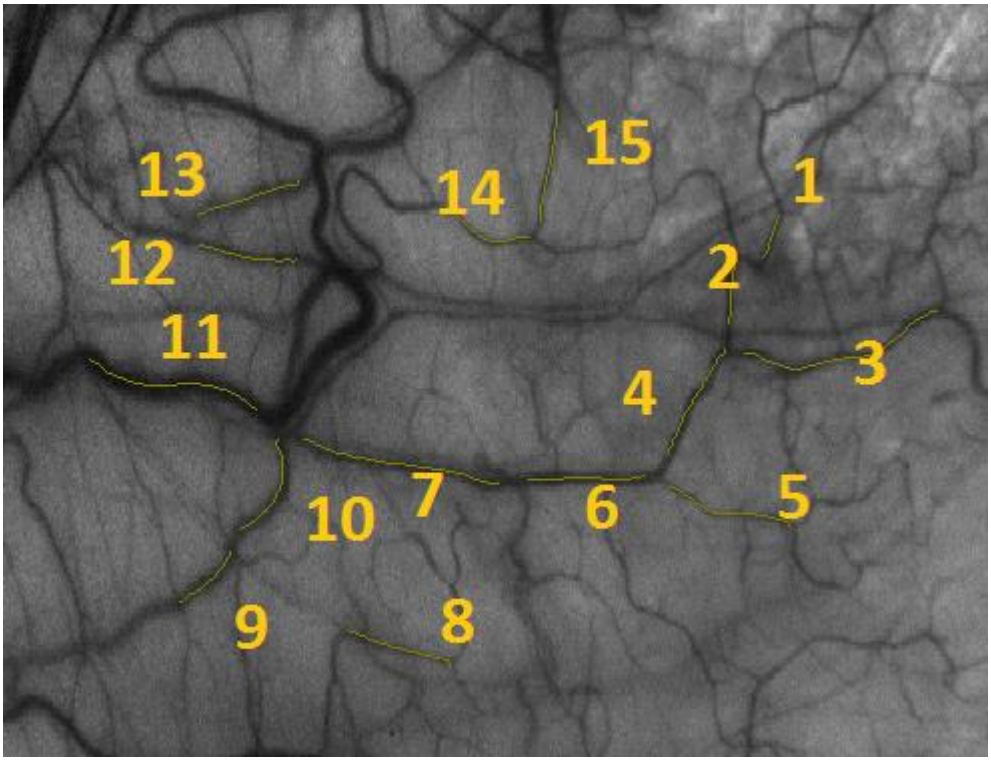

Figure 3-11. Vessel sections tracked in a single subject. Sections 1-8 are bulbar conjunctival vessel sections, whereas sections 9-13 are episcleral vessel sections.

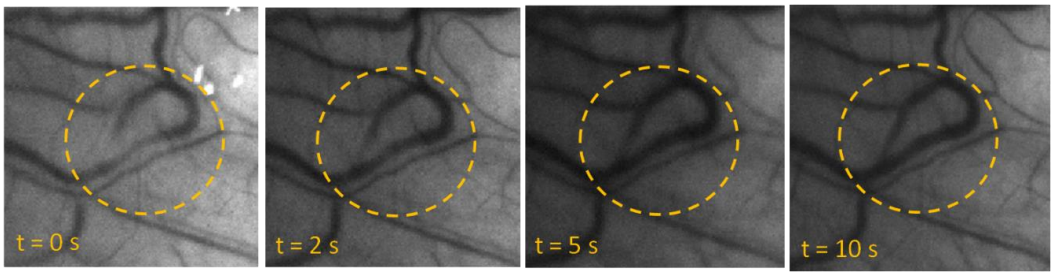

Figure 3-12. Transient aqueous flow observed in an episcleral vessel section. At t = 0 s the vessel section highlighted is partially filled with aqueous humour and thus has low optical absorption. Blood flow returns with time; the vessel section appears to return to normal absorption between t = 5 s and t = 10 s. This measurement was not repeatable due to the transient and unpredictable drainage of aqueous humour in aqueous veins. NB: Variations in apparent

scleral greyscale intensity between time-points are due to image auto-scaling effects.

3.4.4 Repeatability

Repeatability of ODR measurement was assessed for each subject by acquisition of eight consecutive images of the same scleral region in a period of approximately 10 seconds**.** Prior to imaging, subjects held a constant gaze for 2.5 minutes to expose the imaged vasculature to ambient air. 2.5 minutes was an arbitrary time that was selected so as to give enough time for any oxygen diffusion effects to occur. As seen in Section 3.4.7, oxygen diffusion occurs on the timescale of ~ 0 - 10 seconds, so this time could be reduced greatly in any future studies.

3.4.5 Eyelid closure

In this study eyelid closure was used to block oxygen diffusion from ambient air to the scleral surface; closing the eyelid creates an oxygen impermeable barrier of tissue. To assess the effect of eye closure on vascular oxygenation, and hence on ODR of vessels, subjects were imaged before and after a period of eyelid closure. As before, subjects gazed at the fixation target for 2.5 minutes to expose the target vasculature to ambient air prior to imaging and subjects then closed their eyelids for a further 2.5 minutes. Synchronized imaging of the sclera followed opening of the eyelid.

3.4.6 Acute mild hypoxia

To assess the effect of acute mild hypoxia, subjects were imaged in a normoxia/hypoxia sequence designed to provide a repeatable pattern and minimise sensitivity random physiological variations. This sequence was: (1) normoxia 1; (2) hypoxia; (3) normoxia 2; (4) hypoxia 2; (5) normoxia 3. When the results are plotted, this sequence would produce an characteristic and highly distinct 'M' shape if ODR varied with SO_2.

For normoxia measurements, subjects inhaled room air (21% FiO_2) for 2.5 minutes whilst fixating on the red LED fixation target, after which they were imaged. To induce acute mild hypoxia, subjects then closed their eyelids and began 2.5 minutes of inhalation of hypoxic air mixture (15% FiO_2). After 2.5 minutes of hypoxic-

air inhalation, subjects opened their eyelid and synchronised imaging occurred. Subjects were then returned to normoxia by breathing room air.

3.4.7 Oxygen diffusion sub-study

To enable a comparative study of the oxygen diffusion process between bulbar conjunctival and episcleral vasculature, a sub-group of four subjects (three male, one female) were selected for further imaging. These subjects were selected because they presented episcleral and bulbar conjunctival vessels suitable for analysis within in a single scleral region, enabling concurrent comparison between the two vascular beds. Whilst breathing room air, subjects gazed at the fixation target for 2.5 minutes and an image recorded. Subjects then breathed hypoxic air for 2.5 minutes during eyelid closure and, following opening of the eyelid, a synchronised imaging sequence was recorded for 30 seconds with an image acquisition rate of ~ 1 Hz. After this sequence subjects were returned to normoxia by breathing room air. This procedure was conducted twice for each subject.

3.5 Results

3.5.1 Variability of vessel morphology

Bulbar conjunctival vessel morphology (i.e. size, tortuosity, and vessel density) was observed to vary greatly both between subjects between scleral regions in individual subjects. Episcleral vessels also showed considerable variation in tortuosity, but were generally large and similar in size. Figure 3-13 shows the scleral regions imaged for each of the ten subjects.

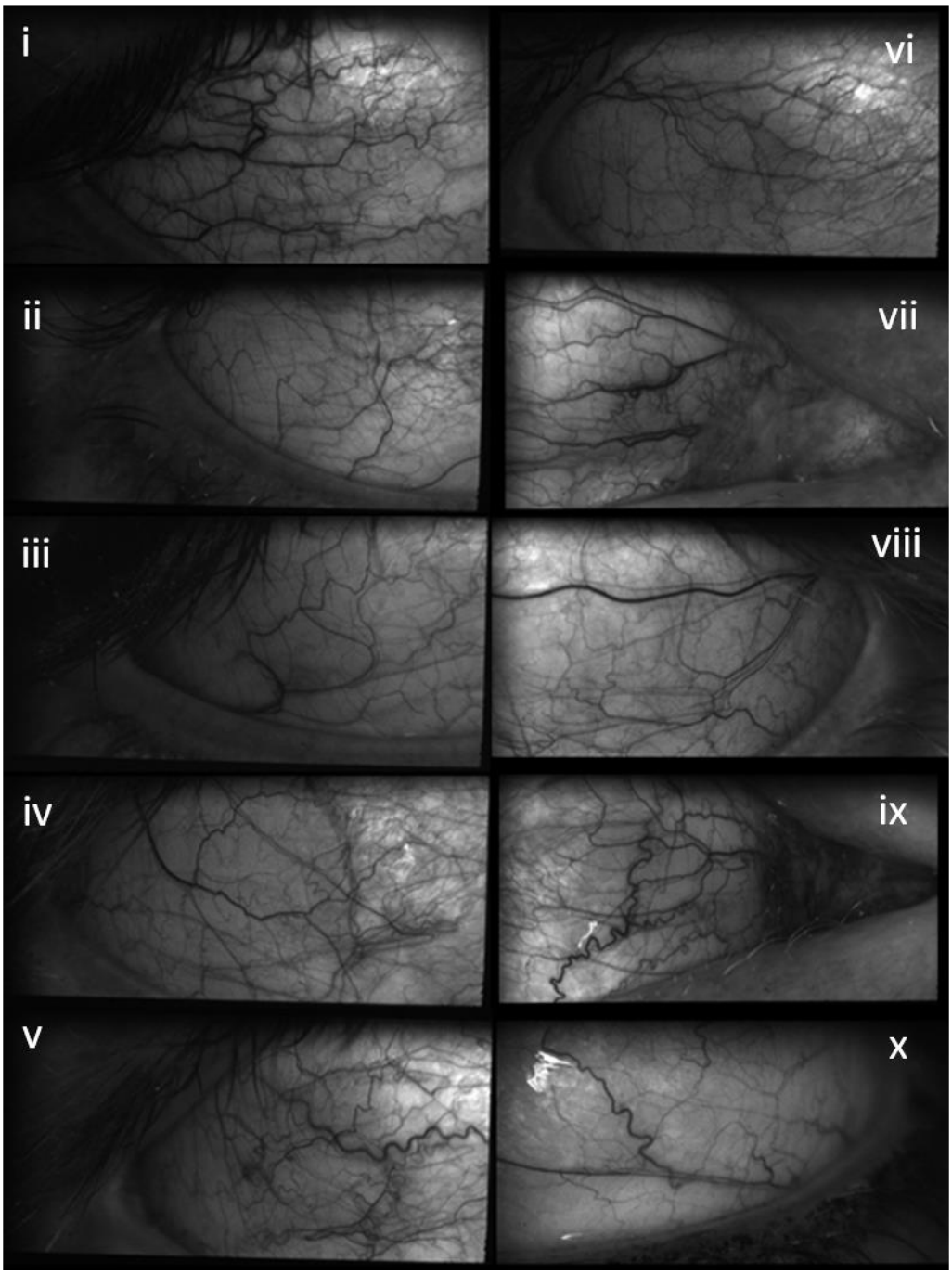

Figure 3-13. Images of the scleral regions selected for imaging for each of the ten subjects. The large inter-subject variety of bulbar conjunctival and episcleral vessel morphology can be seen. Subjects i-iv: right eye temporal quadrant. Subjects vii and x: left eye temporal quadrant. Subjects vi and ix: right eye nasal quadrant. Images are at the 584 nm (highest absorption) IRIS waveband. Bright regions are due to scleral glare or specular reflection. Approximate field of view is 10 mm x 3 mm.

3.5.2 Repeatability

Repeatability of ODR measurements is summarised in Table 3-3. The average standard deviation for repeated measurements of ODR for individual vessel sections was 2.27% for bulbar conjunctival and 2.28% for episcleral vessel sections. When ODR of vessels were averaged by vessel type (i.e. as results are presented in section 3.5.5) the standard deviation of repeat ODR measurements for bulbar conjunctival vessel sections was 0.96% and 1.55% for episcleral vessel sections. The lower variability when grouped by vessel type is probably due to the larger number of bulbar conjunctival vessel sections analysed (57 in total) compared to episcleral vessel sections (22 in total). In each case, standard deviations were calculated for eight image of each subject, and then averaged across all subjects.

Table 3-3 ODR repeatability for bulbar conjunctival and episcleral vessels**.**

Parameter	Bulbar Conjunctiva	Episclera
Number of subjects	10	7
Total number of sampled vessel sections	57	22
ODR repeatability: individual vessels*	2.27%	2.28%
ODR repeatability**	0.96%	1.55%

* Standard deviation of 8 repeated measurements of individual vessels, averaged across all subjects. ** Standard deviation of the average ODR of vessels when averaged by vessel type, averaged across all subjects

3.5.3 Eyelid closure

Eyelid closure resulted in no statistically significant change in ODR for either bulbar conjunctival or episcleral vessels (see Figure 3-14). ODR of bulbar conjunctival vessels was 0.90 ± 0.08 (mean ± standard deviation) when the eyelid was open and 0.90 ± 0.08 after eyelid closure ($p = 0.99$, paired t-test). ODR of episcleral vessels was 0.94 ± 0.09 when the eye was open and 0.93 ± 0.08 after eye closure ($p = 0.72$, pairwise t-test).

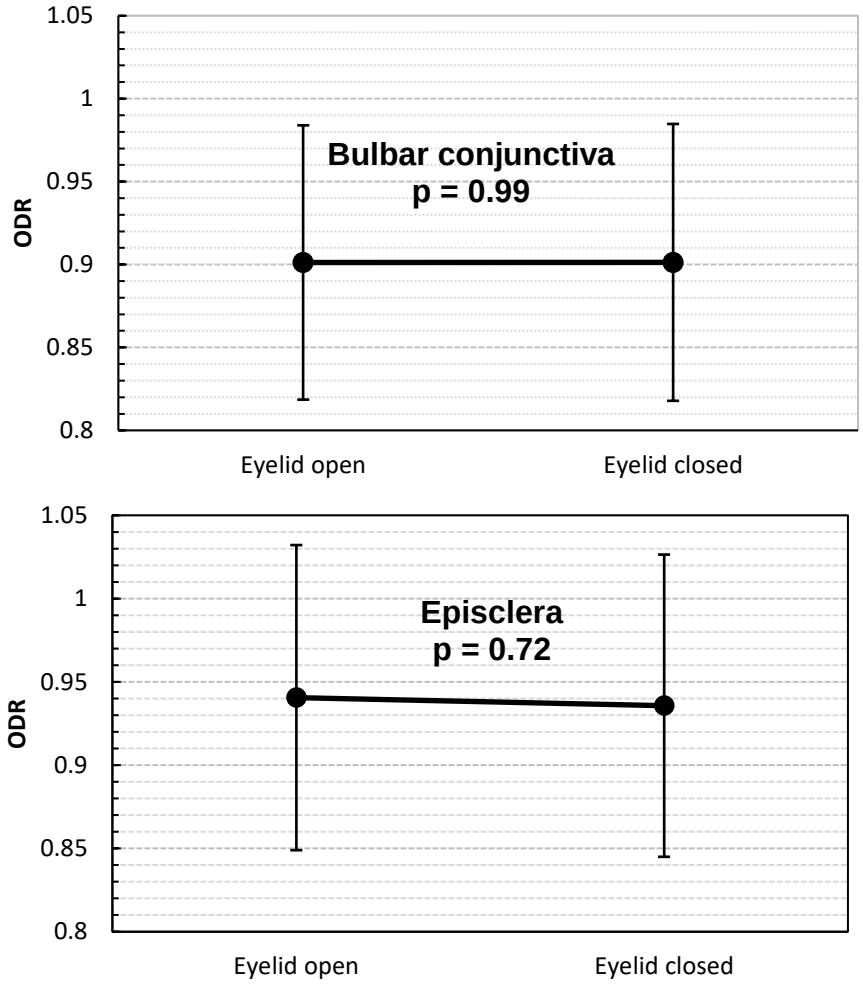

Figure 3-14. ODR before and after eyelid closure. No statistically significant difference was observed.

3.5.4 Acute mild hypoxia

Average vessel ODR and diameter at normoxia and hypoxia are summarised in Table 3-4 and Figure 3-15. Across all subjects, bulbar conjunctiva ODR increased with hypoxia (indicating a reduction in SO_2) from 0.846 ± 0.014 (mean ± standard error) at normoxia to 0.916 ± 0.011 at hypoxia ($p<0.001$, paired t-test) (see Figure 3-15b). Episcleral ODR increased on average, from 0.881 ± 0.019 (mean ± standard error) at normoxia to 0.938 ± 0.018 at hypoxia ($p = 0.03$, paired t-test) (see Figure 3-15c). ODR throughout the entire normoxia/hypoxia sequence is shown in Figure 3-15a; clear variations in ODR correlated to pulse oximeter data can be seen.

Across all subjects, bulbar conjunctival vessel diameter did not change significantly between normoxia and hypoxia ($p=0.89$, paired t-test), however an

increase diameter was apparent in some subjects, whereas a decrease in diameter was seen in others (see Figure 3-15d). Episcleral vessels were observed to increase from 78.9 ± 8.65 μm (mean ± standard deviation) at normoxia to 97.6 ± 1.43 μm at hypoxia (see Figure 3-15e).

Figure 3-16 shows a comparison of vasculature at normoxia and hypoxia in one subject where vasodilatation was observed in both bulbar conjunctival and episcleral vessels with hypoxia. Deeper episcleral vessels can be seen due to increased light absorption by blood. An ODR map of vessels at normoxia and hypoxia is shown in Figure 3-17.

Table 3-4. Blood vessel ODR, blood vessel diameter, and pulse oximeter SO_2 at normoxia and hypoxia.

Parameter	# of subjects	# sections analysed	Normoxia	Hypoxia	p-value*
Conjunctival ODR (mean ± SE)	10	64	0.846 ± 0.014	0.916 ± 0.011	<0.001
Episcleral ODR (mean ± SE)	7	24	0.880 ± 0.019	0.938 ± 0.018	0.03
Conjunctival diameter (μm) (mean ± SD)	10	64	80.1 ± 7.56	80.6 ± 6.95	0.89
Episcleral diameter (μm) (mean ± SD)	7	24	78.9 ± 8.65	97.6 ± 14.3	0.02
Pulse oximeter SO_2 (%) (mean ± SD)	10	N/A	97.1 ± 1.67	86.7 ± 4.24	<0.001

* Pairwise t test. SE = standard error. SD = standard deviation.

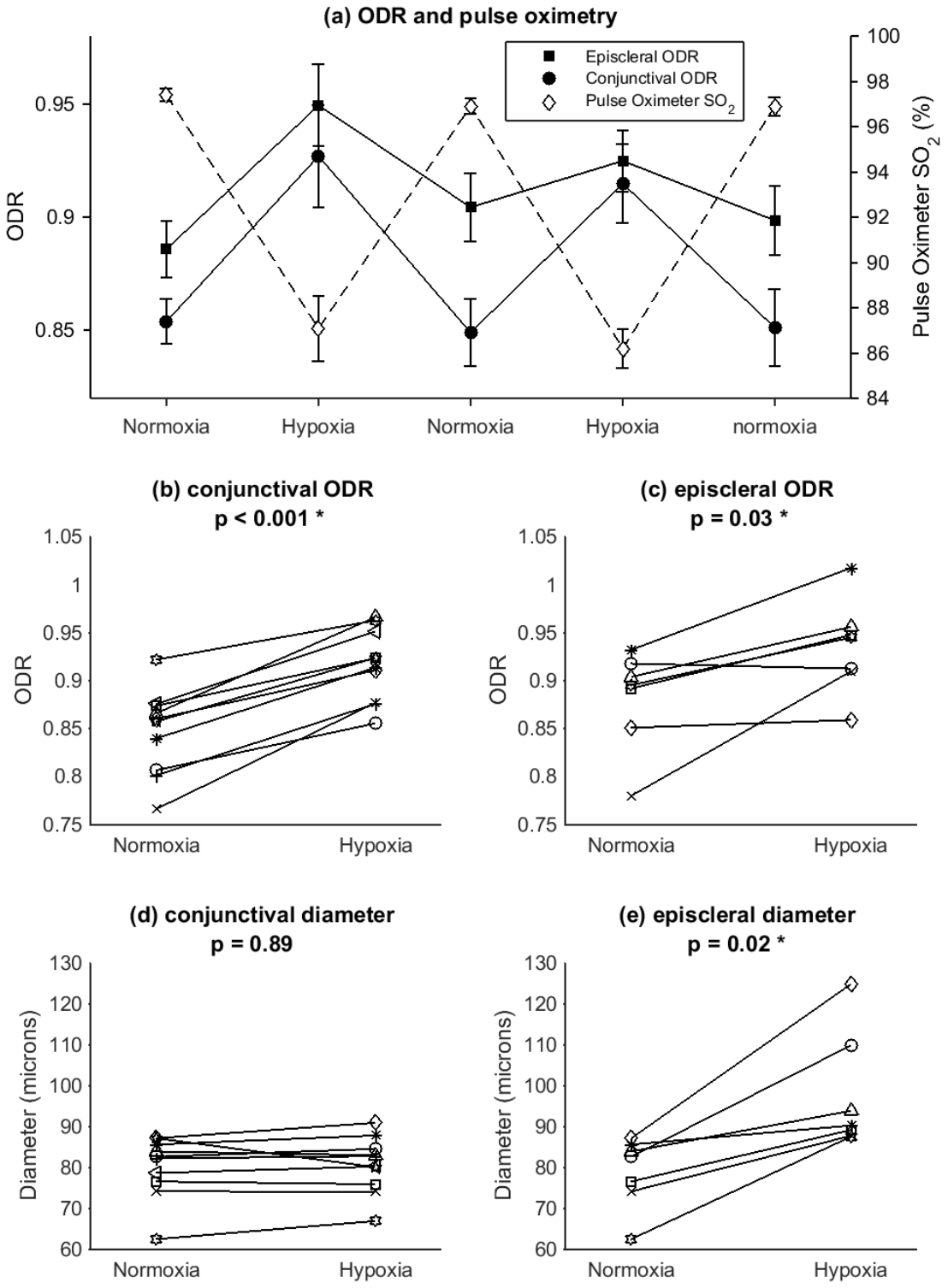

Figure 3-15. Vessel diameter and ODR at normoxia and hypoxia for all subjects. Marker symbols are the same for subjects across sub-figures **(b - e).** Error bars in sub-figure **(a)** are ± standard error.

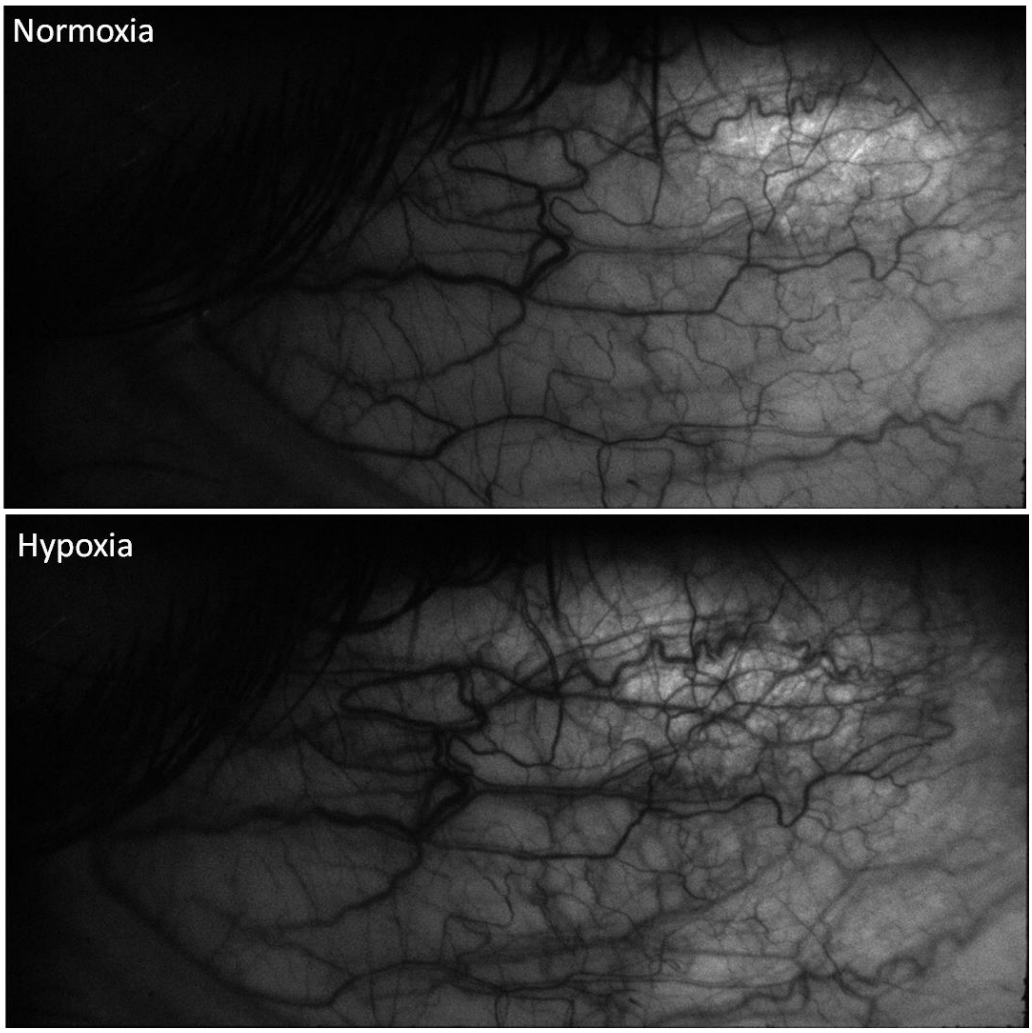

Figure 3-16. Vasodilatation observed in the right eye temporal scleral region of a single subject in response to hypoxia. Image acquired at 570 nm (an isobestic waveband). Deeper episcleral vessels are more apparent in the hypoxia image due to increased vessel diameter, and thus increased absorption of light.

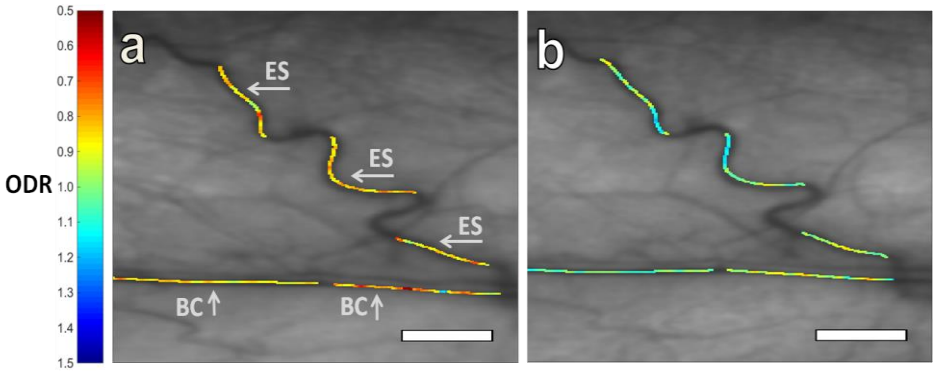

Figure 3-17. ODR map of vessels at normoxia and hypoxia in a single subject. BC = bulbar conjunctival, ES = episcleral. Scale bar represents 500 µm.

3.5.5 Oxygen diffusion

For all eight datasets (four subjects, each imaged twice) (see Figure 5-18) bulbar conjunctival ODR rapidly decreased in an exponential manner (indicating an increase in SO_2), tending asymptotically to an ODR corresponding to normoxia. The variation in ODR was well-fitted by an exponential-decay function representing re-oxygenation of the conjunctival vessels plus a linear drift in ODR, representing the incoming hypoxic blood supply from the ophthalmic artery:

$$OD = ae^{-bt} + ct + d, \qquad 3\text{-}3$$

where t is time, and a, b, c,and d are empirically calculated constants. The half-time to full reoxygenation (T) can then be calculated by:

$$T = -\frac{\ln(2)}{b}. \qquad 3\text{-}4$$

T varied on both an intra and inter-subject basis. The average value for T across all subjects was 3.4 ± 1.4 seconds (mean ± standard deviation) (see Table 3-5).

Table 3-5. Estimated values of the half-time to full reoxygenation (T) for each subject.

Subject	Data set	T (s)
A	(i)	6.6
	(ii)	4.1
B	(i)	3.0
	(ii)	2.9
C	(i)	2.1
	(ii)	3.4
D	(i)	2.2
	(ii)	3.2
	Average	**3.4**
	Standard Deviation	**1.4**

Episcleral vessel ODR remained higher (lower SO_2) than normoxia levels after eyelid opening and was well fitted by a linear trend. Pulse oximeter SO_2 followed a similar trend to episcleral ODR. The lack of change in episcleral ODR indicates that the change in increase in SO_2 of bulbar conjunctival vessels is due to oxygen diffusion from ambient air. Such diffusion does not take place in episcleral vessels because they are embedded into the sclera.

Figure 3-18 shows the typical variation in ODR upon eyelid opening (i.e. exposure to ambient air and thus commencement of oxygen diffusion) in two representative subjects. Figure 3-19 shows the same measurement in all four subjects, repeated twice. It is of note that bulbar conjunctival ODR of subjects B and D increased (i.e. SO_2 decreased) after reaching normoxia baseline ODR (see Figure 3-19); this is likely due to the fact that the rate of oxygen diffusion is directly proportional to the partial pressure gradient between ambient air and the vessels: once the vessels reach equilibrium with the air, the rate of oxygen diffusion will be low, allowing incoming hypoxic blood supply to lower SO_2 without oxygen diffusion swamping the decrease in SO_2. This agrees with the trend towards decreasing systemic SO_2 seen in the pulse oximeter readings of subjects B and D. Increased-duration (> 30s) observations could be beneficial.

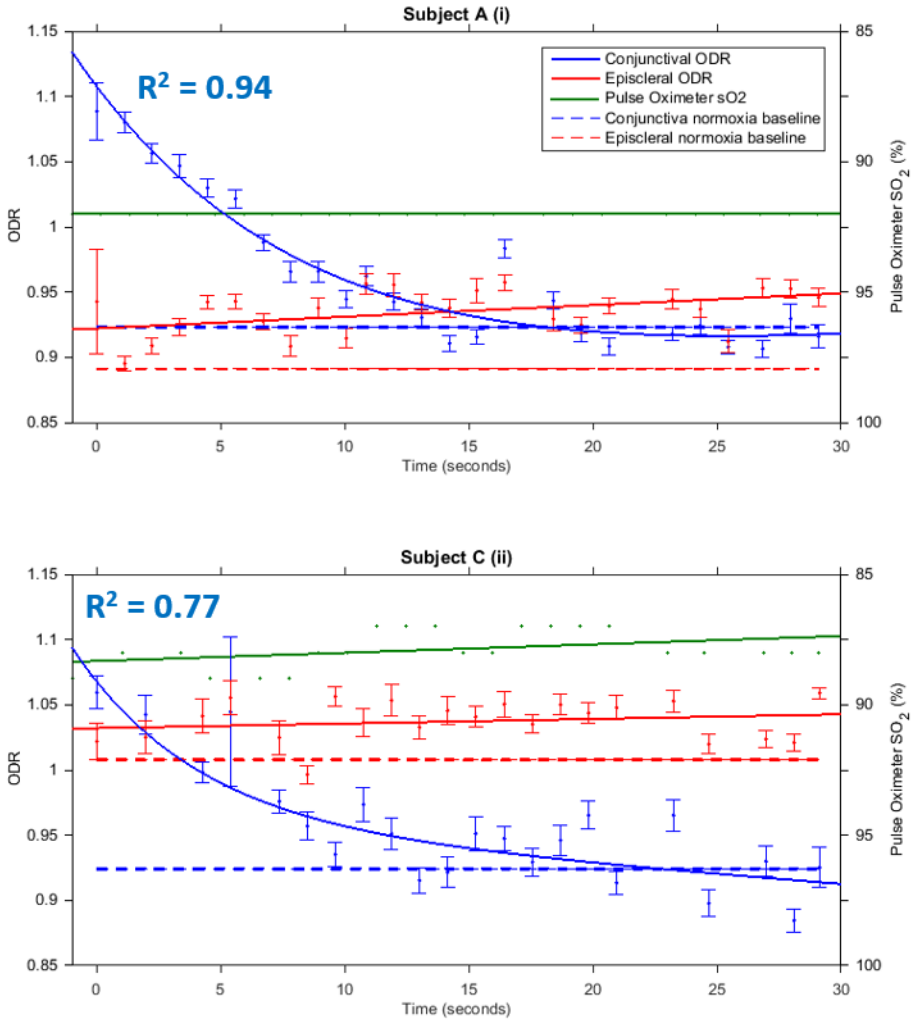

Figure 3-18. ODR of hypoxic vessels vs. time after eyelid opening in two subjects. The blue line is an exponential decay fit to bulbar conjunctival ODR; the red line is a linear fit to episcleral ODR. R^2 value is for decay fit to bulbar conjunctival ODR. The green line is a linear fit to pulse oximeter SO_2. Dashed lines represent normoxia baseline values. Error bars are ± the standard error of the mean. For clarity, the pulse oximeter error (± 2% SO_2 quoted by the manufacturer) is not depicted.

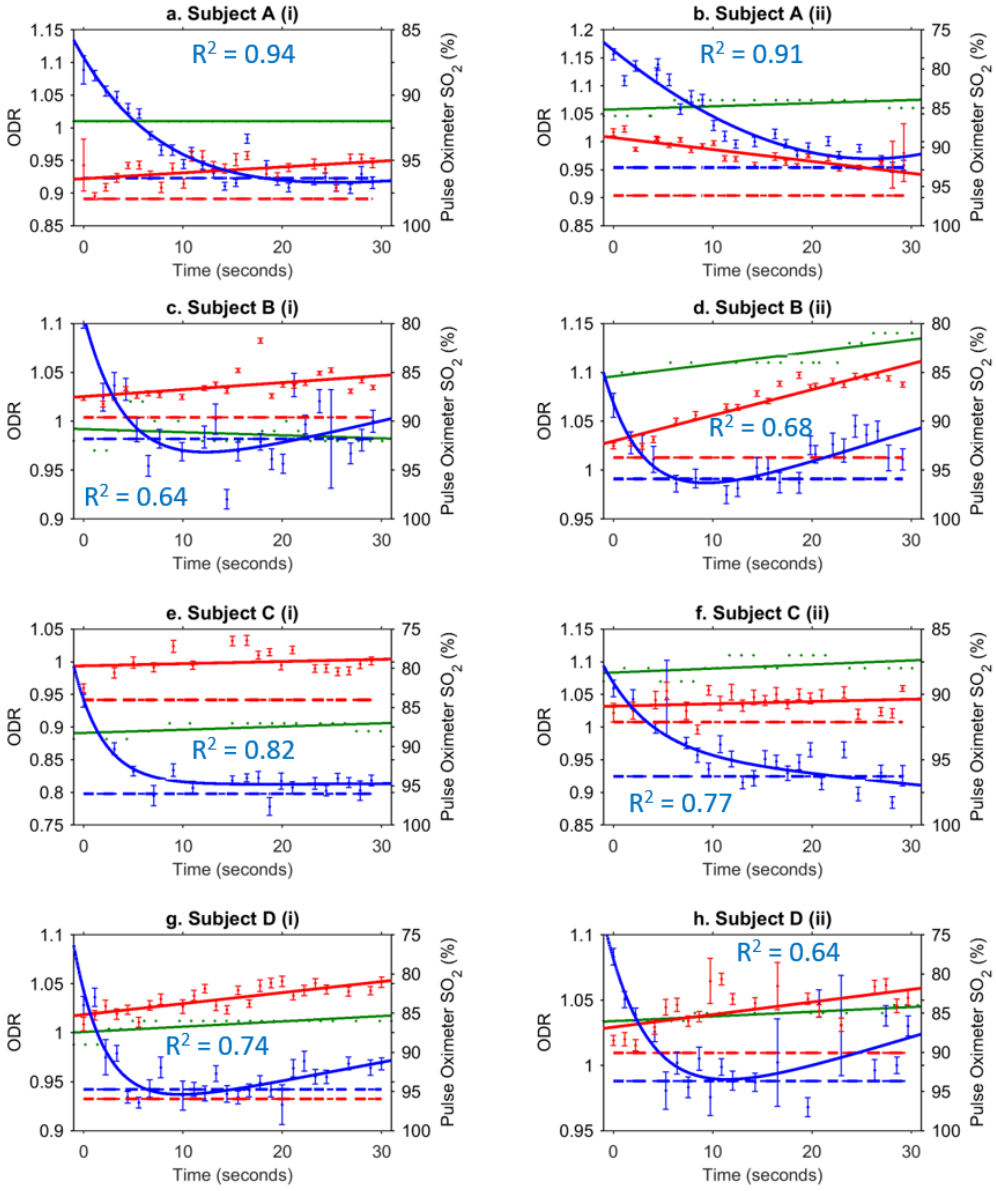

Figure 3-19. ODR of hypoxic vessels versus time after eyelid opening in all four subjects, repeated twice per subject. All formatting represents the same variables as Figure 3-18.

3.6 Discussion

3.6.1 Vessel classification

Episcleral and bulbar conjunctival vessels were successfully identified based upon relative motion of the semi-mobile bulbar conjunctival with respect to scleral features when subject gaze was changed. Comprehensive identification of arteries and veins was not possible in either bulbar conjunctival or episcleral vessels based upon morphology alone. In some subjects, bulbar conjunctival arterioles and venules form characteristic pairs of parallel vessels, where the arteriole is smaller than the venule.[47] However, in many subjects these pairs were not observed. Studies of episcleral vessels have traditionally had to rely on fluorescein angiography to identify arteries and veins,[43,44] but this approach was not possible in this study because it was not covered by ethical approval. Thus results of this study are reported in terms of generalised 'vasculature': i.e. averaged across all bulbar conjunctival or episcleral vessels. It should be noted that vessels < 60 µm were not analysed due to the low number of pixels across such vessels. The inclusion of only larger vessels likely introduced a selection bias for venules, which are generally larger than arterioles.[47]

3.6.2 Influence of optical scattering

3.6.2.1 Sources of optical scattering

Overlying scleral tissue will scatter light towards the detector, resulting in reduced contrast of vessels. We assume negligible scattering from the thin (~ 33 µm)[46] bulbar conjunctiva, and so can discount this source of scattering for bulbar conjunctival vessels. However, there will be a significant degree of scattering for both episcleral vessels (which are embedded in scleral tissue) and the FEP capillary (made out of highly scattering plastic) used in the phantom. Optical scattering by both scleral tissue and by blood should be considered when interpreting ODR. It can be assumed that the effects of scattering are equal for both 560 nm and 570 nm wavebands due to their proximity in wavelength.[93]

Scattering of light by blood will act to increase the optical path length through blood vessels. This will increase absorption by vessels, resulting in a lower transmission. The degree of scattering will be greater for large vessels and will

increase if vessels dilate in response to hypoxia.[101,103,105] Light transmission and scattering is described by the modified Beer-Lambert law (see Section 1.4.2.2).

It is well established that the scattering optical properties of blood are altered due to alignment of RBCs within a vessel: blood vessel reflectivity increases across all wavelengths until a constant velocity is reached (see Section 1.3.2.5). In a 50 μm vessel reflectivity was measured to be constant at a blood flow speed of 6 mm/s and higher.[36,66] However, the mean velocity of blood in small bulbar conjunctival vessels has been measured to be < 1 mm/s[222]; much less than 6 mm/s threshold. Thus, any increase in blood flow velocity could influence our oximetry measurement. Unfortunately blood flow velocity was not quantified in this experiment.

3.6.2.2 Influence of scattering on measured ODR

Quantifying the influence of scattering is not possible with simple two-wavelength oximetry. However, it is possible to make some generalised statements for the cases of ODR <1, ODR = 1, and ODR >1 by assuming that the magnitude of scattering is equal for both 560 nm and 570 nm wavebands.

If ODR = 1 (i.e. $OD_{560} = OD_{570}$), then the measured ODR will be equal to 1 as the degree of scattering is the same for both wavebands.

If ODR >1, then scattering will act to increase OD_{560} more than OD_{570}, resulting in an increase in measured ODR.

If ODR < 1, then scattering will act to increase OD_{570} more than OD_{560}, resulting in a decrease in measured ODR.

In the absence of detailed modelling, we can assess the magnitude of the effect of scattering by inducing a change in OD and carrying this through to ODR. Assuming ODR >1, a 10% increase in OD (e.g. due to vessel dilation) decreases ODR by ~ 1% only. Decreasing OD by 10% (e.g. due to contrast loss) also increases ODR by only ~ 1%. The converse is true for ODR <1. This reveals that our ODR measurement is relatively insensitive to scattering, thus the large ~ 10% changes in ODR measured in this study must be dominated by changes in SO_2. The influence of scattering could however, be better determined by three-wavelength oximetry analysis of this data.

3.6.3 Phantom validation

3.6.3.1 Design

The phantom enabled validation of the oximetry capability of the imaging system and analysis method. De-fibrinated *ex vivo* whole horse blood was used as a substitute for human blood. It has been shown that there is minimal difference in absorption spectra of haemoglobin derived from various animals,[223,18] so we assume that there is negligible different between horse and human blood.

Spectralon was used as a backing to the phantom to simulate the human sclera because of its diffuse scattering properties; both Spectralon and the sclera are diffuse scatterers.[224] Spectralon and scleral tissue also have similar wavelength-dependent reflectance properties (i.e. almost uniform reflectance at visible wavelengths), but the reflectance of Spectralon (99%)[219] is much higher than the reflectance of sclera (55%).[62] This will increase the proportion of reflected single-pass light in the phantom compared to *in vivo* bulbar conjunctival vessels. In future, capillaries could be embedded into the Spectralon to simulate episcleral vessels. This could allow a direct measurement of how scattering may affect ODR measurement.

3.6.3.2 Oximetry measurements

ODR of *ex vivo* blood samples was found to be inversely proportional to SO_2 as expected (see Figure 3-9). The repeatability of ODR measurements was found to be 0.5% (standard deviation of 10 repeated consecutive measurements in a single sample of 100% SO_2 blood). This is much less than the change in ODR seen due to deoxygenation (~ 25%).

There was however, some variability in ODR measurements compared to blood gas analyser measurements. This may be due to inhomogeneities in the optical properties of the blood sample, such as aggregates of red blood cells, which will alter the optical path length of light, and thus alter the absorption properties of blood. Non-uniform deoxygenation of the blood sample by discrete crystals of sodium dithionite may also contribute to the spatial variations in ODR. In future, the bubbling of nitrogen through blood could be used as an alternative deoxygenation process.

3.6.4 Repeatability of *in vivo* measurements

The repeatability (standard deviation of 8 consecutive images) for *in vivo* measurements of ODR when averaged by vessel type was ± 0.96% for bulbar conjunctival vessels and ± 1.55% for episcleral vessels. Repeatability of *in vivo* measurements for individual vessels was ± 2.28% for both bulbar conjunctival and episcleral vessels. These repeatability figures are much smaller than the 8% change ODR change observed due to induced hypoxia. This provides confidence in our measurement.

3.6.5 Eyelid closure

No change in ODR was observed in bulbar conjunctival or episcleral ODR after 2.5 minutes of eyelid closure. This was expected for episcleral vessels which were not seen to be affected by oxygen diffusion. However, some change in ODR was expected due to oxygen uptake by the conjunctiva in the absence of oxygen diffusion. ODR change may not have been evident either because of low oxygen uptake by the bulbar conjunctiva or by some occurrence of uncontrolled oxygen diffusion.

3.6.6 Acute mild hypoxia

Acute mild hypoxia resulted in a statistically significant increase in ODR of both bulbar conjunctival and episcleral vessels, indicating a decrease in SO_2. However, vessel diameter was observed to change significantly in episcleral vessels only. This provides confidence that the observed change in ODR is due to a change in SO_2 and due to increased optical scattering due to increased blood volume.

3.6.7 Oxygen diffusion

This study is the first to directly observe the reoxygenation of hypoxic blood vessels due to oxygen diffusion *in vivo*. Average ODR of all bulbar conjunctival vessels at normoxia was found to be consistently 0.85 (Figure 3-15a); this is consistent with constant oxygen diffusion. The pO_2 of these vessels will be close to 100% SO_2, because they will be at pO_2 equilibrium with ambient air (161 mmHg), which is significantly greater than the pO_2 of normal arterial blood (97 - 100% SO_2) at 100 mmHg.[225,226]

Oxygen diffusion has important consequences for oximetry of the bulbar conjunctival vessels, in particular, the procedures for testing oximetry capability. Normally, oximetry capability is confirmed by testing artery-vein SO_2 difference, or inducing a change in SO_2 by either increasing FiO_2 (hyperoxia)[41,107] or decreasing FiO_2 (hypoxia).[12] Oxygen diffusion will be detrimental to the effectiveness of each of these experimental tests for the following reasons. (1) Artery-vein SO_2 difference will be negligible in the exposed bulbar conjunctiva because all vessels will be close to 100% SO_2. (2) Induced hyperoxia will result in either a very small increase in SO_2 – because the vessels will already be close to 100% SO_2 - which would be hard to reliably detect in a statistically significant manner - or no increase at all. (3) Hypoxia will be mitigated by oxygen diffusion unless diffusion to vessels is blocked by eyelid closure or other oxygen impermeable barrier. These procedures would however, still be valid tests in the episcleral vasculature, which does not undergo significant oxygen diffusion.

In some subjects, bulbar conjunctival ODR was observed to slowly increase (i.e. SO_2 and pO_2 of the vessel decreased) after oxygen diffusion equalised the pO_2 of blood vessels with that of the ambient air (see subjects B and D in Figure 3-19). This can be explained by applying Ficke's law of diffusion (see Equation 1-2 in Section 1.2.3.4); when blood vessels are hypoxic, a large pO_2 gradient between blood vessels and the ambient air will drive oxygen diffusion at a fast rate. After blood vessels reach pO_2 equilibrium with the ambient air, oxygen diffusion occurs at a slower rate, enabling the incoming systemic hypoxic blood supply to decrease pO_2 and thus increase ODR; essentially, this will be an oscillation in pO_2 and thus an oscillation in observed SO_2. Although longer time-series was not studied here, the following sequence of events follows logically:

1. A hypoxic blood vessel will reach pO_2 equilibrium with ambient air.
2. Oxygen diffusion into vessel will slow to a negligible rate.
3. Incoming hypoxic blood supply will reduce pO_2.
4. Oxygen diffusion will resume and increase pO_2.
5. Points 1-4 will repeat as long as the incoming blood supply is hypoxic and as long as the vessel is exposed to ambient air.

This will be seen as damped driven oscillations in the pO_2 (and thus SO_2) of bulbar conjunctival blood vessels. A potential observation of such an oscillation occurring may be seen in data in Figure 3-19, subject B (ii), however, further research is required for this to be confirmed. The period and magnitude of these damped driven oscillations will be dependent on degree of systemic hypoxia, size of blood vessels, blood vessel wall thickness, and pO_2 of the ambient air. Because of these dependencies, such oscillations could potentially be used as a probe of oxygen diffusion and associated parameters in the microvasculature. However, this concept requires experimental validation.

3.6.8 Future Work

3.6.8.1 Calibration-free oximetry algorithms

Development of calibration-free absolute oximetry algorithms (see Section 1.4.7) is a challenging prospect, particularly for application in the retina, where scattering and absorption by overlying tissue and pigmentation may alter spectral transmissions significantly. The bulbar conjunctiva makes a tempting target for application of such algorithms because of the lack of pigmentation and overlying tissue. Additionally, the high oxygen saturation (100% SO_2) of bulbar conjunctival vessels at normoxia can provide a known reference value for testing algorithms. Episcleral vessels could be used to assess the influence of scattering and contrast lost on such oximetry algorithms *in vivo*. Application of such absolute oximetry algorithms would be particularly beneficial because there are no references values of SO_2 reported in the literature for the calibration of two-wavelength oximetry studies.

3.6.8.2 Capillary oximetry

The fundus camera provided insufficient resolution to reliably image capillaries, which are typically < 10 µm in diameter; however a high-magnification slit-lamp could be adapted for multispectral snapshot imaging. This would potentially enable non-contact *in vivo* oximetry of capillaries and groups of erythrocyte in humans.[215] Currently, *in vivo* capillary oximetry studies have been limited to studies in small animals either by photoacoustic microscopy of the mouse ear[168] or by optical imaging of dorsal skin-fold window chambers.[9,123] Capillary/erythrocyte oximetry may be of interest for studying oxygen uptake by red blood cells *in vivo*.

3.6.8.3 Measurement of oxygen diffusion

The bulbar conjunctiva may provide an easy test bed to probe oxygen diffusion rate into the microvasculature. By measuring the rate of re-oxygenation it may be possible to infer if vascular conditions alter oxygen diffusion properties of blood vessels. Perhaps the most immediate application of bulbar conjunctival SO_2 is the direct *in vivo* measurement of hypoxia in vasculature resulting from the wearing of semi-permeable contact lenses that slow or block oxygen diffusion.[195]

3.6.8.4 Disease development

Bulbar conjunctival oximetry may be of interest for studying disease development; for example, the bulbar conjunctival is certainly influenced by diabetes,[4,108] but it is unknown if SO_2 changes in the retinal circulation are seen in the conjunctival too.[197,199] Bulbar conjunctival oximetry may also be of interest in studying recovery from ocular burns when using oxygen-therapy,[227] and possibly in the study of ischemic conditions such as dry-eye syndrome.[228] Episcleral vessels could be used as a proxy for ophthalmic artery oximetry when retinal vessels are not accessible for imaging (e.g. due to cataracts or surgery). Episcleral vessel SO_2 may also be altered by high intra-ocular pressure.[229]

3.7 Conclusions

This is the first study to quantify changes in SO_2 of bulbar conjunctival and episcleral vessels by using non-contact multispectral imaging oximetry. The ODR of bulbar conjunctival and episcleral vessels was observed to increase at hypoxia, indicating a decrease in SO_2. Only episcleral vessels were observed to dilate in response to hypoxia, indicating that the change in ODR seen in the bulbar conjunctiva was due to a decrease in SO_2, not due to a change in the optical properties of vessels due to dilation.

The high temporal resolution of snapshot multispectral imaging (~ 1 Hz) enabled the direct observation of the reoxygenation of hypoxic vessels due to oxygen diffusion from ambient air. Episcleral vessels were not observed to reoxygenate because overlying scleral tissue blocked oxygen diffusion. The bulbar conjunctival microvasculature may be unique in that they are the only vessels outwith the alveolar capillaries observed to undergo such oxygen diffusion. Because of this, all

bulbar conjunctival vessels will be close to 100% SO_2 when exposed to ambient air under normoxia conditions.

Snapshot multispectral imaging oximetry of the bulbar conjunctiva and episclera may be of interest in investigating oxygen dynamics in a variety of microvasculature conditions where hypoxia may play a role, such as diabetes,[108] sickle-cell disease,[201] dry-eye syndrome,[228] contact lens wear,[195] high intra-ocular pressure,[229] and ocular-burn recovery.[227] Further, measurement of re-oxygenation due to oxygen diffusion could provide a method of probing the oxygen diffusion capabilities of vessels. The role of oxygen diffusion must be carefully considered in order for bulbar conjunctival oximetry experiments to provide meaningful results.

4 Oximetric Ratio Contrast Angiography (ORCA)

Summary: *this chapter motivates and describes a new method for non-invasive retinal angiography: Oximetric Ratio Contrast Angiography (ORCA). ORCA visualises blood flow by using snapshot multispectral imaging to monitor a small perturbation in SO_2 of blood circulating in the retina. The change in spectral absorption of blood due to this perturbation is then enhanced by computational image processing to create an angiographic sequence, similar in appearance to conventional fluorescence angiography. A pilot study of ORCA was conducted in human subjects. SO_2 perturbation was induced by subjects breathing a hypoxic air mixture. This pilot study demonstrates that that ORCA can reveal flow features previously only seen with fluorescein angiography, i.e. sequential vessel filling and laminar flow in branching retinal veins. The advantages and disadvantages of ORCA are discussed and contrasted with existing angiography techniques. Improvements for the implementation and testing of ORCA in future are discussed.*

4.1 Introduction and background

4.1.1 Motivation

Fluorescein angiography (FA) is a workhorse technique used worldwide to visualise retinal blood flow and diagnose a variety of conditions such as diabetic retinopathy,[230] glaucoma,[7] myopia,[231] age-related macular degeneration,[232] neo-vascularisation,[233] malarial retinopathy,[234] and retinal vessel occlusion.[235] However, FA requires the intravenous injection of a mildly toxic dye, which has numerous associated risks, including nausea (6% of patients), severe skin irritation (4% of patients), and even a small risk of death (1 in 220,000)[236–239] Alternative non-invasive blood-flow based angiography techniques are available (see Section

4.1.3), but these techniques cannot visualise prominent blood features seen in FA, i.e. sequential filling of arteries and veins, and laminar flow in branching veins.

This chapter describes the development and demonstration of an entirely-new non-invasive retinal angiography concept: Oximetric Ratio Contrast Angiography (ORCA). A pilot study of ORCA was conducted in human subjects. This pilot study demonstrates that ORCA is capable of retinal angiography, and further, that ORCA reveals sequential vessel filling and laminar flow; features only previously seen with FA.

4.1.2 Fluorescein angiography

4.1.2.1 Principle

FA is a widely used technique for ophthalmologists to visualise blood flow in the retinal circulation. FA is enabled by intra-venous injection of a fluorescent dye which circulates around the body in blood, eventually reaching the retina. When illuminated with the appropriate excitation wavelength, the fluorescent dye will strongly fluoresce, making fluorescein-filled blood vessels appear bright when imaged at the correct emission wavelength, whereas blood vessels with no fluorescein remain dark. The circulating fluorescein can be seen sequentially in arteries, capillaries, and veins. Where multiple veins combine, fluorescein can be seen as laminar flow streams. Further, FA can also reveal vessel micro-haemorrhages (e.g. due to diabetic retinopathy).[230] An example image from a retinal FA is shown in Figure 4-1.

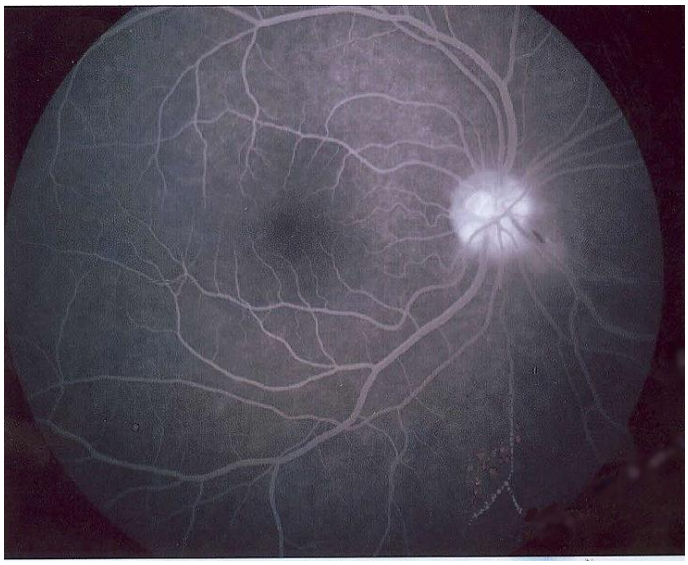

Figure 4-1. A late-phase retinal fluorescein angiography of a healthy subject.[o]

4.1.2.2 Characteristic features of retinal FA

FA reveals the following characteristic features of blood circulation:

Sequential vessel filling: fluorescein can be observed to first fill arteries, capillaries, and then veins. Choroidal vessel filling may also be observed as a diffuse increase in the background fluorescence of retinal tissue. The visibility of choroidal filling is dependent on the emission wavelength of fluorescent dye used, and the degree of retinal pigmentation in individual subjects.

Laminar flow: apparent in retinal veins where multiple venules join a larger vein. Each venule will contain a different concentration of fluorescein (due to variations in blood circulation time). The variations in fluorescein concentration can then be seen in the vein because blood from each venules flows in a laminar fashion in the larger vein. This gives the appearance of multiple light and dark streaks of fluorescein in the vein.

[o] Image reproduced from Wikimedia Commons under Creative Commons Attribution-ShareAlike 3.0 Unported license.[298]

Vessel leakage: damage to blood vessels (e.g. due to diabetes) will result in the small sodium fluorescein molecules leaking from micro-haemorrhages in blood vessels into surrounding tissue (see Figure 4 2).

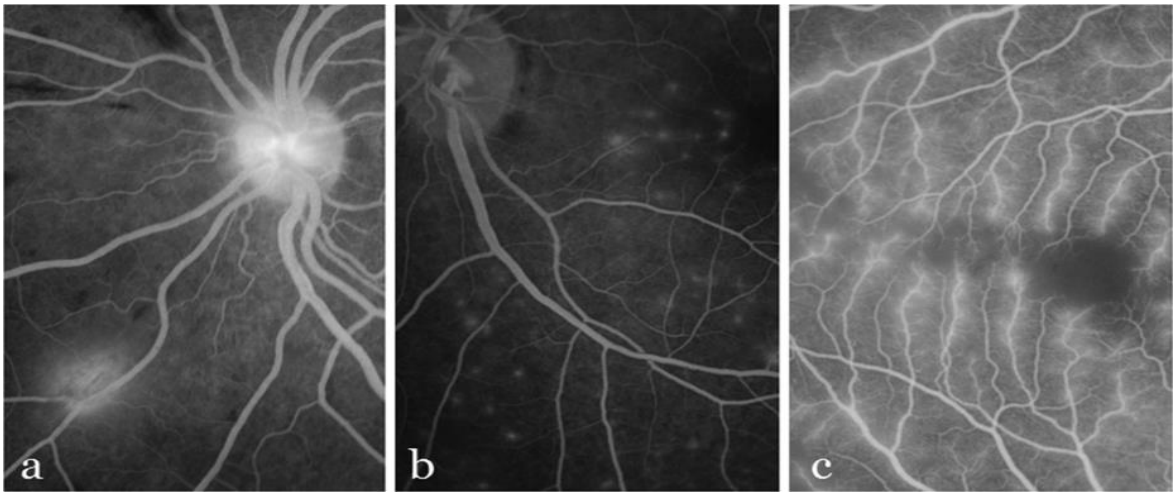

Figure 4-2. Three examples of vessel leakage revealed by FA.[p]

4.1.2.3 Phases of fluorescein angiography

The circulation of fluorescein produces several distinct FA phases:

(1) Diffuse brightening of the choroid (the choroidal flush) occurring approximately ten seconds post injection.[213,240]
(2) Fluorescein starts to fill retinal arteries approximately 12 seconds post-injection. This is known as *the arterial phase*.
(3) Fluorescein flows through retinal capillaries and can be seen to enter veins.
(4) Laminar flow of fluorescein is observed in branching veins.
(5) Veins will be completely filled with fluorescein approximately 30 seconds post injection. This is known as *the venous phase*.
(6) Arteries and veins will be equal in fluorescence brightness at 2-4 minutes post injection.

[p] Image reproduced under a Creative Commons Attribution 4.0 International License from Zhao et al. “Automated detection of leakage in fluorescein angiography images with application to malarial retinopathy.” *Scientific Reports.* 2015.[234]

(7) At 7-15 minutes post injection, overall fluorescence will be diminished and vessel leakages may be discernible as regions of hyper-fluorescence (see Figure 4-1).[241–243] This is known as *the late phase*.

4.1.3 Alternative non-invasive angiography techniques

Several non-invasive angiography techniques have been reported; each of which use the blood flow velocity or motion of RBCs to map flow. Non-invasive angiography techniques and their contrast methods are summarised in Table 4-1. None of these techniques can visualise sequential vessel filling or laminar flow seen in FA.

Table 4-1. Contrast mechanisms of non–invasive angiography techniques.

Angiography technique	Contrast mechanism
Retinal Functional Imaging	Motion of distinct groups erythrocytes.[244,245]
Laser Speckle Contrast Imaging	Contrast reduction of laser speckle due to blood flow.[187,246]
Laser Doppler Imaging	Doppler shift of laser light induced by blood flow.[187]
Optical Coherence Tomography	Doppler shift, speckle, and phase variations induced by blood flow. [247,248]

4.2 Oximetric Ratio Contrast Angiography (ORCA)

4.2.1 Concept of ORCA

Oximetric Ratio Contrast Angiography (ORCA) is an entirely new non-invasive angiography concept. ORCA utilises the SO_2-dependent endogenous contrast of haemoglobin circulating in blood as a contrast agent. In ORCA, SO_2 of arterial blood is perturbed; multispectral imaging records the resulting change in absorption spectra of flowing blood; and computational processing is used to visualise the change in spectral contrast. The principle of oximetric contrast is shown in Figure 4-3.

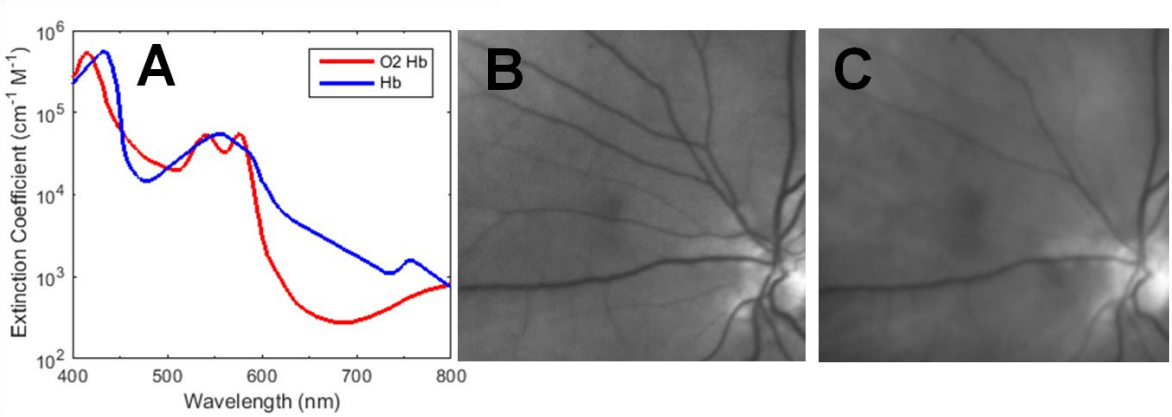

Figure 4-3. Oximetric contrast. **(A)** The SO_2-dependent optical absorption spectra of haemoglobin. **(B)** 577 nm image of a retina: arteries and veins have similar transmission. **(C)** 600 nm image of the same retina; arteries (~ 97% SO_2) appear almost totally transparent due to high SO_2 whereas veins (~ 70% SO_2) absorb significantly more light.

4.2.2 Implementation of ORCA

4.2.2.1 Overview

The four main processes required to produce an ORCA sequence are:

(1) Video-rate multispectral video acquisition of target blood vessels.
(2) SO_2 perturbation.
(3) Video sequence registration.
(4) Computational image subtraction.

The implementation of these processes for a pilot study of ORCA are outlined in Sections 4.2.2.2 - 4.2.2.13. Details and results of the pilot study are presented in Section 4.3 onwards.

4.2.2.2 Video-rate multispectral retinal imaging

A retinal fundus camera (TRC50-IA, Topcon) modified with an Image Replicating Imaging Spectrometer (IRIS) (see Section 2.1.3.2) and a monochromatic cooled scientific CCD (Charge Coupled Device) detector (Retiga 4000R, QImaging) enabled video-rate multispectral imaging. The system was configured for orthogonal polarisation imaging to null specular reflections from blood vessels and reduce glare from the cornea.[216] The imaging system is shown in Figure 4-4.

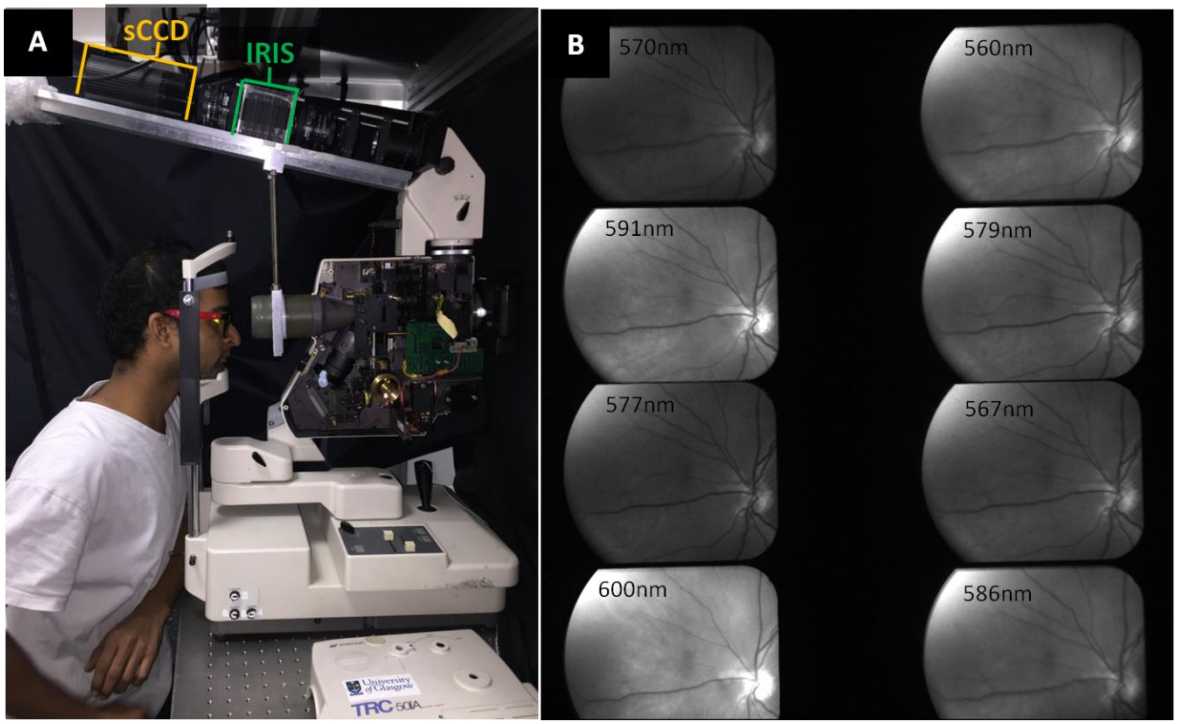

Figure 4-4. The video-rate multispectral retinal imaging system. **(A)** Retinal fundus camera modified with IRIS and a cooled sCCD detector. **(B)** Representative 8-band retinal image.

4.2.2.3 Waveband choice for ORCA

To maximise light throughput to the detector, the IRIS filter plate (see Section 2.1.3.2) was not used because the IRIS filter plate was found to reduce light throughput, and waveband purity of all eight IRIS wavebands is not required for ORCA. Instead, a bandpass filter (530 - 610 nm) was placed in the illumination path of the fundus camera. This configuration resulted in some spectral side-lobes in each IRIS waveband (see Figure 4-5) but enabled high-quality imaging with the 577 nm and 600 nm wavebands.

To account for the influence of spectral side-lobes on blood vessel transmission measurement, the effective extinction coefficient of blood was calculated from spectral measurements of each IRIS waveband combined with tabulated values for the extinction coefficient of haemoglobin.[19] The resulting effective extinction coefficient of each IRIS waveband vs. SO_2 is shown in Figure 4-6. The waveband combination of 577 nm (pseudo-isobestic) and 600 nm (high contrast) was selected for ORCA analysis due to their good image quality and appropriate effective extinction coefficients for tracking changes in SO_2.

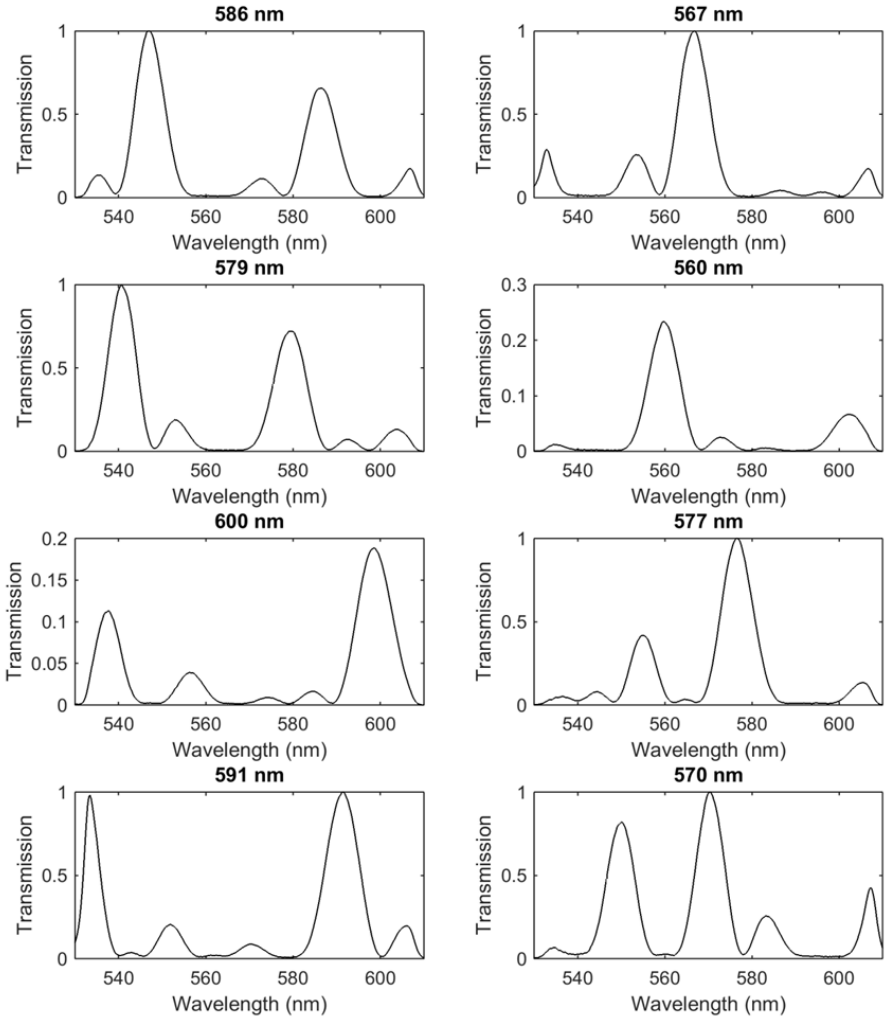

Figure 4-5. Spectra of IRIS wavebands without the filter plate.[q]

[q] Data provided by Javier Fernandez-Ramos.

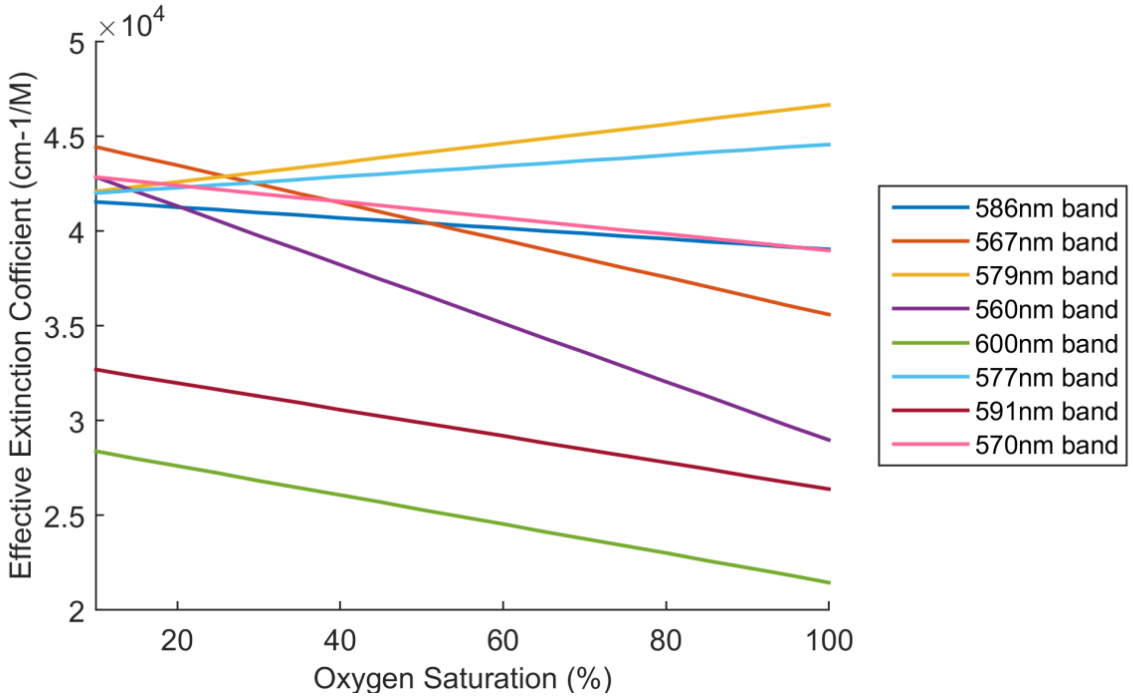

Figure 4-6. The effective extinction coefficient vs. SO_2 for each IRIS waveband.

4.2.2.4 Camera and detector settings

To minimise integration time required to acquire images, the fundus camera inspection lamp was set to maximum intensity. Flash illumination was not used because the flash limited to a recycle rate of 1 Hz. However, in future flash may be advantageous as it would allow high-quality imaging with minimal motion blur. Maximum field-of-view of the fundus camera was selected to maximise light collection. Image acquisition was controlled via MicroManager.[249] Images were saved as uncompressed .TIFF format. The sCCD was set to 12-bit acquisition (maximum sensitivity), with an exposure time of 1/3rd of a second (~ 3 frames per second).

4.2.2.5 Retinal light exposure levels

The retinal irradiance for this system configuration was calculated from experimentally obtained intensity measurements. The intensity of light incident on the retina was estimated to be ~ 1.5 mW cm^{-2}. Assuming an imaging period of ~ 3 minutes, this is ~ 1/500th of the photothermal damage threshold and ~ 1/10th of the limit for photochemical damage as set out by International Commission on Non-

Ionizing Radiation Protection.[31,250] Thus, the system was deemed safe for human imaging.

4.2.2.6 SO_2 perturbation by inhalation of a hypoxic air mixture

Inhalation of a hypoxic air mixture was used to perturb arterial SO_2 of circulating blood and thus produce a transient deoxygenation wave (TDOW) that circulates around the body. A medical-grade hypoxic air mixture of 5% Oxygen, 95% Nitrogen (pO_2 ~ 40 mmHg) for this purpose.[r] When a subject inhales this hypoxic air mixture, the pO_2 in the lungs is reduced to between 40 mmHg and 100 mmHg; i.e. between the pO_2 of the hypoxic air mixture and the normal pO_2 of air in the lungs. It is not possible to know exactly what pO_2 is reached because this depends on many factors such as gas exchange, temperature, and moisture in the lungs. However, 100 mmHg corresponds to a normal arterial SO_2 of ~ 100%, and 40 mmHg corresponds to venous SO_2 of ~ 70%,[251] so it is likely that the SO_2 of arterial blood leaving the alveolar capillaries will be between 70% and 97% SO_2. The relationship between pO_2 and SO_2 of blood is described by the oxygen dissociation curve, which is shown in Figure 4-7. This deoxygenated blood then begins to circulate around the body. pO_2 will decrease with time as the oxygen reservoir in the lungs diffuses into alveolar blood. Theoretically, if subjects held their breath for long enough, then pO_2 of lungs will reach equilibrium with pO_2 of incoming venous blood (40 mmHg).

[r] A mixture of 10% Oxygen, 90% Nitrogen (pO2 ~ 75 mmHg) was previously tested for the purpose, but this was not sufficient to repeatable perturb arterial SO_2 by >5% in most subjects.

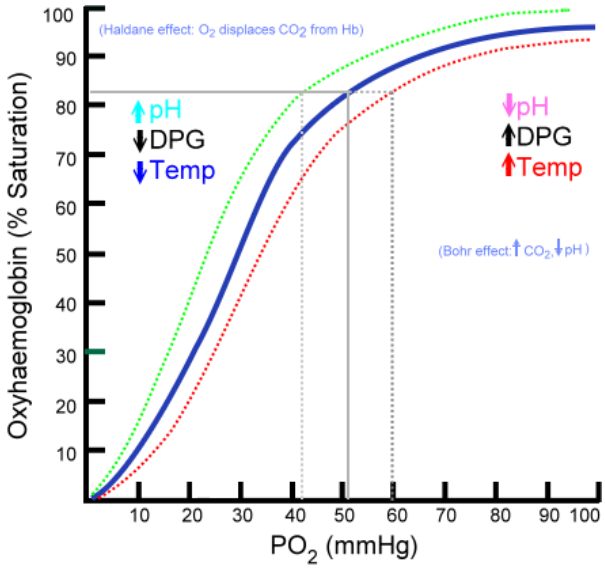

Figure 4-7. The sigmoid-shaped haemoglobin oxygen dissociation curve. The typical oxygen dissociation curve (i.e. at pH = 7.4, T = 37 °C) is shown as solid blue. Various factors can alter the oxygen dissociation curve, such as pH of blood (e.g. due to changes in dissolved carbon dioxide in the blood; i.e. the Bohr effect), temperature, and concentration of diphosphoglycerate (DPG) in blood.[1][s]

4.2.2.7 Multispectral video processing

Once a multispectral retinal video sequence with a transient deoxygenation wave present has been obtained, the multispectral video data must be processed appropriately to generate an ORCA sequence. The following steps are needed:

(1) Co-registration of IRIS waveband images.
(2) Removal of low-quality video frames.
(3) Temporal registration of video sequence.
(4) Calculation of intensity ratio.
(5) Reference frame selection.
(6) Image subtraction.

[s] Figure modified from the public domain. Image originally from Wikimedia Commons.[290]

4.2.2.8 IRIS image co-registration

IRIS wavebands are cropped and spatially co-registered using a Matlab algorithm based upon maximising the auto-correlation of IRIS wavebands.[150,252,253] This serves to compensate for small optical distortions introduced by IRIS. Once the appropriate registration is calculated, it is applied to all retinal images in the sequence, creating a 4D multispectral video sequence (i.e. a sequence in spatial dimensions, wavelength, and time).[254] See Section 2.1.2.1 for details of this algorithim.

4.2.2.9 Frame quality check

ORCA requires high quality images, free of artefacts such as motion blur or corneal glare. Image quality was checked manually by viewing each frame in the open-source image analysis program, *Image J*.[255] Video frames which exhibit reduced quality due to eyelid blinking, motion blur, or excessive corneal glare were omitted from further analysis. This manual frame quality checking process was time consuming, taking roughly 30 - 40 minutes for a three-minute retinal video sequence (~ 560 frames). Examples of the various retinal image artefacts possible are shown in Figure 4-8.

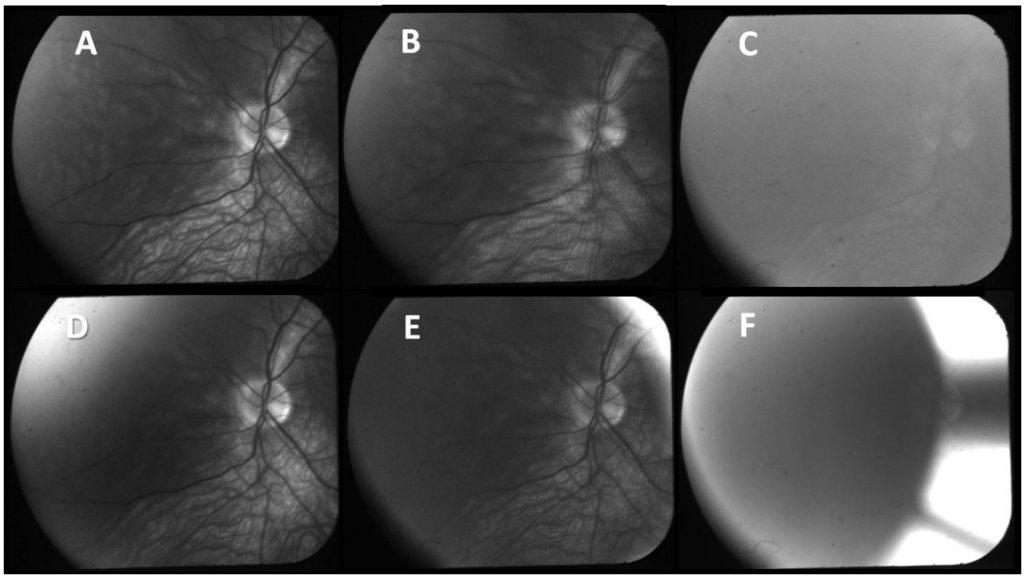

Figure 4-8. Examples of artefacts in a retinal video sequence. **(A)** High quality image. **(B)** Motion blur. **(C)** Eyelid blink. **(D)** Moderate corneal glare from left. **(E)** Moderate corneal glare from the right. **(F)** Extreme corneal glare from the right.

4.2.2.10 Temporal registration using a feature-identification algorithm

Temporal co-registration of the video-sequence was required to remove bulk-retinal motion due to eye motion. An image feature-detection and feature-matching algorithm was used to calculate the affine image transforms required to co-register each image with a high quality reference image. This registration algorithm was implemented using code from the open-source VL_FEAT Matlab toolbox.[256] This algorithm identifies registration control-points based on features such as vessel intersections, vessel edges, and the optic disk. It then matches these features between images (see Figure 4-9) and computes an affine transform between them, enabling co-registration of retinal images in a video sequence.

This algorithm worked best when the number of detectable features was high (e.g. close to the optic disk), however away from the optic disk, fewer vessels are present, thus fewer features, and registration proved to be significantly more challenging. Success of temporal co-registration was determined by manual analysis. Any frames which were not successfully registered were omitted from further analysis. In a reasonable quality video sequence, approximately 50 - 75% of frames were included for ORCA analysis.

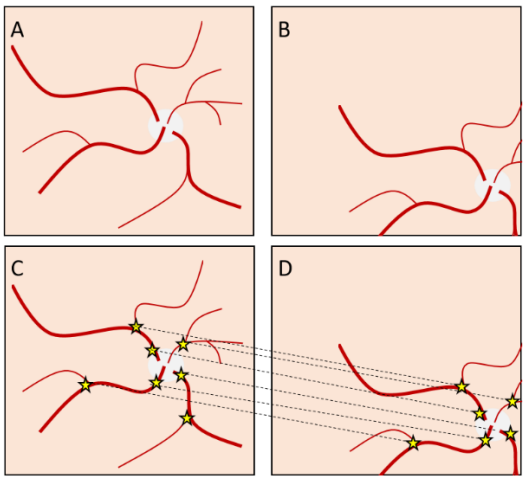

Figure 4-9. Retinal feature matching for SIFT registration. **(A)** Retinal image. **(B)** Arbitrarily displaced retinal image. **(C)** Features identified in image A. **(D)** Matching features identified in image B. From this information, an affine transform can be computed and applied.

4.2.2.11 Calculation of intensity ratio

Once a retinal video sequence has been temporally registered, the next step is to calculate the pixel-by-pixel intensity ratio, $IR(\mathrm{x,y})$, of two wavebands for each image in the retinal video sequence:

$$IR(\mathrm{x,y}) = \frac{I_{600}(\mathrm{x,y})}{I_{577}(\mathrm{x,y})}, \qquad 4\text{-}1$$

where $\mathrm{I}_{600}(\mathrm{x,y})$ and $\mathrm{I}_{577}(\mathrm{x,y})$ represent the pixel-by-pixel greyscale intensity of 600 nm and 577 nm IRIS wavebands respectively. $IR(\mathrm{x,y})$ is dependent on the intensity at each point in the image, $I_\lambda(\mathrm{x,y})$, which can be described by the modified Beer-Lambert Law:

$$I_\lambda(\mathrm{x,y}) = I_{\lambda\mathrm{o}} \exp\left(-c\, d_\lambda\, \varepsilon_\lambda + B_\lambda\right), \qquad 4\text{-}2$$

where ε_λ is the SO_2-dependent extinction coefficient of haemoglobin, c is the concentration of absorbers, d_λ is the path length of light through tissue and blood vessels, and B_λ is an additive scattering term. To measure the total change in absorption due to a TDOW, the average intensity ratio (IR) for the entire image is calculated by:

$$IR = \frac{1}{p} \sum_{i=1:\,p}^{p} IR(x,y)_i, \qquad 4\text{-}3$$

where p is the number of pixels in an image. When a TDOW circulates through the retina, IR will decrease and eventually increase in a characteristic manner, as shown in Figure 4-10.

4.2.2.12 Selection of reference image for image subtraction

ORCA enables visualisation of blood flow by calculating the change of $IR(\mathrm{x,y})$ with respect to a reference image. There are three generalised points in a video sequence which can be used; (i) baseline normoxia, (ii) maximum of transient hypoxia, and (iii) return to normoxia. These points are depicted in Figure 4-10. Point ii is the optimal choice because it represents a return from hypoxic blood flow to normoxia, allowing indefinite continuation of an ORCA sequence. Further, point ii avoids the period of hypoxic air mixture inhalation and associated subject motion.

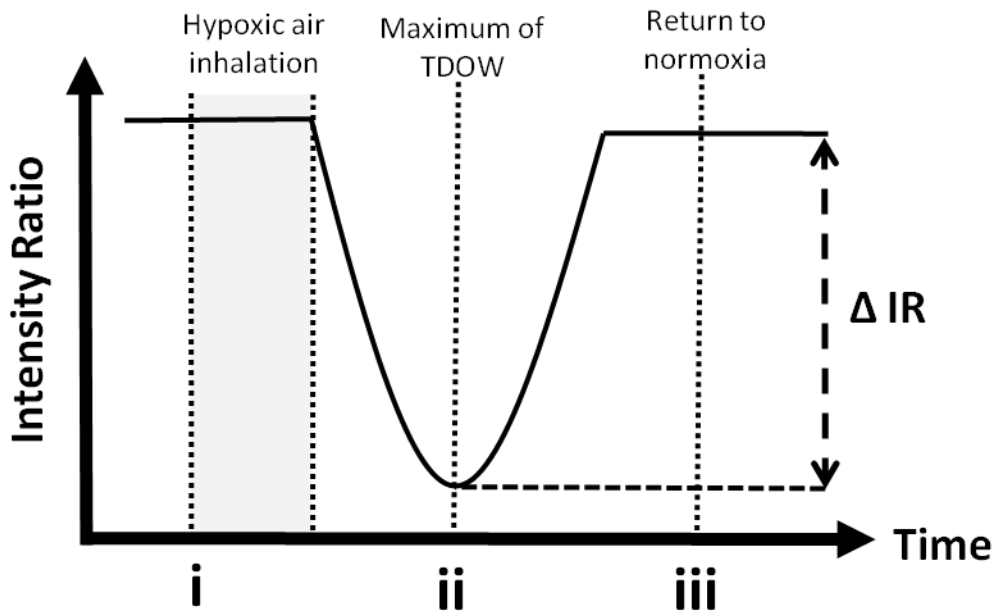

Figure 4-10. The characteristic change in average intensity ratio (IR) of the retina as a transient deoxygenation wave circulates. The grey shaded area represents time of hypoxic air inhalation. Points i, ii, and iii are potential points for reference frame selection.

4.2.2.13 Image subtraction

Once a reference frame (donated by *n*), is selected, image subtraction is performed to enable visualisation and enhance the change in pixel-by-pixel intensity ratio, $\Delta IR(\mathrm{x,y})$. Image subtraction is performed by:

$$\Delta IR(\mathrm{x,y}) = |IR_{\mathrm{n}}(\mathrm{x,y}) - IR_{\mathrm{ref}}(\mathrm{x,y})|, \qquad 4\text{-}4$$

where $IR_{\mathrm{n}}(\mathrm{x,y})$ is the pixel-by-pixel intensity ratio of a frame in the video sequence, and $IR_{\mathrm{ref}}(\mathrm{x,y})$ is the intensity ratio of the reference frame. The resulting sequence is normalised and displayed in greyscale so that points of maximum $\Delta IR(\mathrm{x,y})$ appears white, and regions of no change (i.e. $\Delta IR(\mathrm{x,y}) = 0$) appear black.

To reduce the influence of random fluctuations in greyscale intensity (e.g. due to thermal noise in the CCD), frames are averaged by:

$$IR_{\mathrm{n}}(\mathrm{x,y}) = \frac{1}{z} \sum_{i=n\text{-}z}^{n} IR(x,y)_i, \qquad 4\text{-}5$$

$$IR_{\mathrm{ref}}(\mathrm{x,y}) = \frac{1}{z} \sum_{i=ref\text{-}z}^{ref} IR(x,y)_{\mathrm{i}}, \qquad 4\text{-}6$$

where n is number of the current frame, ref is the reference frame number, and z is the number of frames averaged. Assuming random fluctuations, this gives a reduction in random noise proportional to $\sqrt{z}$.

4.3 Pilot study in humans

4.3.1 Aims

The aim of this pilot study was to demonstrate the feasibility of ORCA in humans and to determine the repeatability of the technique and how motion or other factors may influence ORCA sequences.

4.3.2 Subject recruitment

This pilot study was approved by University of Glasgow Medical, Veterinary and Life Sciences ethics committee. 11 healthy human volunteers were recruited; 9 male, 2 female, age 28 ± 10 years (mean ± standard deviation). All volunteers provided informed written consent before participation and all procedures were performed in accordance with the tenets of the Declaration of Helsinki.

Subjects reported no history of ocular, respiratory, or cardiovascular disease. Subjects did not regularly wear contact lenses. Degree of retinal pigmentation was quantified for each subject by grading iris colour on a scale of 1 (minimal pigmentation) to 25 (maximal pigmentation) as per the procedure described in Franssen et al. (2008).[257] Figure 4-11 shows the retinal images in subjects with the minimum and maximum pigmentation scores.

Subjects were asked to refrain from drinking alcohol 24 hours prior to the study, and not consume caffeinated beverages or smoke for 1 hour prior to the

commencement of the study. 9 subjects were non-smokers. Subjects D and E were smokers.

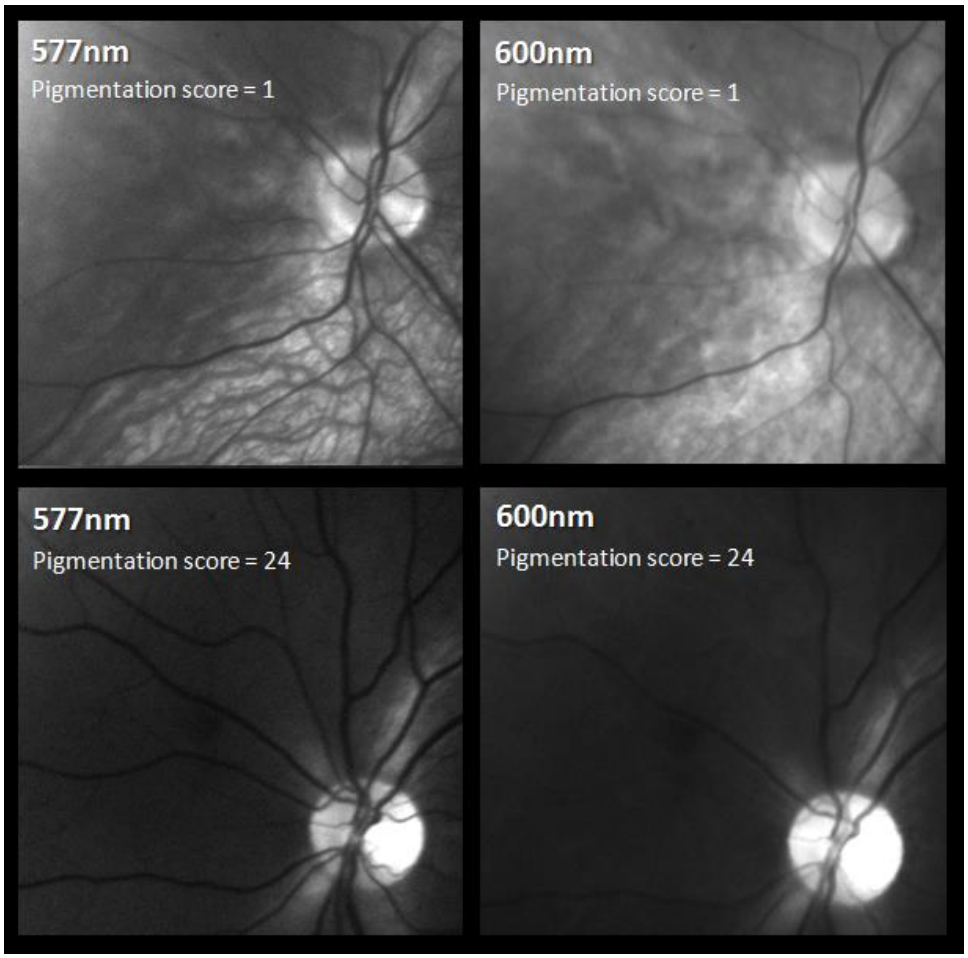

Figure 4-11. Retinal images two subjects with minimum pigmentation score (top) and maximum pigmentation score (bottom) at the 577 nm and 600 nm wavebands respectively. Choroidal vessels can only be seen in the subject with minimal pigmentation.

4.3.3 Experimental Procedure

Prior to imaging, pupils were dilated with 1% Tropicamide eye drops (*Bausch & Lomb*, *Chauvin Pharmaceuticals, Ltd*.) Arterial SO_2 was monitored throughout the study by a fingertip pulse oximeter (Biox 3740, *Ohmeda*). This pulse oximeter was selected due to its three second integration time, maximising temporal resolution for quantification of a TDOW. Earlobe pulse oximetry was not used due to its unreliability.[258,259] Image acquisition, hypoxic air inhalation, and pulse oximeter data were all synchronised by recording both the pulse oximeter display and room audio with a DSLR camera (D90, *Nikon*).

Subjects positioned their head in the fundus camera headrest and fixated their gaze on a fixation target situated approximately thirty degrees to the right of the subject. The left eye was chosen for ease of imaging and consistency between subjects. Before imaging began, subjects were given around one minute to adapt to the illumination light. Retinal video acquisition then started. A normoxia baseline measurement was recorded for approximately 30 seconds. Subjects exhaled for five seconds to evacuate air from their lungs and then inhaled the medical-grade hypoxic air mixture (5% Oxygen, 95% percent Nitrogen) [*BOC Gases*] orally from a Douglas bag via a single deep breath. Subjects subsequently held their breath for fifteen seconds. After fifteen seconds subjects resumed breathing room air normally. Video acquisition continued until 1 minute after the pulse oximeter indicated a return to normoxia (defined as 95 - 100% SO_2). Total time of retinal dataset acquisition was approximately 180 seconds.

This procedure was repeated to produce up to five TDOW retinal video datasets per subject. The number of repeated sequences depended on how comfortable the subject was with duration of the imaging procedure. To provide a control measurement, a dataset was recorded where subjects inhaled room air instead of the hypoxic air mixture.

4.3.4 Dataset inclusion criteria

To maximise the chances of a good ORCA sequence, only retinal video sequences which met the following inclusion criteria were analysed:

1. Minimal corneal glare
2. Minimal eye movement
3. >5% ΔSO_2 as measured by the fingertip pulse oximeter

4.4 Pilot study results

4.4.1.1 Subject demographics

Subject demographics are summarised in Table 4-2.

Table 4-2. Subject demographics.

	Subject										
Parameter	**A**	**B**	**C**	**D**	**E**	**F**	**G**	**H**	**I**	**J**	**K**
Gender (M/F)	M	F	M	F	M	M	M	M	M	M	M
Age (years)	34	21	54	25	24	23	25	24	20	26	27
IRIS pigmentation (1 = least, 24 = most)	22	22	6	10	4	24	11	20	1	21	10

4.4.2 Average intensity ratio

The average intensity ratio of retinal images at baseline normoxia was strongly correlated with retinal pigmentation score (correlation = -0.88): see Figure 4-12. This is expected as increasing melanin will result in a greater increase of absorption at the 577 nm waveband than the 600 nm waveband.

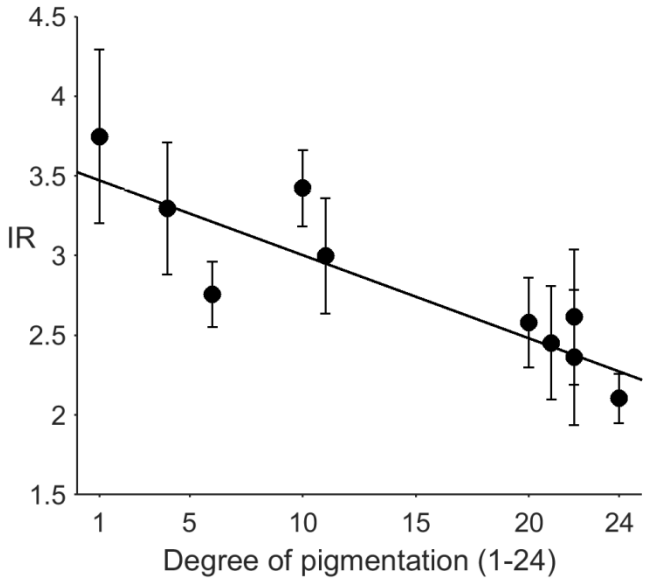

Figure 4-12. Average intensity ratio (IR) of a single retinal image of each subject normoxia vs. retinal pigmentation score (1 = minimum pigmentation, 24 = maximum pigmentation). Correlation = -0.88. Error bars are ± the standard deviation of the pixel-by-pixel intensity ratio of each image.

4.4.3 Observation of transient deoxygenation waves

Observable TDOWs were generated in all included datasets and were observed as a transient decrease in arterial SO_2 as measured by the fingertip pulse oximeter. TDOWs resulted in a transient decrease in arterial SO_2 between 5 and 20% (see Table 4-3).

TDOWs were observed in the retina as a transient decrease in IR prior to decrease in pulse oximeter SO_2. This indicates that the lung-to-eye circulation time is less than the lung-to-finger circulation time. The minimum IR due to the TDOW was typically observed in the retina about 30 seconds after hypoxic air inhalation and was recorded by the fingertip pulse oximeter around 45 seconds after hypoxic air inhalation, returning to normoxia levels at ~ 1 minute after hypoxic air inhalation. The exact timing of TDOWs varied considerably between subjects and repeat inhalations; it is assumed that this will be dependent on factors such as lung capacity, subject seating position, and lung to retina/finger circulation distance. Subjects generally reported no adverse effects due to the transient deoxygenation waves. In some instances, subjects reported a very slight sensation of light-headedness which lasted for less than five seconds and approximately coincided with the time when a decrease in IR was observed in the retina.

Figure 4-13 shows example TDOWs in two subjects. Subject A inhaled the hypoxic air mixture for fifteen seconds whilst subject B inhaled for thirty seconds; the duration of the TDOW can be seen to be longer in duration in subject B as a result. In both subjects the maximum of the TDOW is recorded in the retina approximately 40 - 60 seconds prior to the maximum TDOW recorded by the fingertip pulse oximeter

Table 4-3. Number of TDOWs observed and ORCA sequences produced.

	Subject										
Parameter	**A**	**B**	**C**	**D**	**E**	**F**	**G**	**H**	**I**	**J**	**K**
# of datasets included	3	5	3	3	3	4	3	3	4	1	-
# of TDOWs observed	3	5	3	3	1	4	3	3	1	-	-
Average fingertip SO_2 decrease (%)	5	21	9	13	10	19	15	7	10	12	-
# of complete ORCA Sequences	**1**	**4**	**1**	**1**	-	-	-	-	-	-	-
# of partially complete ORCA sequences	**1**	-	-	-	**1**	-	**1**	**3**	**1**	-	-

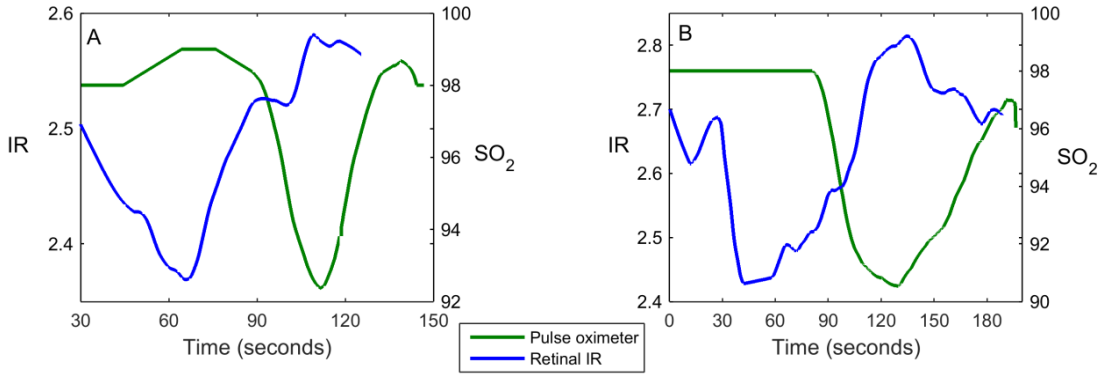

Figure 4-13. Transient deoxygenation waves observed in two subjects. In dataset A, a subject inhaled the hypoxic air mixture for 15 seconds. In dataset B, the hypoxic air mixture was inhaled for 1 minute, and as such, the TDOW was longer duration.

4.4.4 Complete and partially complete ORCA sequences

A *partially complete ORCA* sequence is defined as an ORCA sequence that shows a filling of all retinal and choroidal vessels at some point in the ORCA sequence, but sequential vessel filling was not observed due to omitted frames or artefacts. Seven partially-complete ORCA sequences were produced (subjects A, E, G, H, I).Figure 4-14 shows partially complete ORCA sequence compared to a retinal image. The ORCA image clearly visualises all retinal blood vessels.

For purposes of reporting results, a *complete ORCA sequence* is defined as a ORCA sequence where sequential vessel filling can be clearly observed. Of the 26

datasets where a transient deoxygenation wave was observed, seven complete dye-free angiography sequences were produced (subjects A, B, C, D).Three complete ORCA sequences in different subjects are shown in Figure 4-15.

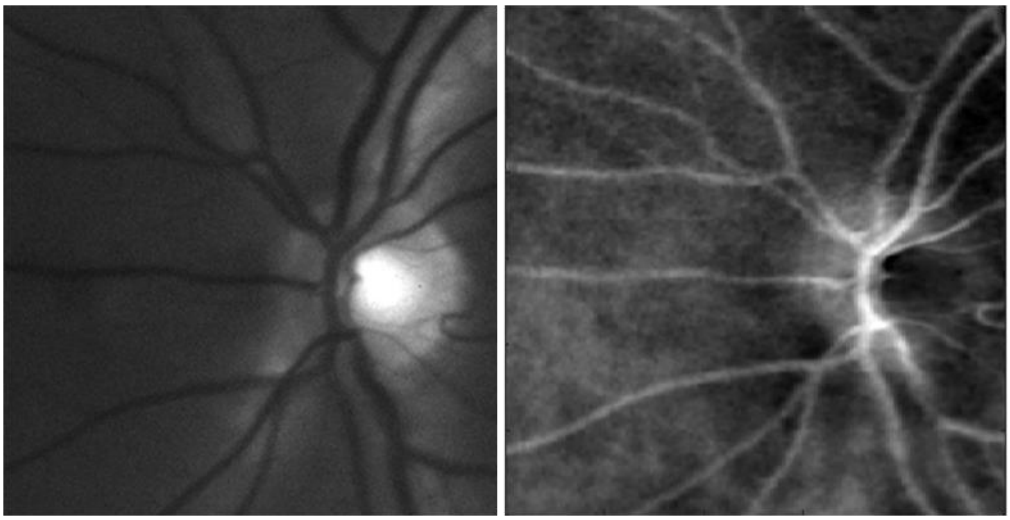

Figure 4-14. (Left) retinal image of subject H acquired at the 577 nm IRIS waveband. **(Right)** Corresponding late-phase ORCA image. Note that the bright region of the optic disk in the 577 nm image corresponds with the dark region in the ORCA image.

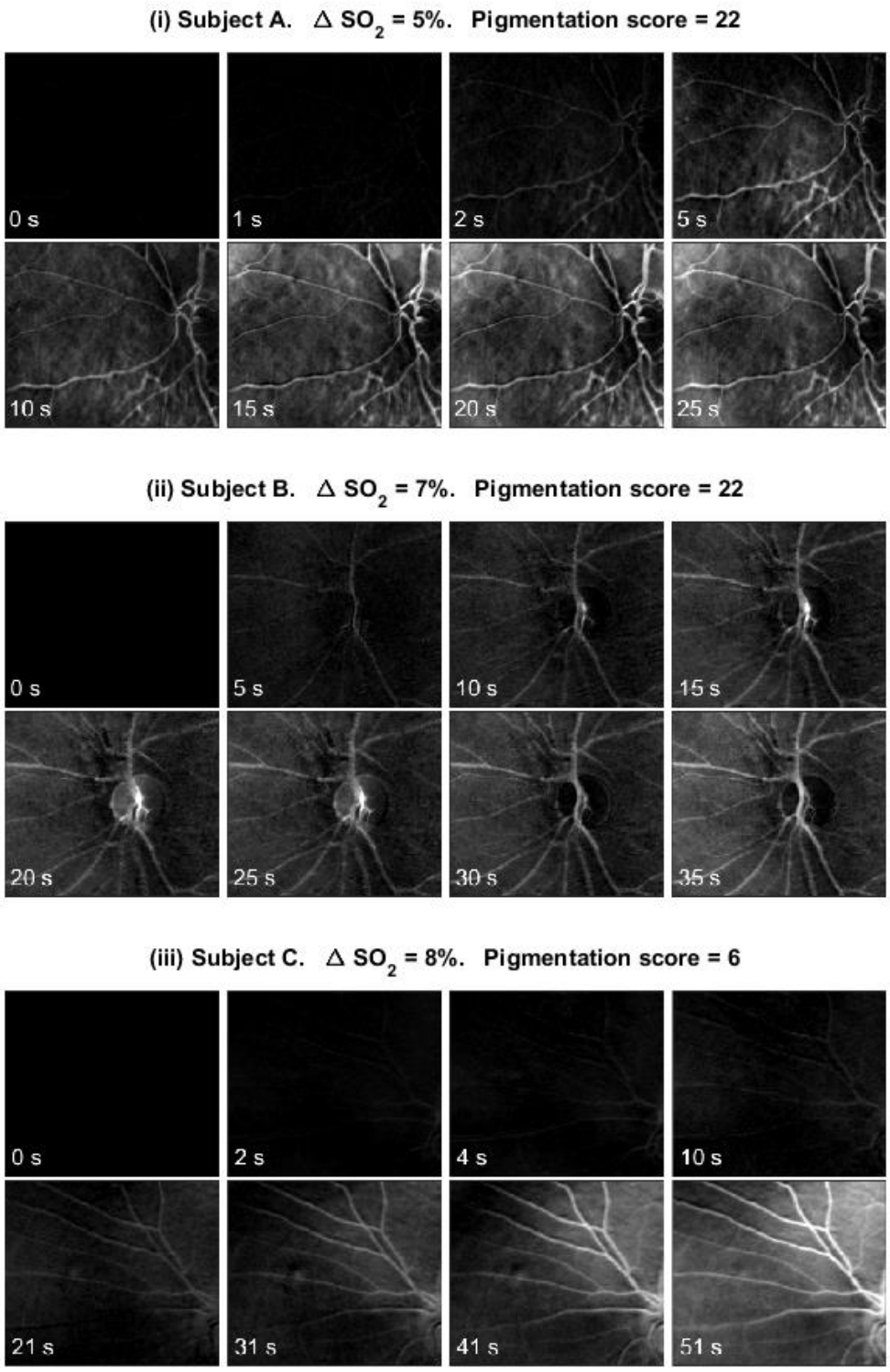

Figure 4-15. Complete ORCA sequences observed in three subjects.

4.4.5 Repeated measurements

Only one subject (subject B), successfully produced repeated ORCA sequences. These repeated sequences are shown in Figure 4-16, where good reproducibility of blood vessel visualisation can be seen. However the optic disk appears as different brightness in each sequence; this is likely an artefact, possibly due to motion artefacts or due to a change in intensity ratio due to spectral contamination from surrounding tissue. However, the exact cause of this artefact has not be ascertained.

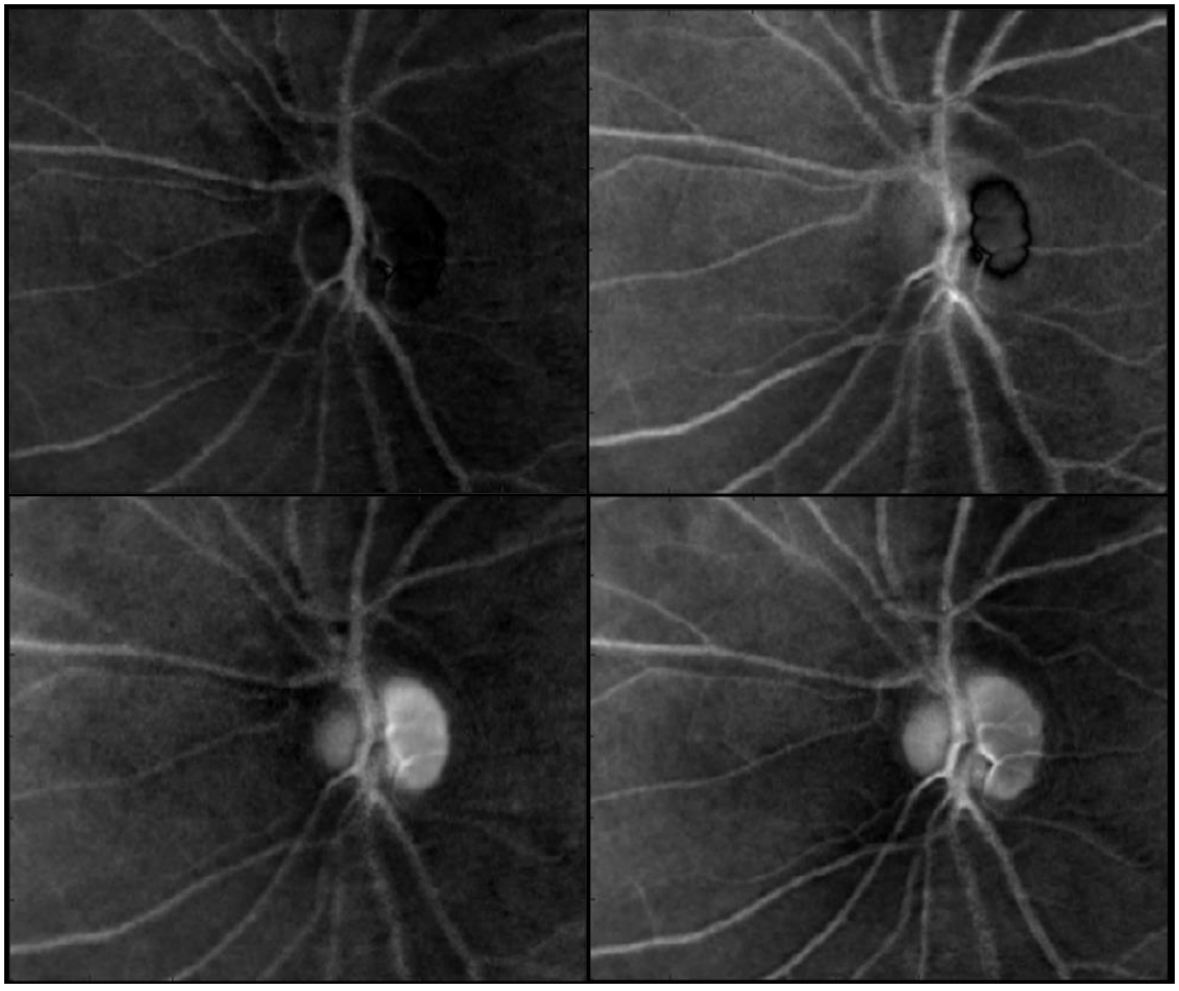

Figure 4-16. Four repeated late-phase ORCA sequences in subject B.

4.4.6 Sequential vessel filling

To measure how fast blood vessels appear to fill, arteries and veins were manually tracked and the greyscale intensity of vessels vs. time was calculated. The results were then plotted against time from the ORCA sequence null frame. Figure

4-17 shows an ORCA sequence with clear sequential arterial and venous filling. However, Figure 4-18 shows another ORCA sequence in the same subject, but sequential vessel filling is less distinct in this dataset, possibly due to sub-optimal choice of ORCA reference frame. Figure 4-19 and Figure 4-20 show similar datasets to Figure 4-18 in other subjects. In all datasets, choroidal filling consistently lags behind retinal vessels filling. These results indicate that ORCA can reveal sequential vessel filling, but also that measurement of vessel filling can be marred by spurious motion artefacts or sub-optimal reference frame selection.

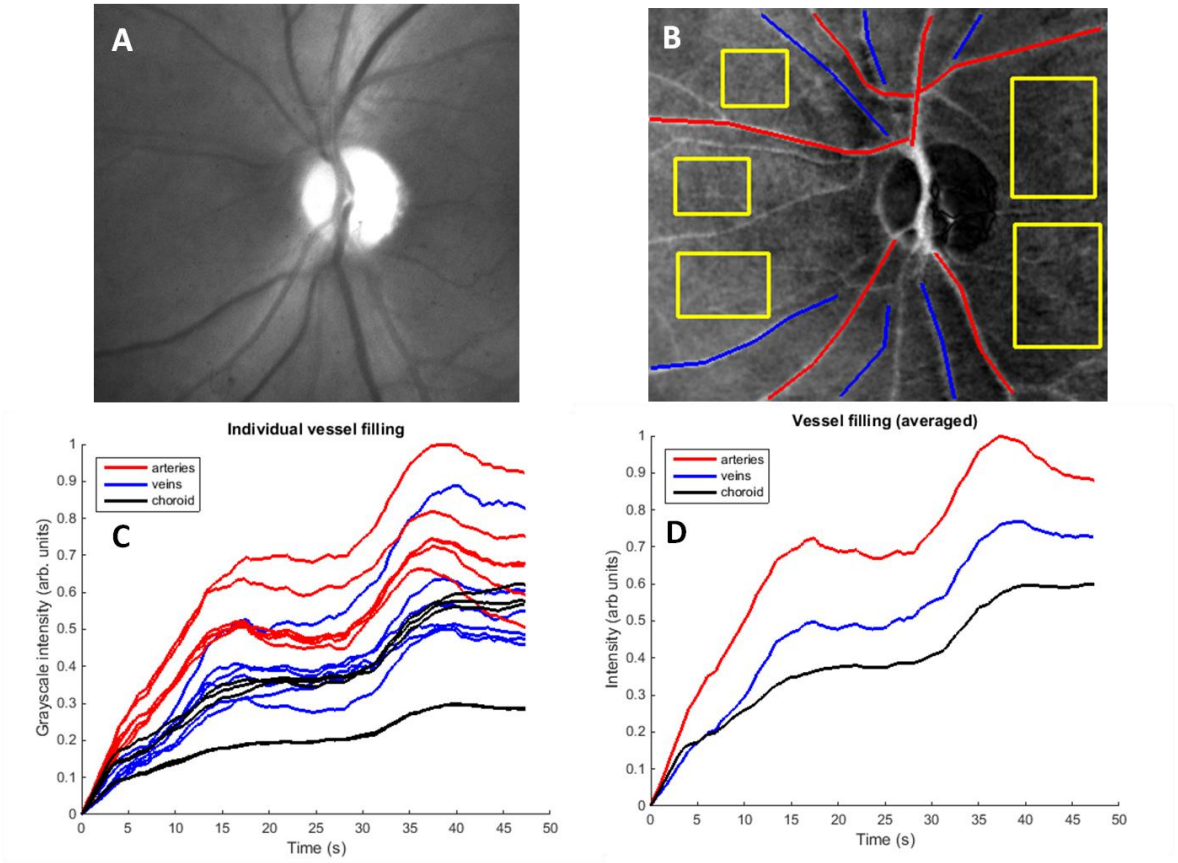

Figure 4-17. Sequential vessel filling observed in subject B. **(A)** 600 nm retinal image. **(B)** Vessels tracked for analysis overlaid above final ORCA frame. **(C)** Average greyscale intensity of individual vessels vs. time from reference frame. **(D)** Greyscale of all vessels, averaged by type, vs. time from reference frame. **Key:** (red) arteries, (blue) veins, (yellow boxes) choroid regions. Arteries fill before veins and the choroid.

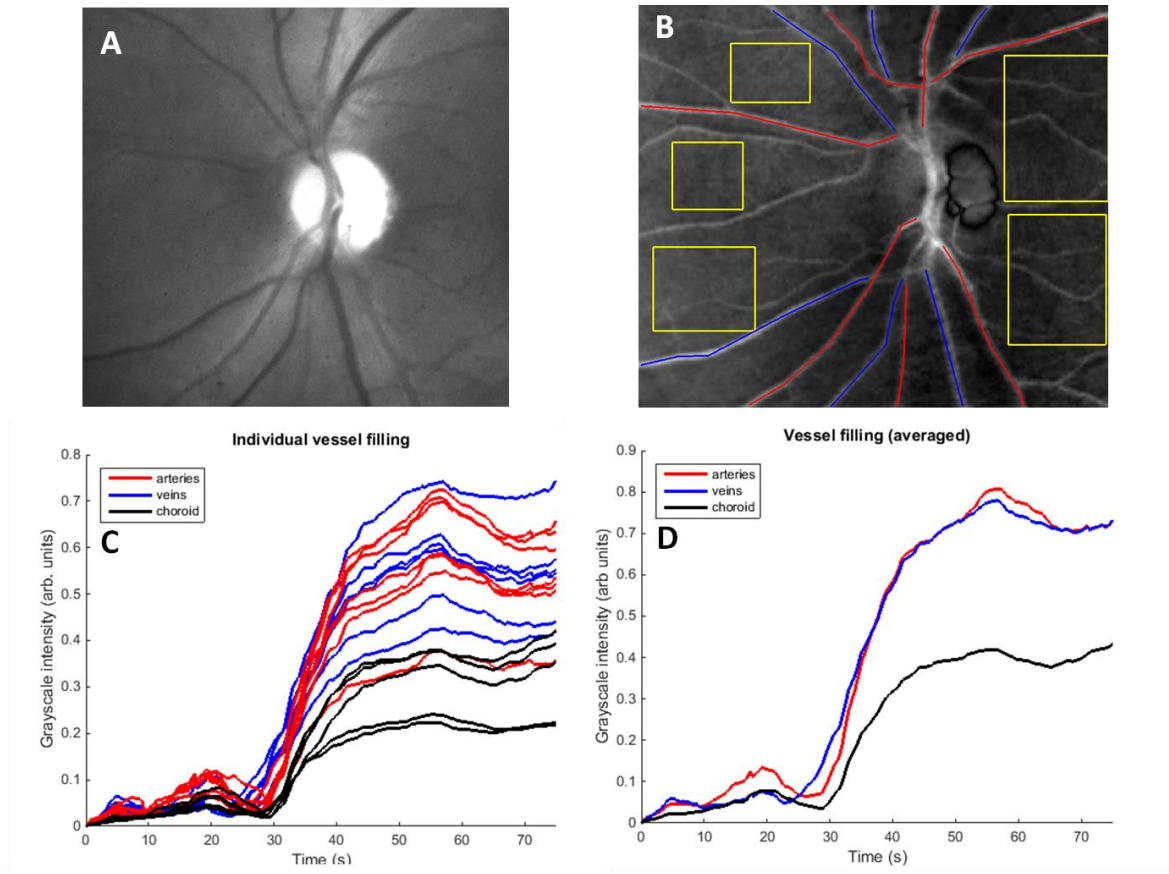

Figure 4-18. Vessel filling in subject B. **(A)** 570 nm retinal image. **(B)** Vessels tracked for analysis overlaid above final ORCA frame. **(C)** Average greyscale intensity of individual vessels vs. time from reference frame. **(D)** Greyscale of all vessels, averaged by type, vs. time from reference frame. **Key:** (red) arteries, (blue) veins, (yellow boxes) choroid regions. Sequential filling in this dataset is less distinct than in the dataset in Figure 4-17 but the choroid can be seen to fill after the retinal vessels. In this dataset the subject held their breath for 30 seconds, producing a longer TDOW, and thus a duration from reference frame before intensity of vessels change.

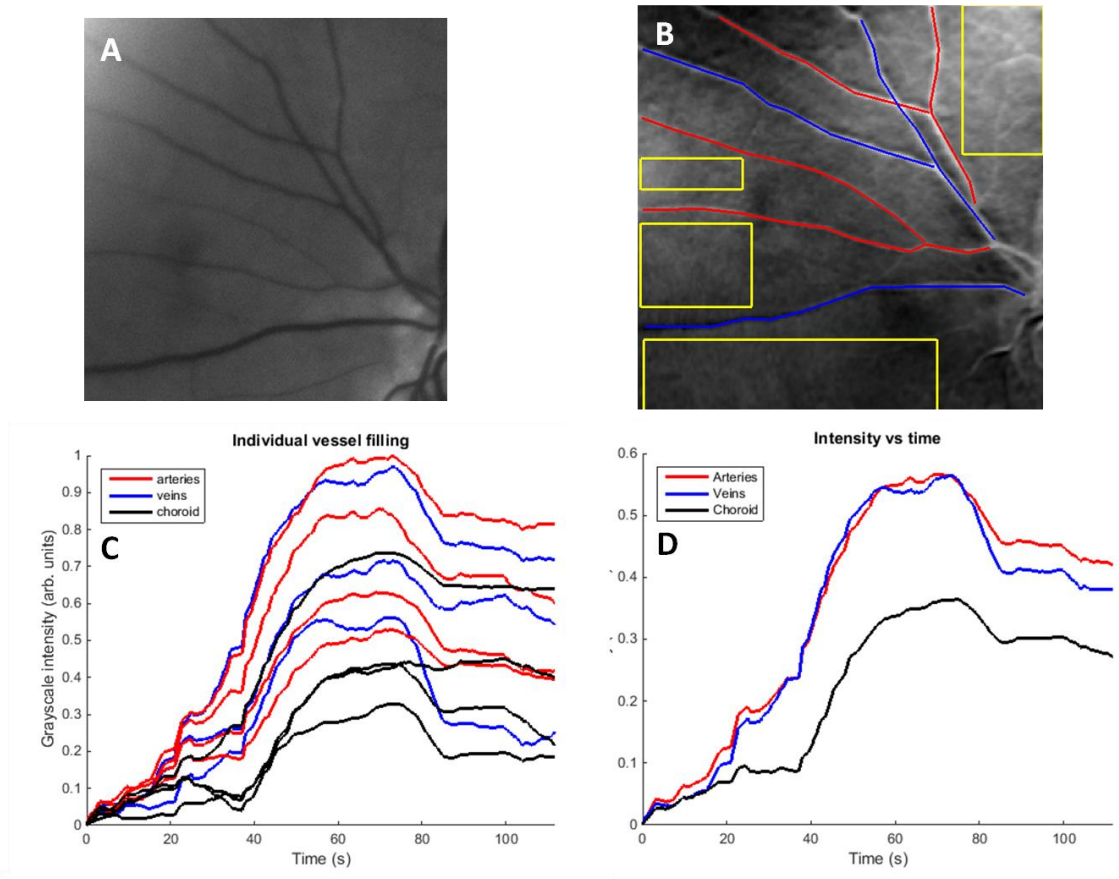

Figure 4-19. Vessel filling in subject C. **(A)** 570 nm retinal image. **(B)** Vessels tracked for analysis overlaid above final ORCA frame. **(C)** Average greyscale intensity of individual vessels vs. time from reference frame. **(D)** Greyscale of all vessels, averaged by type, vs. time from reference frame. **Key:** (red) arteries, (blue) veins, (yellow boxes) choroid regions. Sequential filling is less distinct than in the dataset in Figure 4-17 but the choroid can be seen to fill after the retinal vessels

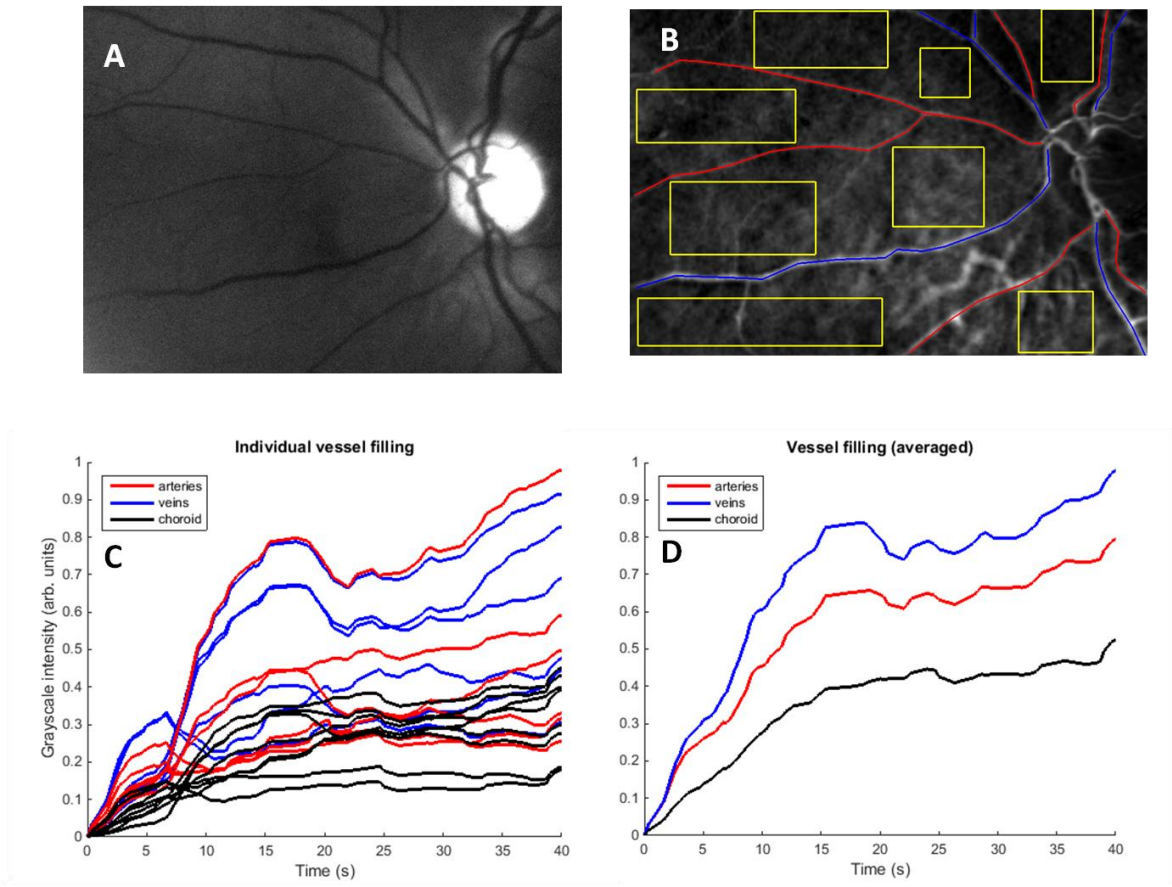

Figure 4-20. Vessel filling in subject A. **(A)** 570 nm retinal image. **(B)** Vessels tracked for analysis overlaid above final ORCA frame. **(C)** Average greyscale intensity of individual vessels vs. time from reference frame. **(D)** Greyscale of all vessels, averaged by type, vs. time from reference frame. **Key:** (red) arteries, (blue) veins, (yellow boxes) choroid regions. Arteries fill before veins and the choroid. Sequential filling is less distinct than in the dataset in Figure 4-17 but the choroid can be seen to fill after the retinal vessels. Veins fill before arteries, which may indicate spurious measurement (e.g. due to artefacts).

4.4.7 Laminar flow

Persistent laminar flow was observed in veins of Subject D (see Figure 4-21).

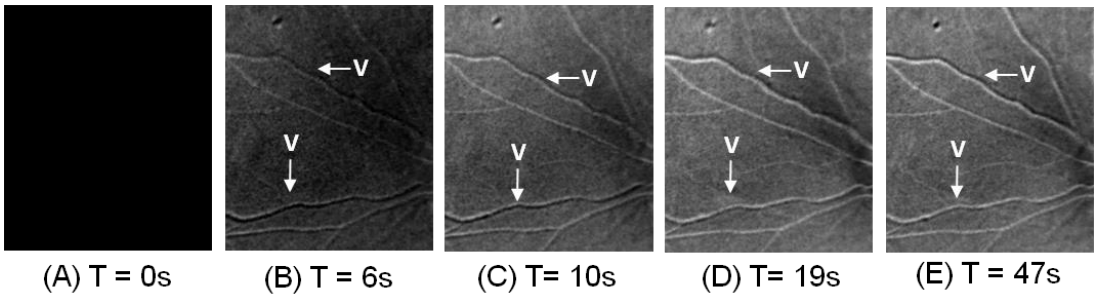

Figure 4-21. Persistent laminar flow observed in retinal veins of subject D. Veins are marked with 'V'. All other vessels are arteries. The circular object in top-left is an artefact caused by dust in the imaging system.

4.4.8 Control measurements and spurious artefacts

No TDOW was observed in control measurements (i.e. where room-air was inhaled instead of the hypoxic air mixture), instead a temporary increase in arterial SO_2 of 1 - 2% was recorded by the fingertip pulse oximeter, lasting around 30 seconds in duration. Attempts to produce ORCA sequences from control datasets did not produce ORCA sequences, but instead enabled the study of spurious artefacts, such as those shown in Figure 4-22. Increasing the number of frames averaged reduced apparent random variations but also extended the duration of temporary spurious artefacts observed.

Dust in the imaging system (see Figure 4-21) can cause spurious artefacts. Once the retinal video sequence is registered, any static dust in the imaging system will appear to move. This will change the intensity ratio in images thus appear as an artefact.

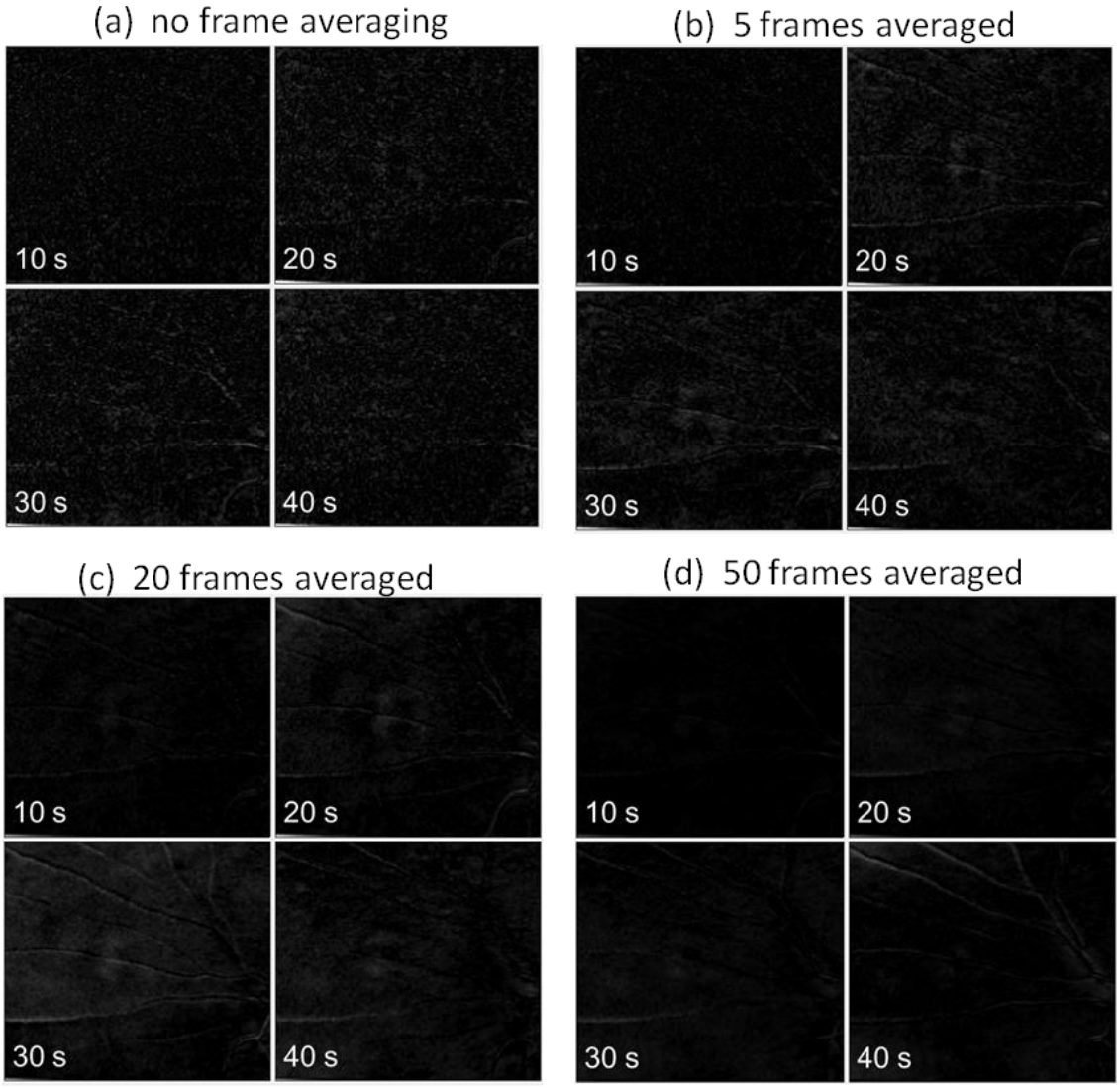

Figure 4-22. Frame averaging vs. prominence of spurious artefacts. As frames averaging increases, the random noise due to fluctuations in individual pixels decreases, but the spurious apparent appearance of vessels increases. Note that contrast was enhanced to increase the visibility of spurious artefacts.

4.5 Discussion

4.5.1 Factors influencing intensity ratio measurement

Several factors may influence the measurement of intensity ratio and may spuriously affect the ORCA process.

4.5.1.1 Motion

Motion of a subject's eye will alter measured intensity ratio because: (1) the illumination intensity ratio of the fundus camera inspection lamp is not spatially uniform; and (2) a different region of the retina will be imaged, altering optical path of light through tissue. Thus, motion will alter measured $\Delta IR(x,y)$ and cause spurious artefacts.

4.5.1.2 Pigmentation

Pigmentation (melanin) in the retina is contained within the retinal pigment endothelium, between the retinal and choroidal blood vessels. Absorption by melanin decreases with wavelength; melanin strongly absorbs blue and green wavelengths, but weakly absorbs red and infra-red wavelengths. Thus, in subjects with a high pigmentation score, it is expected that more red light will be absorbed than in subjects with a low pigmentation score. This was confirmed by observations that baseline intensity ratio was strongly negatively correlated with degree of retinal pigmentation (see Figure 4-12).

A high degree of pigmentation may be problematic for ORCA; in subject F (who had maximum pigmentation score), large TDOWs were recorded by the fingertip pulse oximeter, but minimal change in retinal intensity ratio was observed. Despite high-quality retinal video sequences and a large TDOW, no ORCA sequence was produced for this individual. It is also notable that recorded greyscale was lower for this subject due to high light absorption by retinal pigmentation.

4.5.1.3 Image misregistration

In this study, robust misregistration error-checking was not employed. However, image misregistration could produce spurious features which look like filled blood vessels. Such features are likely to be highly transient, with only one or two frames effected. However, increased duration frame averaging will result in longer duration

appearance of such spurious features. If robust misregistration checking is used in future to quantify accuracy of registration, then information can be gleaned from ORCA sequences with increased confidence.

4.5.2 Repeatability of results

Repeating *in vivo* ORCA results proved to be extremely challenging for two reasons: (1) some subjects found the imaging light intensity uncomfortable, and (2) ORCA is highly sensitive to motion induced artefacts. Due to these challenges complete ORCA sequences were only replicated in Subject B; these are shown in Figure 4-16. These repeat measurements show good reproducibility of blood vessel flow, however the optic disk appears as a different intensity in each sequence. The cause of this variability in optic disk appearance is yet to be ascertained.

Repeated measurement of vessel filling in this subject provided to be highly challenging. Whilst choroidal filling lagged behind retinal vessels in all subjects, sequential retinal arterial and venous filling was only seen clearly in a single dataset (Figure 4-17). This is because retinal vessel filling will result in a very small change in intensity ratio, which can be easily overwhelmed by small spurious artefacts, e.g. caused by random motion or glare.

Assessing the repeatability of ORCA in humans *in vivo* is extremely challenging. Alternative experimental methods are required to test the intrinsic repeatability of ORCA in better controlled experiments (e.g. phantoms or anesthetized animals).

4.5.3 Laminar flow

In FA, laminar flow is observed in retinal branching veins due to the multiple circulation paths of fluorescein through the retinal capillaries. Laminar flow was seen in a retinal branching vein by ORCA (see Figure 4-21). Laminar flow will only be visualised in ORCA if there is a significant SO_2 difference between separate blood streams within a branching vein; however, it is unknown how large this difference needs to be for laminar flow to be visualised.

The visualisation of laminar flow indicates several blood oxygen saturations flowing in a single vein. This may have implications for analysis of retinal oximetry, where it is assumed that only a single oxygen saturation flows within a vein. By identifying if a vein has multiple oxygen saturations within, it may be possible to

modify analysis methods accordingly, and thus improve the accuracy of venous oximetry.

4.5.4 Comparison of ORCA to Fluorescein Angiography

The key differences of features of ORCA and FA are summarised in Table 4-4.The main advantage of ORCA in comparison to FA is that ORCA does not require a semi-invasive intra-venous injection of mildly-toxic fluorescein dye. Intra-venous fluorescein injection is associated with risks of nausea (6% of patients), severe skin irritation (4% of patients), and even a small risk of death (1 in 220,000 chance).[236–239] In contrast, inducing the TDOWs required for ORCA appears to have minimal risk and consequences. However, the risk of inducing TDOWs in healthy and unhealthy subjects has yet to be studied.

A key feature of FA that ORCA cannot replicate is detection of vessel leakage. In FA, fluorescein molecules in blood can leak out of micro-haemorrhages. However with oximetric contrast, the majority of contrast agent (haemoglobin) is contained within RBCs, which are too large to leak from micro-haemorrhages.[239]

This study has demonstrated that ORCA is susceptible to motion-induced artefacts. FA does not have this issue. Further, ORCA requires computational processing, whereas FA does not.

Table 4-4. ORCA vs. FA.

	FA	ORCA
Intra-venous injection	✓	×
Mildly-toxic fluorescein	✓	×
Vessel filling	✓	✓
Laminar flow	✓	✓
Choroidal filling	✓	✓
Vessel leakage	✓	×
Computational processing	×	✓
Spurious motion artefacts	×	✓

4.5.5 Future work

4.5.5.1 Improvement to the fundus camera-based imaging system

The light levels of the imaging system were found to be somewhat uncomfortable for subjects; as a result, no ORCA sequences were produced in two of the eleven subjects and eye motion was induced in many of the other subjects. Thus, it would be desirable to reduce light intensity. However there is a trade-off between illumination intensity and frame-rate of videos. A decrease in illumination intensity could be achieved by waveband-matching illumination and imaging wavelengths, rather than using a broad-band illumination spectra. Alternatively, because precise oximetry is not required, frame-rates could be increased by imaging at two broad-band wavebands (green and red) by a simple two-wavelength imaging system. Another possibility to increase light-efficiency would be to image with unpolarised light. This would greatly increase light intensity reaching the detector, but doing so would result in stronger specular reflections from the cornea and additionally blood vessels will have a strong central reflex due to specular reflection. Another possibility would be to use, flash-illumination, which may be more comfortable for subjects. The rapid flash-duration would also serve to decrease motion artefacts, allowing a greater proportion of images to be included for ORCA analysis. However, to achieve a frame-rate > 1 Hz would require modification of the fundus camera flash lamp. It should be noted that "flicker illumination" (flash at 12.5 Hz) will increase metabolic demand of the retina and thus alter SO_2.[37]

4.5.5.2 Improvements to image quality checking

In this study, the detection of poor-quality retinal images was performed manually. This was a time consuming process, requiring 30 - 45 minutes for a typical 3-minute retinal video sequence. Automating detection of low quality images could greatly reduce operator time required to produce an ORCA sequence. To this end, an undergraduate project was conducted by Liam Mitchell. This projected investigated the use of a variety of image metrics to classify images as either good quality or low quality. Robust classification of poor-quality frames proved to be challenging, with some human input still required. However the total time to classify images in a dataset was reduced to approximately five minutes, indicating that this automation

technique may be highly promising. Full details of Liam's work can be found in his honours project report on the subject.[260]

4.5.5.3 Potential improvements to temporal video registration procedure

Our temporal image registration method was based on automatic feature detection, with no human input. This method worked well in images with minimal corneal glare and particularly well in subjects where choroidal vessels were visible. However, registration proved to be significantly more challenging in subjects with a high degree of pigmentation because fewer features were available for identification.

In future, more sophisticated image registration strategies could be adopted. Strategies such as robust vessel tracking, quorum-validation, and human-computer hybrid feature matching could be used.

4.5.5.4 Improving the robustness of computational ORCA analysis

Robustness of computational ORCA processing could be improved in several ways. Firstly, vessel-fitting algorithms could be used to measure changes in vessel transmission; this approach would be more robust than measuring the simple change in intensity ratio. However, this would be much more computationally intensive and not applicable to the areas outwith large retinal vessels.

Secondly, spectral classification of several wavelengths would perhaps be more robust than intensity ratio measurements and allow for identification and exclusion of artefacts such as glare. This could be implemented in a similar approach to the spectral unmixing presented by Fernandez-Ramos et al., (2014).[11]

Thirdly, the optic disk could perhaps provide an *in vivo* reflectance calibration target. However, the optic disk may not be suitable for this due to vascularisation, spectral contamination by fundus reflectance, and the non-uniform illumination intensity ratio of the fundus camera.

4.5.5.5 Image subtraction reference frame selection

Choice of reference frame for image subtraction is currently semi-subjective; the reference frame was mainly determined by which point maximises the change in intensity ratio, however in some sequences the shape of the TDOW was flat-bottomed, so there were several frames which maximised ΔIR. Thus, trial and error

was used determine which reference frame enabled the generation of a good ORCA sequence. A strategy for automatic and optimal reference frame selection is unclear.

4.5.5.6 Further testing of ORCA

This proof-of-concept study demonstrated that ORCA is feasible *in vivo* in the human retina. However, subject discomfort and eye motion made repeat measurements extremely challenging. Subject discomfort could be decreased by making various improvements to the imaging system outlined in Section 4.5.5.1. Subject eye motion could be decreased by better control of a subjects head by using an anchor device such as a bite-ring. Also, the hypoxic air mixture delivery system could be improved to reduce subject movement; the current system was simply a tube with a valve that subjects inhaled from.

The intrinsic repeatability of ORCA could be better investigated in well controlled measurements such as in phantoms or anaesthetised animals. Improvements to bio-mimicking retinal phantoms would enable study of vessel filling and laminar flow without motion induced artefacts.[124,261]

The ability of ORCA to detect lack of blood flow (e.g. due to vessel occlusion) has not yet been demonstrated. The minimum change in SO_2 required to produce an ORCA sequence is also currently unknown. Both of these questions could investigated incrementally by first of all imaging a simple dynamic *ex vivo* blood phantom with a variable and flowing SO_2 blood supply (e.g. from two reservoirs of known oxygenation).[262] Minimising the change in SO_2 required would minimise the risks of *in vivo* application of ORCA.

Inducing TDOWs for medical diagnostic purposes is an entirely new concept. It is currently assumed that subject lung capacity, seating position, inhalation rate and breath hold duration will alter the magnitude, duration, and overall shape of the TDOW. Better understanding of the variability and characteristics of TDOWs could benefit ORCA and also potentially enable time-of-arrival (TOA) studies using TDOWs. TOA of TDOWs could be used to probe carotid artery occlusion, which is a major risk factor for stroke (see Section 6.1).

4.5.5.7 Alternative imaging modalities for ORCA

The retinal fundus camera with IRIS was sufficient to demonstrate the concept of ORCA in human retinal imaging. However, there are alternative imaging methods/modalities which could be utilised for ORCA measurements, and which offer unique advantages. For ORCA, a modality must be capable of rapid acquisition (< 1 Hz) of blood vessels images at two or more wavelengths.

The most promising modality for retinal ORCA is scanning laser ophthalmoscopy (SLO). SLO provides several advantages in comparison to retinal fundus cameras, including a larger FOV, improved vessel contrast, lower light exposure levels, and the potential for stabilised retinal imaging with adaptive optics.[263] Further, no dilation of pupils is required and SLO imaging will produce minimal corneal glare. Commercially-available multispectral SLOs have already been used for retinal oximetry of adults and infants (see Section 2.1.2.3).

Eye motion artefacts could be avoided entirely by developing contact lens-mounted imaging systems. Several contact-lens fundus reflectometry systems were developed in the 1970s[264] and no injuries by their use on 500 human subjects was reported.[265] However the design of such a system would be highly challenging.

Multi-spectral photoacoustic tomography (MS-PAT) (see Section 2.2.2) could be used to provide deep-tissue ORCA. This could be advantageous for applications such as tumour development where metabolic rate could be estimated from combined oximetry and blood flow measurements.[266] However, PAT requires high-energy laser pulses, which makes it unsuitable for non-invasive retinal ORCA.

4.5.5.8 Conditions that may affect ORCA

It is necessary to consider conditions that may affect the application of ORCA in subjects. For example, the spectral transmission of the lens of the eye in patients with cataracts will be altered. This may mar the observation of ΔIR by reducing apparent spectral contrast. Patients with sickle-cell anaemia may present multiple challenges, namely abnormal haemoglobin functionality and abnormal haemoglobin distribution in diseased red blood cells.[22] This may alter the contrast achieved with ORCA.[266] Further, inducing a TDOW in patients with sickle-cell anaemia will present heightened risk which would need to be considered in any ethical approval.

4.6 Conclusions

This pilot study has proven that ORCA is a feasible non-invasive angiography technique. ORCA revealed sequential vessel filling and laminar flow; features which have only previously been visualised by using FA. This study did, however, demonstrate that the current implementation of ORCA is highly sensitive to spurious artefacts induced by motion of the subject being imaged.

In future, subject motion could be decreased by various improvements to the imaging system, improved subject anchoring (e.g. with a bite-ring), and improvements to the hypoxic air mixture delivery system. ORCA could also be tested in phantoms and/or anesthetized animals, where motion can be controlled more effectively than in human subjects.

Further, the image registration and procedure for ORCA could be improved; potentially increasing robustness of ORCA. Considerable work can be done in future to robustly test ORCA, including studies in phantoms and in anesthetised animals. Whilst it is fully expected that ORCA will be able to detect a lack of blood flow (e.g. due to vessel occlusion), this too needs to be directly assessed. Questions remain about the minimum SO_2 perturbation required to create an ORCA sequence and the minimum SO_2 difference required to visualise laminar flow in branching retinal veins.

This study implemented ORCA with a multispectral fundus camera, but ORCA could be implemented with a SLO, which could potentially increase FOV and contrast in ORCA sequences, as well as reduce retinal illumination intensity when compared to fundus camera imaging. Implementing ORCA with photoacoustic tomography could also enable non-invasive deep-tissue angiography.

5 Rat spinal cord oximetry

Summary: *this chapter describes the development and implementation of a multispectral microscope for in vivo oximetry of the spinal cord dorsal vein of rats. The development and testing of this multispectral microscope is described. The microscope is applied to oximetry in the dorsal vein of rats with the EAE disease model of multiple sclerosis (MS) and also to healthy controls. Results show that rats with the EAE disease model of MS have lower venous SO_2 than healthy controls, but arterial SO_2 is similar. This indicates that oxygen extraction by spinal cord tissue is increased in the EAE disease model of MS compared to healthy controls.*

Additional disclaimer: *as stated in the acknowledgments, this work as carried out collaboratively. All animal handling was done by Andrew Davies and Roshni Desai, who are appropriately licenced by the UK Home Office. Javier Fernandez-Ramos and Marieke van der Putten developed the multispectral oximetry algorithm. Marieke van der Putten contributed to analysis of final data. Data and figures provided by her are acknowledged where appropriate.*

Additional note: *part of this work has been submitted to the journal 'Physiological Measurement'.*

5.1 Introduction

5.1.1 Motivation and aims

Multiple Sclerosis (MS) is an auto-immune disease which causes inflammation in the nervous system; it is a debilitating disease that affects over 100,000 people in the UK alone, severely impairing their mobility and quality of life.[267] A recent study by Davies et al., (2013)[10] demonstrated that hypoxia in spinal cord tissue correlates strongly with the severity of the experimental auto-immune encephalomyelitis (EAE) rat disease model of MS; indicating that the supply of oxygen to spinal cord tissue is altered. However, it is not clear how EAE may alter the spinal cord blood supply.

The aim of this research was to develop a multispectral microscope (MSM) and complimentary oximetry algorithm to provide quantitative oximetry in the spinal cord dorsal vein of both healthy and EAE disease model rats.

5.1.2 Anatomy of the spinal cord

The spinal cord is part of the central nervous system, connecting the brain and peripheral nervous system. Normal function of the spinal cord is essential for functions controlled by the nervous system, such as movement and sensory feedback. Thus, disruption to the function of the spinal cord can be severely debilitating.

The spinal cord is approximately cylindrical in cross-section [t] and consists of grey and white matter. The grey matter is located in the interior of the spinal cord, whist the white matter surrounds the grey matter. Both the white and grey matter consist of a variety of neural cells of different functions. In the centre of the spinal cord is the central canal, which contains cerebrospinal fluid. The white tissue is surrounded by three protective membranes (the meninges): the pia mater, the arachnoid mater, and the dura mater (see Figure 5-1 and Figure 5-2). The white tissue is further protected by the vertebra of the backbone.[251]

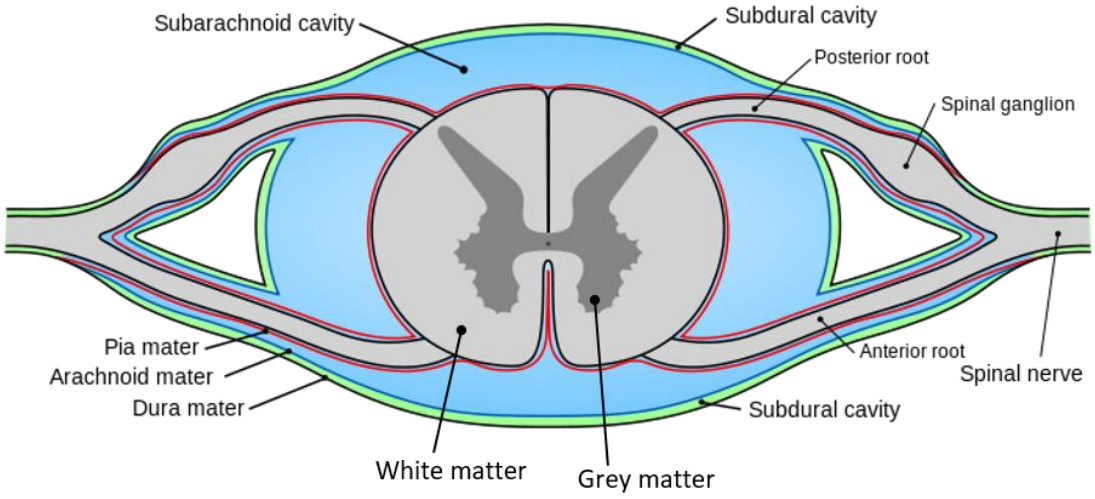

Figure 5-1. A cross-sectional representation of the spinal cord showing the various tissue layers.[u]

[t] This is a physicist's approximation.

[u] Figure in the public domain, reproduced from Wikimedia Commons.[299]

The blood supply to the spinal cord (see Figure 5-2) consists of a variety vessels arranged around the circumference of the spinal cord, with smaller perforating vessels supplying the white and grey matter.[268] In rats, the dorsal vein is the only blood vessel that can be reliably exposed for imaging with non-lethal surgery.

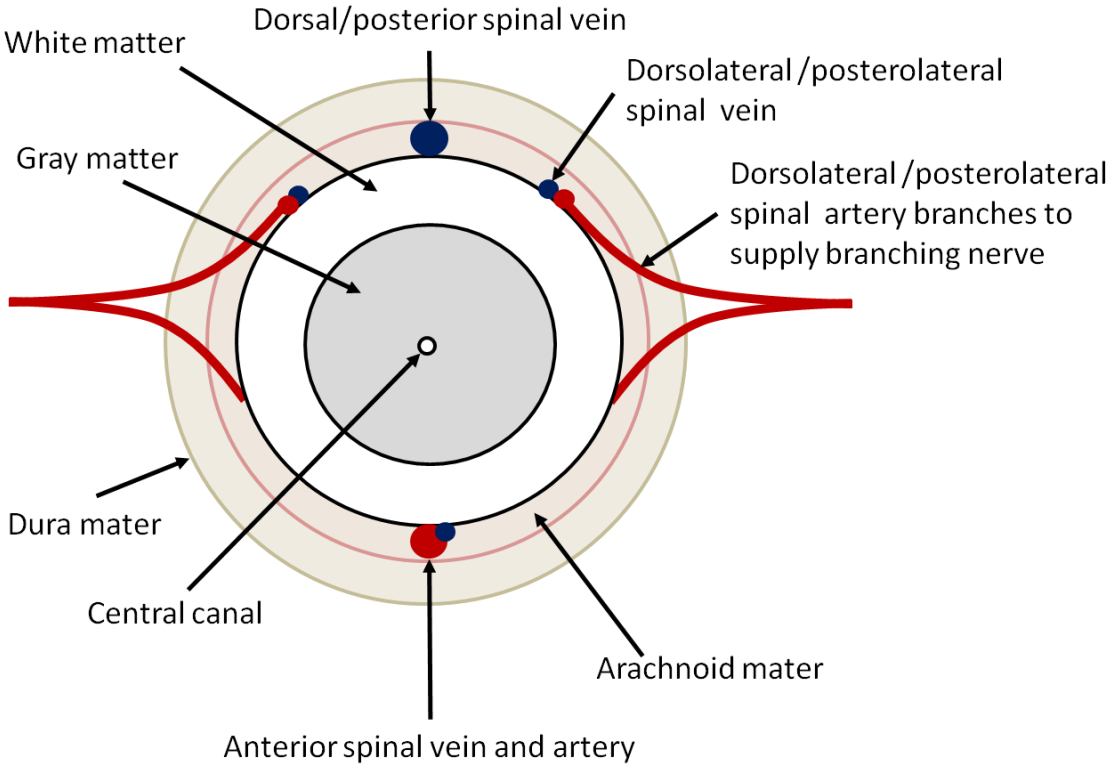

Figure 5-2. A highly simplified cross-sectional representation of the spinal cord and its associated major blood vessels.

5.1.3 A review of prior dorsal vein oximetry studies

The only study of oximetry of the dorsal vein was reported by Figley et al., (2013),[165] who utilised a commercial photoacoustic tomography system to estimate dorsal vein SO_2 in a single rat at normoxia (21% FiO_2) and hypoxia (7% FiO_2) conditions. They reported an estimated venous SO_2 of ~ 45% at normoxia, decreasing to ~ 20% at hypoxia. These estimated venous SO_2 values are somewhat lower than the typical range of 55 - 70% venous SO_2 expected in the human retina (a region of notably high metabolic demand).[12,105] Further, calibration photoacoustic tomography of the system was not reported and no further validation of measurements was conducted. These results validate that decreasing FiO_2 results in a decrease in venous spinal cord SO_2, but the reported absolute SO_2 values

cannot be used as a reliable reference for comparison of the results presented in this chapter (see Section 5.5.2).

Other studies have used multispectral imaging and non-imaging light-reflectance spectroscopy to monitor changes in Hb and HbO_2 concentration in the spinal cord due to electrical stimulus. However, absolute SO_2 values were not reported.[269,270]

Motion due to respiration is a significant challenge for functional dorsal vein imaging. However, this can be minimised by careful application of mechanical stabilisation. Cardotte et al., (2012) used two pairs of forceps to stabilise the spinal cord and reduce motion due to breathing and the heart beating.[271] Davalos et. al. (2012) used a custom-built stabilisation device consisting of four clamps to enable high resolution two-photon microscopy of blood vessels and glial cells in the spinal cord of mice.[272]

5.2 Multispectral microscope (MSM)

5.2.1 Design requirements

Oximetry of the spinal cord dorsal vein of rats is a challenging prospect. The dorsal vein has to be surgically exposed for imaging, so an imaging system must provide reasonable working room for surgical sutures and general access. Further, a field of view of several millimetres is required to maximise the number of blood vessels that could be potentially analysed. Further, to provide near-optimal quantitative absolute oximetry in a wide range of vessel sizes, the MSM has to be capable of imaging across a large part of the visible wave range (~ 500 – 700 nm).

Two MSM configurations are described in this chapter. Both designs have identical illumination, imaging, and wavelength filtering-optics, but had different detectors. The first configuration (the Mark 1 MSM) utilised a cooled scientific CCD detector, but this detector eventually malfunctioned, necessitating the development of a second configuration (the Mark 2 MSM) which utilised a readily-available consumer digital SLR CMOS detector. An improved control GUI was also implemented for the mark 2 MSM.

5.2.2 Mark 1 Multispectral microscope

The Mark 1 MSM (shown in Figure 5-3 and Figure 5-4) was assembled from a variety of off-the-shelf components. Illumination was provided by a white LED (MWWHL3, *Thorlabs*) with a collimator lens (COP-5A, *Thorlabs*) controlled by a 4-channel driver (DC4100, *Thorlabs*). A simple convex lens served as a condenser for illumination, which was further focused on the target by the objective lens. The microscope objective was a reversed SLR lens (AF Nikkor 50 mm, *Nikon*) with aperture set to 2.8 and focus set to infinity. Focus was adjusted by manual translation of the SLR lens with a translation stage. The working distance of this lens was ~ 50 mm, with a FOV of ~ 4.1 mm x 2.6 mm ; this proved to be clearly capable of resolving all inner lines of a Siemen's star target (7.14 line pairs per mm) (see Figure 5-6).

A pellicle beam splitter (CM1-BP145B1, *Thorlabs*) was used to combine the illumination and imaging paths; glass cube beam splitters were found to produce ghosting effects. Spectral filtering was provided by an electronically-controllable liquid crystal tuneable filter (LCTF) (VIS-7-HC-20, *Varispec*), incrementable between 400 nm and 700 nm in 1 nm increments. Orthogonal polarisation imaging was achieved by polarising the illumination light with a linear polariser (LPVISE200-A, Thorlabs) orientated orthogonally to the polarisation axis of the LCTF. This ensured that only light which had been multiply scattered through tissue was imaged.[216]

A cooled scientific CCD (sCCD) (Retiga 4000R, *Qimaging*) was used as the detector. Peak quantum efficiency of the sCCD was ~ 550 – 580 nm.[273] Images were saved in uncompressed 12-bit .TIFF format. Image sequences could be acquired rapidly because the sCCD detector utilises a uses a high data-throughput Firewire connection to read out images rapidly. The maximum image read-out of the sCCD detector was ~ 4 frames per second (data transfer rate ~ 40 MB/S, with an uncompressed image size of ~ 10 MB).

A custom LabVIEW control graphic user interface (GUI) was created to control MSM image acquisition in an automated manner. This GUI controlled the LCTF and sCCD. Details of the final control GUI developed can be found in Section 5.2.7.

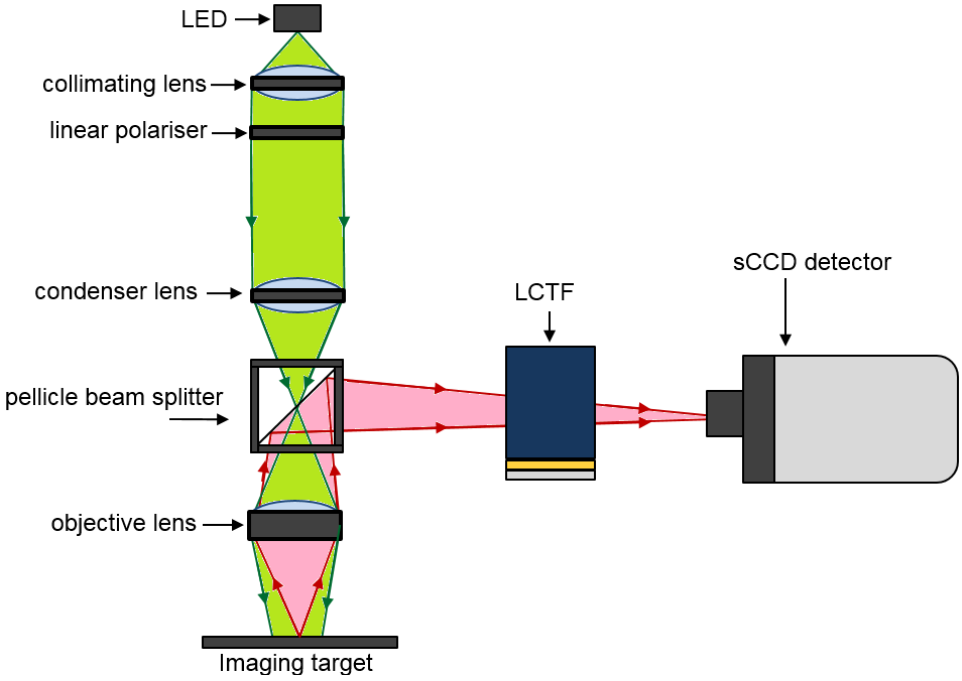

Figure 5-3. Basic schematic of the mark 1 MSM. The Illumination path is highlighted as green, and imaging path is highlighted as red.

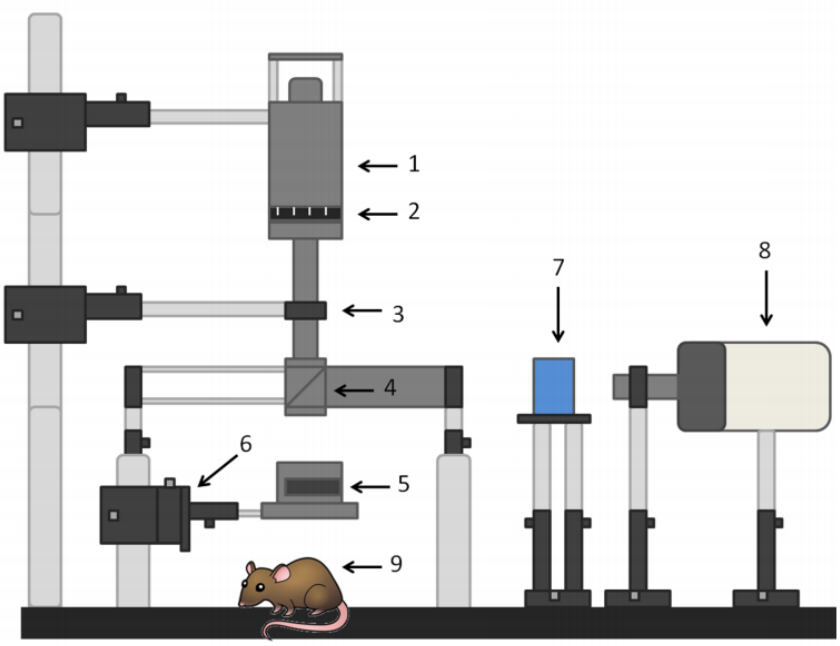

Figure 5-4. Representation of the Mark 1 multispectral microscope set up. 1. White LED with collimator; 2. Linear polariser; 3. Convex condenser lens; 4. Pellicle beam splitter; 5. Objective lens (reversed SLR lens); 6. Translation stage for focus adjustment; 7. LCTF; 8. sCCD detector; 9. Imaging target.

5.2.3 Mark 1 MSM performance

The spectral filtering of the LCTF was tested by measuring transmitted light with a spectrometer (HR4000, *Ocean Optics*) at key wavelengths between 500 nm and 630 nm. The central wavebands measured agreed with the user-specified wavebands (see Figure 5-5).

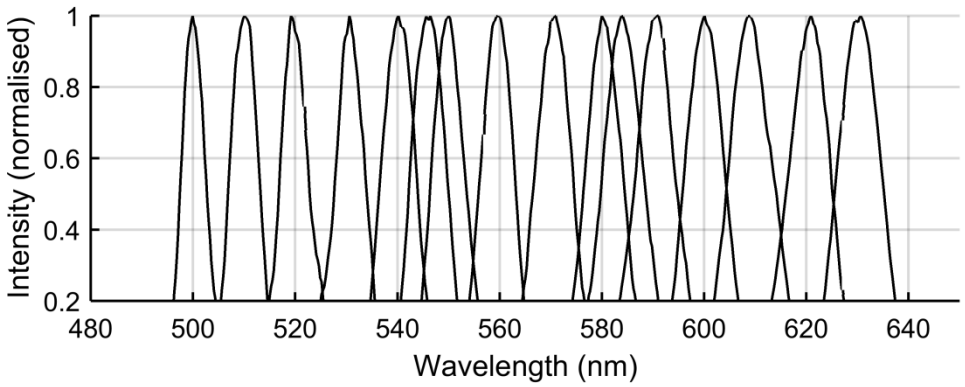

Figure 5-5. Experimentally measured LCTF wavebands.

The Mark 1 MSM did however exhibit non-uniform response due to non-uniform responsivity of the sCCD detector (see Figure 5-6A). This issue was thought to be caused by previous high-intensity optical radiation damage of the detector. However, the optics of the system provided good magnification, clearly resolving the inner edge of a standard Siemens star target (7.14 line pairs/mm) (see Figure 5-6 B).

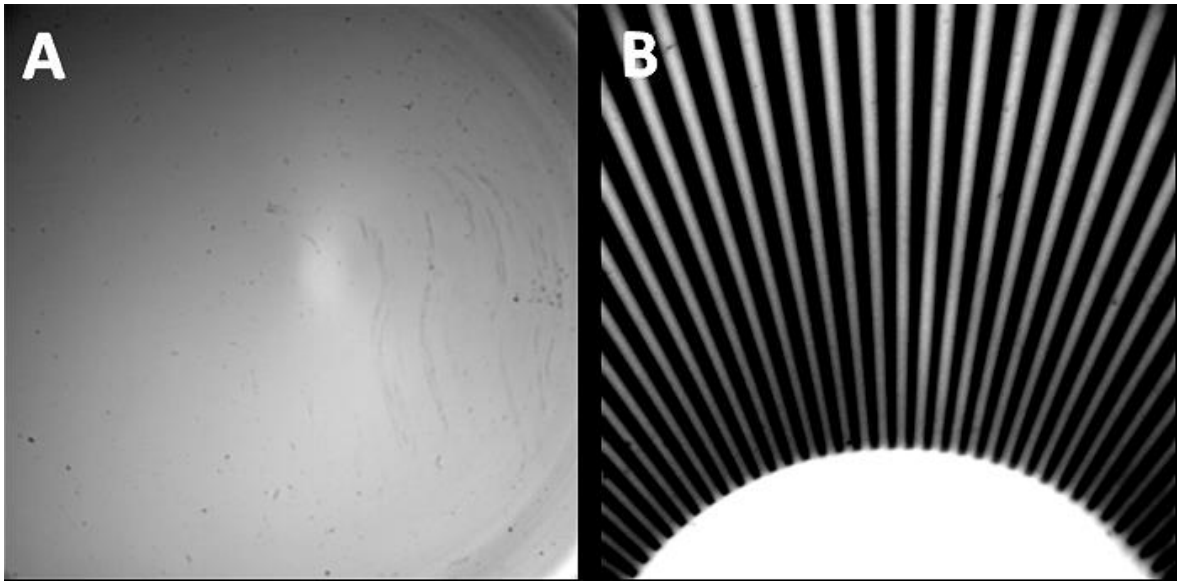

Figure 5-6. Imaging performance of the mark 1 multispectral microscope. Note contrast has been enhanced to highlight artefacts. **(A)** A defocused image of a uniform white reflectance target; non-uniform detector response can be clearly seen, in particular a central bright peak and concentric rings of alternating response. Small regions of decreased responsibility can also be seen. **(B)** Inner edge of a Seimens star target (inner frequency 7.14 line pairs per mm). Effects of non-uniform detector response can be seen.

5.2.4 Oximetry validation using a phantom

5.2.4.1 Phantom construction

A simple phantom was constructed to simulate a blood vessel on rat spinal cord white matter tissue. The phantom consisted of a Fluorinated Ethylene Propylene (FEP) capillary of 100 µm inner-diameter (Zuess inc.), filled with *ex vivo* horse blood (E&O labs) under feed from a syringe pump (KDS260, Linton Instrumentation). The capillary was placed on a white Spectralon backing to simulate the white matter of the spinal cord. Spectralon is a diffuse reflectance material with uniform spectral reflectance in the visible wave-range and thus appears white.[219] These reflectance properties are assumed to be similar to the reflectance spectra of white matter, however the albedo of white matter will be much less than the 99% reflectance of Spectralon. To reduce optical scattering from the FEP capillary wall, the entire

phantom assembly was immersed in saline solution (n = ~ 1.34),[274] index matching the FEP capillary (n = 1.34).[275] The phantom set up is shown in Figure 5-7.

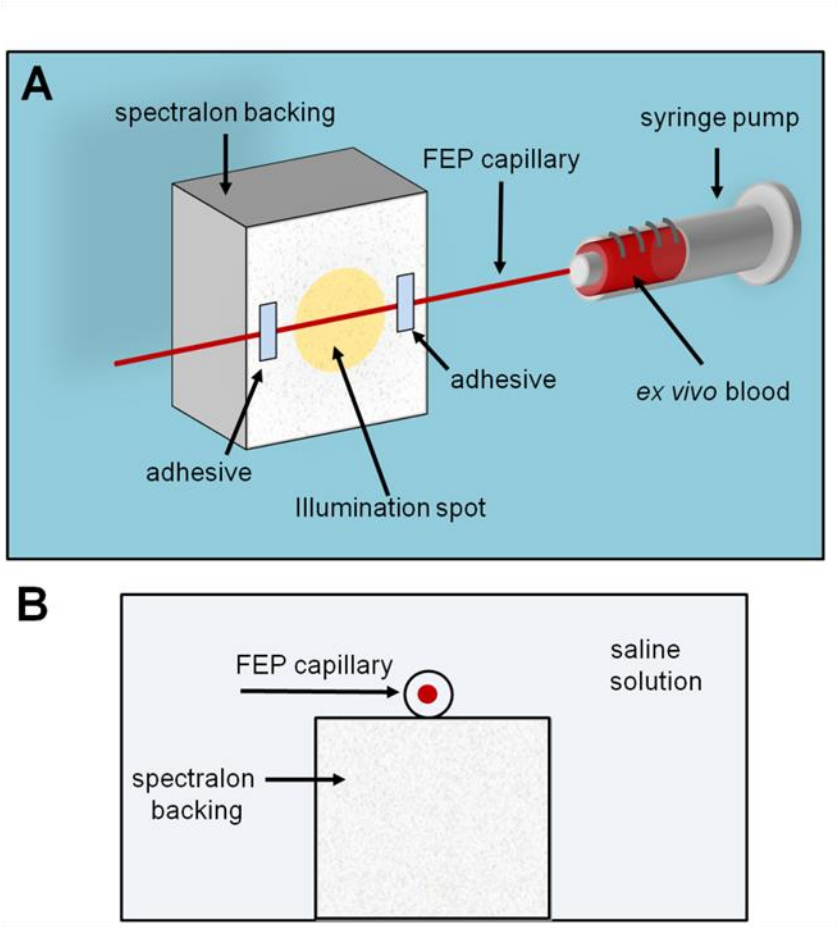

Figure 5-7. The phantom. **(A)** Components of the phantom (rotated 90 degrees for clarity). **(B)** Cross-sectional view of the phantom immersed in saline solution for imaging.

5.2.4.2 Experimental procedure

SO_2 of *ex vivo* blood was varied by adding measured quantities of sodium dithionite ($Na_2S_2O_4$) (EMD Millipore, Fisher Scientific) to 5 mL blood samples in varying quantities as per Table 3-2.[220] The blood was then stirred and placed into a plastic syringe for 30 minutes to allow the reaction of sodium dithionite to stabilise. After 30 minutes the resulting SO_2 of blood samples was then verified by analysis with an optical blood-gas analyser (GEM OPL, *Instrumentation Laboratory*) with a quoted uncertainty of ± 1.8% SO_2.[221]

The blood was flowed through the capillary under feed from a syringe pump. A total of eight SO_2 samples ranging between 9% and 100% SO_2 were imaged at 10 nm increments and at isobestic/maximum contrast points between 500 nm and 650 nm (i.e. 500, 510, 520, 530, 540, 546, 550, 560, 570, 580, 584, 590, 600, 610, 620, 630, 640, and 650 nm). This imaging process was repeated 5 times for each sample to provide repeat measurements and reduce variability due to random effects such as red blood cell aggregation.

To test the variability of ODR measurement in *ex vivo* blood, a single sample of 100% SO_2 blood was imaged at two-wavelengths (600 nm and 584 nm) for approximately 9 minutes as blood was flowed by the syringe pump.

5.2.4.3 Analysis

Background intensity and intensity inside the capillary were estimated by a simple vessel fitting algorithm. Average OD along the capillary was computed as per Equation 3-1 and the ODR with respect to the 584 nm (isobestic) waveband was computed for each waveband.

5.2.4.4 Results and discussion

ODR of flowing blood with a constant oxygenation (100% SO_2 as measured by the blood-gas analyser) was observed to fluctuate significantly with time, as shown in Figure 5-8. This variability is due to non-uniform optical properties of blood, which could be due either to non-uniform deoxygenation by sodium dithionite, or by aggregates of erythrocytes which will have variable scattering properties and increased concentration of haemoglobin in comparison with non-aggregated blood. Such aggregation is not expected *in vivo.*

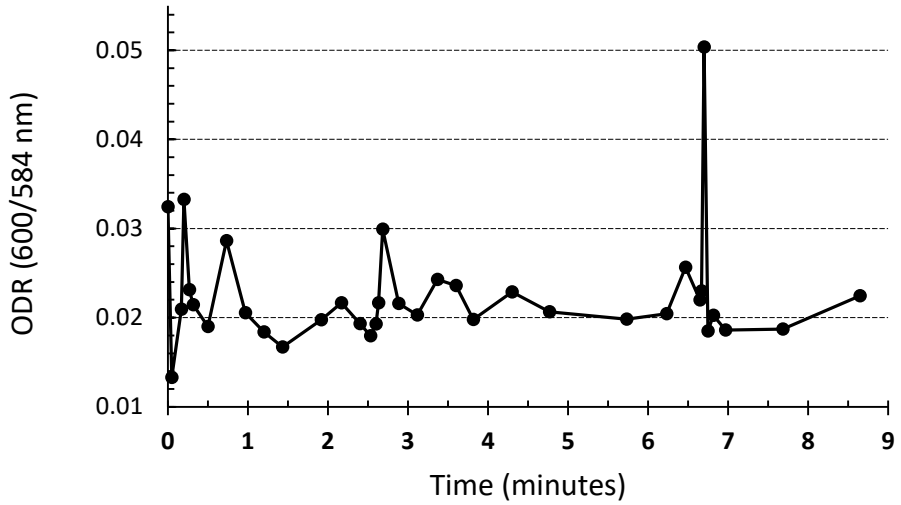

Figure 5-8. ODR of flowing 100% SO_2 blood vs. time. Large transient variations in ODR due to flowing aggregates were recorded.

Optical absorption of *ex vivo* whole blood was clearly dependent on wavelength and SO_2 (see Figure 5-9 and Figure 5-10). ODR varied with wavelength manner similar to the haemoglobin absorption spectra (see Figure 5-11 and Figure 5-12 for comparison). Figure 5-13 shows average ODR across all wavelengths for all SO_2 samples.

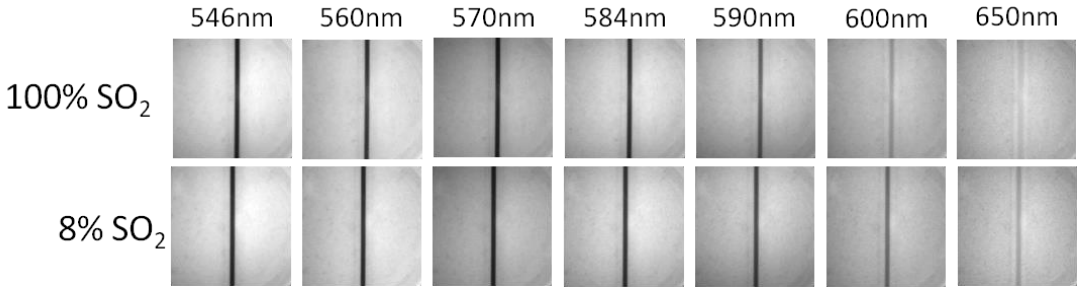

Figure 5-9. A 100 µm capillary filled with deoxygenated (8% SO_2) and oxygenated (100% SO_2) *ex vivo* whole blood at seven key wavelengths.

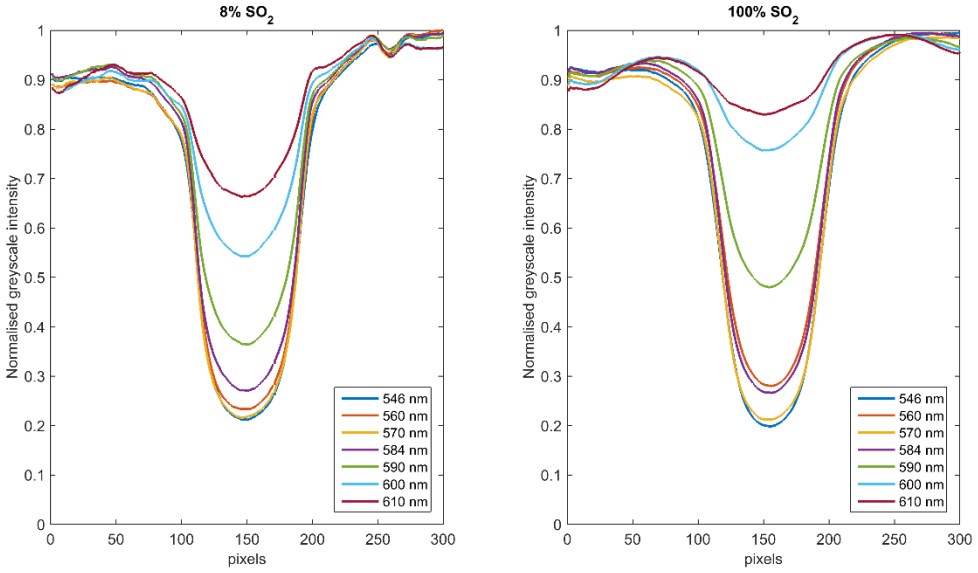

Figure 5-10. Line profiles across a 100 µm at 7 key wavelengths for 7% SO_2 blood and 100 % SO_2 blood.

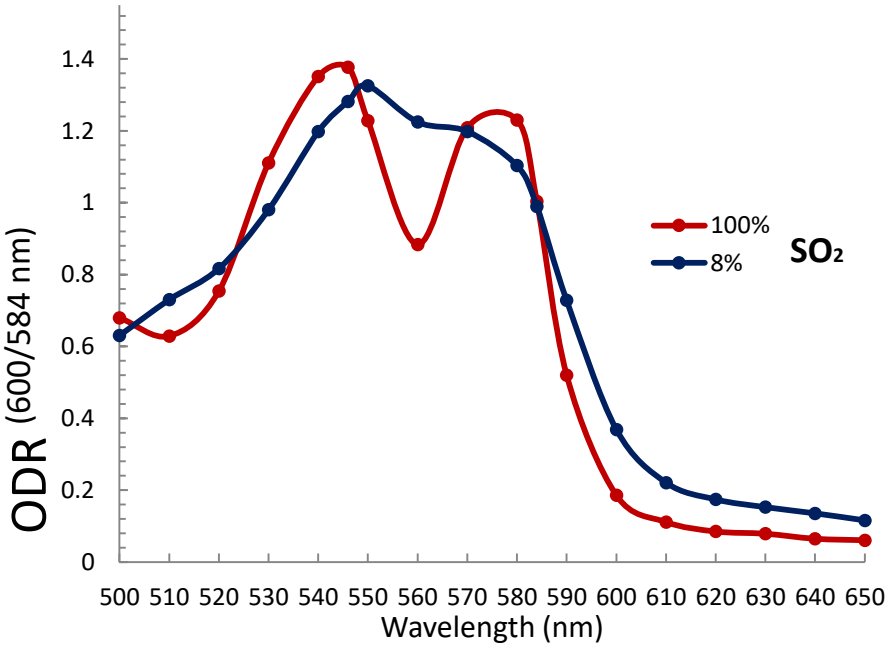

Figure 5-11. Average ODR (600 nm / 584 nm) vs. wavelength for 100% SO_2 and 8% SO_2 blood samples.

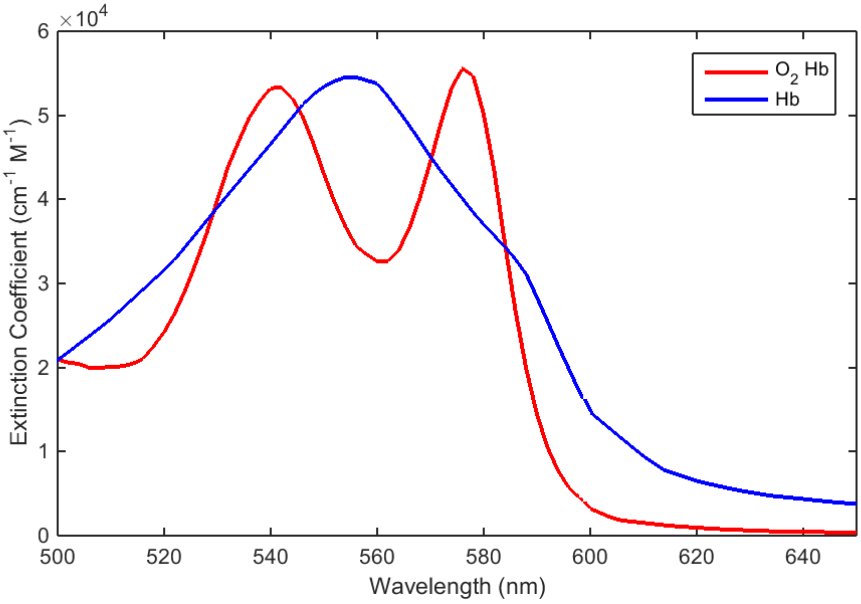

Figure 5-12. The absorption spectra of haemoglobin. Data from Prahl (1999).[19]

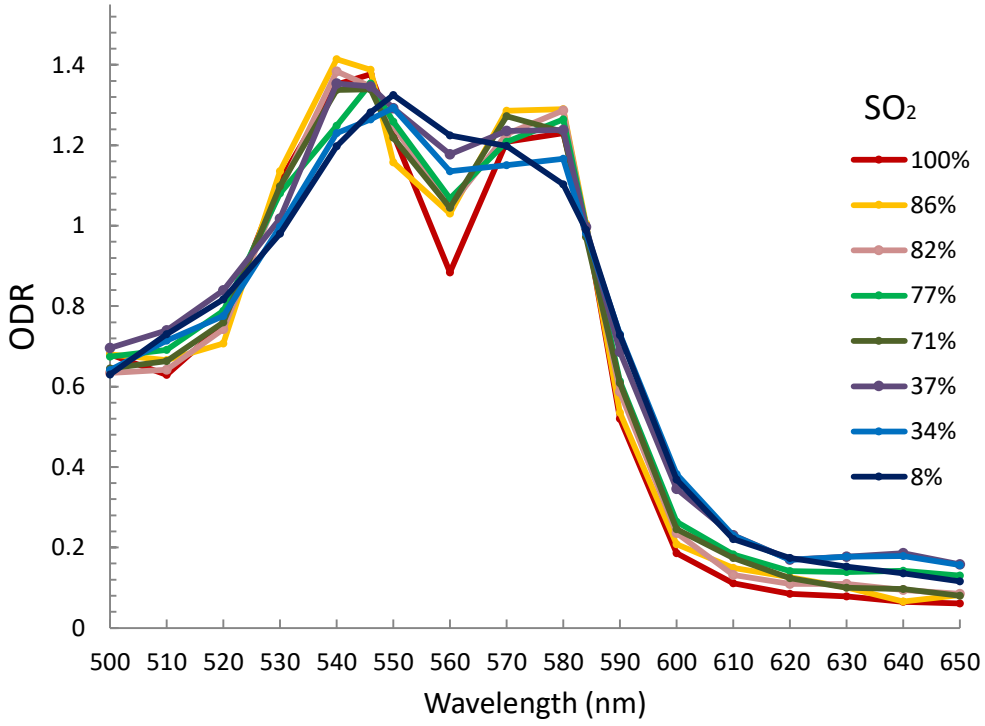

Figure 5-13. ODR vs. wavelengths for eight SO_2 samples.

Oximetry capability was assessed by plotting ODR of 600 nm and 584 nm wavebands against measured SO_2 (see Figure 5-14). As expected, ODR was linearly proportional to SO_2. From a linear fit to this data, ODR was calibrated to SO_2 by Equation 1-11. Estimated SO_2 showed a slight over-estimation of 4.3% when compared to blood gas analyser SO_2 (see Figure 5-15). This may be due to some systematic re-oxygenation in the time between blood-gas analyser SO_2 measurement and multispectral imaging.

5.2.4.5 Conclusions

This phantom study demonstrates that the MSM is capable of multispectral imaging for quantifying optical absorption of blood vessels for multi-wavelength oximetry. Simple two-wavelength oximetry was demonstrated. However, two-wavelength oximetry is limited for applications where there are no reference values for SO_2 calibration, such as the rat spinal cord. For such applications, a multispectral oximetry algorithm is required (see Section 5.3 onwards).

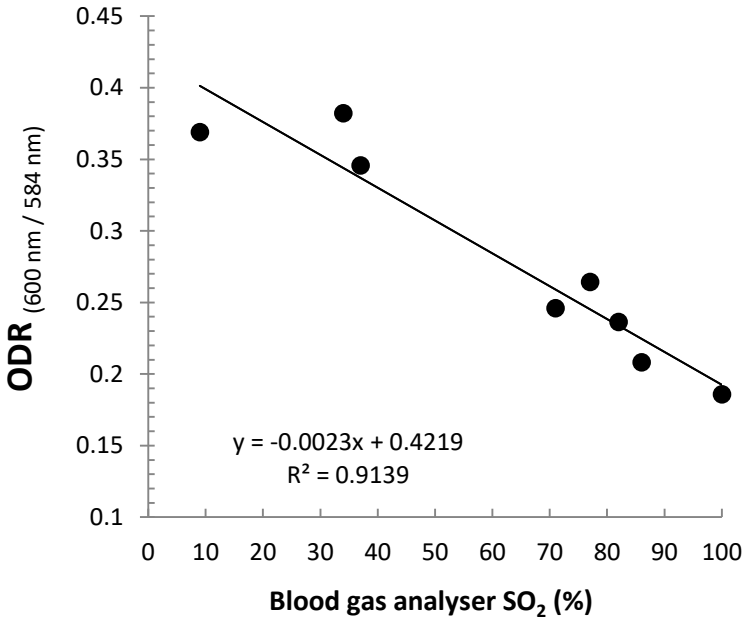

Figure 5-14. ODR vs. blood gas analyser SO_2. NB: manufacturers quoted uncertainty of blood gas SO_2 measurements is ± 2%.

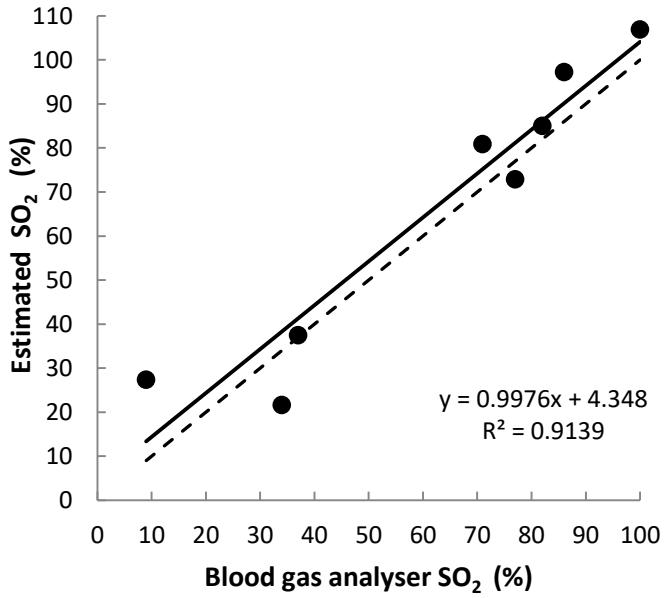

Figure 5-15. Estimated SO_2 vs. blood gas analyser SO_2. The black solid line is a linear fit to estimated SO_2 and the dashed line represents a 1:1 relation between blood gas analyser SO_2 and estimated SO_2. NB: manufacturers quoted uncertainty of blood gas SO_2 measurements is ± 2%.

5.2.5 Preliminary *in vivo* imaging of a rat dorsal vein

5.2.5.1 Experimental methods

To test the suitability of the MSM for *in vivo* oximetry of the rat spinal cord dorsal vein, a preliminary imaging study in a single rat was conducted. Surgery to expose the spinal cord dorsal vein of the rat was conducted by A. Davies as described in Section 5.5; two surgical sutures were used to minimise motion due to breathing and heartbeat. This enabled imaging of the main dorsal vein and several branching tributary venules, as shown in Figure 5-16.

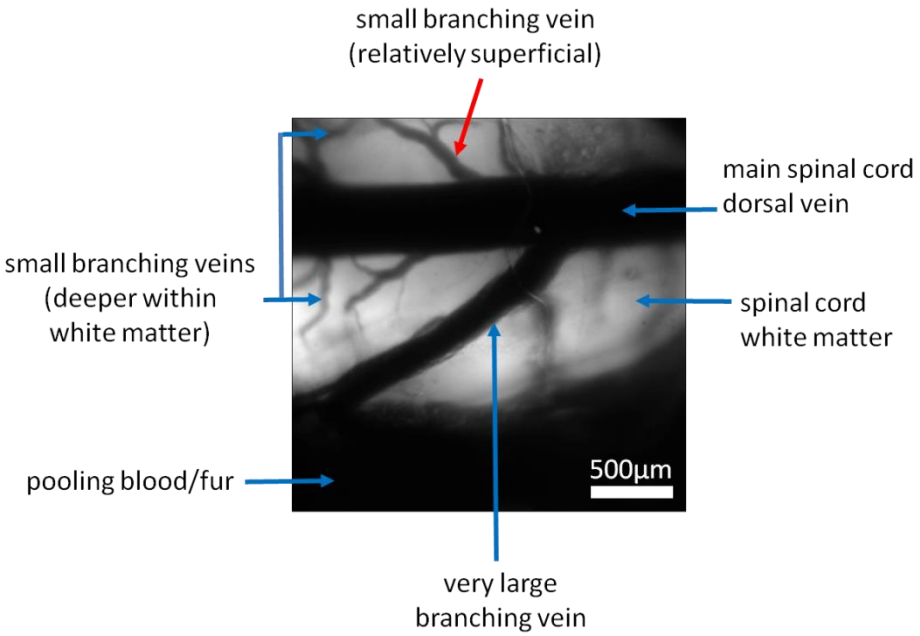

Figure 5-16. Annotated image of a rat spinal cord dorsal vein. The red arrow indicates the tributary branching venule selected for data analysis.

To test response to changes in SO_2, FiO_2 was varied from normoxia (21% FiO_2), to hyperoxia (100% FiO_2), returning to normoxia (21% FiO_2), and then to hypoxia (10% FiO_2). Arterial SO_2 was recorded by a paw pulse oximeter. Images were acquired at each FiO_2 state once arterial SO_2 reached a stable level. Images were acquired at six key contrast and isobestic wavelengths (546, 560, 570, 584, 600, and 610 nm). ODR (600 nm / 584 nm) of a single tributary venule was computed at each FiO_2 state as a proxy for SO_2.

5.2.5.2 Preliminary *in vivo* results

Absorption of the main dorsal vein was too high for oximetry at visible wavelengths, so a single tributary venule was selected for analysis (see Figure 5-16). This venule was selected because it was not close to other branching vessels, was in a sharp focus, and because it was a suitably large (~ 100 µm) so as to have good transmission for oximetry (an optical transmission between 10% and 70%).

ODR vs. FiO_2 is summarised in Figure 5-17; ODR of this vein decreased from 0.120 ± 0.002 (mean ± standard deviation) at normoxia to 0.079 ± 0.003 at hyperoxia, indicating an increase in SO_2. ODR subsequently increased to 0.140 ± 0.005 when returned to normoxia, indicating a decrease in SO_2 lower than initial baseline. The rat died when FiO_2 was decreased to 10%. From Figure 5-18 it can be seen that tributary venules are highly transparent at hyperoxia. This indicates that the 610 nm waveband is sub-optimal for oximetry in these smaller vessels. Imaging waveband choice is discussed in more detail in Section 5.4.

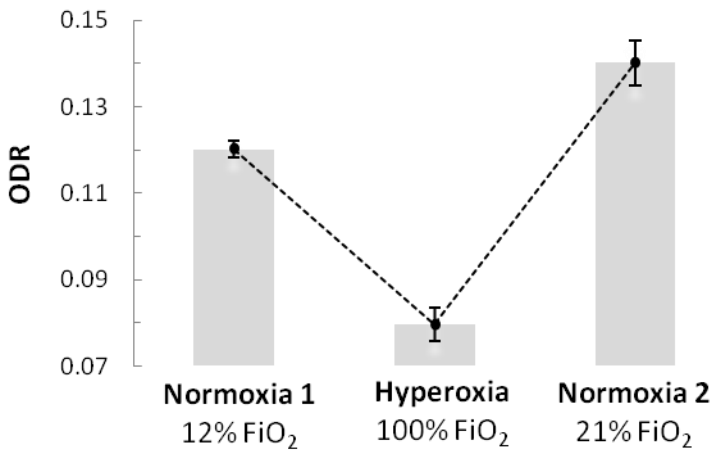

Figure 5-17. ODR (600 nm / 584 nm) of a single tributary venule at normoxia, hyperoxia, and return to normoxia. Error bars are ± the standard deviation of three repeat ODR measurements.

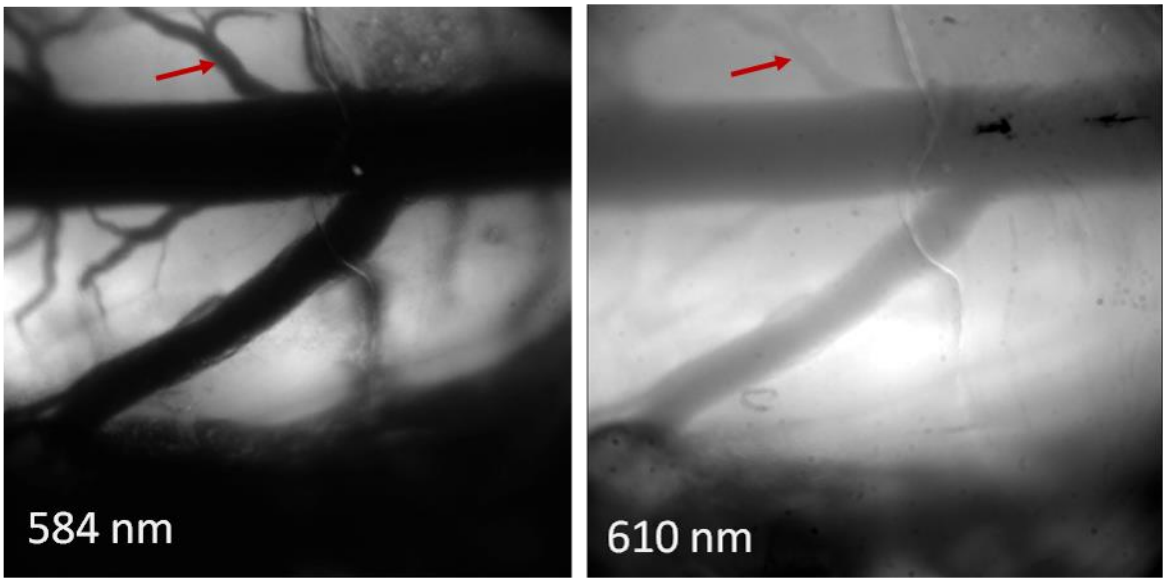

Figure 5-18. Rat spinal cord dorsal vein and tributary venules at hyperoxia. Vessel analysed is indicated with a red arrow. Branching tributary vessels can be observed to be nearly completely transparent at 610 nm at hyperoxia.

5.2.5.3 Discussion & conclusion of preliminary *in vivo* results

This preliminary *in vivo* imaging trial demonstrates that the MSM is suitable for oximetry of spinal cord tributary venules in rats. However, oximetry in the largest vessel is not possible due to a lack of low-absorption isobestic wavelengths at <700 nm. Simple ODR analysis indicated that SO_2 of a tributary venule increased and decreased with changes in FiO_2 as expected. However, a quantitative multispectral oximetry algorithm is required for inter-vessel and inter-animal comparison. The use of such an algorithm for quantitative oximetry in the spinal cord dorsal veins is described Section 5.3 onwards.

5.2.6 Mark 2 multispectral microscope

Due to a malfunction of the Retiga 4000R detector, a second iteration of the MSM was developed. Instead of the Retiga 4000R, this version utilised a colour DSLR (RGB Bayer matrix) CMOS sensor (D300s, *Nikon*), consisting of 4288 x 2842 pixels, each 5.5 μm in size.[276] The effective magnification of this Mark 2 MSM was measured to be roughly 6.4x with a field of view of ~ 3.73 x 2.43 mm. No change in illumination or imaging optics were required to incorporate this sensor. A simple diagram of the set-up is shown in Figure 5-19 and an image of the set up in the UCL animal lab is shown in Figure 5-20.

Wavelength switching, illumination, and image acquisition were controlled by a custom LabVIEW GUI (Section 5.2.7). Images from the sensor were saved as RAW (.NEF) files, and subsequently converted to uncompressed 16 bit .TIFF RGB format using Capture NX-D software (Nikon). The image was saved by taking the highest signal colour channel and saving this in uncompressed greyscale 16 bit .TIFF format.

The image acquisition rate was limited by the requirement of the DSLR control drivers (LabVIEW camera control for Nikon SLR, Ackerman Automation) to save images only to the computer hard-drive via USB 2.0 instead of the on-board flash memory. This limited acquisition rate of RAW images to seven seconds per image. The use of JPG image compression for more rapid imaging was investigated, but JPG compression was found to result in decreased vessel contrast; see Section 5.6.1 for more details.

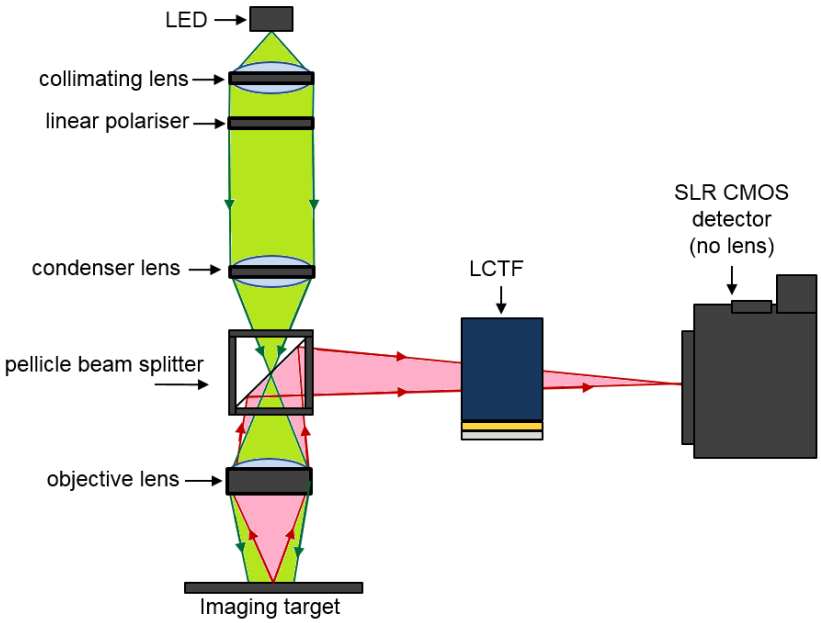

Figure 5-19. Basic schematic of the mark 2 MSM. The Illumination path is highlighted as green, and imaging path is highlighted as red.

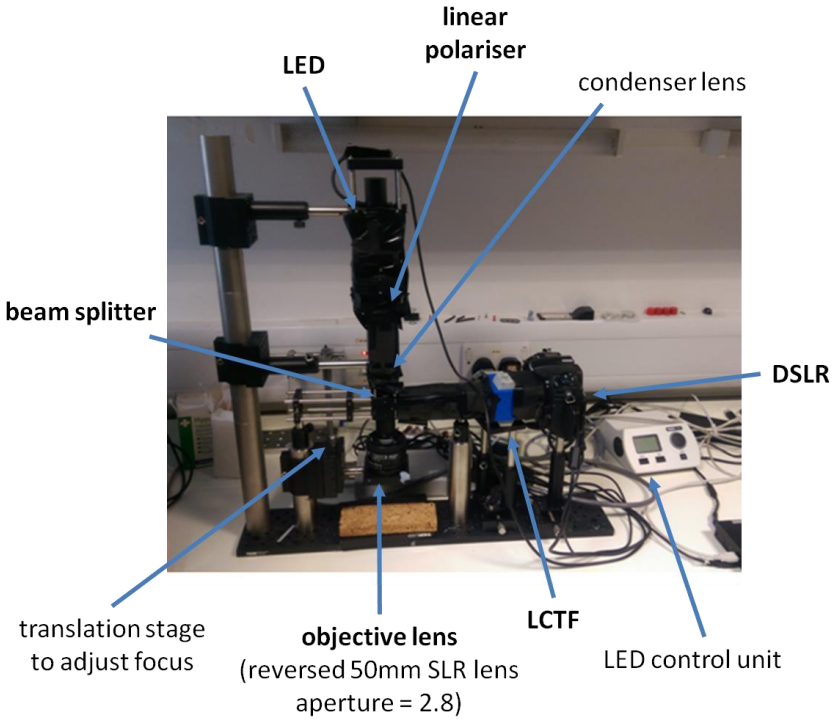

Figure 5-20. The Mark 2 MSM *in situ*.

5.2.7 Software interfacing and control

A Graphic User Interface (GUI) was developed in LabVIEW (LabVIEW 2014, *National Instruments)* to automate illumination control, wavelength switching, and image acquisition. The GUI enabled the user to specify imaging wavebands, illumination light intensity, image file name, image format, and COM ports of hardware. Amongst many parameters, the GUI displays a live image preview, the most recent saved image, and a line-profile of the most recent saved image for transmission estimation *in situ*. A screenshot of this GUI is shown in Figure 5-21.

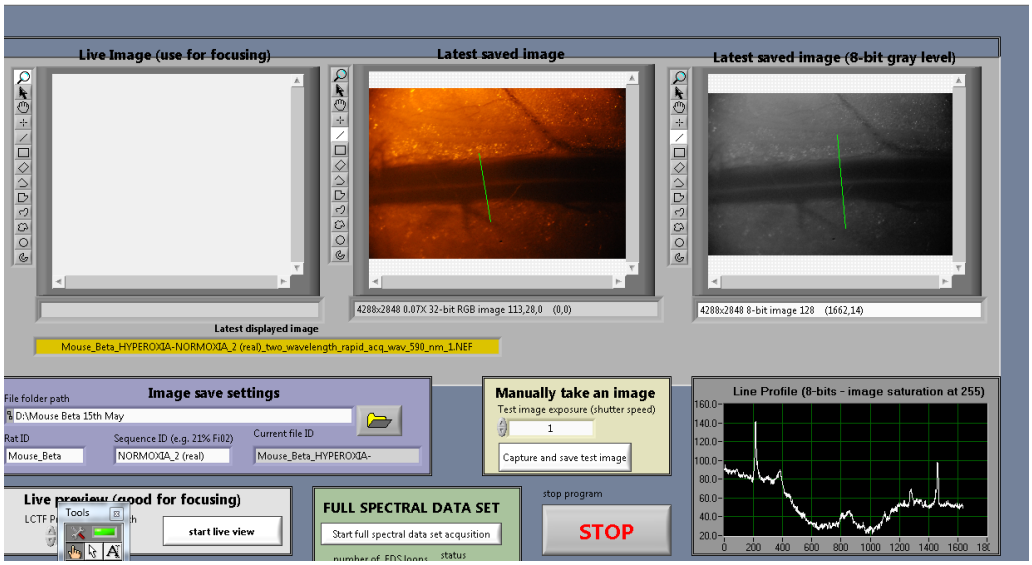

Figure 5-21. The MSM control GUI.

The microscope control GUI was based upon an event-driven interrupt system. The interrupts logic is shown in Figure 5.22. Remote control of the microscope was performed by remote control of the laptop on which the GUI was installed. Remote control was achieved with *TeamViewer 10* software (*TeamViewer GmbH*). After acquisition, image files were losslessly compressed into .zip format and transferred to University of Glasgow server using the TeamViewer file transfer function.

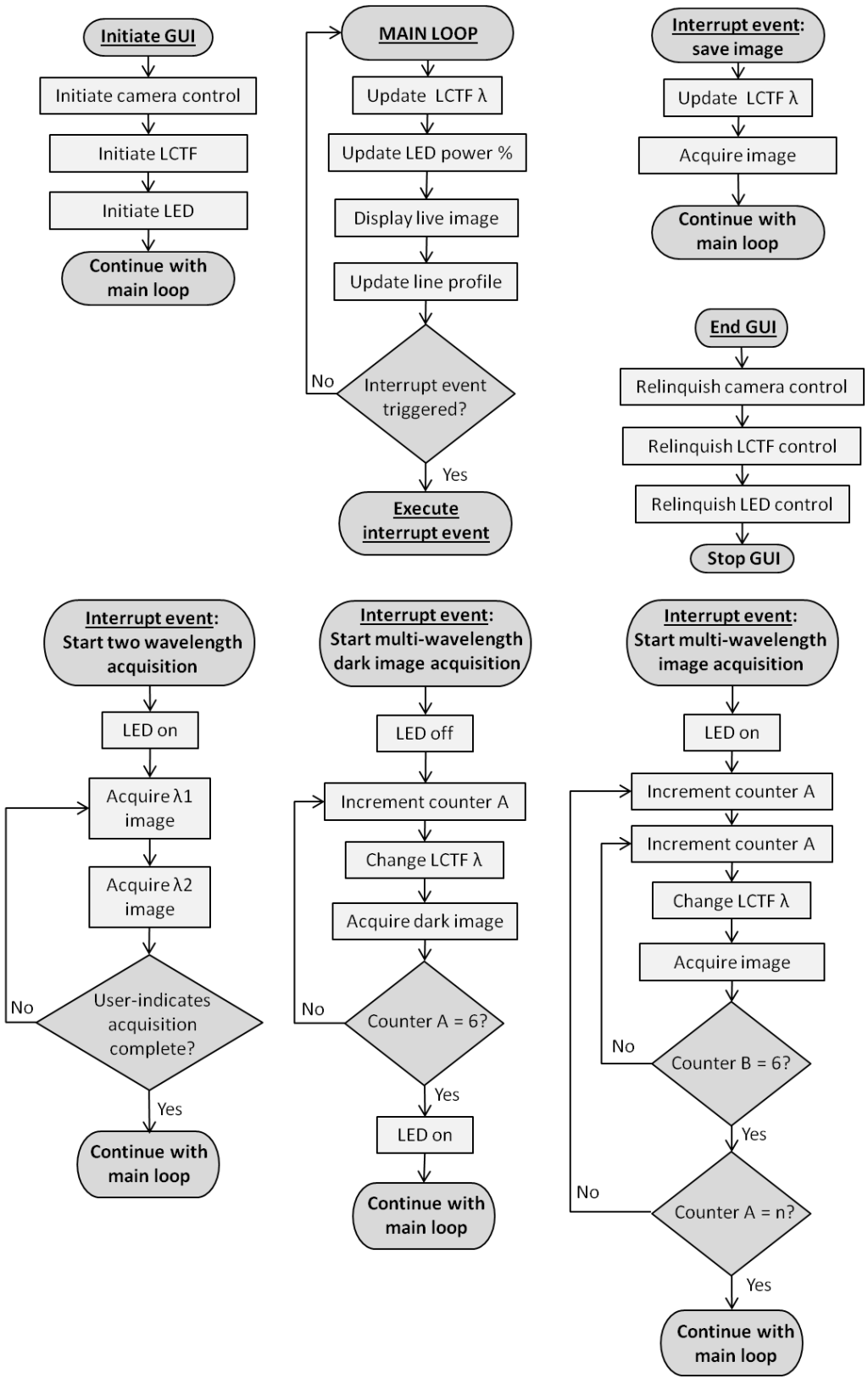

Figure 5-22. Software logic flow chart for the MSM LabVIEW GUI.

5.3 Multi-waveband calibration-free oximetry algorithm

For meaningful inter-vessel and inter-animal comparison on SO_2, the following calibration-free multispectral oximetry algorithm was developed by Javier Fernandez-Ramos and Marieke van der Putten (both researchers in the Imaging Concepts Group, University of Glasgow). The model estimates SO_2 by fitting experimentally-measured vessel transmissions to a theoretical transmission model that incorporates multiple optical parameters, including SO_2, vessel diameter, optical scattering, single/double pass contribution, and contrast-reduction. The transmission model was derived as follows: from the Beer-Lambert law, the optical density $OD(\lambda)$ of a blood vessel is described by:

$$OD(\lambda) = -\log_{10}(T) = \varepsilon(\lambda)\, C_{\mathrm{HbT}}\, d, \tag{5-1}$$

where T is vessel transmission, d is blood vessel diameter, C_{HbT} is the molar concentration of total haemoglobin, and $\varepsilon(\lambda)$ is the optical extinction coefficient of haemoglobin. $\varepsilon(\lambda)$ can be expressed by:

$$\varepsilon(\lambda) = \left(SO_2\, \varepsilon_{\mathrm{HbO_2}}(\lambda)\right) + \left([1\text{-}SO_2]\, \varepsilon_{\mathrm{Hb}}(\lambda)\right), \tag{5-2}$$

where SO_2 is the fractional oxygen saturation, and $\varepsilon_{\mathrm{HbO_2}}(\lambda)$ and $\varepsilon_{\mathrm{Hb}}(\lambda)$ are the molar extinction coefficients of oxygenated (HbO_2) and deoxygenated (Hb) haemoglobin. By defining $C_{\mathrm{HbO_2}}$ and C_{Hb} as the fractional concentrations of HbO_2 and Hb, Equation 5-1 can be rewritten as:

$$OD(\lambda) = \varepsilon_{\mathrm{HbO_2}}(\lambda)\, C_{\mathrm{HbO_2}}\, d + \varepsilon_{\mathrm{Hb}}(\lambda) C_{\mathrm{Hb}} d, \tag{5-3}$$

SO_2 can be written as:

$$SO_2 = \frac{C_{\mathrm{HbO_2}}}{C_{\mathrm{HbO_2}} + C_{\mathrm{Hb}}}, \tag{5-4}$$

substituting 5-4 into 5-3 gives:

$$OD(\lambda) = C_{\mathrm{Hb}} d \left[\left(\varepsilon_{\mathrm{HbO_2}}(\lambda) - \varepsilon_{\mathrm{Hb}}(\lambda)\right) SO_2 + \varepsilon_{\mathrm{Hb}}(\lambda)\right], \tag{5-5}$$

the additive reduced scattering coefficient $\mu'(\lambda)$ from the modified Beer-Lambert law is then added to account for scattering from red blood cells:

$$OD(\lambda) = C_{\mathrm{Hb}} d\left[\left(\varepsilon_{\mathrm{HbO_2}}(\lambda) - \varepsilon_{\mathrm{Hb}}(\lambda)\right) SO_2 + \varepsilon_{\mathrm{Hb}}(\lambda)\right] + \mu'(\lambda) d. \quad 5\text{-}6$$

Values of $\mu'(\lambda)$ are taken from Faber et. al., (2004).[67] Single and double pass light paths through the vessel are accounted for by adding two multiplicative parameters, α and β respectively, which service to model the relative contribution of single and double-pass illumination. Transmission is related to OD by the relation $T(\lambda) = 10^{-OD}$, so Equation 5-6 can be rewritten as:

$$T(\lambda) = \left[\alpha\, 10^{-\left(C_{\mathrm{Hb}}\, d\left[\left(\varepsilon_{\mathrm{HbO_2}}(\lambda) - \varepsilon_{\mathrm{Hb}}(\lambda)\right) SO_2 + \varepsilon_{\mathrm{Hb}}(\lambda)\right] + \mu'(\lambda) d\right)} + \beta 10^{-\left(2C_{\mathrm{Hb}}\, d\left[\left(\varepsilon_{\mathrm{HbO_2}}(\lambda) - \varepsilon_{\mathrm{Hb}}(\lambda)\right) SO_2 + \varepsilon_{\mathrm{Hb}}(\lambda)\right] + 2\mu'(\lambda) d\right)}\right]. \quad 5\text{-}7$$

A reduction in contrast of the vessel due to neighbouring or overlying tissue may be included as a contrast-reduction parameter, modelled as an arbitrary increase in greyscale intensity (I_c), both in the centre of the vessel (I_v) and outside the vessel (I_o). This can be described giving a contrast parameter, K:

$$K = \frac{I_c}{I_o + I_c}. \quad 5\text{-}8$$

In the case of altered contrast, transmission can be rewritten as:

$$T'(\lambda) = \left(\frac{I_v + I_c}{I_o + I_c}\right) = T(\lambda)(1 - K) + K, \quad 5\text{-}9$$

substituting Equation 5-9 into Equation 5-7 gives the final transmission model:

$$T'(\lambda) = \left[\alpha\, 10^{-\left(C_{\mathrm{Hb}}(\lambda) d\left[\left(\varepsilon_{\mathrm{HbO_2}}(\lambda) - \varepsilon_{\mathrm{Hb}}(\lambda)\right) SO_2 + \varepsilon_{\mathrm{Hb}}(\lambda)\right] + \mu'(\lambda) d\right)} + \beta 10^{-\left(2C_{\mathrm{Hb}}(\lambda) d\left[\left(\varepsilon_{\mathrm{HbO_2}}(\lambda) - \varepsilon_{\mathrm{Hb}}(\lambda)\right) SO_2 + \varepsilon_{\mathrm{Hb}}(\lambda)\right] + 2\mu'(\lambda) d\right)}\right] (1 - K) + K. \quad 5\text{-}10$$

Experimentally measured blood vessel transmissions and diameters are fitted to theoretical transmission model described by Equation 5-10 by using a nonlinear least-squares fit. From this fit, values of single pass contribution (α), double pass contribution (β), contrast parameter (*K)*, and *SO₂* are estimated.

5.4 Imaging waveband selection

For optimal oximetry, blood vessels should have a transmission between 10% and 70%. Imaging wavebands must be selected so as to have appropriate transmission for oximetry in target blood vessels. In the dorsal vein of rats, the large

central dorsal vessel is too large for oximetry at visible wavelengths, so tributary venules ~ 100 μm have to be analysed instead. Wavelength selection is also constrained by the need for fast integration times (<1 second) to minimise motion effects. This rules out wavelengths < 540 nm due to the low efficiency of the light source, LCTF, and sensor at these wavelengths which results in a relatively long integration time of > 1 second.

To estimate theoretical transmission of blood vessels, the effective extinction coefficient of haemoglobin for each LCTF waveband (see Figure 5-5) must be first be calculated. To do this, the wavelength-dependent intensity of the experimentally measured LCTF wavebands [$I(\lambda)$]was normalised so that the area under the curve of the waveband summed to one,[105] i.e:

$$I'(\lambda) = \int_{\lambda_1}^{\lambda_2} I(\lambda) d\lambda = 1, \qquad 5\text{-}11$$

where λ_1 and λ_2 are the minimum and maximum wavelengths of each waveband, and $I'(\lambda)$ is the resulting weighted intensity-contribution for each wavelength. The weighted intensity-contribution was then multiplied by the known values of haemoglobin extinction coefficient, $\varepsilon(\lambda)$, to give the effective haemoglobin extinction coefficient of the LCTF waveband, $\varepsilon'(\lambda)$:

$$\varepsilon'(\lambda) = I'(\lambda)\, \varepsilon(\lambda) \qquad 5\text{-}12$$

The effective extinction coefficient of some wavebands varied by as much as 12% from their central wavelength (see Table 5-1 and Table 5-2).

Table 5-1. Estimated effective extinction coefficients of O_2Hb.

Waveband (nm)	Central waveband extinction coefficient (cm^{-1}/M)	Full waveband effective extinction coefficient (cm^{-1}/M)	Difference (%)
546	49868	48527	-2.8
560	32613	33763	3.4
570	44496	45164	1.5
578	54728	50374	-8.6
584	34639	33976	-1.9
590	14400	15598	7.7
594	7678	8501	9.7
600	3200	3632	11.9
610	1506	1506	0.0
650	357	367	2.8

Table 5-2. Estimated effective extinction coefficients of Hb.

Waveband (nm)	Central waveband extinction coefficient (cm^{-1}/M)	Full waveband effective extinction coefficient (cm^{-1}/M)	Difference (%)
546	51268	51145	0.2
560	53788	52893	1.7
570	45072	45005	0.1
578	38467.6	38455	0.0
584	34332	33933	1.2
590	28324	27699	2.2
594	22574	22360	0.9
600	14677	15421	- 5.1
610	9443	9497.809	-0.6
650	3750.12	3740.92	0.2

To estimate how sensitive each waveband was to changes in SO_2, the rate of change of extinction coefficient with SO_2, $(\Delta \varepsilon(\lambda)/\Delta SO_2)$, for each LCTF waveband was calculated. The results are summarised in Table 5-3 and shown graphically in Figure 5-23.

Table 5-3. Rate of change of extinction coefficient with SO_2 for each waveband.

LCTF waveband (nm)	Δ ε(λ)/ΔSO_2	Use
546	-262	Isobestic
560	-1913	Contrast
570	16	Isobestic
578	1192	Contrast
584	4	Isobestic
590	-1210	Contrast
594	-1386	Contrast
600	-1179	Contrast
610	-799	Contrast
650	-337	Contrast

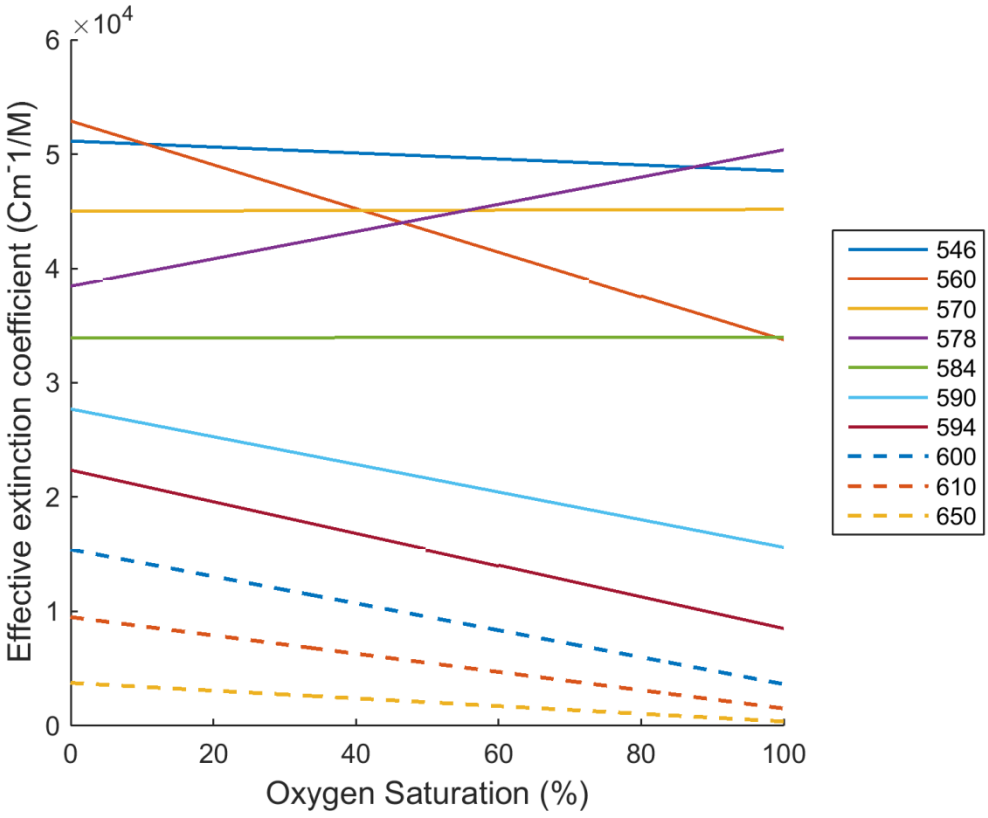

Figure 5-23. Effective extinction coefficient of LCTF wavebands vs. SO_2.

To ensure that wavelengths with good transmission for oximetry were selected, the theoretical vessel transmission vs. vessel diameter were calculated by the Beer-Lambert law assuming single-pass transmission. From Figure 5-25, it can be seen that the 546, 560, 570, 584, and 590 nm wavebands provide suitable transmission for oximetry (between 10 and 70%) in a wide-range of vessel diameters and oxygen saturations. The 600 nm waveband will however be sub-optimal for highly oxygenated vessels. In reality, vessel transmissions will be less than these theoretical estimations due to the effects of multiple scattering and double-pass transmission. The six wavebands selected for multispectral imaging were 546, 560, 570, 584, 590, and 600 nm. The position of these wavebands on the haemoglobin absorption spectra are shown in Figure 5-24.

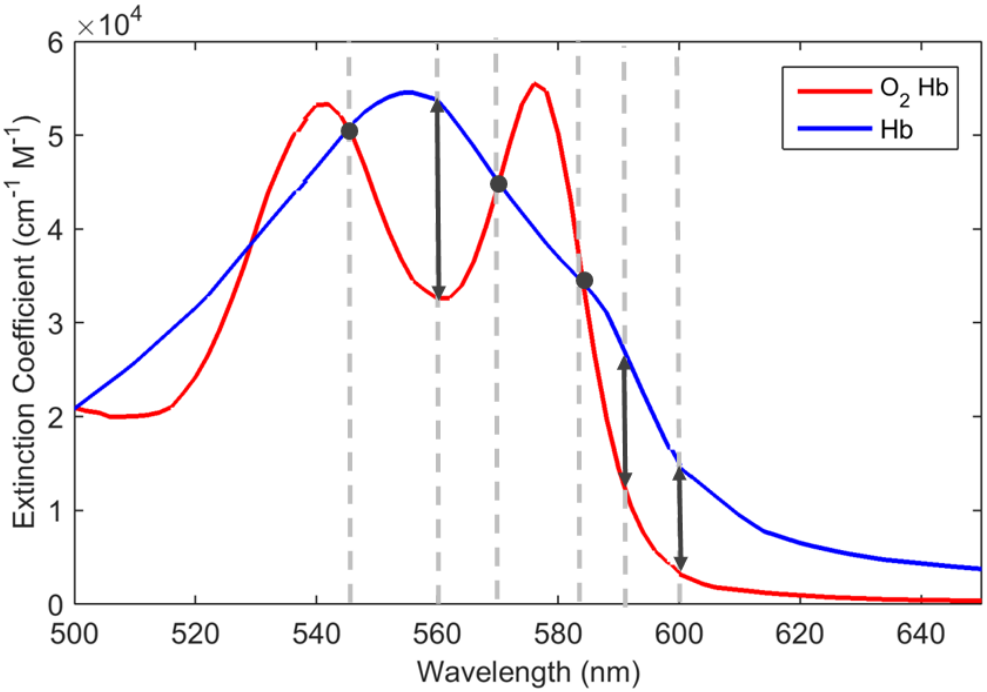

Figure 5-24. Central wavelengths of wavebands selected for *in vivo* imaging.

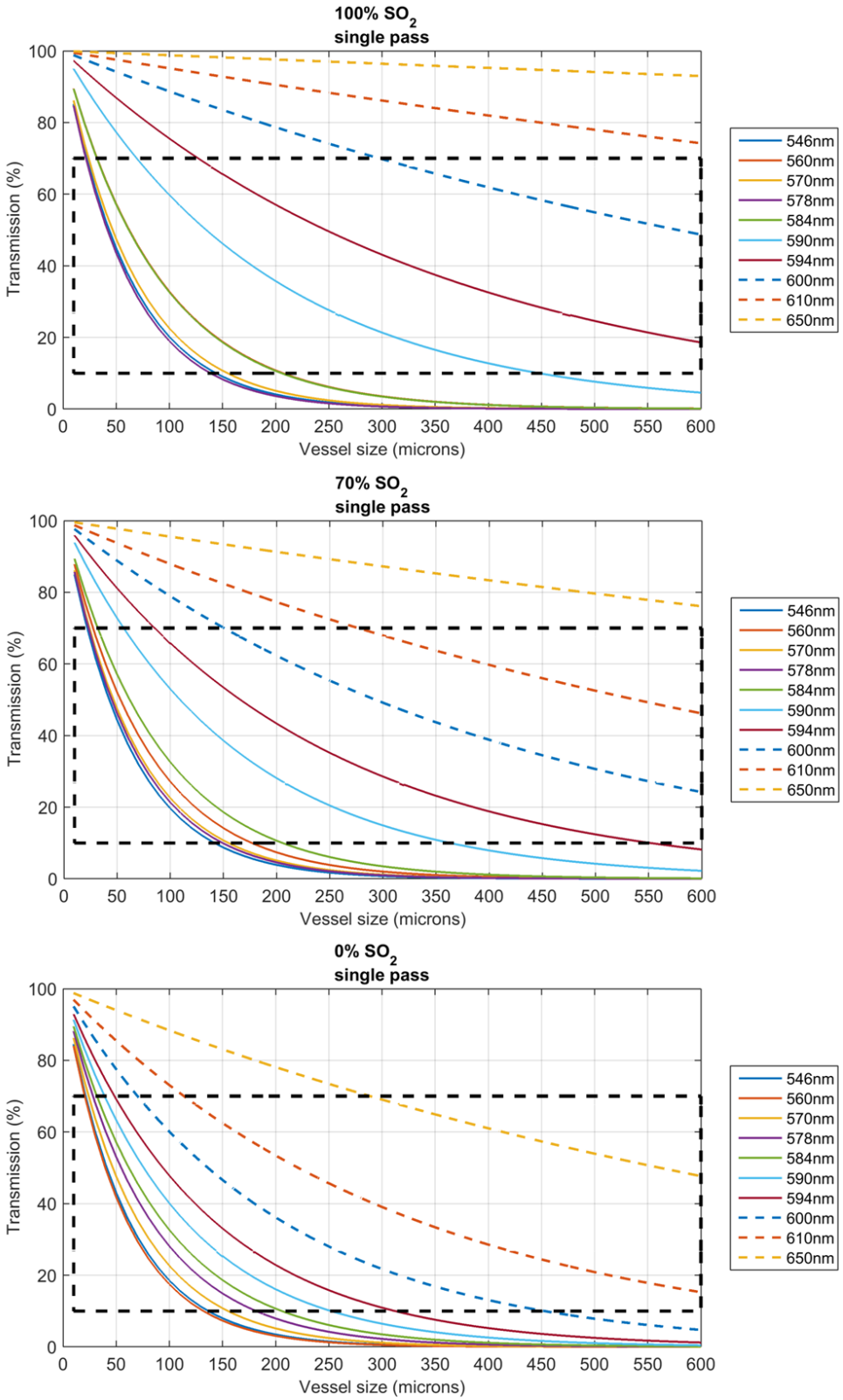

Figure 5-25. Theoretical transmission vs. vessel diameter for 100, 70, and 0% SO_2 (assuming single pass transmission). The black dashed box indicates the region of good transmission for oximetry (between 10% and 70%).[102]

5.5 Dorsal vein SO_2 in healthy and EAE rats

5.5.1 Methodology

A study of dorsal vein SO_2 in healthy controls and EAE disease model rats was conducted to compare relative SO_2. All procedures involving animals were carried out in accordance with the Home Office Animals (Scientific Procedures) Act 1986 by Andrew Davies and Roshni Desai. Thirteen female dark agouti rats (average weight 180 g) were used for this study, six healthy controls and seven with maximum EAE disease model severity. Two controls and two EAE rats died prematurely during experimental procedures and are thus not included in the results of this study. The final number of animals included for analysis was four controls and five EAE rats. All image acquisition and data analysis was conducted in a blind manner.

For each animal, the following procedure was conducted. First, the animal was anesthetized by inhalation of a mixture of 2% isoflurane and room air administered via a nasal mask. The back of the animal was shaved to remove hair and a laminectomy was then performed to remove the dorsal aspect of vertebral segment (lumbar 1) and expose the spinal cord dorsal vein for imaging. Two surgical sutures were used to reduce the weight loading on the rat ribcage and thus reduce motion due to respiration. After initial surgery, the concentration of isoflurane was reduced to 1.5% for the remainder of the experiment. Throughout the experiment the body temperature of the rat was maintained at 37°C by a heating mat and arterial SO_2 was recorded by a collar-mounted carotid artery pulse-oximeter with a computer interface. The MSM was then manoeuvred into position to image the rat. Sensor integration time for each waveband was calibrated in a dark environment to ensure sufficient exposure and to avoid saturation of images. Dark images then acquired for the appropriate exposure time for each waveband to account for thermal noise and sensor bias.

FiO_2 was varied in the following sequence to provide insight into physiological response: (1) baseline normoxia (21% FiO_2 for 10 minutes); (2) hyperoxia (100% FiO_2 for 10 minutes); (3) normoxia 2 (21% FiO_2 for 5 minutes); (4) hypoxia 1 (18% FiO_2 for five minutes); (5) hypoxia 2 (15% FiO_2 for five minutes); and (6) hypoxia 3

(10% FiO_2 for five minutes). If the rats survived the entire experimental procedure, they were then terminated by lethal dose of isoflurane and disposed of according to UK Home Office procedure. Three spectral data sets of six wavebands (546, 560, 570, 584, 590, and 600 nm) were acquired at each FiO_2 stage, taking approximately 3 minutes to acquire in total.

Tributary venules were included for analysis based on the following inclusion criteria: (1) vessels were between 50 and 130 μm in diameter; (2) vessel sections should have no vessels within one vessel diameter either side; (3) vessel sections that tapered due to overlying tissue were omitted. Typically, only one or two tributary venules met these criteria per rat. These vessels were tracked semi-automatically and SO_2 and vessel diameter estimated using a similar vessel fitting algorithm to that shown in Figure 3-7. SO_2 was estimated using the multispectral oximetry algorithm described in Section 5.3.

5.5.2 Results

Images obtained of spinal cord dorsal vein and tributary vessels are shown in Figure 5-26 (healthy controls) and Figure 5-27 (EAE). Vessels of EAE rats can be seen to be significantly greater in diameter than healthy controls.

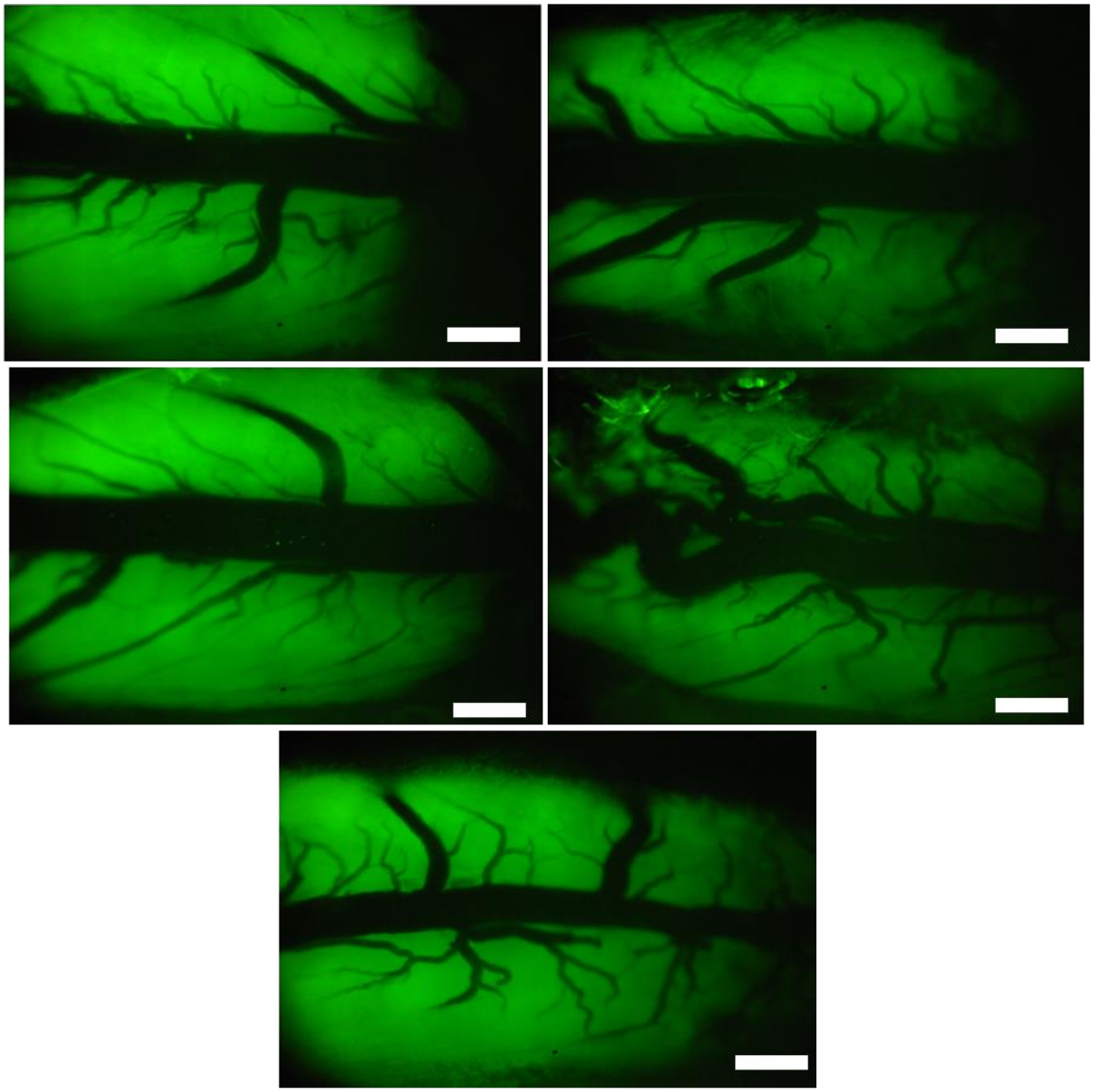

Figure 5-26. Spinal cord dorsal vein blood vessels of five healthy controls at the 570 nm waveband. Scale bar represents 500 μm.

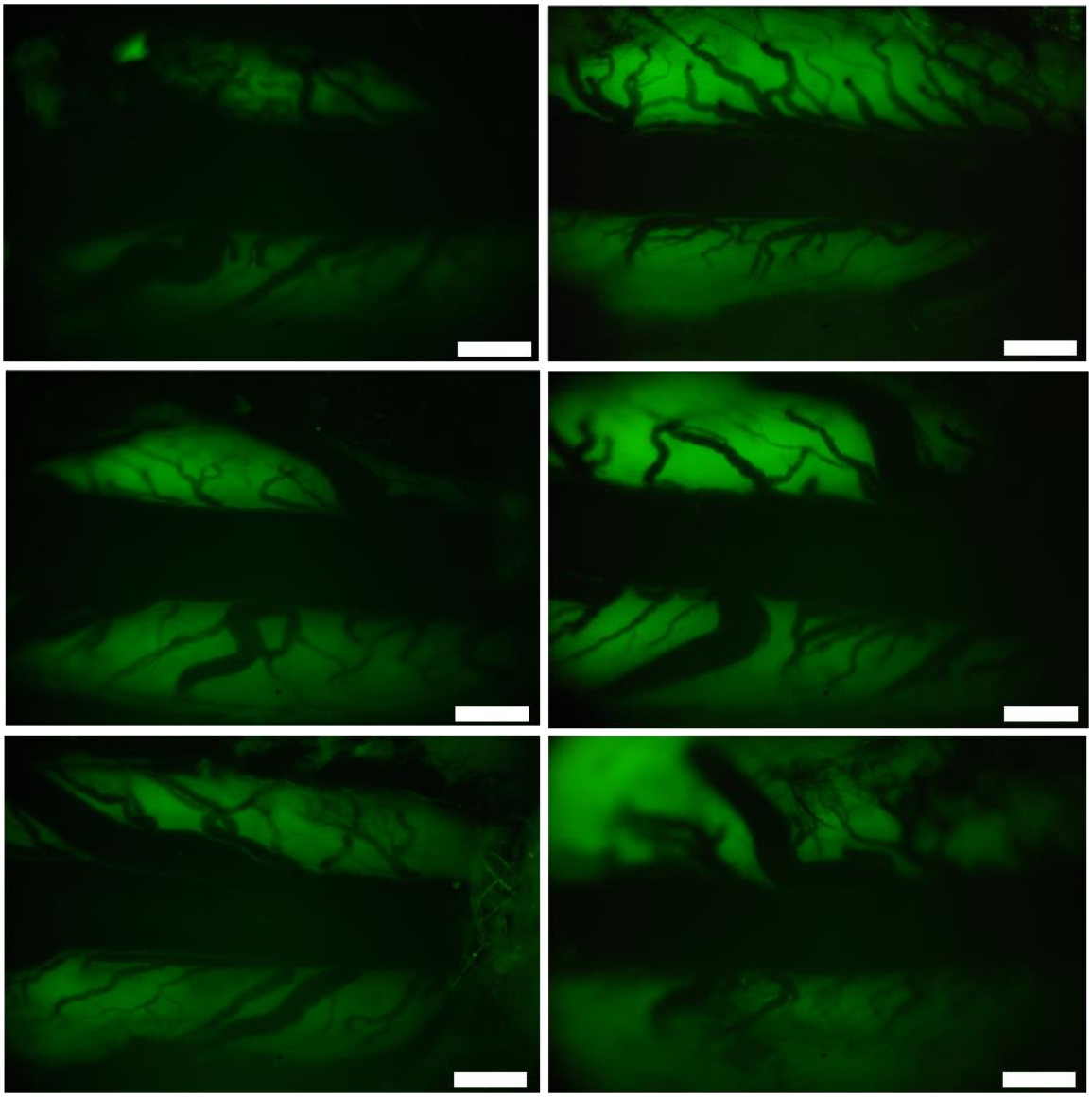

Figure 5-27. Spinal cord dorsal vein in six EAE rats at the 570 nm waveband. Scale bar represents 500 µm. Vessels can be seen to be significantly larger in EAE rats than in healthy controls (see Figure 5-26).

SO_2 values in healthy controls show some inter-animal variation (see Figure 5-31). Normoxia baseline SO_2 values were between 53.1% and 77.9%, with an average value of 67.8% SO_2 (See Table 5-4).

Venous SO_2 varied in a similar manner to FiO_2 across all rats (see Figure 5-28 and Figure 5-29) and correlated well with changes in arterial SO_2 as measured by the pulse oximeter (see Figure 5-30; correlation coefficient = 0.69).

In healthy controls, the average venous SO_2 changed in a statically significant manner between normoxia 1, hyperoxia, normoxia 2, and hypoxia 1 ($p < 0.01$, pairwise t-test) (see Table 5.6 and Figure 5-31). The difference between hypoxia 1 and hypoxia 2 was also significant, but to a lesser extent ($p < 0.05$) (see Table 5-4).

In healthy controls, vessel diameter did not change significantly throughout the experiment. No relation between changes in SO_2 and changes in vessel diameter was found (see Table 5-5).

The average venous SO_2 of EAE rats was consistently significantly lower than average SO_2 of healthy controls at ($p < 0.01$, pairwise t-test) at normoxia 1, hyperoxia; normoxia 2, and hypoxia 1. However the difference was not statistically significant at hypoxia 2 (see Table 5-6 and Figure 5-32). Data for hypoxia 3 was not reported due to high mortality of animals at 10% FiO_2.

No statistically significant difference between arterial SO_2 was recorded between EAE and healthy controls (see Figure 5-33). Artery – vein difference was lower for healthy controls than EAE rats at normoxia 1 and hyperoxia; however, this difference was only statistically significant at hyperoxia ($p = 0.05$). Artery – vein difference was similar for both EAE and control rats at normoxia 2 and hypoxia 1 ($p \sim 0.98$).

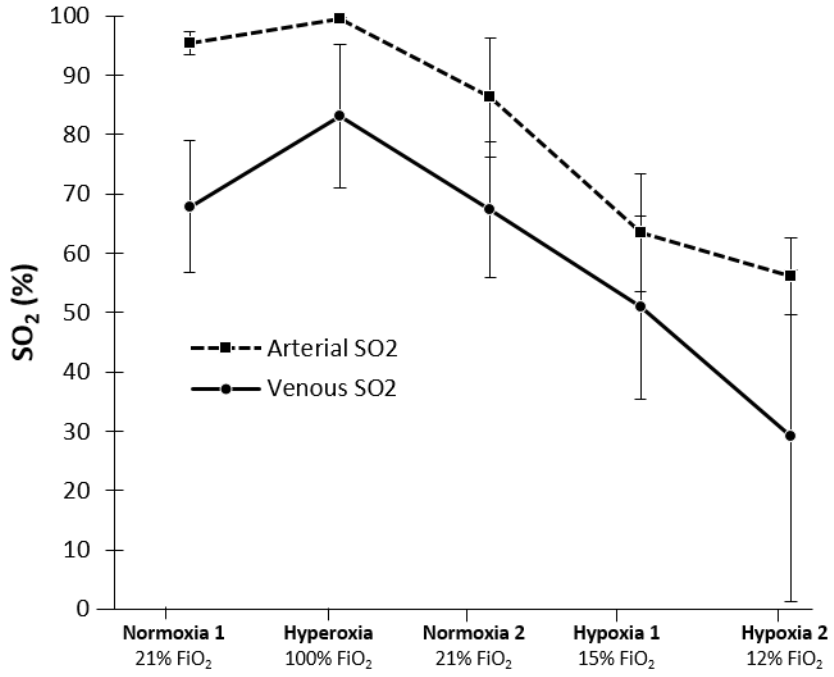

Figure 5-28. Venous SO_2 and arterial SO_2 of healthy controls vs. FiO_2. Error bars are ± standard deviation. n = 4 rats, except at hypoxia 2 where n = 3.

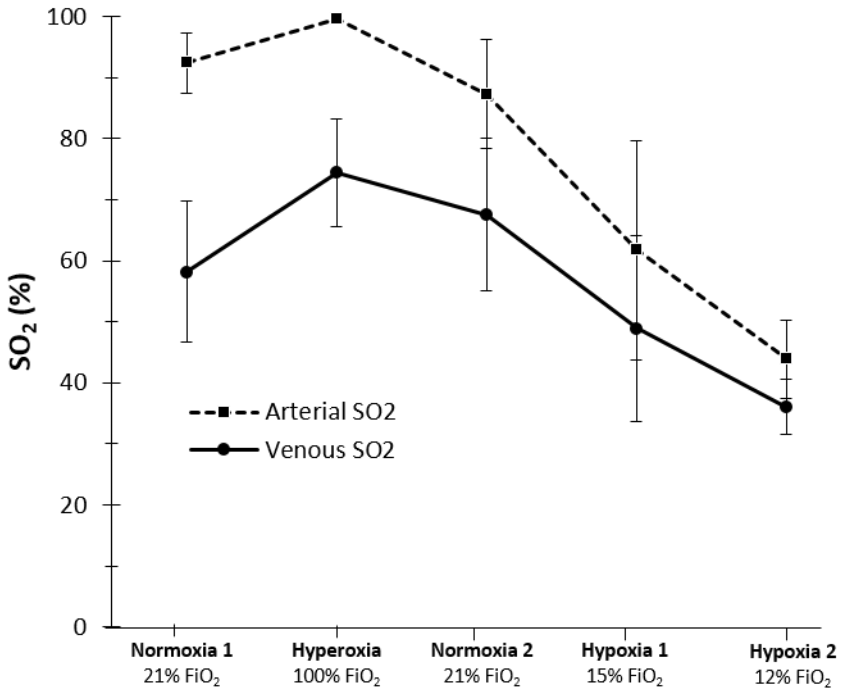

Figure 5-29. Venous SO_2 and arterial SO_2 of EAE rats vs. FiO_2. Error bars are ± standard deviation; n = 4.

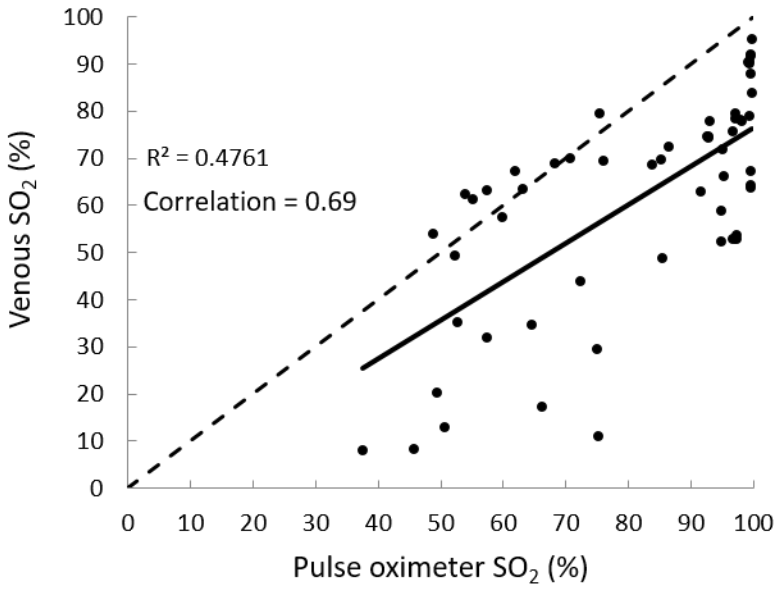

Figure 5-30. Pulse oximeter SO_2 vs. estimated venous SO_2. Solid line is a least-squares fit to venous SO_2; dashed line is 1:1 relation (i.e. unity).

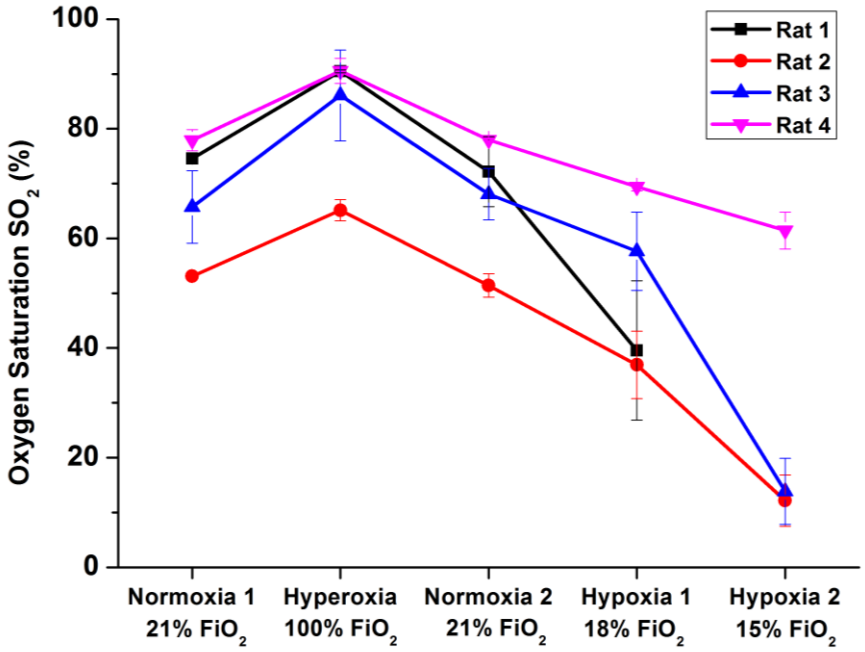

Figure 5-31. Venous SO_2 of four healthy control rats throughout the duration of the experiment. Three repeated measurements are shown for each rat.[v]

[v] Figure created by Marieke van der Putten.

Table 5-4. Venous SO_2 of healthy controls.[w]

	SO_2 ± standard deviation (%)					
	Rat 1	**Rat 2**	**Rat 3**	**Rat 4**	**Average**	**Change (p-value)**
Normoxia 1 (21% FiO_2)	74.6 ± 0.1	53.1 ± 0.5	65.8 ± 6.6	77.9 ± 1.9	67.8 ± 10.4	N/A
Hyperoxia (100% FiO_2)	90.5 ± 0.3	65.2 ± 1.9	86.1 ± 8.3	90.6 ± 2.3	83.1 ± 11.6	<0.01
Normoxia 2 (21% FiO_2)	72.2 ± 6.4	51.4 ± 2.1	68.1 ± 4.7	78.0 ± 0.2	67.4 ± 10.9	<0.01
Hypoxia 1 (18% FiO_2)	39.6 ± 12.7	36.9 ± 6.2	57.7 ± 7.2	69.4 ± 0.7	50.9 ± 15.5	<0.01
Hypoxia 2 (15% FiO_2)	N/A	12.2 ± 4.7	13.8 ± 6.0	61.5 ± 3.4	29.2 ± 24.6	<0.05

Table 5-5. Vessel diameter of healthy controls.[x]

	Vessel diameter ± standard deviation (µm)					
	Rat 1	**Rat 2**	**Rat 3**	**Rat 4**	**Average**	**Change (p-value)**
Normoxia 1 (21% FiO_2)	104.5 ± 0.9	87.7 ± 0.6	59.5 ± 1.4	100.5 ± 1.1	88.0 ± 20.3	N/A
Hyperoxia (100% FiO_2)	108.1 ± 0.6	89.8 ± 1.8	59.3 ± 1.4	103.0 ± 3.3	90.1 ± 20.9	0.89
Normoxia 2 (21% FiO_2)	105.5 ± 1.6	87.6 ± 0.7	57.9 ± 5.0	97.7 ± 1.3	87.1 ± 20.8	0.81
Hypoxia 1 (18% FiO_2)	107.0 ± 0.7	86.0 ± 0.7	60.8 ± 1.7	99.4 ± 1.4	88.3 ± 20.3	0.88
Hypoxia 2 (15% FiO_2)	N/A	81.7 ± 0.6	61.7 ± 1.3	99.3 ± 0.2	80.9 ± 18.8	0.34

[w] Data courtesy of Marieke van der Putten.
[x] Data provided by Marieke van der Putten.

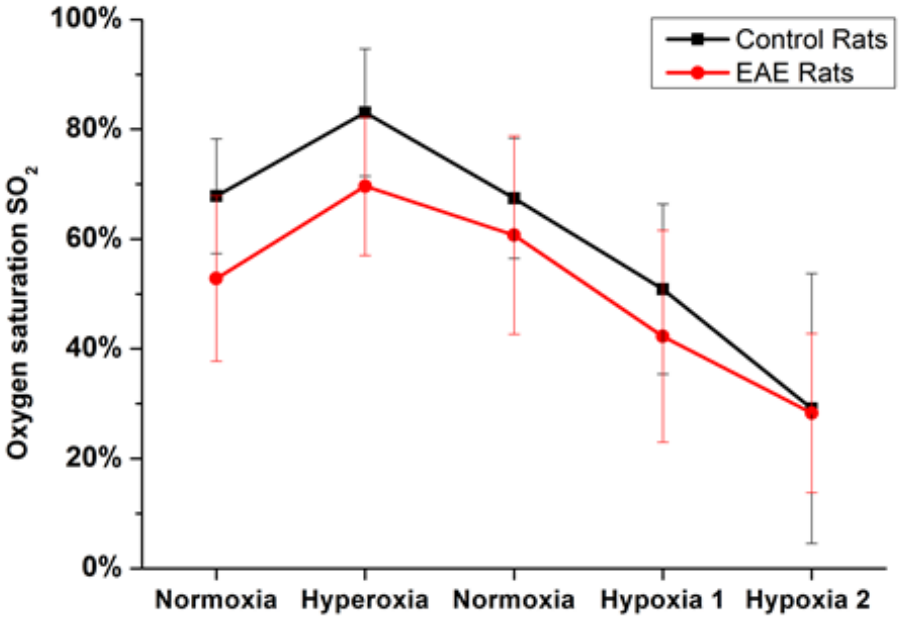

Figure 5-32. Average venous SO_2 of healthy controls and EAE rats throughout the experiment. Error bars are ± standard deviation of average SO_2 across each group.[y]

Table 5-6. Average venous SO_2 of healthy controls vs. EAE rats.[z]

	Control SO_2 (% ± SD)	EAE SO_2 (% ± SD)	Difference (p-value)
Normoxia 1 (21% FiO_2)	67.8 ±10.4	52.8 ± 15.1	<0.01
Hyperoxia (100% FiO_2)	83.1 ±11.6	69.6 ± 12.6	<0.01
Normoxia 2 (21% FiO_2)	67.4 ± 10.9	60.7 ± 18.1	<0.01
Hypoxia 1 (18% FiO_2)	50.9 ± 15.5	42.3 ± 19.3	<0.01
Hypoxia 2 (15% FiO_2)	29.2 ± 24.6	28.3 ± 14.5	0.92

SD = standard deviation.

[y] Figure created by Marieke van der Putten.
[z] Data provided by Marieke van der Putten.

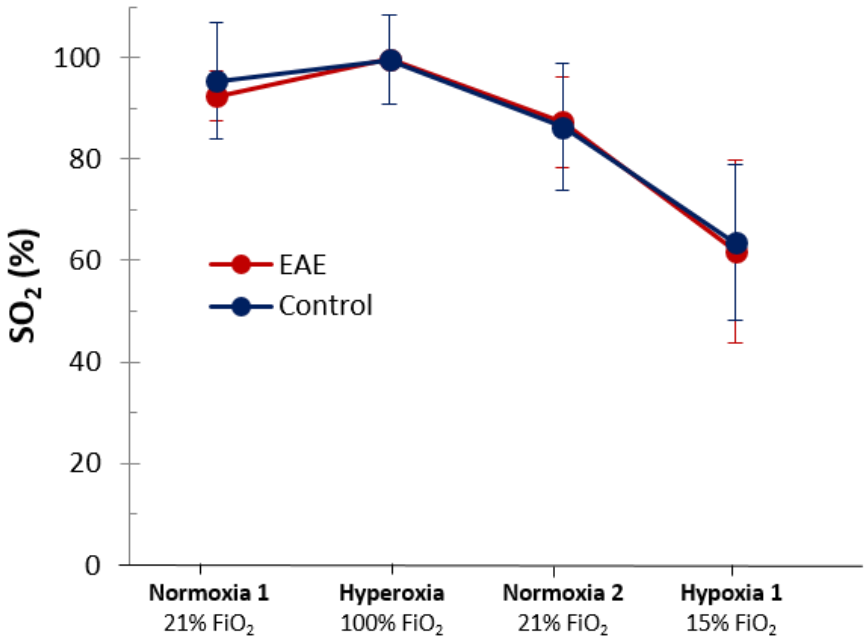

Figure 5-33. Pulse oximetry for healthy controls and EAE rats. No significant difference in arterial SO_2 was observed ($0.3 < p < 0.99$). NB: data for hypoxia 2 is not depicted due to the death of a control rat, which introduced large statistical anomalies.

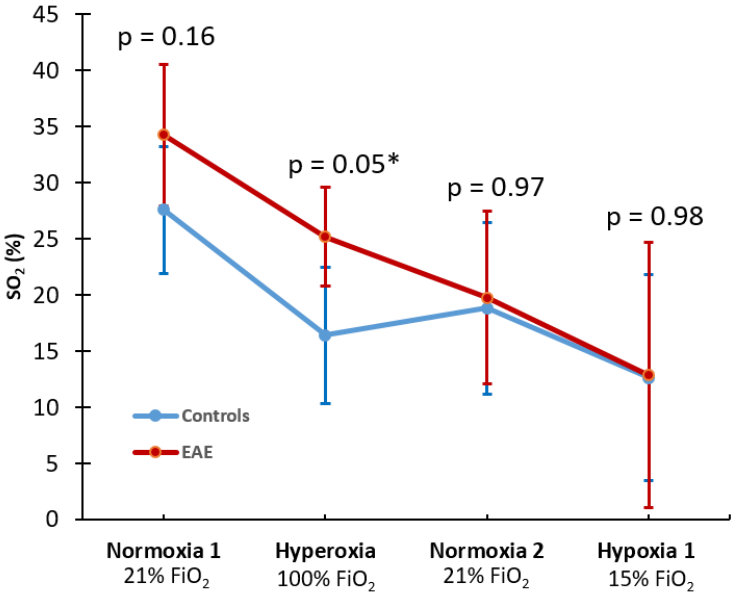

Figure 5-34. Artery – vein difference for healthy controls and EAE rats. Error bars are derived from the standard error of the mean of arterial and venous SO_2. NB: data for hypoxia 2 is not depicted due to the death of a control rat, which introduced large statistical anomalies.

5.6 Discussion

5.6.1 Mark 2 MSM image acquisition rate

Image acquisition rate of the mark 2 MSM was limited to approximately one image every seven seconds. Improving the time required for image acquisition would be desirable to decrease overall duration of the experiment and to increase temporal resolution to monitor fast changes in SO_2. In the future, image acquisition rate could be improved by a factor of ~ 62 by simply using a USB 3.0 enabled DSLR sensor; the data transfer rate of USB 2.0 is ~ 10 MB/s compared with 625 MB/s for USB 3.0. This improved data transfer rate would enable maximum image acquisition rate of ~ 8.3 Hz compared to the current rate of ~ 0.13 Hz. Further, this would require minimal changes to the existing LabVIEW microscope control GUI. An alternative approach to improve image acquisition rate could be to use .jpg image format. This approach was investigated, however it was found that .jpg format resulted in a reduction in apparent contrast of image features (Figure 5-35), and so is unsuitable for oximetry.

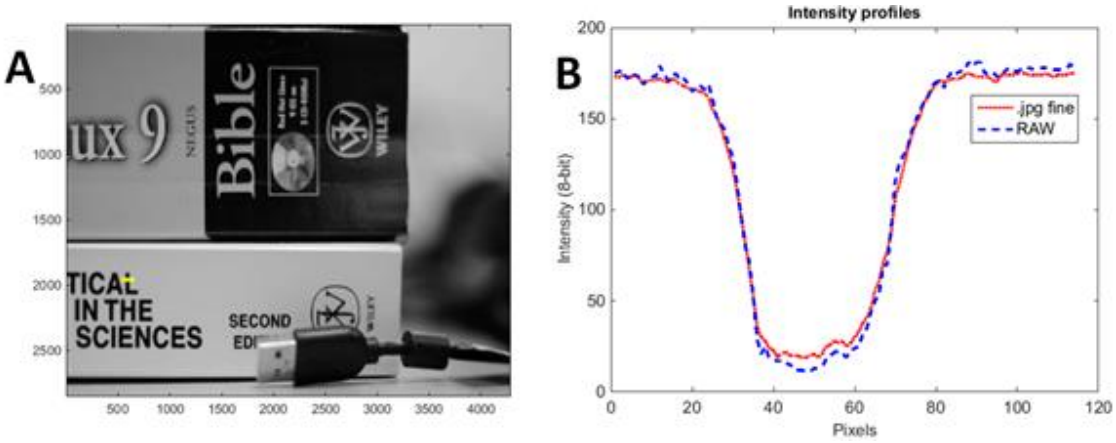

Figure 5-35. A comparison of 8-bit .jpg (fine) and 8-bit .TIFF image formats. **(A)** An image saved in both formats, with a line-profile highlighted as a yellow line. **(B)** Comparison of the line profile in .jpg and RAW format. Contrast is decreased in the .jpg image.

5.6.2 Performance and validation of oximetry algorithm

Estimated venous SO_2 values were physiologically plausible, with an average baseline normoxia venous SO_2 of 67.8% in healthy controls. This is close to the

"textbook" value of ~ 70% SO_2 for veins, indicating a believable estimated average SO_2. The inter-animal spread between 53.1% and 77.9% SO_2 is similar to the spread of inter-subject venous SO_2 values reported in human retinal oximetry studies.[105]

Estimated venous SO_2 correlated well with changes in FiO_2 (see Figure 5-28 and Figure 5-31). Further, a strong correlation (correlation coefficient = 0.69) between venous SO_2 and arterial SO_2 was observed (see Figure 5-30); this gives further confidence to venous SO_2 estimation.

However, *in vivo* validation of SO_2 measurements is extremely challenging. Measurements of partial pressure of oxygen (pO_2) using an oxygen quenching phosphorescence were not possible because this invasive measurement would rupture interrogated blood vessels, expose blood directly to ambient air, and result in the rat dying. An alternative approach in future experiments could be to use intra-venously injected phosphorescence probes for pO_2. However, this requires a significantly more complex imaging system.[122] No relation between estimated SO_2 and blood vessel diameter was found; this indicates that the oximetry algorithm was insensitive to vessel diameter.

Validation of the multispectral oximetry algorithm with a simple phantom was attempted. However, the scattering optical parameters of the phantom varied considerably in comparison to *in vivo* blood vessels due to both the plastic capillary used and changes in RBC shape due to sodium dithionite deoxygenation. This resulted in inaccurate estimation of *ex vivo* SO_2 when compared to blood gas analyser results.[277]

5.6.3 Oxygen diffusion considerations

The potential for oxygen diffusion from ambient air into blood vessels must be considered in any experiment where blood vessels are artificially exposed for imaging. Oxygen diffusion would act to increase SO_2 and it would affect small vessels more than large vessels. Our observations indicate that the small vessels in healthy controls have a higher SO_2 than larger EAE vessels, which could be consistent with oxygen diffusion. A characteristic feature of oxygen diffusion would be an increase in SO_2 along a tributary venule in the direction of the dorsal vein.

However, no such increase in SO_2 was observed (see Figure 5-36), giving confidence that the difference in SO_2 observed is due to altered metabolic demand of the spinal cord and not due to oxygen diffusion from ambient air.

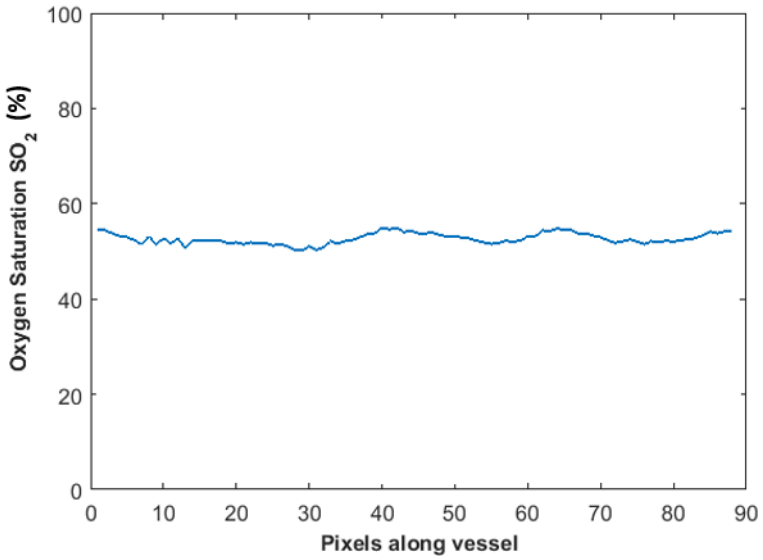

Figure 5-36. Typical oxygen saturation along a tributary vein. No increase in SO_2 was observed.[aa]

The use of mineral oil to create a barrier between air and blood vessels/tissue was investigated, however it was found that the mineral oil simply flowed away from the surgically sutured and raised spinal cord. This indicates that a more viscous substance would be required to stay in place for the duration of the experiment (~ 1 hour in total). The use of surgically-fitted spinal cord windows would block oxygen diffusion and enable longitudinal imaging studies of spinal cord vessels, reducing total animal usage.[165] The simplest method would however be the use of cling-film to block oxygen diffusion.[278]

5.6.4 Hypoxia in EAE and future work

Our results show that venous blood of EAE rat spinal cords is hypoxic in comparison with healthy controls. This indicates that more oxygen is being extracted from blood in the spinal cord tissue of EAE rats in comparison with healthy controls. This study opens the possibility of further *in vivo* study of hypoxia due to MS and

[aa] Figure courtesy of Marieke van der Putten.

EAE in both humans and animals, and it is planned that the results presented here will eventually be published as part of a larger study of EAE induced hypoxia in the spinal cord.

This study is, however, limited in that venous SO_2 was quantified in only nine rats (four healthy controls, five EAE). Imaging more animals would increase statistical power of the study and thus increase confidence in results. To maximise potential effect size, all EAE rats were of maximum EAE disease model severity (EAE score 9). It is expected that if this study were repeated with rats lower EAE scores (e.g. EAE scores 2-8), then observed venous hypoxia would correlate with EAE disease score.[10] Longitudinal imaging studies may be desirable to enable study SO_2 with EAE remission and in response to oxygen therapy.[10] Such longitudinal studies could be enabled by spinal cord dorsal windows or surgically implanted sensors.[165]

Non-invasive retinal oximetry in humans could provide insight into oxygen metabolism in MS. MS in the retina manifests as inflammation of the blood vessel wall of veins (phlebitis) and inflammation of the uvea (the layer of the eye between the retina and sclera, which includes the choroid),[279] so it is possible that retina oxygen metabolism may be altered. Retinal oximetry would enabled estimation of SO_2 in both arteries and veins, allowing a measure of metabolic uptake by retinal vessels.

5.6.5 Artery–vein difference

Artery–vein difference consistently decreased for EAE rats throughout the experiment. Further, artery – vein difference was lower for healthy controls at normoxia 1 and hyperoxia, although this was only statistically significant at hyperoxia (see Figure 5-34). There was no statistically significant difference in artery–vein difference between healthy controls and EAE rats at normoxia 2 and hypoxia 1. It is challenging to draw conclusive statements as to the significant of this because of the low statistical power of this study (4 controls rats and 4 EAE rats). Further, measurements of blood flow velocity were not made; such measurements are required to fully understand any potential auto-regulatory response.

A study of the metabolic demand of the rat retina was conducted by Yi et al., (2015).[179] Yi et al. conducted measurements of SO_2, vessel diameter, and blood

flow velocity using S-OCT. They found that artery-vein difference decreased under hypoxia. They concluded that this is due to auto-regulation of blood supply which resulted in increased blood flow rate, and thus a lower oxygen uptake from blood. A separate oximetry study human retina under acute-mild hypoxia (15% FiO_2) found that artery-vein difference did not change between normoxia and hypoxia, but did observe an increase in vessel diameter at hypoxia, indicating an auto-regulation response.[12]

To fully understand auto-regulatory response to changes in FiO_2, future studies of spinal cord dorsal vein SO_2 should include measurements of blood flow velocity. Further, a number of animals would be diserable to increase stastical power of results.

5.7 Conclusions

A multispectral microscope was developed for multispectral imaging of the rat spinal cord dorsal vein. The oximetry capability of the multispectral microscope was verified by imaging *ex vivo* blood samples of varying SO_2 levels and comparing recovered ODR and estimated SO_2 with blood gas analyser SO_2 measurements.

A calibration-free multispectral oximetry algorithm was developed to enable quantitative oximetry for comparison of SO_2 on an inter-vessel and inter-animal basis. Estimated SO_2 varied proportionally with FiO_2 as expected. The average venous SO_2 at normoxia was estimated to be ~ 68% and the spread of estimated venous SO_2 values was similar to inter-subject variability in retinal oximetry studies. The venous blood supply of EAE rats was found to be hypoxic in comparison with healthy controls, indicating that more oxygen is extracted from the blood of EAE rats than healthy controls. This is consistent with previous evidence for hypoxia in spinal cord tissue[10] and provides further evidence that hypoxia plays a crucial role in the development of the EAE disease model of MS.

Part of the research in this chapter has been submitted as a manuscript for review in the Institute of Physics journal '*Physiological Measurement'.*

6 Development of video-rate red eye oximetry: towards measurement of transient deoxygenation waves

Summary: *this chapter details the development of video-rate infra-red red eye reflection oximetry, with the eventual aim to measure the time-of-arrival of a transient deoxygenation wave to both eyes. This could potentially provide a method for screening of carotid artery occlusion, a major risk-factor for stroke. The motivation and background for video-rate red eye oximetry is detailed. Experimental considerations and the challenges for optimising video-rate red eye oximetry demonstrated and discussed. Recommendations for future research are made.*

6.1 Motivation

Chapter 4 details the use of a circulating transient deoxygenation wave (TDOW) for non-invasive retinal angiography. However, TDOWs could also potentially be used to probe lung to retina blood circulation time. Lung to retina circulation time is of particular interest for investigation of stenosis of the carotid artery; a major risk factor in stroke. Stenosis of one of the carotid arteries (see Figure 6-1) results in reduced blood flow rate, and thus an increased lung-to-eye circulation time in that side of the head, and thus generates a difference in time-of-arrival (TOA) of circulating blood between the left and right eye.

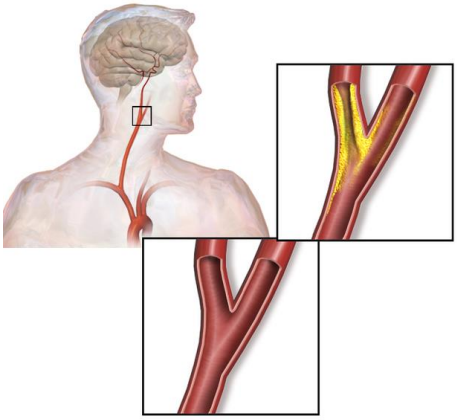

Figure 6-1. Carotid artery stenosis, a major risk-factor for stroke. Bottom inset: a healthy common carotid artery. Top inset: stenosis of the carotid artery caused by a build-up of plaque.[bb]

6.2 Retinal time of arrival and carotid stenosis: a review

A series of experiments conducted in the 1960s and 70s demonstrated that the TOA of circulating in blood could be used to investigate and screen for carotid artery stenosis. The first fundus reflectometry study was by Broadfoot et al., (1961)[280] which demonstrated the ability of a fundus reflectometer system to measure changes in several parameters *in vivo* in a rabbit, including changes in SO_2 due to an induced TDOW. Gloster (1967)[281] used fundus reflectometry to measure TOA of a TDOW to the eye.

Trokel (1964)[282] developed binocular fundus reflectometry to measure time-of-arrival of intra-venously injection fluorescein in both left and right eyes simultaneously in human subjects. They found no difference in the TOA left and right eyes in healthy subjects.

Oosterhuis et al., (1970)[264] developed a contact-lens mounted binocular fundus reflectometry system to measure fundus reflectance in both eyes of humans with minimal eye-motion artefacts. Measuring the TOA of intra-venously injected fluorescein, they found that carotid occlusion resulted in a delay of two seconds in

[bb] Figure reproduced from the Blausen Gallery under the Creative Commons 3.0 license.[300]

the arm-to-retina circulation time of fluorescein. NB: art-to-retina circulation time was normally 13 seconds in patients without carotid artery stenosis.

Lavenstein et al., (1971)[283] used a similar contact-lens reflectometry system to measure TOA of fluorescein to both the left and right eyes of a rabbit simultaneously. It was found carotid artery occlusion delayed the TOA of fluorescein by ~ 10% (i.e. a ~ 0.5 second delay with a circulation time of ~ 5 seconds).

Posthumus Meyjes and de Wilde (1977)[284] used the binocular fundus reflectometer system developed by Oosterhuis et al., (1970)[264] to measure the left-right delay in time-of-arrival due to carotid artery occlusion in 18 human subjects. Healthy controls showed no left-right delay in TOA, but subjects with carotid occlusion exhibited left-right delay ranging between 1 and 4.8 seconds. They concluded that a left-right difference in arm-to-retina circulation time of more than 1 second indicates a serious obstruction in the common carotid artery.

Bakker et al., (1979)[265] used a binocular reflectometry system to measure left-right circulation delay of humans in 50 healthy controls and 24 subjects with suspected carotid artery occlusions, 9 of which had total carotid artery occlusion. They found that in healthy subjects, on average, fluorescein arrived in the right eye 0.1 seconds after the left eye. Subjects with total carotid artery occlusion exhibited a left-right delay of between 1.3 and 3.5 seconds.

After the 1970s no further studies were conducted - perhaps due to the development of ultrasound techniques for non-invasive carotid artery diagnosis. However, these experiments demonstrated that carotid artery occlusion delays the TOA of intra-venously injected fluorescein by 1 to 5 seconds, and that the TOA of a TDOW could be detected in the eye. This logically progresses to the idea that the time of arrival of a TDOW could be used to probe carotid artery occlusion.

6.3 Red eye reflection oximetry

Near infra-red (NIR) red eye reflection oximetry has been developed by Choudhary et al.[153] to measure SO_2 of blood in the choroid of both eyes. It is possible to use red eye reflection for oximetry because NIR light is weakly absorbed by blood, so sufficient light can pass through the densely vascularised choroid (~

250 ± 80 µm thick),[39] before reflecting off of the sclera at the backing of the eye, passing through the choroid once again, and then eventually reaching the detector to be imaged. This results in a bright reflection from each eye of a subject (see Figure 6-2). The ability of NIR red eye reflection to measure acute mild hypoxia has been demonstrated by Choudhary et al,[153] who demonstrated that a change in intensity ratio (780 nm / 800 nm) of red reflection corresponded to changes in arterial oxygen saturation as measured by a pulse oximeter. In this experiment, single measurements at each SO_2 state (normoxia/hypoxia) were conducted.[153] However, sub-second red eye reflectometry measurements are possible with IRIS.

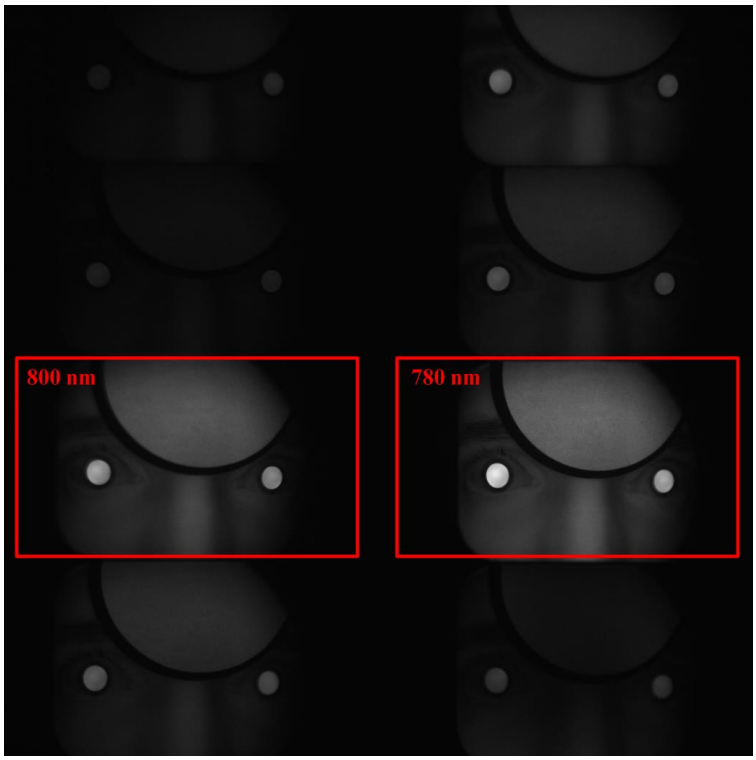

Figure 6-2. Red eye reflection in a single subject at eight NIR IRIS wavebands. The intensity ratio of the 780 nm and 800 nm wavebands can be used to measure changes in SO_2 in choroidal vasculature.[153] [cc]

Red eye reflection can be used to measure changes in SO_2 simultaneously in both eyes of a subject with sub-second temporal precision. This could be theoretically used to measure the TOA of a circulating TDOW to the retina. For TOA

[cc] Figure courtesy of Tushar Choudhary.

measurement, the retinal region imaged by red-eye (i.e. the visual angle) must be sufficiently small to avoid contamination of the optic disk and to measure a relatively limited choroidal area. Measurement of a limited choroidal area is important because the choroid fills with blood from several perforating ciliary arteries, resulting in a slightly different filling time across the choroid. Gloster (1967)[281] found that a visual angle of 6° was sufficient to measure a TDOW in the choroid. The visual angle imaged by red eye reflection can be calculated by:

$$\text{Visual angle} = 2\theta \; = \; 2\tan^{-1}\left(\frac{1}{2}\frac{d4}{d3}\right), \qquad 6\text{-}1$$

where each term is given by the geometry shown in Figure 6-3.

The relation between the distance of a subject from a fundus camera and visual angle is shown in Figure 6-4. From Figure 6-4., it can be seen that to obtain a visual angle of 6°, subjects must be situated ~ 35 cm from the objective lens of a fundus camera. Figure 6-5 shows the relation between retinal FOV imaged and distance from the fundus camera. This is calculated by assuming that a 1° FOV corresponds to ~ 0.28 mm of the retina.[285]

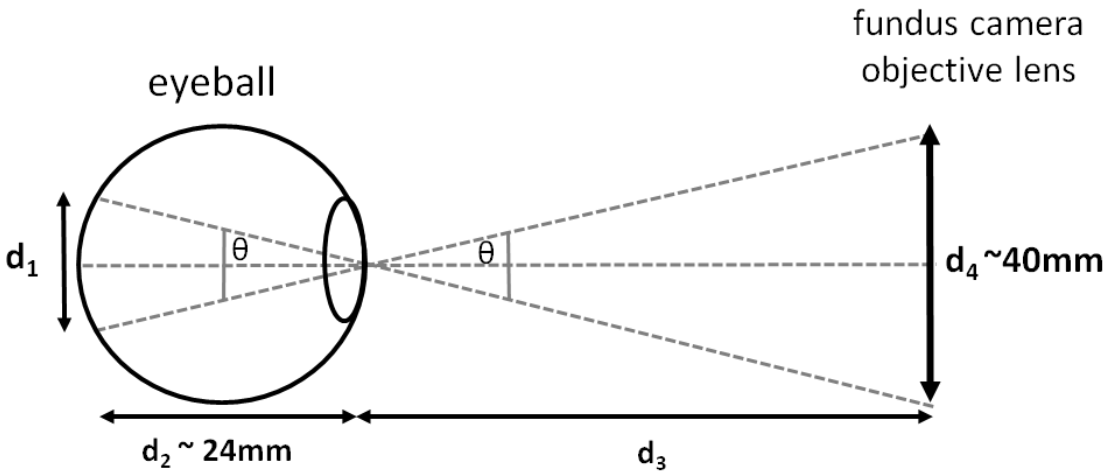

Figure 6-3.Geometry for the calculation of visual angle subtended by a red eye reflection image. d_1 is the diameter of the retinal region imaged; d_2 is the diameter of the eyeball (24 mm); d_3 is the distance between the pupil and the imaging system; and d_4 is the diameter of the fundus camera objective lens (~ 40 mm).

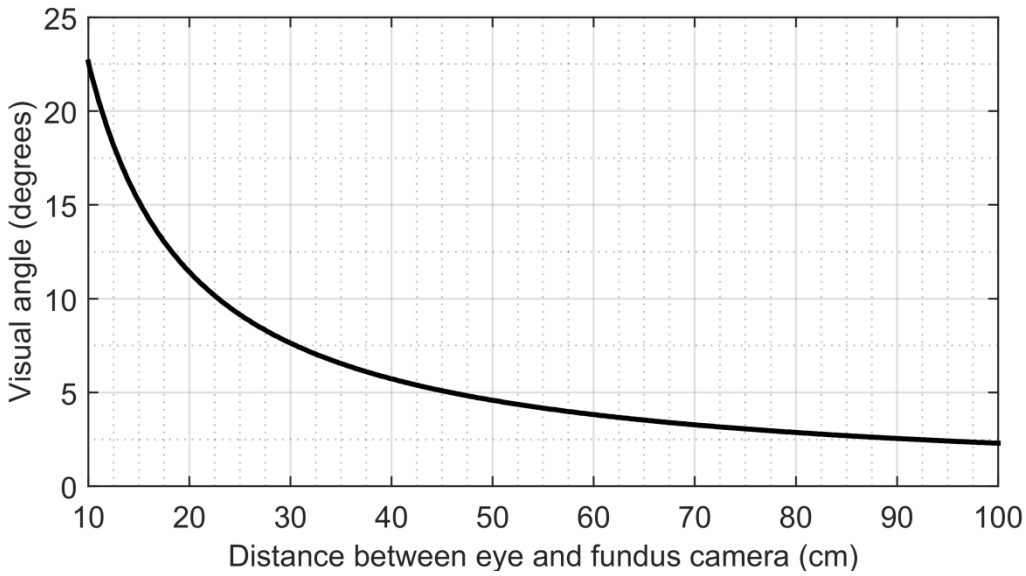

Figure 6-4. Visual angle subtended by red eye reflection imaging vs. distance of a subject from the fundus camera.

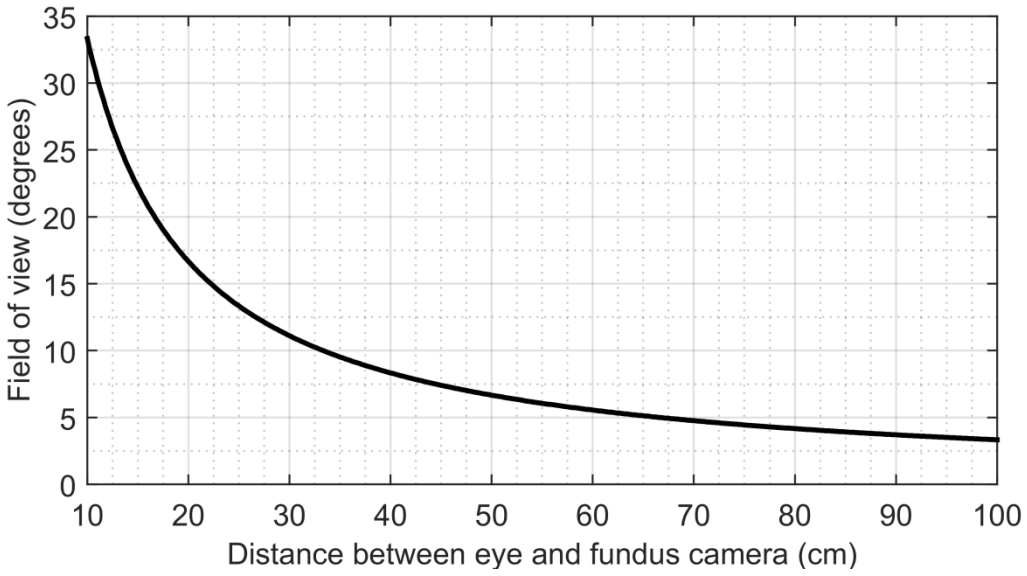

Figure 6-5. Field of view subtended by red eye reflection imaging vs. distance of a subject from the fundus camera.

6.4 Imaging set-up

Data for this study was recorded with a retinal fundus camera (TR50-DX; *Topcon*) modified with IRIS and a cooled sCMOS detector (Zyla 5.5; *Andor*). Image acquisition was controlled by *Image J* [255] and images were saved in uncompressed .TIFF format. A bandpass filter (770 – 815 nm) was placed in the illumination path of the fundus camera, with illumination provided by the fundus camera inspection lamp. IRIS was configured without the filter plate,[11] enabling near infra-red spectral imaging. The resulting infra-red spectral transmission of the bandpass filter and IRIS wavebands are shown in Figure 6-6.[dd] The corresponding effective extinction coefficients of O_2Hb and Hb for each of these wavebands was estimated as per Section 5.4 and are summarised in Table 6-1. From this, the 780 nm waveband was suitable for a high-contrast, oxygen-sensitive waveband, and the 800 nm waveband was suitable as an isobestic reference.

[dd] Data for spectral transmission of IRIS wavebands was provided by Javier Fernandez Ramos.

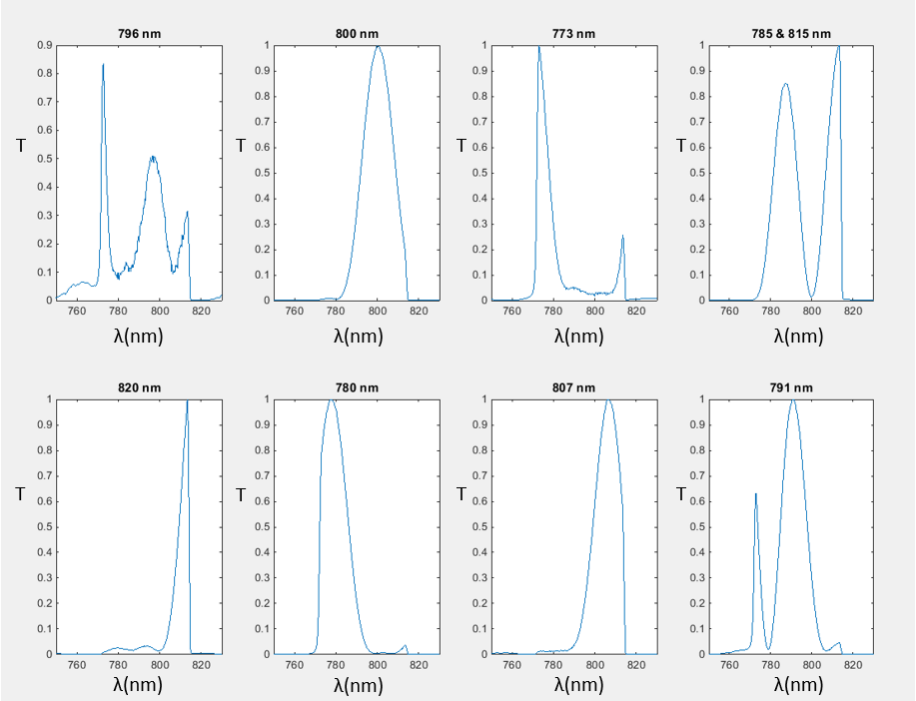

Figure 6-6. The normalised spectral transmissions of each IRIS waveband in the range 760 – 820 nm with the 770 – 815 nm bandpass filter in place. The 780 nm waveband was used as oxygen-sensitive, whilst the 800 nm waveband was used as an isobestic reference.

Table 6-1. Estimated effective extinction coefficients (ε_λ) of near infra-red IRIS wavebands for O_2Hb and Hb.

Visible IRIS waveband (nm)	**Corresponding near infra-red IRIS waveband** (nm)	**ε_λ O_2Hb** (cm^{-1} M^{-1})	**ε_λ Hb** (cm^{-1} M^{-1})	**Note**
587	796	756	958	Medium contrast
567	800	807	789	Isobestic
579	773	707	1113	High contrast
560	7815	785	870	Pseudo-isobestic
600	820	837	759	Pseudo-isobestic
577	780	704	1099	High contrast
591	807	828	759	Pseudo-isobestic
570	791	746	944	Medium contrast

6.5 Automated intensity ratio calculation

For objective measurement of intensity ratio, information must be extracted from images in an automatic manner. This can be achieved by simple binary thresholding of a red eye reflection image as shown in Figure 6-7 and Figure 6-8. After thresholding, the binary mask can be multiplied with the intensity image to provide intensity only in the region of interest. Example of binary masking is shown in Figure 6-9.

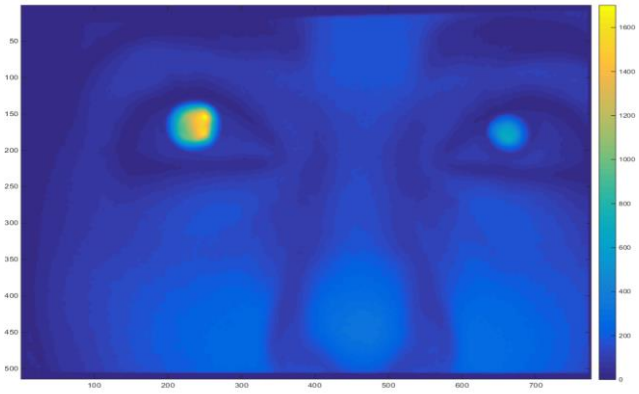

Figure 6-7. A red eye reflection image. NB: the subject's left eye was dilated using 1% Tropicamide, whilst the right eye was not (see Section 6.6).

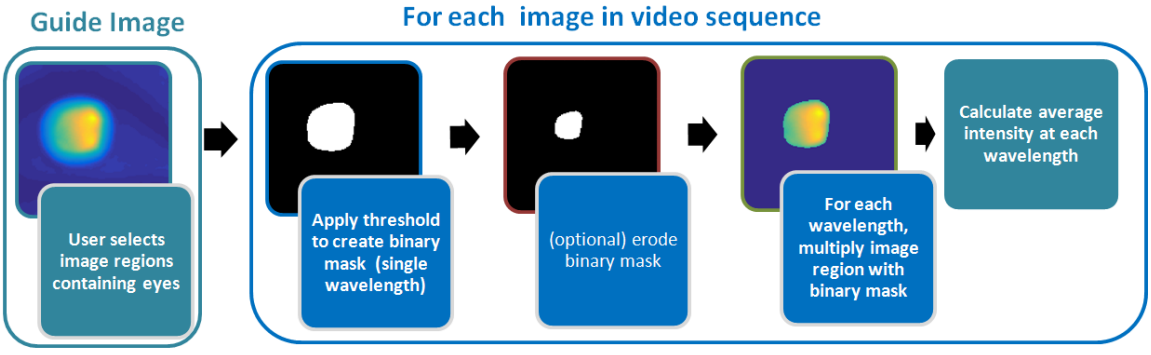

Figure 6-8. Flow-chart depicting image processing steps to select regions of interest for red eye reflection intensity measurement.

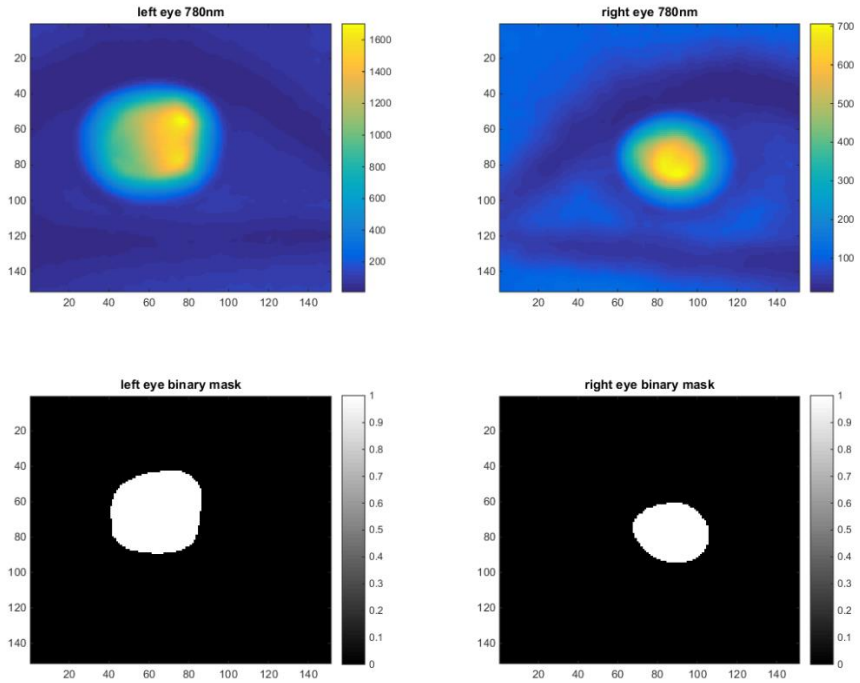

Figure 6-9. Binary thresholding to automatically extract red eye reflection. (Top) cropped images of left and right eyes. (Bottom) binary thresholding of left and right eyes.

6.6 Challenges of red-eye reflectometry measurement

Measuring intensity of red eye reflection continuously for several minutes creates several challenges. These influence of these parameters were tested in human subjects.

1. Firstly, the eye gaze position of subjects tends to drift with time, even when a fixation target is used. This will change the region of the retina being imaged and will thus create a slow and spurious change intensity ratio, which could be misinterpreted as corresponding to a change in SO_2 (see Figure 6-10).
2. Similarly, when subjects inhale a hypoxic air mixture, they are likely to move their head, even when using a headrest. This may result in spurious measurement.
3. The retinal region imaged may encompass the optic disk. This will result in a very bright spurious reflection from the optic disk (see Figure 6-11).

4. Small involuntary eye movements (i.e. micro-saccades) will introduce variability in measurement.[81,286] This may be the cause of noise seen in Figure 6-12.
5. The subject's eyelashes may cover part of their eye, resulting in spurious binary thresholding, and adding variability to measurements.
6. Subjects blink, resulting in no useful data from some video frames. When the subject's eyelid are closed the recorded intensity is decreased dramatically, but intensity-ratio shows minimal change (see Figure 6-12).
7. Subjects sitting further from the fundus camera objective lens will have a smaller retinal region imaged (see Figure 6-4 and Figure 6-5). This reduced retinal image region results in a lower intensity of light reaching the detector, and also increased sensitivity to random variations due subject motion (see Figure 6-14). Such random variations are likely due to micro-saccades of the eye.[81,286]
8. If mydriasis is not employed (e.g. if 1% Tropicamide eye drops are not applied), then the subject's pupil size may change, altering the size of the retinal region imaged. This effect is shown in Figure 6-15.

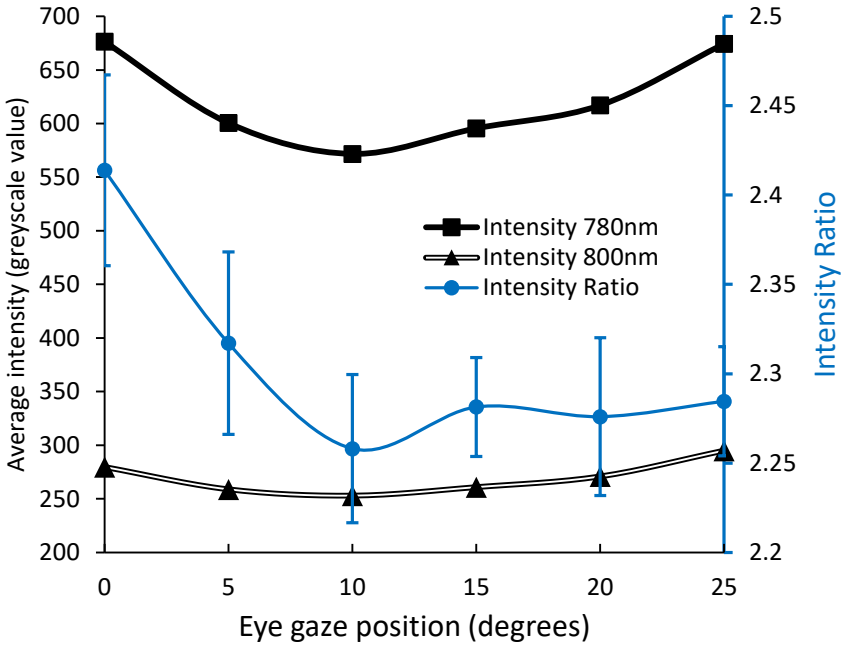

Figure 6-10. Intensity and intensity ratio of red eye reflection from the left eye of a subject vs eye gaze position. Subject's eye gaze position was changed from straight ahead (0 degrees) incrementally to the left, up to a maximum of 25 degrees.

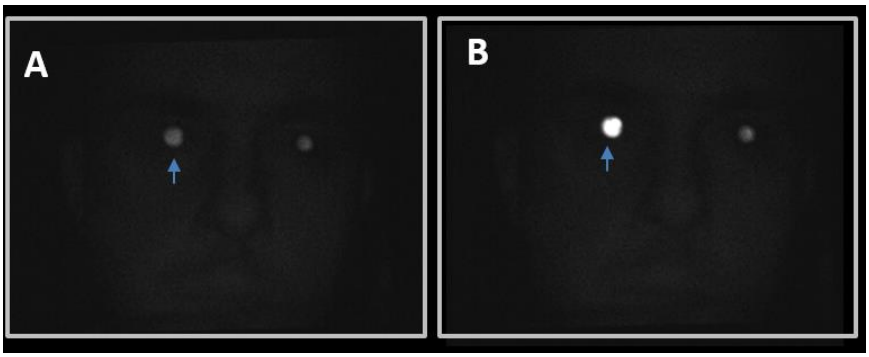

Figure 6-11. Red eye reflection is increased when optic disk is present within imaged retinal region. **(A)** Red eye reflection image of a subject without the optic disk in imaged region. **(B)** Red eye image when gaze position was changed so that the optic disk was within the imaged region of the eye. The blue arrow denotes the relevant eye.

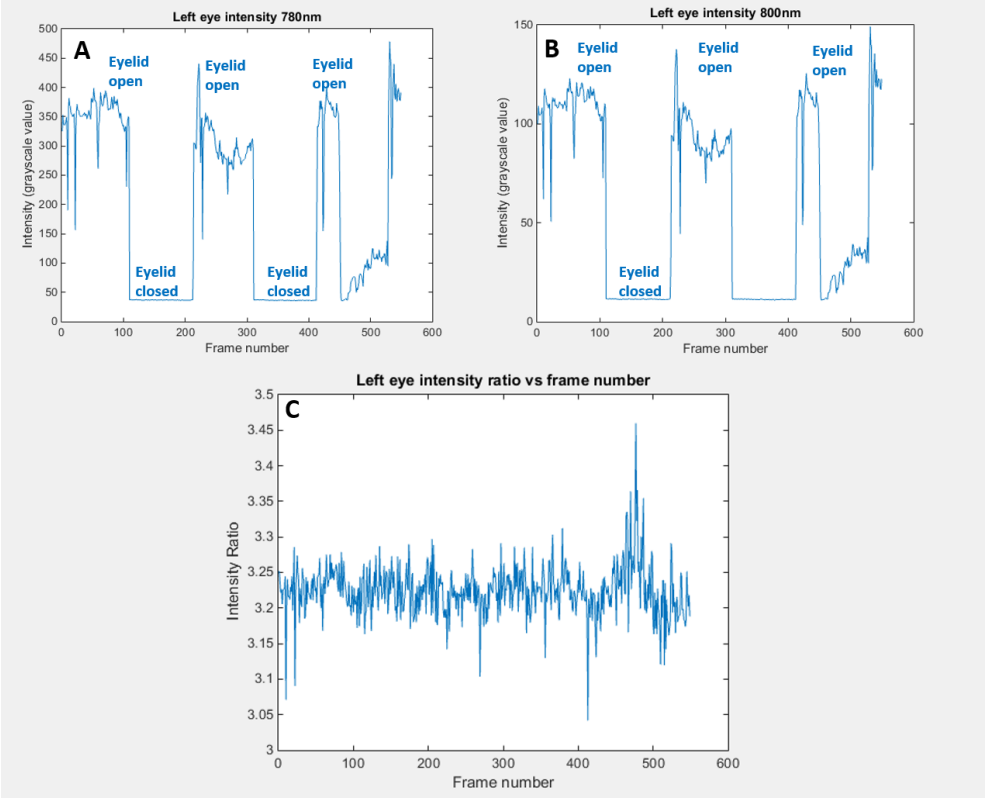

Figure 6-12. The effect of eyelid closure on measured intensity and intensity ratio. **(A)** Intensity of eye at 780 nm vs frame number (3 frames per second). **(B)** Intensity of eye at 800 nm waveband vs frame number. **(C)** Resulting intensity ratio vs frame number.

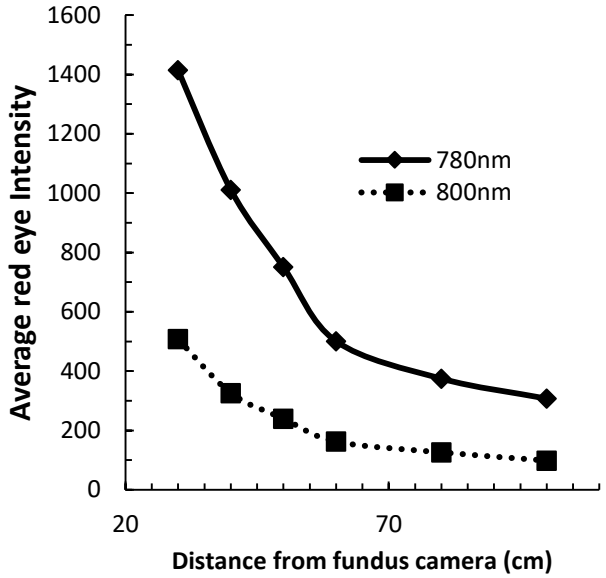

Figure 6-13. Average intensity of red eye reflection vs. distance of the subject from the fundus camera objective lens.

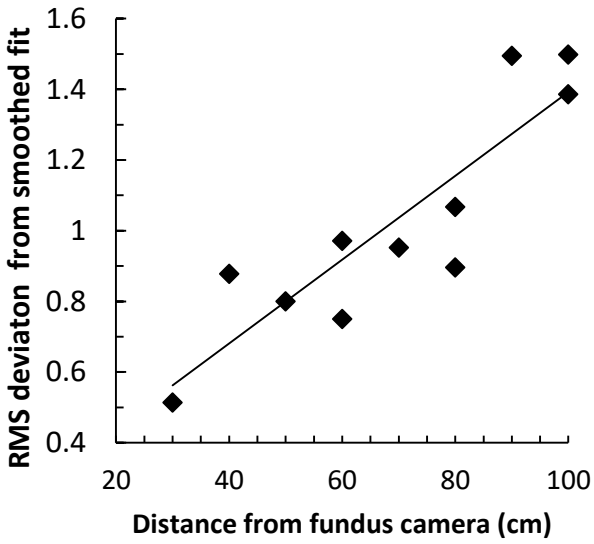

Figure 6-14. Average RMS deviation from a smoothed fit of intensity ratio (i.e. a measure of random variation) vs. distance from the fundus camera objective lens. RMS deviation increases with distance, indicating that a smaller visual angle results in greater variability, likely due to random motion of subject with respect to the camera.

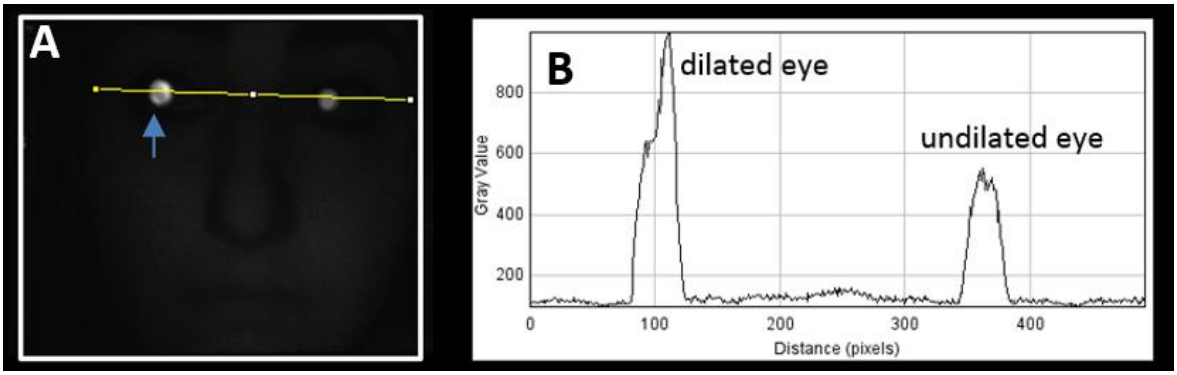

Figure 6-15. Intensity of red eye reflection increases with mydriasis. **(A)** Red eye image with one eye dilated (indicated by blue arrow). **(B)** Intensity profile of the yellow line. The dilated eye has a peak intensity approximately 2 times that of the undilated eye.

6.7 Conclusions and future work

Applying video-rate red eye reflection oximetry to measurement of a circulating TDOW has the potential to provide a screening method for carotid artery occlusion. Studies in the literature have shown that carotid artery occlusion results in a delay in left-right retinal TOA of a circulating fluorescein by 1 - 5 seconds. This should also apply to the TOA of a TDOW, which should theoretically be measurable simultaneously in both eyes with video-rate infra-red red eye reflection oximetry using a fundus camera and IRIS.

Several variables which can mar video-rate red eye intensity ratio measurement have been explored. These include subject gaze position, subject blinking, the subject's eyelashes, accidental imaging of the optic-disk, and changes in subject pupil size (if mydriasis is not used).

Future work to measure TOA of a TDOW should be conducted in an incremental manner to help troubleshoot any problems. The major challenges are expected to be characterisation of circulating TDOWs, and the low spectral contrast between Hb and HbO_2 at near infra-red wavelengths. To eliminate the problems with low spectral contrast, these problems be explored first with visible-waverange red eye reflection, where contrast between Hb and O_2Hb is strong, and where the detection of TDOWs has been established (see Chapter 4). Once the feasibility of visible-waverange

measurement of TDOWs is established, then measurements should be conducted in the near infra-red waverange, where oximetric contrast is weaker. Infra-red measurement is more comfortable for subjects. However, the challenges of subject gaze control and motion will have to be considered and well controlled to provide high-quality measurements.

7 Conclusions

The aim of the research presented in this thesis was to develop new applications of *in vivo* oximetry using multispectral imaging. Four applications were investigated:

(1) Oximetry in bulbar conjunctival and episcleral microvasculature.
(2) Non-invasive retinal angiography using multispectral imaging (ORCA).
(3) Oximetry of the spinal cord dorsal vein of rats to investigate hypoxia associated with the EAE disease model of Multiple Sclerosis.
(4) Development of video-rate red eye oximetry to measure the time-of-arrival of circulating transient deoxygenation waves.

7.1 Bulbar conjunctival and episcleral oximetry

The aim of the research in Chapter 3 was to use snapshot multispectral imaging to investigate the oxygen dynamics of the bulbar conjunctival and episcleral microvasculature. In particular, it aimed to establish the oxygen dynamics of these microvascular beds at normoxia and acute mild hypoxia conditions, and characterise any effects associated with oxygen diffusion from ambient air.

Hypoxic bulbar conjunctival vessels were observed to undergo rapid oxygen diffusion from ambient air, reaching normoxia oxygen levels in just a few seconds. To the best of the author's knowledge, this is the first direct observation of this reoxygenation effect *in vivo* anywhere in the body. Apart from the bulbar conjunctiva, the only other blood vessels known to extract oxygen directly from air are the alveolar capillaries in the lungs. From this observation of reoxygenation, it is possible to conclude that the bulbar conjunctival microvasculature will always be close to 100% SO_2 when exposed to air (i.e. when the eyelid is open) because the bulbar conjunctival vessels will be in pO_2 equilibrium with ambient air. In contrast, episcleral vessels were not observed to undergo oxygen diffusion because episcleral vessels are embedded within scleral tissue.

Oximetry was however, limited by the lack of calibration SO_2 values for two-wavelength oximetry, so results were reported in terms of ODR. This is problematic because ODR can be influenced not only by SO_2, but also by changes in blood vessel diameter and blood flow. Whilst these factors are were not thought to

influence the study significantly, quantitative oximetry would be preferable. In future, multi-waveband oximetry algorithms could be used to estimate SO_2; the bulbar conjunctival and episcleral vessels could be an ideal test-bed for such oximetry algorithms because the sclera contains no pigmentation and the bulbar conjunctiva has minimal overlying tissue to scatter light.

This study opens for the potential for high-magnification multispectral imaging for oximetry of the bulbar conjunctival microvasculature. This could enable oximetry in individual capillaries and groups of erythrocytes *in vivo.* Bulbar conjunctival oximetry may be useful for providing insight into oxygen dynamics in studies of a variety of conditions where hypoxia is thought to play a role, including diabetes, sickle-cell anaemia, ocular burn recovery, surgical or traumatic wound healing, dry eye syndrome. Bulbar conjunctival oximetry could also be of interest for studies of hypoxia induced by contact lens wear. However, the effects of oxygen diffusion must be taken into account for any such studies to provide meaningful oximetry results.

Episcleral oximetry could potentially serve as a proxy for oximetry of the ophthalmic artery if retinal imaging is not possible (e.g. due to cataracts). Further, episcleral SO_2 may be altered by high intra-ocular pressure, so SMSI oximetry could potentially provide insights into the effects of high intra-ocular pressure.

7.2 Oximetric Ratio Contrast Angiography

The aim of the research in Chapter 4 was to develop and demonstrate an entirely new and non-invasive angiography technique: Oximetric Ratio Contrast Angiography (ORCA). ORCA utilises non-invasive perturbation in SO_2, multispectral imaging, and computational processing to visualise blood flow. A pilot study of ORCA for non-invasive human retinal angiography was conducted *in vivo*. This pilot study demonstrated that ORCA is capable of visualising flow features such as sequential vessel filling and laminar flow. No other non-invasive angiography technique is capable of visualising these features.

Whilst ORCA is highly promising, considerable work can be done in future to improve subject comfort, image acquisition, and computational processing procedures. Further validation in better-controlled experiments such as phantoms or anesthetized animals would be highly beneficial in testing the intrinsic robustness

and repeatability of ORCA. The procedure used here to induce a transient deoxygenation wave seems to have no adverse consequences in healthy humans, however the risks of inducing such a transient deoxygenation wave have not been clinically studied. It is currently unknown what the minimum change in SO_2 required for ORCA is; minimising the change in SO_2 required would be desirable as it would reduce any potential risks.

The implementation of ORCA described in Chapter 4 could be improved in several ways. Firstly, subject motion could be better controlled by employing a bite-ring (or similar) to minimise bulk motion of the subjects head, and optimising the ergonomics of the imaging and gas delivery systems. Secondly, the light intensity of the imaging system could be reduced, making ORCA imaging more comfortable for subjects. Thirdly, more advanced image processing methods could be employed to reduce computation time and improve robustness of ORCA analysis.

The retinal fundus camera with IRIS was adequate for ORCA measurements. However, any imaging technique capable of multispectral oximetric imaging with high temporal resolution (~ 1 Hz) could be employed. Commercial multispectral scanning laser ophthalmoscopy systems could potentially reduce corneal glare, reduce illumination intensity, provide a wider field of view, and eliminate the need for pupil dilation. Multispectral photoacoustic tomography could potentially be used for deep-tissue ORCA. Combined ORCA blood flow and oximetry measurements could potentially provide measurements of metabolic rate, which would be beneficial for studying applications such as blood-oxygen uptake in the development of tumours. Currently two separate imaging systems are required to do this: one to measure blood flow, and one to measure oxygen saturation. However, a system capable of ORCA could measure both simultaneously. This could decrease experimental complexity, reduce cost, and increase experimental information yield.

7.3 Rat spinal cord oximetry

The aim of the research in Chapter 5 was to develop a multispectral microscope for oximetry of spinal cord dorsal vein blood vessels in rats. This multispectral microscope was applied to investigate venous SO_2 in both healthy rats, and in rats with the EAE disease model of Multiple Sclerosis. The key finding of this research is that the venous SO_2 of EAE rats was significantly lower in comparison to healthy

controls, suggesting a greater uptake of oxygen from blood due to EAE. This agrees well with prior studies of hypoxia in spinal cord tissue.[10]

This is the first study to use a multispectral oximetry algorithm for quantitative oximetry in spinal cord blood vessels. The algorithm estimated physiologically plausible values for SO_2, with an average venous SO_2 of 68% in healthy controls at normoxia; this is close to the textbook value of 70% SO_2 for venous blood.[15] Estimated SO_2 in all rats varied in proportion with altered FiO_2 at hyperoxia and hypoxia. Direct quantitative *in vivo* validation of oximetry was not possible with the techniques at our disposal. However, in future studies, a injected pO_2-sensitive phosphorescence probe could be used to validate oximetry.[122] This would however, required a considerably more complex imaging system, requiring the temporal modulation of luminesce, as well as development and application of an oxygen-sensitive phosphorescent molecular probe.

Future work may include longitudinal studies of dorsal vein SO_2 in rats for observation of EAE remission or in response to oxygen therapy. The snapshot capability of IRIS could be very useful for studying rapid changes in SO_2 that were not observable with the current imaging system. In humans, non-invasive retinal oximetry could be used to directly measure if metabolic demand is altered in MS patients.

7.4 Development of video-rate red eye oximetry: towards measurement of transient deoxygenation waves

The aim of Chapter 6 was to develop the technique of video-rate red eye reflection oximetry to the sensitivity required to measure transient deoxygenation waves as they circulate around the body. If red eye oximetry could detect transient deoxygenation waves, then it could potentially be employed as a screening method for carotid artery stenosis; a major risk-factor for ischemic stroke.

Whilst video-rate red eye oximetry is feasible, the challenges of involuntary subject motion are considerable. Factors such as eye gaze position, blinking, eyelashes, imaging the optic disk, and pupil dilation can all influence red eye measurements. In future work, involuntary subject motion must be well controlled to provide good measurements.

Unfortunately, due to time constraints it was not possible to test if near infra-red red eye reflection oximetry can measure transient deoxygenation waves. However, there are good prospects in future to do so at both visible and near infra-red wavebands.

7.5 Concluding remarks

The work described in this thesis demonstrates that there are novel and highly-innovative prospects for multispectral oximetry. In particular, the high temporal-resolution provided by IRIS enables novel observations that are simply not possible with slower time-sequential imaging modalities. In this thesis, these novel insights include the observation oxygen diffusion into bulbar conjunctival microvasculature and the measurement circulating TDOWs in the retina, both for the first time. The development of TDOWs as an angiographic contrast agent for blood flow is highly innovative. As well as non-invasive angiography, TDOWs could be used to measure blood circulation time, which could be useful in studying and screening for vascular impairment in cardiovascular diseases, such as carotid artery occlusion: a major risk-factor for ischemic stroke.

Throughout the research in this thesis, the challenges of non-invasive *in vivo* imaging are highly apparent. For example, measurement of intensity ratio for ORCA and red eye reflection oximetry can be marred by involuntary subject movement. Further, it will always be highly challenging to account for the optical scattering and absorption properties of diverse biological tissues; thus the problem of imperfect information will still persist. *Ex vivo* validation of oximetry measurements is also a persistent challenge. Controlled deoxygenation of blood is challenging, and ensuring that the optical properties of phantoms are as close to that of tissue is highly problematic. However, bio-mimetic 3D-printed biological phantoms could improve future prospects. Despite these challenges, the field of multispectral imaging oximetry holds great potential for new technologies, applications, and scientific discoveries.

8 References

1. Kaur C, Foulds WS, Ling E-A. Hypoxia-ischemia and retinal ganglion cell damage. *Clin Ophthalmol*. 2008;2(4):879-889. doi:10.2147/OPTH.S3361.
2. Saugstad OD. Oxygen and retinopathy of prematurity. *J Perinatol*. 2006;26(February):S46-S50. doi:10.1097/IIO.0b013e3182009916.
3. Tiedeman JS, Kirk SE, Srinivas S, Beach JM. Retinal oxygen consumption during hyperglycemia in patients with diabetes without retinopathy. *Ophthalmology*. 1998;105(1):31-36. doi:10.1016/S0161-6420(98)71029-1.
4. Hammer M, Vilser W, Riemer T, et al. Diabetic patients with retinopathy show increased retinal venous oxygen saturation. *Graefes Arch Clin Exp Ophthalmol*. 2009;247(8):1025-1030. doi:10.1007/s00417-009-1078-6.
5. Olafsdottir OB, Hardarson SH, Gottfredsdottir MS, Harris A, Stefánsson E. Retinal oximetry in primary open-angle glaucoma. *Invest Ophthalmol Vis Sci*. 2011;52(9):6409-6413. doi:10.1167/iovs.10-6985.
6. Mordant DJ, Al-Abboud I, Muyo G, Gorman A, Harvey AR, McNaught AI. Oxygen saturation measurements of the retinal vasculature in treated asymmetrical primary open-angle glaucoma using hyperspectral imaging. *Eye (Lond)*. 2014;28(10):1190-1200. doi:10.1038/eye.2014.169.
7. Boeckaert J, Vandewalle E, Stalmans I. Oximetry: recent insights into retinal vasopathies and glaucoma. *Bull Soc Belge Ophtalmol*. 2012;(319):75-83.
8. Hardarson SH, Elfarsson A, Agnarsson BA, Stefansson E. Retinal oximetry in central retinal artery occlusion. *Acta Ophthalmol*. 2013;91(2):189-190. doi:10.1111/j.1755-3768.2012.02393.x.
9. Sorg BS, Moeller BJ, Donovan O, Cao Y, Dewhirst MW. Hyperspectral imaging of hemoglobin saturation in tumor microvasculature and tumor hypoxia development. *J Biomed Opt*. 2005;10(4):44004. doi:10.1117/1.2003369.
10. Davies AL, Desai RA, Bloomfield PS, et al. Neurological deficits caused by tissue hypoxia in neuroinflammatory disease. *Ann Neurol*. 2013;74(6):815-825. doi:10.1002/ana.24006.
11. Fernandez Ramos J, Brewer LR, Gorman A, Harvey AR. Video-rate multispectral imaging: application to microscopy and macroscopy. In:

Classical Optics 2014, OSA Technical Digest. Washington, D.C.: Optical Society of America; 2014. doi:10.1364/COSI.2014.CW1C.3.

12. Choudhary TR, Ball D, Fernandez Ramos J, McNaught AI, Harvey AR. Assessment of acute mild hypoxia on retinal oxygen saturation using snapshot retinal oximetry. *Invest Ophthalmol Vis Sci*. 2013;54(12):38-43. doi:10.1167/iovs.13-12624.
13. Jiang H, Zhong J, DeBuc DC, et al. Functional slit lamp biomicroscopy for imaging bulbar conjunctival microvasculature in contact lens wearers. *Microvasc Res*. 2014;92:62-71. doi:10.1016/j.mvr.2014.01.005.
14. Germann WJ, Stanfield CL. The cardiovascular system: cardiac function. In: *Principles of Human Physiology*. Second Ed. Pearson Custom Publishing; 2005:413-450.
15. Germann WJ, Stanfield CL. The cardiovascular system: blood. In: *Principles of Human Physiology*. Second Ed. Pearson Custom Publishing; 2005:496-515.
16. Germann WJ, Stanfield CL. The respiratory system: gas exchange and regulation of breathing. In: *Principles of Human Physiology*. Second Ed. Pearson Custom Publishing; 2005:516-577.
17. Germann WJ, Stanfield CL. The cardiovascular system: blood vessels, blood flow, and blood pressure. In: *Principles of Human Physiology*. Second Ed. Pearson Custom Publishing; 2005:451-496.
18. Zijlstra WG, Buursma A. Spectrophotometry of hemoglobin: absorption spectra of bovine oxyhemoglobin, deoxyhemoglobin, carboxyhemoglobin, and methemoglobin. *Comp Biochem Physiol*. 1997;118(4):743-749.
19. Prahl S. Optical absorption of hemoglobin. Oregon Medical Laser Center. http://omlc.org/spectra/hemoglobin/index.html. Published 1999. Accessed January 1, 2015.
20. Clerbaux T, Gustin P, Detry B, Cao ML, Fiuns A. Comparitive study of the oxyhaemoglobin dissociation curve of four mammals: man, dog, horse, and cat. *Comp Biochem Physiol*. 1993;106:687-694.
21. Bauer C, Forster M, Gros G, et al. Analysis of bicarbonate binding to crocodilian hemoglobin. *J Biol Chem*. 1981;256(16):8429-8435.
22. Marengo-Rowe AJ. Structure-function relations of human hemoglobins.

Baylor Univ Med Cent Proc. 2006;19(3):239-245.

23. Krogh A. The number and distribution of capillaries in muscles with calculations of the oxygen pressure head necessary for supplying the tissue. *J Physiol*. 1919;52(6):409-415. doi:10.1113/jphysiol.1919.sp001839.
24. Tovée MJ. The eye and forming the image. In: *An Introduction to the Visual System*. 2nd ed. Cambridge Univeristy Press; 2008:19-43.
25. Bekerman I, Gottlieb P, Vaiman M. Variations in eyeball diameters of the healthy adults. *J Ophthalmol*. 2014. doi:http://dx.doi.org/10.1155/2014/503645.
26. Riordan-Eva P, Whitcher JP. Anatomy and Embryology of the Eye. In: Reinhardt S, Boyle PJ, Ransom J, eds. *Vaughn & Astbury's General Ophthalmology*. 16th ed. Lange Medical Books/McGraw-Hill; 2004:1-28.
27. Vurgese S, Panda-Jonas S, Jonas JB. Scleral thickness in human eyes. *PLoS One*. 2012;7(1). doi:10.1371/journal.pone.0029692.
28. Liang J, Williams DR. Aberrations and retinal image quality of the normal human eye. *J Opt Soc Am A Opt Image Sci Vis*. 1997;14(11):2873-2883. doi:10.1364/JOSAA.14.002873.
29. Larrea X, Bu P. A Transient Diffusion Model of the Cornea for the Assessment of Oxygen Diffusivity and Consumption. *Investig*. 2009;50(3):1076-1080. doi:10.1167/iovs.08-2479.
30. Filas B a, Shui Y-B, Beebe DC. Computational model for oxygen transport and consumption in human vitreous. *Invest Ophthalmol Vis Sci*. 2013;54(10):6549-6559. doi:10.1167/iovs.13-12609.
31. Youssef PN, Sheibani N, Albert DM. Retinal light toxicity. *Eye*. 2011;25:1-14. doi:10.1038/eye.2010.149.
32. Bournias TE. Anatomy and physiology of the lids, eye, orbit, and visual system. In: *Blueprints Ophthalmology*. 1st ed. Blackwell Publishing; 2005:1-14.
33. Lang J, Kageyama I. The ophthalmic artery and its branches, measurements and clinical importance. *Surg Radiol Anat*. 1990;12:83-90.
34. Sjöström P, Wiklund L, Odlind B. Conjunctival oxygen tension is influenced by plasma and blood volume, and flow through the external carotid artery. *Int J Clin Monit Comput*. 1994;11(2):99-103.

http://www.ncbi.nlm.nih.gov/pubmed/7930856.

35. Yu D-Y, Cringle SJ. Oxygen Distribution and Consumption within the Retina in Vascularised and Avascular Retinas and in Animal Models of Retinal Disease. *Prog Retin Eye Res*. 2001;20(2):175-208.
36. Schweitzer D, Hammer M, Kraft J, Thamm E, Königsdörffer E, Strobel J. In vivo measurement of the oxygen saturation of retinal vessels in healthy volunteers. *IEEE Trans Biomed Eng*. 1999;46(12):1454-1465.
37. Hammer M, Vilser W, Riemer T, et al. Retinal venous oxygen saturation increases by flicker light stimulation. *Invest Ophthalmol Vis Sci*. 2011;52(1):274-277. doi:10.1167/iovs.10-5537.
38. Mansouri K, Medeiros FA, Marchase N, Tatham AJ, Auerbach D, Weinreb RN. Assessment of choroidal thickness and volume during the water drinking test by swept-source optical coherence tomography. *Ophthalmology*. 2013;120(12):2508-2516. doi:10.1016/j.surg.2006.10.010.Use.
39. Manjunath V, Mohammad T, Fujimoto JG, Duker JS. Choroidal Thickness in Normal Eyes Measured Using Cirrus-HD Optical Coherence Tomography. *Am J Ophthalmol*. 2010;150(3):325-329. doi:10.1016/j.ajo.2010.04.018.Choroidal.
40. Alm A, Bill A. Blood flow and oxygen extraction in the cat uvea at normal and high intraocular pressures. *Acta Physiol Scand*. 1970;80(1):19-28. doi:10.1111/j.1748-1716.1970.tb04765.x.
41. Kristjansdottir JV, Hardarson SH, Harvey AR, Olafsdottir OB, Eliasdottir TS, Stef E. Choroidal oximetry with a noninvasive spectrophotometric oximeter. *Invest Ophthalmol Vis Sci*. 2013;54(5):3234-3239. doi:10.1167/iovs.12-10507.
42. Hassenstein A, Meyer CH. Clinical use and research applications of Heidelberg retinal angiography and spectral-domain optical coherence tomography - a review. *Clin Experiment Ophthalmol*. 2009;37(1):130-143. doi:10.1111/j.1442-9071.2009.02017.x.
43. Ormerod LD, Fariza E, Webb RH. Dynamics of external ocular blood flow studied by scanning angiographic microscopy. *Eye*. 1995;9:605-614.
44. Meyer PA. Patterns of blood flow in episcleral vessels studied by low-dose

fluorescein videoangiography. *Eye*. 1988;2(5):533-546. doi:10.1038/eye.1988.104.

45. Johnstone M, Martin E, Jamil A. Pulsatile flow into the aqueous veins: manifestations in normal and glaucomatous eyes. *Exp Eye Res*. 2011;92(5):318-327. doi:10.1016/j.exer.2011.03.011.
46. Efron N, Al-Dossari M, Pritchard N. In vivo confocal microscopy of the bulbar conjunctiva. *Clin Experiment Ophthalmol*. 2009;37(4):335-344. doi:10.1016/j.jfma.2013.10.003.
47. Meighan SS. Blood vessels of the bulbar conjunctiva in man. *Br J Opthalmology*. 1956;40:513-526.
48. Duench S, Simpson T, Jones LW, Flanagan JG, Fonn D. Assessment of variation in bulbar conjunctival redness, temperature, and blood flow. *Optom Vis Sci*. 2007;84(6):511-556. doi:10.1097/OPX.0b013e318073c304.
49. Provine RR, Nave-blodgett J, Cabrera MO. The emotional eye : red sclera as a uniquely human cue of emotion. *Int J Behav Biol*. 2013;119:993-998. doi:10.1111/eth.12144.
50. Horak F, Berger U, Menapace R, Schuster N. Quantification of conjunctival vascular reaction by digital imaging. *J Allergy Clin Immunol*. 1996;98(3):495-500.
51. Owen CG, Newsom RSB, Rudnicka AR, Ellis TJ, Woodward EG. Vascular Response of the Bulbar Conjunctiva to Diabetes and Elevated Blood Pressure. *Ophthalmology*. 2005;112(10):1801-1808.
52. Wanek J, Gaynes B, Lim JI, Molokie R, Shahidi M. Human bulbar conjunctival hemodynamics in hemoglobin SS and SC disease. *Am J Hematol*. 2013;88(8):661-664. doi:10.1002/ajh.23475.
53. Pavlou AT, Wolff HG. The bulbar conjunctival vessels in occlusion of the internal carotid artery. *AMA Arch Intern Med*. 1959;104(1):53-60.
54. Jacques SL. Optical properties of biological tissues: a review. *Phys Med Biol*. 2013;58(11):R37-61. doi:10.1088/0031-9155/58/11/R37.
55. Chandrasekhar S, Elbert DD. The illumination and polarisation of the sunlight sky on Rayleigh scattering. *Trans Am Philos Soc*. 1954;44(6):643-728. http://www.biodiversitylibrary.org/item/111242.
56. Mie G. Beiträge zur Optik trüber Medien, speziell kolloidaler Metallösungen.

Ann Phys. 1908;330(3):377-445. doi:10.1002/andp.19083300302.

57. Hahn DW. Light Scattering Theory. *Dep Mech Aerosp Eng Florida*. 2006.
58. Bashkatov AN, Genina E a., Tuchin V V. Optical properties of skin, subcutaneous, and muscle tissues: a review. *J Innov Opt Health Sci*. 2011;4(1):9-38. doi:10.1142/S1793545811001319.
59. Bashkatov AN, Genina EA, Kochubey VI, Tuchin V V. Optical properties of human skin, subcutaneous and mucous tissues in the wavelength range from 400 to 2000 nm. *J Phys D Appl Phys*. 2005;38(15):2543-2555. doi:10.1088/0022-3727/38/15/004.
60. Van Gemert MJC, Jacques SL, Sterenborg HJCM, Star WM. Skin optics. *IEEE Trans Biomed Eng*. 1989;36(12):1146-1154. doi:10.1109/10.42108.
61. Sardar DK, Yow RM, Tsin ATC, Sardar R. Optical scattering, absorption, and polarization of healthy and neovascularized human retinal tissues. *J Biomed Opt*. 2005;10(5):51501. doi:10.1117/1.2065867.
62. Bashkatov AN, Genina EA, Kochubey VI, Tuchin V V. Optical properties of human sclera in spectral range 370-2500 nm. *Opt Spectrosc*. 2010;109(2):197-204. doi:10.1134/S0030400X10080084.
63. Friebel M, Helfmann J, Netz U, Meinke M. Influence of oxygen saturation on the optical scattering properties of human red blood cells in the spectral range 250 to 2,000 nm. *J Biomed Opt*. 2009;14(3):34001. doi:10.1117/1.3127200.
64. Meinke M, Müller G, Helfmann J, Friebel M. Optical properties of platelets and blood plasma and their influence on the optical behavior of whole blood in the visible to near infrared wavelength range. *J Biomed Opt*. 2015;12(1):14024. doi:10.1117/1.2435177.
65. Faber DJ, van der Meer FJ, Aalders MCG, van Leeuwen TG. Hematocrit-dependence of the scattering coefficient of blood determined by optical coherence tomography. *Proc SPIE 6163, Saratov Fall Meet 2005 Opt Technol Biophys Med VII*. 2006;6163. doi:10.1117/12.697299.
66. Klose HJ, Volger E, Brechtelsbauer H, Heinich L, Schmid-Schönbein H. Microrheology and light transmission of blood. *Pflügers Arch - Eur J Physiol*. 1972;333(2):126-139. doi:10.1007/BF00586912.
67. Faber D, Aalders M, Mik E, Hooper B, van Gemert M, van Leeuwen T.

Oxygen saturation-dependent absorption and scattering of blood. *Phys Rev Lett*. 2004;93(2):2-5. doi:10.1103/PhysRevLett.93.028102.

68. Steinke JM, Shepherd AP. Comparison of Mie theory and the light scattering of red blood cells. *Appl Opt*. 1988;27(19):4027-4033. doi:10.1364/AO.27.004027.
69. LeBlanc SE, Atanya M, Burns K, Munger R. Quantitative impact of small angle forward scatter on whole blood oximetry using a Beer-Lambert absorbance model. *Analyst*. 2011;136(8):1637-1643. doi:10.1039/c0an00996b.
70. Cimalla P, Walther J, Mittasch M, Koch E. Shear flow-induced optical inhomogeneity of blood assessed in vivo and in vitro by spectral domain optical coherence tomography in the 1.3 μm wavelength range. *J Biomed Opt*. 2011;16(11):116020. doi:10.1117/1.3653235.
71. Hammer M, Leistritz S, Leistritz L, Schweitzer D. Light paths in retinal vessel oxymetry. *IEEE Trans Biomed Eng*. 2001;48(5):592-598. doi:10.1109/10.918598.
72. Smith MH, Denninghoff KR, Lompado A, Hillman LW. Effect of multiple light paths on retinal vessel oximetry. *Appl Opt*. 2000;39(7):1183-1193.
73. Rodmell PI, Crowe JA, Gorman A, et al. Light path-length distributions within the retina. *J Biomed Opt*. 2014;19(3):36008. doi:10.1117/1.JBO.19.3.036008.
74. Salyer DA, Beaudry N, Basavanthappa S, et al. Retinal oximetry using intravitreal illumination. *Curr Eye Res*. 2006;31(7-8):617-627. doi:10.1080/02713680600760493.
75. MacKintosh FC, Zhu JX, Pine DJ, Weitz DA. Polarization memory of multiply scattred light. *Phys Rev B - Rapid Commun*. 1989;40:9342-9345. doi:10.1103/PhysRevB.40.9342.
76. Ntziachristos V. Going deeper than microscopy: the optical imaging frontier in biology. *Nat Methods*. 2010;7(8):603-614. doi:10.1038/nmeth.1483.
77. Jeon M, Kim C. Multimodal Photoacoustic Tomography. *IEEE Trans Multimed*. 2013:975-982. doi:10.1109/TMM.2013.2244203.
78. Wen X, Mao Z, Han Z, Tuchin V V, Zhu D. In vivo skin optical clearing by glycerol solutions: mechanism. *J Biophotonics*. 2010;3(1-2):44-52.

doi:10.1002/jbio.200910080.

79. Tuchin V V, Xu X, Wang RK. Dynamic optical coherence tomography in studies of optical clearing, sedimentation, and aggregation of immersed blood. *Appl Opt*. 2002;41(1):258-271.
80. Xiang L, Wang B, Ji L, Jiang H. 4-D photoacoustic tomography. *Sci Rep*. 2013;3. doi:10.1038/srep01113.
81. Rolfs M. Microsaccades: small steps on a long way. *Vision Res*. 2009;49(20):2415-2441. doi:10.1016/j.visres.2009.08.010.
82. Li H, Lu J, Shi G, Zhang Y. Measurement of oxygen saturation in small retinal vessels with adaptive optics confocal scanning laser opthalmoscopy. *JBO Lett*. 2011;16(11). doi:10.1364/BOE.1.000031.
83. Fariza E, O'Day T, Jalkh a E, Medina a. Use of cross-polarized light in anterior segment photography. *Arch Ophthalmol*. 1989;107(4):608-610. http://www.ncbi.nlm.nih.gov/pubmed/2705935.
84. Cense B, Chen TC, Park BH, Pierce MC, De Boer JF. Thickness and birefringence of healthy retinal nerve fiber layer tissue measured with polarization-sensitive optical coherence tomography. *Investig Ophthalmol Vis Sci*. 2004;45(8):2606-2612. doi:10.1167/iovs.03-1160.
85. DeHoog E, Schwiegerling J. Fundus camera systems: a comparative analysis. *Appl Opt*. 2009;48(2):221-228. doi:10.1364/AO.48.000221.
86. Artigas JM, Felipe A, Navea A, Fandiño A, Artigas C. Spectral transmission of the human crystalline lens in adult and elderly persons: Color and total transmission of visible light. *Investig Ophthalmol Vis Sci*. 2012;53(7):4076-4084. doi:10.1167/iovs.12-9471.
87. Kessel L, Lundeman JH, Herbst K, Andersen TV, Larsen M. Age-related changes in the transmission properties of the human lens and their relevance to circadian entrainment. *J Cataract Refract Surg*. 2010;36(2):308-312. doi:10.1016/j.jcrs.2009.08.035.
88. Peli E, Schwartz B. Enhancement of fundus photographs taken through cataracts. *Ophthalmology*. 1987;Pt 2:10-13. doi:10.1016/S0161-6420(87)33604-8.
89. Heitmar R, Kalitzeos AA. Reliability of retinal vessel calibre measurements using a retinal oximeter. *BMC Ophthalmol*. 2015;15(1):184.

doi:10.1186/s12886-015-0174-0.

90. Hickam JB, Sieker HO, Frayser R. Studies of retinal circulation and A-V oxygen difference in man. *Trans Am Clin Climatol Assoc*. 1959;71(657):34-44.
91. Beach J. Pathway to retinal oximetry. *Transl Vis Sci Technol*. 2014;3(5):1-9. doi:10.1167/tvst.3.5.2.
92. Twersky V. Absorption and multiple scattering by biological suspensions. *J Opt Soc Am*. 1970;60(8):1084-1093. doi:10.1364/JOSA.60.001084.
93. Pittman R, Duling B. A new method for the measurement of percent oxyhemoglobin. *J Appl Physiol*. 1975;38(2).
94. Delpy DT, Cope M, van der Zee P, Arridge S, Wray S, Wyatt J. Estimation of optical pathlength through tissue from direct time of flight measurement. *Phys Med Biol*. 1988;33(12):1433-1442. doi:10.1088/0031-9155/33/12/008.
95. Matthes K, Gross F. Untersuchungen über die Absorption von rotem und ultrarotem Licht durch kohlenoxydgesättigtes, sauerstoffgesättigtes und reduziertes Blut. *Naunyn Schmiedebergs Arch Pharmacol*. 1938;191(2):369-380.
96. Squire JR. Instrument for measuring quantity of blood and its degree of oxygenation in web of the hand. *Clin Sci*. 1940;4:331-339.
97. Aoyagi T. Pulse oximetry: its invention, theory, and future. *J Anesth*. 2003;17(4):259-266. doi:10.1007/s00540-003-0192-6.
98. Taylor M., Whitwam JG. The accuracy of pulse oximeters. *Anesthesia*. 1988;43(April 1987):229-232.
99. Hanning CD, Alexander-Williams, Jm. Pulse oximetry: a practical review. *Bmj*. 1995;311(August):367-370. doi:10.1136/bmj.311.7001.367.
100. Avidan A, Levin PD. Pulse oximetry. *N Engl J Med*. 2011;365(2):185-6; author reply 187. doi:10.1056/NEJMc1104834#SA1.
101. Hickam JB, Frayser R, Ross JC. A study of retinal venous blood oxygen saturation in human subjects by photographic means. *Circulation*. 1963;27(3):375-385. doi:10.1161/01.CIR.27.3.375.
102. Smith MH. Optimum wavelength combinations for retinal vessel oximetry. *Appl Opt*. 1999;38(1):258-267. doi:10.1364/AO.38.000258.
103. Hammer M, Vilser W, Riemer T, Schweitzer D. Retinal vessel oximetry-

calibration, compensation for vessel diameter and fundus pigmentation, and reproducibility. 2008;13(5):1-7. doi:10.1117/1.2976032.

104. Hickam JB, Frayser R. Studies of the retinal circulation in man. Observations on vessel diameter, arteriovenous oxygen difference, and mean circulation time. *Circulation*. 1966;XXXIII(February):302-316.
105. Beach JM, Schwenzer KJ, Srinivas S, Kim D, Tiedeman JS. Oximetry of retinal vessels by dual-wavelength imaging: calibaration and influence of pigmentation. *JAP*. 1999;86(2):748-758.
106. Hendargo HC, Zhao Y, Allenby T, Palmer GM. Snap-shot multispectral imaging of vascular dynamics in a mouse window-chamber model. *Opt Lett*. 2015;40(14):3292–3295. doi:10.1364/OL.40.003292.
107. Hardarson SH, Harris A, Karlsson RA, et al. Automatic retinal oximetry. *Invest Ophthalmol Vis Sci*. 2006;47(11):5011-5016. doi:10.1167/iovs.06-0039.
108. Hardarson SH, Stefánsson E. Retinal oxygen saturation is altered in diabetic retinopathy. *Br J Ophthalmol*. 2012;96(4):560-563. doi:10.1136/bjophthalmol-2011-300640.
109. Kristjansdottir JV, Hardarson SH, Halldorsson GH, Karlsson RA, Eliasdottir TS, Stefánsson E. Retinal oximetry with a scanning laser ophthalmoscope. *Investig Opthalmology Vis Sci*. 2014;55(5):3120. doi:10.1167/iovs.13-13255.
110. Li C, Wang L V. Photoacoustic tomography and sensing in biomedicine. *Phys Med Biol*. 2009;54(19):R59-97. doi:10.1088/0031-9155/54/19/R01.
111. Needles A, Heinmiller A, Sun J, et al. Development and initial application of a fully integrated photoacoustic micro-ultrasound system. *IEEE Trans Ultrason Ferroelectr Freq Control*. 2013;60(5):888-897. doi:10.1109/TUFFC.2013.2646.
112. van Assendelft OW. *Spectrophotometry of Haemoglobin Derivatives*.; 1970.
113. Kramer K, Elam JO, Saxton GA, Elam WN. Influence of oxygen saturation, erythrocyte concentration and optical depth upon the red and near-infrared light transmittance of whole blood. *Am J Physiol*. 1951;165(1):229-246.
114. Delori FC. Noninvasive technique for oximetry of blood in retinal vessels. *Appl Opt*. 1988;27(6):1113-1125. doi:10.1364/AO.27.001113.
115. Drewes J, Smith M, Hiliman L, et al. Instrument for the measurement of

retinal vessel oxygen saturation. *BiOS'99 Int Biomed Opt Symp Int Soc Opt Photonics*. 1999;3591(January):114-120.

116. Smith MH, Denninghoff KR, Lompando A, Hillman LW. Retinal vessel oximetry: toward absolute calibration. *Proc SPIE*. 2000;3908:217-226.
117. Alabboud I, Muyo G, Gorman A, et al. New spectral imaging techniques for blood oximetry in the retina. Depeursinge CD, ed. *Proc SPIE 6631, Nov Opt Instrum Biomed Appl III*. 2007;6631. doi:10.1117/12.728535.
118. Mordant DJ, Al-Abboud I, Muyo G, et al. Spectral imaging of the retina. *Eye*. 2011;25(3):309-320. doi:10.1038/eye.2010.222.
119. Khoobehi B, Ning J, Puissegur E, Bordeaux K, Balasubramanian M, Beach J. Retinal oxygen saturation evaluation by multi-spectral fundus imaging. 2007;6511:65110B-65110B-6. doi:10.1117/12.710030.
120. Arimoto H, Furukawa H. Retinal oximetry with 510 - 600 nm light based on partial least-squares regression technique. *Jpn J Appl Phys*. 2010;49(11). doi:10.1143/JJAP.49.112401.
121. Gao L, Smith RT, Tkaczyk TS. Snapshot hyperspectral retinal camera with the Image Mapping Spectrometer (IMS). *Biomed Opt Express*. 2012;3(1):48-54. doi:10.1364/BOE.3.000048.
122. Shonat RD, Wachman S. Near-simultaneous hemoglobin saturation and oxygen tension maps in mouse brain using an AOTF microscope. *Biophys J*. 1997;73(September):1223-1231.
123. Sorg BS, Hardee ME, Agarwal N, Moeller BJ, Dewhirst MW. Spectral imaging facilitates visualization and measurements of unstable and abnormal microvascular oxygen transport in tumors. *J Biomed Opt*. 2008;13(1):14026. doi:10.1117/1.2837439.
124. Wang J, Ghassemi P, Melchiorri A, et al. 3D printed biomimetic vascular phantoms for assessment of hyperspectral imaging systems. 2015;9325:932508. doi:10.1117/12.2084720.
125. Clancy N, Arya S, Saso S, Singh M. Laparoscopic intraoperative oxygenation mapping using multispectral imaging. *Hsi2014*. 2014. - imaging.pdf.
126. Yudovsky D, Nouvong A, Schomacker K, Pilon L. Assessing diabetic foot ulcer development risk with hyperspectral tissue oximetry. *J Biomed Opt*.

2011;16(2):26009. doi:10.1117/1.3535592.

127. Chin MS, Freniere BB, Lo Y-C, et al. Hyperspectral imaging for early detection of oxygenation and perfusion changes in irradiated skin. *J Biomed Opt*. 2012;17(2):26010. doi:10.1117/1.JBO.17.2.026010.
128. Levenson R. Spectral imaging in biomedicine: A selective overview. *Proc SPIE*. 1998;3438:300-312. doi:10.1117/12.328111.
129. Alabboud I. Human retinal oximetry using hyperspectral imaging. Heriot Watt University. 2009.
130. Hirohara Y, Okawa Y, Mihashi T, et al. Validity of retinal oxygen saturation analysis: hyperspectral imaging in visible wavelength with fundus camera and liquid crystal wavelength tunable filter. *Opt Rev*. 2007;14(3):151-158. doi:10.1007/BF02919416.
131. Mordant DJ, Al-Abboud I, Muyo G, et al. Validation of human whole blood oximetry, using a hyperspectral fundus camera with a model eye. *Invest Ophthalmol Vis Sci*. 2011;52(5):2851-2859. doi:10.1167/iovs.10-6217.
132. Sorg BS, Moeller BJ, Donovan O, Cao Y, Dewhirst MW. Hyperspectral imaging of hemoglobin saturation in tumor microvasculature and tumor hypoxia development. *J Biomed Opt*. 2005;10(4):44004. doi:10.1117/1.2003369.
133. Gupta N, Ramella-Roman JC. Detection of blood oxygen level by noninvasive passive spectral imaging of skin. *Proc SPIE*. 2008;6842:68420C-68420C-8. doi:10.1117/12.768708.
134. Furukawa H, Arimoto H, Shirai T, Ooto S, Hangai M, Yoshimura N. Oximetry of retinal capillaries by multicomponent analysis. *Appl Spectrosc*. 2012;66(8):962-969. doi:10.1366/11-06525.
135. Patel SR, Flanagan JG, Shahidi AM, Sylvestre JP, Hudson C. A prototype hyperspectral system with a tunable laser source for retinal vessel imaging. *Investig Ophthalmol Vis Sci*. 2013;54(8):5163-5168. doi:10.1167/iovs.13-12124.
136. van der Putten M, Fernandez Ramos J, Brewer L, Brewer J, Harvey A. The British Microcirculation Society Abstracts of the 65th annual meeting in University of Manchester. *Microcirculation*. 2015;22:753-781. doi:10.1111/micc.12212.

137. Oishi A, Hidaka J, Yoshimura N. Quantification of the image obtained with a wide-field scanning ophthalmoscope. *Investig Ophthalmol Vis Sci*. 2014;55(4):2424-2431. doi:10.1167/iovs.13-13738.
138. Topcon Medical Systems Inc. Topcon TRC-50DX datasheet. http://www.topconmedical.com/products/trc50dx-literature.htm. Published 2014. Accessed June 20, 2003.
139. Vehmeijer WB, Magnusdottir V, Eliasdottir TS, Hardarson SH, Schalij-Delfos NE, Stefánsson E. Retinal Oximetry with Scanning Laser Ophthalmoscope in Infants. *PLoS One*. 2016;11(2):e0148077. doi:10.1371/journal.pone.0148077.
140. Denninghoff KR, Sieluzycka KB, Hendryx JK, Ririe TJ, Deluca L, Chipman RA. Retinal oximeter for the blue-green oximetry technique. *J Biomed Opt*. 2011;16(10):107004. doi:10.1117/1.3638134.
141. Denninghoff, K.R., Smith, M.H., Chipman, R.A., Hillman, L.W., Jester, P.M., Hughes, C.E., Kuhn, F. and Rue LW. Retinal large vessel oxygen saturations correlate with early blood loss and hypoxia in anesthetized swine. *J Trauma Acute Care Surg*. 1997;43(1):29-34.
142. Denninghoff KR, Smith M, Hillman LW, David R, Rue LW. Retinal venous oxygen saturation correlates with blood volume. *Acad Emerg Med*. 1998;5(6):577-582.
143. Ashman RA, Reinholz F, Eikelboom RH. Oximetry with a multiple wavelength SLO. *Int Ophthalmol*. 2001;23(4-6):343-346. doi:10.1023/A:1014406831412.
144. Denninghoff K, Smith M, Lompado A, Hillman L. Retinal venous oxygen saturation and cardiac output during controlled hemorrhage and resuscitation. *J Appl Physiol*. 2003;94(3):891-896. doi:10.1152/japplphysiol.01197.2001.
145. Liang H. Advances in multispectral and hyperspectral imaging for archaeology and art conservation. *Appl Phys A*. 2011;106(2):309-323. doi:10.1007/s00339-011-6689-1.
146. Gowen AA, O'Donnell CP, Cullen PJ, Downey G, Frias JM. Hyperspectral imaging - an emerging process analytical tool for food quality and safety control. *Trends Food Sci Technol*. 2007;18(12):590-598.

doi:10.1016/j.tifs.2007.06.001.

147. Beach J. Spectral reflectance technique for retinal blood oxygen evaluation in humans. *Proc 31st Appl Imag Pattern Recognit Work (AIPR '02)*. 2002. doi:10.1109/AIPR.2002.1182264.
148. Khoobehi B, Beach J, Kawano H, Lanoue M, Chander D. Noninvasive measurement of oxygen saturation in optic-nerve head tissue. *Opt Diagnostics Sens IV*. 2004;5325:104-110. doi:10.1117/12.527803.
149. Harvey AR, Fletcher-Holmes DW, Kudesia SS, Beggan C. Imaging spectrometry at visible and infrared wavelengths using image replication. *Proceeding SPIE Electro-Optical Infrared Syst Technol Appl*. 2004;5612:190-198. doi:10.1117/12.580059.
150. Harvey AR, Fletcher-Holmes DW, Gorman A, Altenbach K, Arlt J, Read ND. Spectral imaging in a shapshot. *Proc SPIE Spectr Imaging Instrumentation, Appl Anal III*. 2005;5694:110-119. doi:10.1117/12.604609.
151. Gorman A, Fletcher-Holmes DW, Harvey AR. Generalization of the Lyot filter and its application to snapshot spectral imaging. *Opt Express*. 2010;18(6):5602-5608. doi:10.1364/OE.18.005602.
152. Wong G, Harvey AR, Pilkington R, Rickman R. Real-time SWIR hyperspectral imaging with polarmetric capability. Lewis PE, ed. *Proc SPIE Imaiging Spectometry XV*. 2010;7812. doi:10.1117/12.859812.
153. Choudhary TR, Ball D, Fernandez-Ramos, J Stefánsson E, McNaught AI, Harvey AR. Non-invasive choroidal oximetry using snapshot multispectral imaging. *Submitt Rev*. 2016.
154. Ramella-Roman JC, Mathews SA. Spectroscopic measurements of oxygen saturation in the retina. *IEEE J Sel Top Quantum Electron*. 2007;13(6):1697-1703. doi:10.1109/JSTQE.2007.911312.
155. Gao L, Kester RT, Hagen N, Tkaczyk TS. Snapshot Image Mapping Spectrometer (IMS) with high sampling density for hyperspectral microscopy. *Opt Express*. 2010;18(14):14330-14344. doi:10.1364/OE.18.014330.
156. Gao Y, Wang H. Co-registration method for photoacoustic imaging and laser speckle imaging. *Chinese Opt Lett*. 2012;10(6):1-4. doi:10.3788/COL201210.061101.Photoacoustic.

157. Ford BK, Volin CE, Murphy SM, Lynch RM, Descour MR. Computed tomography-based spectral imaging for fluorescence microscopy. *Biophys J*. 2001;80(2):986-993. doi:10.1016/S0006-3495(01)76077-8.
158. Beard P. Biomedical photoacoustic imaging. *Interface Focus*. 2011;1(4):602-631. doi:10.1098/rsfs.2011.0028.
159. Danielli A, Maslov K, Xia J, Wang L V. Wide range quantitative photoacoustic spectroscopy to measure non-linear optical absorption of hemoglobin. *Photons Plus Ultrasound, Imaging Sens 2012*. 2012;8223. doi:10.1117/12.908900.
160. Yao J, Wang L V. Photoacoustic tomography: fundamentals, advances and prospects. *Contrast Media Mol Imaging*. 2011;6(5):332-345. doi:10.1002/cmmi.443.
161. Wang L V, Hu S. Photoacoustic tomography: in vivo imaging from organelles to organs. *Science*. 2012;335(6075):1458-1462. doi:10.1126/science.1216210.
162. Herzog E, Taruttis A, Beziere N, Lutich AA, Razansky D. Optical imaging of cancer heterogeneity with multispectral optoacoustic tomography. *Radiology*. 2012;263(2):461-468. doi:10.1148/radiol.11111646/-/DC1.
163. Mehrmohammadi M, Yoon SJ, Yeager D, Emelianov SY. Photoacoustic imaging for cancer detection and staging. *Curr Mol Imaging*. 2013;2:89-105.
164. Sun Y, Sobel E, Jiang H. Noninvasive imaging of hemoglobin concentration and oxygen saturation for detection of osteoarthristis in the finger joints using multispectral three-dimenstional quantitative photoacoustic tomography. *J Opt*. 2013;15:1-8.
165. Figley SA, Chen Y, Maeda A, et al. A spinal cord window chamber model for in vivo longitudinal multimodal optical and acoustic imaging in a murine model. *PLoS One*. 2013;8(3):e58081. doi:10.1371/journal.pone.0058081.
166. Wang X, Xie X, Ku G, Wang L V., Stoica G. Noninvasive imaging of hemoglobin concentration and oxygenation in the rat brain using high-resolution photoacoustic tomography. *J Biomed Opt*. 2006;11(2):24015. doi:10.1117/1.2192804.
167. Hu S, Wang L V. Photoacoustic imaging and characterization of the microvasculature. *J Biomed Opt*. 2013;15(1):11101. doi:10.1117/1.3281673.

168. Wang L, Maslov K, Wang L V. Single-cell label-free photoacoustic flowoxigraphy in vivo. *Proc Natl Acad Sci U S A*. 2013;2013:1-6. doi:10.1073/pnas.1215578110.
169. Tan Z, Tang Z, Wu Y, Liao Y, Dong W, Guo L. Multimodal subcellular imaging with microcavity photoacoustic transducer. *Opt Express*. 2011;19(3):2426-2431.
170. Mariampillai A, Standish B a, Moriyama EH, et al. Speckle variance detection of microvasculature using swept-source optical coherence tomography. *Opt Lett*. 2008;33(13):1530-1532. doi:https://doi.org/10.1364/OL.33.001530.
171. Walther J, Gaertner M, Cimalla P, et al. Optical coherence tomography in biomedical research. *Anal Bioanal Chem*. 2011;400(9):2721-2743. doi:10.1007/s00216-011-5052-x.
172. Faber DJ, van Leeuwen TG. Are quantitative attenuation measurements of blood by optical coherence tomography feasible? *Opt Lett*. 2009;34(9):1435-1437.
173. Kagemann L, Wollstein G, Wojtkowski M, et al. Spectral oximetry assessed with high-speed ultra-high-resolution optical coherence tomography. *J Biomed Opt*. 2007;12(4). doi:10.1117/1.2772655.
174. Lu C-W, Lee C-K, Tsai M-T, Wang Y-M, Yang CC. Measurement of the hemoglobin oxygen saturation level with spectroscopic spectral-domain optical coherence tomography. *Opt Lett*. 2008;33(5):416-418.
175. Robles FE, Chowdhury S, Wax A. Assessing hemoglobin concentration using spectroscopic optical coherence tomography for feasibility of tissue diagnostics. *Biomed Opt Express*. 2010;1(1):310-317. doi:10.1364/boe.1.000310/.
176. Yi J, Li X. Estimation of oxygen saturation from erythrocytes by high-resolution spectroscopic optical coherence tomography. *Opt Lett*. 2010;35(12):2094-2096.
177. Robles FE, Wilson C, Grant G, Wax A. Molecular imaging true-colour spectroscopic optical coherence tomography. *Nat Photonics*. 2011;5(12):744-747. doi:10.1038/nphoton.2011.257.
178. Yi J, Wei Q, Liu W, Backman V, Zhang HF. Visible-light optical coherence

tomography for retinal oximetry. *Opt Lett*. 2013;38(11):1796-1798.

179. Yi J, Liu W, Chen S, et al. Visible light optical coherence tomography measures retinal oxygen metabolic response to systemic oxygenation. *Light Sci Appl*. 2015;4(9):e334. doi:10.1038/lsa.2015.107.
180. Chen S, Yi J, Zhang HF. Measuring oxygen saturation in retinal and choroidal circulations in rats using visible light optical coherence tomography angiography. *Biomed Opt Express*. 2015;6(8):2840. doi:10.1364/BOE.6.002840.
181. Chong SP, Merkle CW, Leahy C, Radhakrishnan H, Srinivasan VJ. Quantitative microvascular hemoglobin mapping using visible light spectroscopic Optical Coherence Tomography. *Biomed Opt Express*. 2015;6(4):1429. doi:10.1364/BOE.6.001429.
182. Chen S, Liu Q, Shu X, Soetikno B, Tong S, Zhang HF. Imaging hemodynamic response after ischemic stroke in mouse cortex using visible-light optical coherence tomography. *Biomed Opt Express*. 2016;7(9):3377. doi:10.1364/BOE.7.003377.
183. Kuranov R V, Qiu J, McElroy AB, et al. Depth-resolved blood oxygen saturation measurement by dual-wavelength photothermal (DWP) optical coherence tomography. *Biomed Opt Express*. 2011;2(3):491-504. doi:10.1364/BOE.2.000491.
184. Yin B, Kuranov R V, McElroy AB, et al. Dual-wavelength photothermal optical coherence tomography for imaging microvasculature blood oxygen saturation. *J Biomed Opt*. 2013;18(5). doi:10.1117/1.JBO.18.5.056005.
185. Yin B, Kuranov R V, Mcelroy AB, Milner TE. Dual-wavelength photothermal optical coherence tomography for blood oxygen saturation measurement. *Opt Coherence Tomogr Coherence Domain Opt Methods Biomed*. 2013;8571:1-7. doi:10.1117/12.2006945.
186. Kuranov R V, Kazmi S, McElroy AB, et al. In vivo depth-resolved oxygen saturation by Dual-Wavelength Photothermal (DWP) OCT. *Opt Express*. 2011;19(24). http://www.ncbi.nlm.nih.gov/pubmed/22109408.
187. Briers JD. Laser Doppler, speckle and related techniques for blood perfusion mapping and imaging. *Physiol Meas*. 2001;22(4):R35-R66.
188. Brewer L. Oximetry using laser speckle. Retinal Oximetry Workshop 2016.

http://www.gla.ac.uk/schools/physics/oximetryworkshop/videos of presentations/. Published 2016.

189. Hu S, Wang L V. Optical-resolution photoacoustic microscopy: auscultation of biological systems at the cellular level. *Biophys J*. 2013;105(4):841-847. doi:10.1016/j.bpj.2013.07.017.
190. MacKenzie LE, Choudhary TR, McNaught AI, Harvey AR. In vivo oximetry of human bulbar conjunctival and episcleral microvasculature using snapshot multispectral imaging. *Exp Eye Res*. 2016;149:48-58. doi:10.1016/j.exer.2016.06.008.
191. Shahidi M, Wanek J, Gaynes B, Wu T. Quantitative assessment of conjunctival microvascular circulation of the human eye. *Microvasc Res*. 2010;79(2):109-113. doi:10.1016/j.mvr.2009.12.003.
192. Gartner S. Blood vessels of the conjunctiva, studies with high speed macrophotography. *Arch Ophthalmol*. 1944;32(6):464-476. doi:. doi:10.1001/archopht.1944.00890120044004.
193. Hill R., Fatt I. Oxygen depletion of a limited resovoir by human conjunctiva. *Lett to Nat*. 1963;200:1011-1012. doi:10.1038/2001011b0.
194. Cheung A, Hu B, Wong S, et al. Microvascular abnormalities in the bulbar conjunctiva of contact lens users. *Clincal hemerology Microcirc*. 2012;51(1):77-86. doi:10.3233/CH-2011-1513.
195. Sweeney D. Have silicone hydrogel lenses eliminated hypoxia? *Eye Contact Lens Sci Clin Pract*. 2013;39(1):53-60. doi:10.1097/ICL.0b013e31827c7899.
196. Ditzel J. The in vivo reactions of the small blood vessels to diabetes mellitus. *Acta Medica Scandanavia*. 1967;182(476):123-134.
197. Fenton BM, Zweifach BW, Worthen DM. Quantitative morphometry of conjunctival microcirculation in diabetes mellitus. *Microvasc Res*. 1979;18(2):153-166. doi:10.1016/0026-2862(79)90025-6.
198. Isenberg SJ, Mcree WE, Jedrzynski M. Conjunctival hypoxia in diabetes mellitus. *Invest Ophthalmol Vis Sci*. 1986;27:1512-1515.
199. Cheung ATW, Ramanujam S, Greer DA, Kumagai LF, Aoki TT. Microvascular abnormalities in the bulbar conjunctiva of patients with type 2 diabetes mellitus. *Endrocine Pract*. 2001;7(5):358-363.
200. Fink AI, Funahashi T, Robinson M, Watson RJ. Conjunctival blood flow in

sickle-cell disease. Preliminary report. *Arch Ophthalmol*. 1961;66:824-829. doi:10.1001/archopht.1961.00960010826008.

201. Isenberg SJ, McRee WE, Jedrzynski MS, Gange SN, Gange SL. Effects of sickle cell anemia on conjunctival oxygen tension and temperature. *Arch Intern Med*. 1987;147(1):67-69. doi:10.1016/0736-4679(87)90250-2.
202. Lee RE, Fowler EP. Anatomical and physiological aspects of the capillary bed in the bulbar conjunctiva of man in health and disease. *Angiology*. 1955;6(4):369-382. doi:10.1177/000331975500600408.
203. Harper RN, Moore MA, Marr MC, Watts LE, Hutchins PM. Arteriolar rarefaction in the conjunctiva human essential hypertensives. *Microvasc Res*. 1978;16:369-372.
204. Wolf S, Arend O, Schulte K, Ittel TH, Reim M. Quantification of retinal capillary density and flow velocity in patients with essential hypertension. *Hypertension*. 1994;23(4):464-467. doi:10.1161/01.HYP.23.4.464.
205. Kwan M, Fatt I. A noninvasive method of continuous arterial oxygen tension estimation from measured palpebral conjunctival oxygen tension. *Anesthesiology*. 1971;35(3):309-314.
206. Chapman KR, Liu FL, Watson RM, Rebuck AS. Conjunctival oxygen tension and its relationship to arterial oxygen tension. *J Clin Monit*. 1986;2(2):100-104.
207. Mader TH, Friedl KE, Mohr LC, Bernhard WN. Conjunctival oxygen tension at high altitude. *Aviat Space Environ Med*. 1987;58(1):767-769.
208. Isenberg S, Neumann D, Fink S, Rich R. Continuous oxygen monitoring of the conjunctiva in neonates. *J Perinatol*. 2002;22:46-49. doi:10.1038/sj/jp/7210602.
209. Isenberg SJ, Green BF. Effect of phenylephrine hydrochloride on conjunctival PO2. *Arch Ophthalmol*. 1984;102(8):1185-1186.
210. Vogel A, Dlugos C, Nuffer R, Birngruber R. Optical properties of human sclera, and their consequnces for transscleral laser applications. *Lasers Surg Med*. 1991;11:331-340.
211. Van Buskirk EM. The anatomy of the limbus. *Eye*. 1989;3:101-108. doi:10.1038/eye.1989.16.
212. Papas EB. The limbal vasculature. *Cont Lens Anterior Eye*. 2003;26(2):71-

76. doi:10.1016/S1367-0484(02)00054-1.

213. Hayreh SS. Blood supply of the anterior segment. In: *Ocular Vascular Occlusive Disorders*. ; 2014:111-141. doi:10.1007/978-3-319-12781-1.
214. Meyer PA, Watson PG. Low dose fluorescein angiography of the conjunctiva and episclera. *Br J Ophthalmol*. 1987;71(1):2-10. doi:10.1136/bjo.71.1.2.
215. van Zijderveld R, Ince C, Schlingemann RO. Orthogonal polarization spectral imaging of conjunctival microcirculation. *Graefes Arch Clin Exp Ophthalmol*. March 2014. doi:10.1007/s00417-014-2603-9.
216. Groner W, Winkelman JW, Harris AG, et al. Orthogonal polarization spectral imaging: a new method for study of the microcirculation. *Nat Med*. 1999;5(10):1209-1213. doi:10.1038/13529.
217. Crihalmeanu S, Ross A. Multispectral scleral patterns for ocular biometric recognition. *Pattern Recognit Lett*. 2012;33(14):1860-1869. doi:10.1016/j.patrec.2011.11.006.
218. Fischer MJM, Uchida S, Messlinger K. Measurement of meningeal blood vessel diameter in vivo with a plug-in for ImageJ. *Microvasc Res*. 2010;80(2):258-266. doi:10.1016/j.mvr.2010.04.004.
219. Labsphere Inc. Optical-Grade Spectralon® Diffuse Reflectance Material Specially Fabricated for Optical Components. https://www.labsphere.com/wp-content/uploads/2015/06/Spectralon-Optical-Grade.pdf. Accessed November 4, 2015.
220. Briley-Saebo K, Bjornerud A. Accurate de-oxygenation of ex vivo whole blood using sodium dithionite. *Proc Intl Soc Mag Reson Med*. 2000;8:2025.
221. Instrumentation Laboratory. GEM OPL Operators Manual (Rev. 2). 2003.
222. Jiang H, Ye Y, Cabrera D, et al. Human conjunctival microvasculature assessed with a retinal function imager (RFI). *Microvasc Res*. 2013;85:134-137. doi:10.1016/j.mvr.2012.10.003.
223. Zijlstra WG, Buursma A, Falke HE, Catsburg JF. Spectrophotometry of hemoglobin: absorption spectra of rat oxyhemoglobin, deoxyhemoglobin, carboxyhemoglobin, and methemoglobin. *Comp Biochem Physiol*. 1994;107(I):161-166.
224. Fine I, Loewinger E, Weinreb a, Weinberger D. Optical properties of the sclera. *Phys Med Biol*. 1985;30(6):565-571.

http://www.ncbi.nlm.nih.gov/pubmed/21806288.

225. Williams AJ. Assessing and interpreting arterial blood gases and acid-base balance. *Br Med J*. 1998;317(7167):1213-1216.
226. Verma A, Roach P. The interpretation of arterial blood gases. *Aust Prescr*. 2010;33(4):124-129.
227. Sharifipour F, Baradaran-Rafii A, Idani E, Zamani M, Jabbarpoor Bonyadi MH. Oxygen therapy for acute ocular chemical or thermal burns: a pilot study. *Am J Ophthalmol*. 2011;151(5):823-828. doi:10.1016/j.ajo.2010.11.005.
228. Menezo V, Lightman S. The eye in systemic vasculitis. *Clin Med*. 2004;4(3):250-254. doi:10.1016/S0140-6736(04)17554-5.
229. Nanba K, Schwartz B. Increased diameter of the anterior ciliary artery with increased intraocular pressure. *Arch Opthalmol*. 1986;104(11):1652-1655. doi:10.1001/archopht.1986.01050230090039.
230. Early Treatment Diabetic Retinopathy Study Research Group. Classification of diabetic retinopathy from fluorescein angiograms: ETDRS report number 1. *Ophthalmology*. 1991;98(5):807-822.
231. Wakabayashi T, Ikuno Y. Choroidal filling delay in choroidal neovascularisation due to pathological myopia. *Br J Ophthalmol*. 2010;94(5):611-615. doi:10.1136/bjo.2009.163535.
232. Gewaily DY, Grunwald JE, Pistilli M, et al. Delayed patchy choroidal filling in the comparison of age-related macular degeneration treatments trials (CATT). *Am J Ophthalmol*. 2014;158(3):525-531.e2. doi:10.1016/j.ajo.2014.06.004.
233. Saito J, Roxburgh STD, Sutton D, Ellingford A. A new method of image analysis of fluorescein angiography applied to age-related macular degeneration. *Eye*. 1995;9:70-76.
234. Zhao Y, MacCormick IJ, Parry DG, et al. Automated detection of leakage in fluorescein angiography images with application to malarial retinopathy. *Sci Rep*. 2015;5(April):10425. doi:10.1038/srep10425.
235. Orth DH, Patz A. Retinal branch vein occlusion. *Surv Ophthalmol*. 1978;22(6):357-376. doi:10.1016/0039-6257(78)90132-7.
236. Yannuzzi, Lawrence A, Rohrer KT, et al. Fluorescein angiography

complication survey. *Ophthalmology*. 1989;93(5):611-617.

237. Kwiterovich KA, Maguire MG, Murphy RP, et al. Frequency of adverse systemic reactions after fluorescein angiography: results of a prospective study. *Ophthalmology*. 1991;98(7):1139-1142.
238. Lira RPC, Oliveira CLDA, Marques MVRB, Silva AR, Pessoa CDC. Adverse reactions of fluorescein angiography: a prospective study. *Arq Bras Oftalmol*. 2007;70(4):615-618.
239. Saine PJ, Tyler ME. *Ophthalmic Photography: Retinal Photography, Angiography, and Retinal Imaging.* Second edi. Butterworth-Heinemann; 2002.
240. Bischoff PM, Flower RW. Ten years experience with choroidal angiography using indocyanine green dye: a new routine examination or an epilogue? *Doc Ophthalmol*. 1985;60(3):235-291.
241. Ophthalmic Photographers Society. Interpretation of fluorescein angiography. http://www.opsweb.org/?page=FAinterpretation. Published 2016. Accessed January 22, 2016.
242. Novotny HR, Alvis DL. A method of photographing fluorescence in circulating blood in the human retina. *Circulation*. 1961;24(1):82-86. doi:10.1161/01.CIR.24.1.82.
243. Liang Q, Wong DT, Liang H. The retinal venous laminar flow in fluorescein angiography may be a permanent phenomenon. *IOVS*. 2011;52(14).
244. Witkin AJ, Alshareef RA, Rezeq SS, et al. Comparative analysis of the retinal microvasculature visualized with fluorescein angiography and the retinal function imager. *Am J Ophthalmol*. 2012;154(5):901-907.e2. doi:10.1016/j.ajo.2012.03.052.
245. Izhaky D, Nelson D a., Burgansky-Eliash Z, Grinvald A. Functional imaging using the retinal function imager: Direct imaging of blood velocity, achieving fluorescein angiography-like images without any contrast agent, qualitative oximetry, and functional metabolic signals. *Jpn J Ophthalmol*. 2009;53(4):345-351. doi:10.1007/s10384-009-0689-0.
246. Fercher AF, Briers JD. Flow visualization by means of single-exposure speckle photography. *Opt Commun*. 1981;37(5):326-330. doi:10.1016/0030-4018(81)90428-4.

247. Kim DY, Fingler J, Werner JS, Schwartz DM, Fraser SE, Zawadzki RJ. In vivo volumetric imaging of human retinal circulation with phase-variance optical coherence tomography. *Biomed Opt Express*. 2011;2(6):1504-1513. doi:10.1364/BOE.2.001504.
248. Xu J, Han S, Balaratnasingam C, et al. Retinal angiography with real-time speckle variance optical coherence tomography. *Br J Ophthalmol*. 2015;99(10):1315-1319. doi:10.1136/bjophthalmol-2014-306010.
249. Edelstein AD, Tsuchida MA, Amodaj N, Pinkard H, Vale RD, Stuurman N. Advanced methods of microscope control using μManager software. *J Biol Methods*. 2014;1(2):10. doi:10.14440/jbm.2014.36.
250. Sliney D, Aron-Rose D, Delori F, et al. Adjustment of guidelines for exposure of the eye to optical radiation from ocular instruments. *Appl Opt*. 2005;44(11):2162-2176. doi:10.1364/AO.44.002162.
251. Germann WJ, Stanfield CL. *Principles of Human Physiology*. Second Ed. Benjamin Cummings; 2005.
252. Gorman A, Fletcher-Holmes DW, Harvey AR. Generalization of the Lyot filter and its application to snapshot spectral imaging. *Opt Express*. 2010;18(6):5602-5608.
253. Mordant DJ, Al-Abboud I, Muyo G, et al. Spectral imaging of the retina. *Eye*. 2011;25(3):309-320. doi:10.1038/eye.2010.222.
254. Gorman AS. Snapshot spectral imaging using image replication and birefringent interferometry: principles and applications. 2010.
255. Schneider C a, Rasband WS, Eliceiri KW. NIH Image to ImageJ: 25 years of image analysis. *Nat Methods*. 2012;9(7):671-675. doi:10.1038/nmeth.2089.
256. VLFEAT.org. http://www.vlfeat.org/. Accessed January 29, 2016.
257. Franssen L, Coppens JE, van den Berg TJTP. Grading of iris color with an extended photographic reference set. *J Optom*. 2008;1(1):36-40. doi:10.3921/joptom.2008.36.
258. Haynes JM. The ear as an alternative site for a pulse oximeter finger clip sensor. *Respir Care*. 2007;52(6):727-729.
259. Johnson CL, Ann AM, Hill PD. Comparison of pulse oximetry measures in a healthy population. *MEDSURG Nurs*. 2012;21(2):70-75.
260. Mitchell L. Improving retinal image selection and registration of video

sequences for dye-free angiography. University of Glasgow, School of Physics and Astronomy. *Unpubl Undergrad honours report*. 2016.

261. Ghassemi P, Wang J, Melchiorri AJ, et al. Rapid prototyping of biomimetic vascular phantoms for hyperspectral reflectance imaging. *J Biomed Opt*. 2015;20(12):121312. doi:10.1117/1.JBO.20.12.121312.
262. Lemaillet P, Ramella-Roman JC. Dynamic eye phantom for retinal oximetry measurements. *J Biomed Opt*. 2014;14(6):64008. doi:10.1117/1.3258669.
263. Gramatikov BI. Modern technologies for retinal scanning and imaging: an introduction for the biomedical engineer. *Biomed Eng Online*. 2014;13(1):52. doi:10.1186/1475-925X-13-52.
264. Oosterhuis, J.A Bakker R., van den Berge K. Binocular fundus reflectometry. *Opthal Res*. 1970;1:109-123.
265. Bakker RB, van Odijk EJA, Oosterhuis JA. Binocular fundus reflectometry and ophthalmodynamometry in carotid occlusion. *Neurology*. 1979;29(January):108-111.
266. Comer JT, Lopez BL. Evaluation of pulse oximetry in sickle cell anemia patients presenting to the emergency department in acute vasoocclusive crisis. *Am J Emerg Med*. 1996;14(1):16-18. doi:http://dx.doi.org/10.1016/S0735-6757(96)90005-4.
267. Mackenzie IS, Morant S V, Bloomfield G a, MacDonald TM, O'Riordan J. Incidence and prevalence of multiple sclerosis in the UK 1990-2010: a descriptive study in the General Practice Research Database. *J Neurol Neurosurg Psychiatry*. 2014;85(1):76-84. doi:10.1136/jnnp-2013-305450.
268. Anesthesia UK. Spinal cord. http://www.frca.co.uk/article.aspx?articleid=100360. Published 2004. Accessed February 22, 2016.
269. Lesage F, Brieu N, Dubeau S, Beaumont E. Optical imaging of vascular and metabolic responses in the lumbar spinal cord after T10 transection in rats. *Neurosci Lett*. 2009;454(1):105-109. doi:10.1016/j.neulet.2009.02.060.
270. Sharma V, He J-W, Narvenkar S, Peng YB, Liu H. Quantification of light reflectance spectroscopy and its application: determination of hemodynamics on the rat spinal cord and brain induced by electrical stimulation. *Neuroimage*. 2011;56(3):1316-1328.

doi:10.1016/j.neuroimage.2011.01.020.

271. Cadotte DW, Mariampillai A, Cadotte A, et al. Speckle variance optical coherence tomography of the rodent spinal cord: in vivo feasibility. *Biomed Opt Express*. 2012;3(5):911-919. doi:10.1364/BOE.3.000911.
272. Davalos D, Akassoglou K. In vivo imaging of the mouse spinal cord using two-photon microscopy. *J Vis Exp*. 2012;(59):e2760. doi:10.3791/2760.
273. Qimaging. Retiga 4000R datasheet. http://www.qimaging.com/products/datasheets/Retiga4000R.pdf. Accessed February 22, 2016.
274. Topac Inc. Relationship between Salt Solution and Sugar Concentration (Brix) and refractive index at 20°C. http://www.topac.com/salinity_brix.html. Published 2014. Accessed February 22, 2016.
275. Flurotherm. FEP properties. http://www.fluorotherm.com/technical-information/materials-overview/fep-properties/. Accessed February 22, 2016.
276. Nikon. Nikon D300s specifications. http://imaging.nikon.com/lineup/dslr/d300s/spec.htm. Accessed February 24, 2015.
277. Friebel M, Helfmann J, Meinke M. Influence of osmolarity on the optical properties of human erythrocytes. *J Biomed Opt*. 2010;15(5):055005-055005-6. doi:10.1117/1.3486542.
278. van der Putten M. Deep tissue in vivo oximetry of rats and mice with multispectral imaging. Retinal Oximetry Workshop 2016. http://www.gla.ac.uk/schools/physics/oximetryworkshop/videos of presentations/. Published 2016. Accessed March 8, 2016.
279. Kerrison JB, Flynn T, Greem Richard W. Retinal pathologic changes in multiple sclerosis. *Retina*. 1994;14(5).
280. Broadfoot K., Gloster J, Greaves D. Photoelectric method of investigating the amount and oxygenation of blood in the fundus oculi. *Br J Ophthalmol*. 1961;45:161-182.
281. Gloster J. Fundus oximetry. *Exp Eye Res*. 1967;6(3):187-212.
282. Trokel S. Photometric study of ocular blood flow in man. *Arch Ophthalmol*. 1964;71:528-530.
283. Lavenstein B, Milder B, Winkelman JZ, Zappia RJ, Gay AJ, Louis S. Retinal

and choroidal circulation in rabbits. *Arch Ophthalmol*. 1971;85:723-729.

284. Posthumus Meyjes F, De Wilde A. Study of the circulation in the carotid artery with the aid of binocular fundus reflectometry. *Electroencephalogr Clin Neurol*. 1977;43:425-428.
285. Drasdo N, Fowler CW. Non-linear projection of the retinal image in a wide-angle schematic eye. *Br J Ophthalmol*. 1974;58(8):709-714. doi:10.1136/bjo.58.8.709.
286. Laing RA, Danisch LA, Young LR. The choroidal eye oximeter: an instrument for measuring oxygen saturation of choroidal blood in vivo. *IEEE Trans Biomed Eng*. 1975;22(3):183-195. http://www.ncbi.nlm.nih.gov/pubmed/1116851.
287. Kelvinsong. Diagram of arteries, veins, and capillaries. Wikimedia Commons. https://commons.wikimedia.org/wiki/File:Blood_vessels-en.svg. Published 2013. Accessed March 16, 2016.
288. Noguchi, Rogers S. Micrograph of red blood cells. Wikimedia Commons. https://en.wikipedia.org/wiki/File:Redbloodcells.jpg. Published 2014. Accessed March 16, 2016.
289. Richard Wheeler. Haemoglobin. Wikimedia Commons. https://en.wikipedia.org/wiki/File:1GZX_Haemoglobin.png. Published 2007. Accessed March 16, 2016.
290. Ratznium. The Oxygen Dissociation Curve. Wikimedia Commons. https://commons.wikimedia.org/wiki/File:Oxyhaemoglobin_dissociation_curve.png. Published 2007.
291. Gray H. The anatomy of the eye. Plate 869; Gray's Anatomy. Wikimedia Commons. https://commons.wikimedia.org/wiki/File:Gray869.png. Published 1858. Accessed October 14, 2016.
292. Gray H. Sections of the retina. Plate 881; Gray's Anatomy. Wikimedia Commons. https://commons.wikimedia.org/wiki/File:Gray881.png. Published 1858. Accessed October 14, 2016.
293. Gray H. The long and short ciliary arteries. Plate 873; Gray's Anatomy. Wikimedia Commons. https://en.wikipedia.org/wiki/File:Gray873.png. Published 1858. Accessed October 14, 2016.
294. Gray H. The anterior ciliary arteries. Plate 878; Gray's Anatomy. Wikimedia

Commons. https://en.wikipedia.org/wiki/File:Gray878.png. Published 1858. Accessed October 14, 2016.

295. Thepawn1. Hyperemia of the superficial blood vessels of the conjunctiva. Wikimedia Commons. https://en.wikipedia.org/wiki/File:Hyperemia_conjunctiva.jpg. Published 2010. Accessed October 14, 2016.
296. Sharayanan. Mie scattering. Wikimedia Commons. https://commons.wikimedia.org/wiki/File:Mie_scattering.svg. Published 2007. Accessed March 17, 2016.
297. Epzcaw. Objective speckle. Wikimedia Commons. https://upload.wikimedia.org/wikipedia/commons/1/19/Objective_speckle.jpg. Published 2011.
298. Bacud L. Fluorescein angiography. *Wikimedia Commons*. 2009. https://en.wikipedia.org/wiki/Fluorescein_angiography#/media/File:Fluorescein_angiography.jpg.
299. Mysic. Diagrammatic transverse section of the medulla spinalis and its membranes. Wikimedia Commons. https://commons.wikimedia.org/wiki/File:Gray770-en.svg. Published 2010. Accessed August 4, 2016.
300. Blausen gallery 2014. *Wikiversity, J Med*. 2014;1 (2)(3):144-149. doi:10.15347/wjm/2014.010.